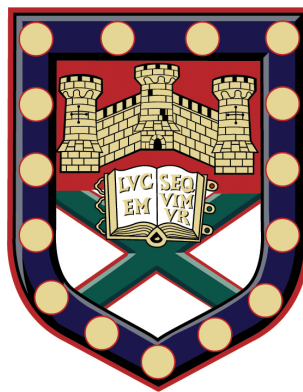# Underwater Acoustic Waves on Structured and Unstructured Plates

Thomas John Graham

Department of Physics and Astronomy

University of Exeter

A thesis submitted for the degree of

*Doctor of Philosophy*

September 2018

# Underwater Acoustics Waves on Structured and Unstructured Plates

Submitted by Thomas John Graham to the University of Exeter as a thesis for
the degree of Doctor of Philosophy
September 2018

I certify that all material in this thesis that is not my own work has been identified
and that no material has previously been submitted and approved for the award of a
degree by this or any other University.

Thomas John Graham
September 2018

Dedicated to

my uncle John Graham

and

my grandparents Jack Goldsworthy,

Sarah Goldsworthy,

and Alice Graham.

# Acknowledgements

# Abstract

This thesis details original experimental work on the observation of the underwater acoustic response of flat plates and acoustic metamaterial-like arrays of holes. There are five main experimental chapters that examine the excitation, detection and analysis of the radiative and evanescent acoustic fields of structured and unstructured surfaces. There are two main types of acoustic excitation and detection methods employed to detect and characterise the transmitted and propagating surface fields of these systems. The first two and the final experimental chapters examine the radiative excitation of plate modes and the remaining two experimental chapters investigate trapped surface modes of structured hole arrays. Using computational Fourier analysis of the acoustic fields, the frequency components and wavevector components are extracted from the spatially scanned time-resolved data. These results are used to characterise the fields by plotting the dispersion relation and identifying the acoustic modes.

The first experimental chapter investigates the Lamb mode responses of mild steel, aluminium alloy and acrylic plates. By comparing the experimentally extracted dispersion relation to an analytic model of layered media, these plates are elastically characterised. Experimentation is performed using ultrasound pulsed through these plates by a transducer and detected using a hydrophone setup with a usable range of 50 to 500 kHz. These results are successfully used to extract values of the elastic modulus and Poisson's ratio for each sample. Whilst results vary, they are reasonably close to that of the industry estimates. This method of non-destructively testing material properties is advantageous compared to the standard methods that render samples unusable after testing.

Plate modes are further investigated in the second experimental chapter which examines the dispersion when an aluminium alloy plate is acoustically excited using a symmetrically aligned source. The experimental results are compared against Finite Element Model (FEM) computational data. The results show a region of transmission where the acoustic fields are focussed. Modelled results of the fields inside the plate agree with the shape of the fields in frequency and wavevector domains. Focussing of the fields is attributed to the region where the symmetric Lamb mode $S_1$ becomes the $S_{1b}$ mode. This region, labelled the Zero or Negative Group Velocity (ZGV or NGV) region, has gained recent interest as a potential application of concentrating sound power. Additionally, a beat pattern in the transmitted fields of the centred plate is observed and an explanation of it is analytically

derived. This focussing phenomenon has applications in enhanced acoustic transmission and absorption.

In the third experimental chapter, lines of holes with differing symmetries are examined. Four samples are scanned using near-field excitation and detection of the surface modes of lines of holes. Single lines of holes, double lines of holes, with mirror and glide symmetry, and three lines of holes, with a pseudo-glide symmetry, are shown to support "trapped" Acoustic Surface Waves (ASWs). These modes are characterised using Fourier analysis of time-domain data to plot the two-dimensional frequency dependent field maps and the evanescent dispersion relation. These experimental results are compared against Finite Element Method (FEM) calculated dispersion. The results show a 2.53 kHz difference between the asymptotic frequency of the mode calculated using a perfectly rigid structure and that of an elastic hole array. This is expanded upon in the fourth experimental chapter, in which the acoustic near-fields of two-dimensional square arrays of holes in aluminium alloy plates are investigated. ASWs are excited and detected over two different thickness plates and characterised using Fourier analysis of the time-domain data. In addition, in-plane acoustic beaming is observed over very narrow frequency ranges. These types of surface mode supporting structures offer a method of controlling the direction and amplitude of sound.

The final results chapter details an array of holes in a pressure-release foam. This sample is excited using a far field source and then the normalised transmission is calculated using a two-dimensionally scanned plane. Spatially scanned frequency dependent results show the propagating fields above the cut-off frequency of the array. Using the spatial plot of the transmitted fields the acoustic cut-off response is plotted. These results are compared to FEM calculated transmission results. In addition, plotting the spatially mapped FEM calculated fields inside the holes shows the Fabry-Perot like resonances inside the holes of the array and the Bessel-function shape of the modes. Comparisons between the experimental and computational results show that the Fabry-Perot-like modes are not visible in the experimental data. In addition, the spatial modulation of the transmitted and reflected diffracting fields is derived. Surfaces that allow the flow of fluid through the structures whilst blocking certain frequencies of sound from propagating through them are already finding commercial applications in air and will have similar sound blocking applications underwater.

The works presented in this thesis has important implications and applications in underwater acoustics that range from the first observations of fundamental and widely used concepts to a method of supporting specific acoustic modes over structured surfaces. Although many of these ideas have been relatively well known in acoustics, they were not observed underwater. In addition, water-solid acoustics proved to be a source of much complexity and interest that this work explores using computational models and analytic theory.

The work presented in this thesis has important implications for and applications in underwater acoustics. These range from initial observations on fundamental and widely-used concepts to a method of supporting specific acoustic modes over structured surfaces. Although many of these ideas are already relatively well-known in the general field of acoustics, they have not yet been observed underwater. Water-solid acoustics proves to be a source of much complexity and interest which this work explores using computational models and analytic theory.

# Contents

# Contents

# Contents

# Contents

# List of Symbols

| | |
|---|---|
| $a$ | Acceleration |
| $A_n$ | The $n^{\text{th}}$ order asymmetric Lamb mode |
| $c$ | Speed of sound in a medium |
| $c_{\text{P}}$ | Compressional wave speed |
| $c_{\text{S}}$ | Shear wave speed |
| $c_{\text{R}}$ | Rayleigh wave speed |
| $c_{\text{SSW}}$ | Scholte-Stoneley wave speed |
| $c_{\text{water}}$ | Speed of sound in water |
| $C_{\text{V}}$ | Heat capacity under constant volume |
| $C_{\text{P}}$ | Heat capacity under constant pressure |
| $d$ | Centre-to-centre distance |
| $d_{\text{pore}}$ | Pore size |
| $E$ | Elastic modulus |
| $f$ | Frequency |
| $\boldsymbol{f}$ | Effective force |
| $F$ | Force |
| $\boldsymbol{g}$ | Body forces |
| $G$ | Shear modulus |
| $\boldsymbol{G}$ | Reciprocal lattice vector or Glide operator |
| $J_{mn}$ | The $m^{\text{th}}$ and $n^{\text{th}}$ mode of the Bessel function |
| $k_{\text{g}}$ | Grating wavevector |
| $K$ | Bulk modulus |
| $L$ | Length |
| $\boldsymbol{k}$ | Wavevector |
| $\boldsymbol{n}$ | Normal vector |
| $n$ | Mode number |
| $p$ | Pressure |
| $P$ | Reflection coefficient |
| $p_{\text{a}}$ | Acoustic pressure |
| $Pr$ | Prandtl number |
| $Q$ | Heat energy |

| | |
|---|---|
| $\boldsymbol{r}$ | Vector |
| $R$ | Radius |
| $Re$ | Reynold's number |
| $S_n$ | The $n^{\text{th}}$ order symmetric Lamb mode |
| $t$ | Time |
| $T$ | Temperature or Transmission coefficient |
| $U$ | Internal energy |
| $v$ | Velocity |
| $V$ | Volume |
| $v_{\text{g}}$ | Group velocity |
| $v_{\text{p}}$ | Phase velocity |
| $w$ | Width |
| $W$ | Work done |
| $z$ | Specific impedance |
| $Z$ | Characteristic impedance |
| $Z_{mn}$ | Zero of the Bessel function |
| $x, y, z$ | Spatial position |
| | |
| $\alpha$ | Coefficient of attenuation |
| $\beta$ | Compressibility |
| $\delta$ | Displacement |
| $\delta_{\text{V}}$ | Viscous boundary thickness |
| $\delta_{\text{T}}$ | Thermal boundary thickness |
| $\delta_{ij}$ | Kronecker delta |
| $\varepsilon ij$ | Strain |
| $\eta$ | Dynamic viscosity |
| $\eta_{\text{B}}$ | Bulk viscosity |
| $\kappa$ | Heat diffusivity |
| $\lambda$ | Wavelength |
| $\lambda_{\text{g}}$ | Grating pitch |
| $\nu$ | Poisson's ratio |
| $\rho$ | Density |
| $\sigma_{ij}$ | Stress |
| $\tau$ | Time period |
| $\psi$ | Wavefunction |
| $\omega$ | Angular frequency |
| $\theta, \gamma$ | Angle |
| $\Gamma, X, M, K$ | Points of high symmetry in reciprocal space |

# Contents

# Initialisms and Acronyms

| | |
|---|---|
| ASW | Acoustic Surface Wave |
| BZ | Brillouin Zone |
| CNC | Computer Numerical Control |
| CW | Continuous Wave |
| EVA | Ethylene-Vinyl Acetate |
| FEM | Finite Element Method |
| FFT | Fast Fourier Transform |
| KH | Krohn-Hite amplifier |
| MEMS | MicroElectroMechanical Systems |
| NDT | Non-Destructive Testing |
| NGV | Negative Group Velocity |
| PA | Precision Acoustics |
| PML | Perfectly Matched Layer |
| SAW | Surface Acoustic Wave |
| SSW | Scholte-Stoneley Wave |
| TTI | Thurlby Thandar Instruments amplifier |
| ZGV | Zero Group Velocity |

# Contents

# Chapter 1

# Introduction

## 1.1 Historical Overview

Acoustics is the study of sound: a vibration in the particles that constitute solids, gases and liquids. The study of sound is one of the earliest fields of science to be studied, with written records by Pythagoras and Aristotle dating back to the time of the Ancient Greeks[1]. This thesis focusses on underwater and solid bound ultrasound, and the progression towards this area of acoustics research has been by no means linear. Studies in the fields of in-air acoustics, underwater acoustics, bulk acoustics, acoustics in structured materials and wave theory have impacted upon this topic.

Some of the earliest research was linked to music theory. In particular, between 1590 and 1627 Vincenzo Galilei, Galileo Galilei and Marin Mersenne remarked on the modes of vibrating strings[2,3]. Later that century, in 1687, Sir Isaac Newton was the first to derive the speed of sound in air in *Philosophiae Naturalis Principia Mathematica*[4]. This was later adapted by Pierre-Simon Laplace to calculate a more accurate approximation including the thermal properties[5,6] set out by Gustav Kirchoff[7]. Parallel to these airborne studies of sound, underwater scientific studies date back to 1490 when Leonardo Da Vinci noted[8], "If you cause your ship to stop and place the head of a long tube in the water and place the other extremity to your ear, you will hear ships at great distances." Yet, it was not until 1827 that an accurate measure of the speed of sound underwater was performed on Lake Geneva by Jean-Daniel Colladon, using the rudimentary equipment of an underwater bell and a listening device[9].

The modern age of electronic underwater acoustics was sparked by the development in transduction and the invention of piezoelectric devices, whereby sound could be converted into electrical currents and vice versa. The invention of speech devices is collectively attributed to scientists such as Jamie Joules Jacques and Pierre Currie[10] between 1840 and 1880. The potential of various transduction mechanisms was demon-

strated by inventors such as Alexander Graham-Bell with his membrane-devices[11]. The applications of underwater sound became clear after the sinking of the ship Titanic in 1912. A month following the disaster, Lewis F. Richardson filed a patent for an underwater echo locating device to detect icebergs[8], although unfortunately the device was not built. It was in 1914 that the Canadian-American inventor Reginald Fessenden created a coil transducer that was used to echo locate underwater[12,13] and which was able to detect icebergs. The outbreak of World War I marked an increased drive to develop SONAR (SOund Navigation And Ranging) as submarine warfare took off. Although early SONAR was found to be unreliable, the development of cost-effective methods of detecting and projecting sound, audible and ultrasound, with synthetic piezoelectric devices became a top priority of international naval research laboratories. During this period the first hydrophones were used to passively record underwater sound. Post-WWI piezoelectric devices improved dramatically and in 1940 Paul Langevin created an improved composite transducer using quartz[14].

Sound travels through any elastic media and can propagate through bulk solids. The study of bulk and surface waves was accelerated through the research of the prolific acoustician Lord Rayleigh (John W. Strutt). His ideas were set out in *The Theory of Sound*[15] in 1894, where he developed the formal theory of sound including surface wave phenomena, non-linear effects and many other acoustic concepts that are still used today. Furthermore, he defined the first the Surface Acoustic Wave (SAW), the Rayleigh Wave, that propagates at the interface between a solid and vacuum. Rayleigh's work was adapted to plates in the early twentieth century to the coupling between two Rayleigh-like interfaces by Horace Lamb[16], as Lamb waves. Additional SAWs were classified by Robert Scholte as Scholte-Stoneley waves[17], which are waves at an interface between two elastic media. The underwater dispersive nature of Lamb modes shows enhanced transmission or absorption over specific ranges and has been examined in varying degrees of detail more recently[18,19,20,21,22,23,24]. Mapping the dispersive properties of elastic solids is a method of acoustic tomography or Non-Destructive Testing (NDT). This is an emerging technique, the use of which ranges from material characterisation to defect identification[25,26,27,28,29,30,31].

The reflection of sound at the interface between a bulk and a fluid is of a particular interest in this work. These bulk solid materials can be shaped to support acoustic resonances. This idea was exploited musically long before it was understood scientifically. Hermann von Helmholtz wrote extensively on music and acoustic theory in the nineteenth century. Notably, he built a device called a Helmholtz resonator that was able to resonate at a select frequency[32]. Much of his work explored acoustic phenomena such as whispering gallery modes[32,33], although he worked on theoretical acoustics too and is known for the Helmholtz wave equation. However, Rayleigh appears to be the

first to define the acoustic boundary conditions[34] fundamental to the understanding of these structures. With these definitions, simple structures were then explored mathematically, with Philip M. Morse explaining boundary conditions for the geometry of pipes[35]. Since then, a variety of studies have explained the dispersion of sound waves within acoustic waveguides with different boundaries[36,37,38,39,40].

Parallel to these studies, research on other wave types has been the driving force behind much of structured acoustics. In 1807, Thomas Young, who worked in optics and acoustics, demonstrated using a double slit experiment that two acoustic or light waves diffracting from slits create an interference pattern as they interact[41,42], showing that wave intensity can be locally modulated with the use of structure. Fundamental structures that support optical resonance were further described by scientists such as Charles Fabry and Alfred Perot, who detailed a type of resonance between two flat surfaces in 1899[43,44]. Extending the research on such devices led to the development of periodically structured surfaces, patterned with resonant features, that support "trapped" surface waves in photonics and phononics[45,46,47,48].

Practical uses of structuring solids to manipulate electro-magnetic and acoustic waves date back to World War II, however recent interest has been stimulated by an eruption of work on structured surfaces and acoustic metamaterials, materials that are designed to modulate wave energy in a way not normally found in nature. This recent interest is in part due to the work by Ebbesen et al. in 1998 on the "extraordinary-optical-transmission" through "tunable" sub-wavelength hole arrays[49], in which the coupling between the "surface-plasmon" excitations of the structured array and the transmitted signal was demonstrated. Pendry later showed that it was possible to mimic this effect in the microwave regime[48] by exciting a "spoof-surface-plasmon" over a structured array of sub-wavelength cavities. Consequently, the same "spoof" effect was realised in air as an "Acoustic Surface Wave" (ASW) excitation over structured arrays of simple resonators[50]. A highly localised and slow travelling ASW has potential applications in acoustic sensing, energy harvesting, signal processing and material characterisation. Most research into ASWs has been undertaken in air[51,52,53] with some studies underwater on two-dimensional structured materials that support surface waves. These include grooves[54,55] and 2D arrays that have been modulated using material-filled arrays of holes[56]. Craster et al. and Cummer et al. have recently summarised the possible broad applications of metamaterials in acoustics research[57,58].

The aim of the research presented in this thesis is to set up an experiment that can be used to study structured and unstructured underwater surfaces. The following work explores a variety of underwater acoustic materials with a range of geometries that demonstrate the manipulation of sound in novel ways.

## 1.2 Thesis Outline

The work detailed in this thesis describes original experimental and computational studies of underwater ultrasound over flat unstructured and structured plates that support acoustic modes. Notably, this investigation includes methods of acoustic tomography, detecting acoustic surface waves and observing the acoustic cut-off frequency. This work aims to add to the research on trapped surface waves in electromagnetism and in air acoustics by applying these concepts to underwater metamaterial-like studies. The structure of the thesis is broadly split into two parts: flat unstructured plates (chapters 4 and 5) and structured plates with lines and arrays of resonating holes (chapters 6, 7 and 8).

Chapter 2, the background theory, covers the fundamental ideas of underwater acoustics, with derivations of the acoustic wave equation and the Navier-Stokes equations. Using these, the importance of thermal-viscous effects in bulk and at a boundary are discussed. Acoustic boundary conditions are introduced and then resonating structures that exploit them are shown. The bulk elastic properties of solids are also introduced and the waves at the interface between two elastic media are described, with example dispersion relations shown. A combination of the techniques developed are then used to describe acoustic waves trapped at the interface of a structured surface. Lastly, the effects of periodicity are explored with the dispersion relation detailed.

Chapter 3 describes the experimental methodology and the data analysis used throughout this work. Here reasoning for the selection of sample materials is given, followed by the experimental setup and pulse method used to explore the acoustic properties of these materials, detailing the ultrasonic sources and detectors. The explanation of the technique is split into the far-field and near-field scanning techniques. To characterise each source-detector pair, the transmitted fields are spatially plotted. Here the speed of sound in the water tank used throughout this work is extracted using a line scan of travelling ultrasound. Further to this, plots are shown of the computational Fourier methods used throughout this work. These methods include time windowing, zero padding and the use of window functions to improve Fourier analysis. Finally, a discussion of the Finite Element Method (FEM) modelling used to verify experimental results in this work concludes this chapter.

The first results chapter is presented in chapter 4, Acoustic Tomography. Here aluminium alloy, mild steel and acrylic plates are investigated using the broadband ultrasound from a source positioned at a finite distance from the sample to excite the response over a range of angles. The experimental Lamb modes of plates are compared to the dispersion relation of the transmitted fields using Leonid Brekhovskikh's plate theory. This method is used to obtain the elastic material properties of the plates: the

Poisson's ratio and the elastic modulus. Although NDT is widely used, this simple method is usable between 50 and 500 kHz. Elastic parameter results obtained are mostly at or close to industry estimates. In the case of aluminium alloy, FEM modelling is used to verify the technique and it is in good agreement. This chapter has a bearing on the rest of the thesis as the same aluminium alloy is used for the majority of this work and its essential characteristics had to be parametrised.

Chapter 5, further investigates the dispersion through a single aluminium alloy plate, focussing on the dispersion of sound transmitted through the plate near the normal incidence. The sample is excited symmetrically with the source central to the plate. The resultant response shows "acoustic beaming" in the frequency domain and dispersion relation, attributed to the regions where symmetric modes of "Negative Group Velocity" (NGV) exist. Spatial plots normal to the surface uncover the frequency dependent shape of the transmitted fields and depict the focussing effect of the symmetric excitation of the plate. Additionally, a beat pattern between the plane wave excitation of the plate and the Lamb mode fields is experimentally and computationally observed, and then explained analytically. These results show enhanced focussing with up to 130% transmission through the sample. FEM modelling is used to plot the fields inside the plate and further investigate the NGV region.

In chapter 6 a near-field scanning technique is used to measure the directional dispersion of one-dimensional arrays of open-ended holes in an aluminium alloy. By varying the number of rows and the form of the symmetry, the dispersion properties of ASWs these structures support are documented. Glide symmetric structures are seen to give modes with linear dispersion over a larger frequency range because of the absence of a band gap at the Brillouin Zone (BZ) boundary. These structures are demonstrated as possible sources of "slow" surface waves. These results are compared to computational FEM models of the array both as perfectly rigid and with the elastic properties of the plate included. These results demonstrate a 2.53 kHz difference between the dispersions at the BZ boundary and signify the importance of the elastic properties of these structures.

Following on naturally from the previous chapter, chapter 7 investigates ASWs bound to the surface of two-dimensional square arrays of open-ended on holes in aluminium alloy. Results of Fourier analysed experimental data demonstrate the presence of ASWs supported on two different thickness water filled hole arrays, with the same pitch and radius holes. Experimental results are compared against FEM-modelled dispersion relations, with good agreement between the two in both cases. Additionally, in-plane acoustic beaming is observed over a very narrow frequency range in both frequency and wavevector results. Finally, the pressure fields in and plate deformation around the holes is visualised using FEM modelling. The resonant frequency reduction

seen between the asymptotic frequencies of the rigid and elastic cases presented in both chapters 6 and 7 is explained following a Biot treatment of the elastic holes.

In the last results chapter, chapter 8, a pressure-release hole array is examined using a radiative source to excite the sample from a distance. The results show a clear cut-off frequency in the normalised mean amplitude of the transmitted signal through the array. Spatially plotted transmission through the array shows the below and above cut-off frequency transmission, confirming the negligible transmission below the cut-off. These results are compared to an FEM model of a perfect pressure-release hole array. The model results show Fabry-Perot like oscillations above the cut-off that are not seen in the experimental data.

The final chapter, chapter 9, summarises the work covered in this thesis and details possible extensions of the work. This includes works in progress that have been established experimentally as well as other ideas that may prove to be worthwhile in the near future.

In addition, appendix A details the point-like source used to excite samples in chapters 6 and 7. Appendix B is the derivation of the spatial modulation of the transmitted fields of the flat plate in chapter 5 and appendix C is a derivation of the spatial modulation of the transmitted and reflection fields around a pressure-release array of holes in chapter 8. Finally, appendix D details the conferences at which this work was presented orally and as posters.

# Chapter 2

# Background

## 2.1 Introduction

Acoustic surface wave phenomena have been studied since the late nineteenth century. Rayleigh explained the boundary between solid materials and air[34]. This was adapted in the early twentieth century to plates and the coupling between two Rayleigh-like interfaces by Horace Lamb[16]. Further to this, J. G. Scholte showed that there are additional waves at the interface between two elastic media, liquid-solid and solid-solid interfaces[17]. Parallel to these, studies of sound-structure interactions date back to the late nineteenth and early twentieth century[15,32]. More recently, the focus has been on the development of surface wave supporting structures called metamaterials and other metamaterial-like systems. These structures make use of near to sub-wavelength features that have been specifically designed to manipulate wave energy and have "tunable" applications.

Acoustic metamaterials use the coupling between the modes supported by the scattering periodic features and the spaces between them to create materials that can project, absorb and direct acoustic energy[57,59]. There are many tunable applications of these materials ranging from defect detection, acoustic energy harvesting, sound absorption and transmission. Underwater, these studies have mainly focussed on the properties of the transmitted fields through metasurfaces whilst generally neglecting their in-plane properties. This area of research has gained a lot of interest recently, in part due to greater access to high-end personal computing and purpose-built software that allow multiple domains of physics to be modelled alongside each other.

The following work will endeavour to bridge the gap between surface wave and metamaterial research, looking at how in-plane elastic waves interact with in-plane surface waves. The research discussed throughout this thesis will cover a range of topics in acoustics looking at material characterisation, boundary conditions, one and

two-dimensional structured surfaces. All experimental work will be conducted underwater and in the ultrasonic regime. First the basic acoustic theory and literature in underwater systems will be described. Any other relevant theory will be mentioned in further chapters as and when it is necessary to explain further. The following derivations in this chapter are based on the works of John William Rayleigh[15], Lawrence E. Kinsler[60], David Cheeke[61] and Benny Lautrup[62].

## 2.2 Fluid Acoustics

To fully describe fluid acoustics mathematically it is necessary to make assumptions that determine the way in which a fluid reacts to acoustic forces. In this section the assumptions and approximations made about the way in which fluid molecules, modelled as particles, interact individually and as a volume will be outlined. For simplicity this work will first describe the nature of a lossless sound wave travelling through a fluid. Later sections of this chapter explain more complicated bulk and structured acoustic cases.

### 2.2.1 A Travelling Pressure Wave

Sound is a pressure wave that will propagate through any medium having mass, density and elasticity. Underwater systems are made up of sub-nanometre size ($\approx 0.275$ nm[63]) molecules that are constantly colliding with each other semi-elastically when perturbed by a change in acoustic pressure, $p_\mathrm{a}$. A plane pressure wave incident on particles of a lossless fluid medium is examined to visualise a simplified travelling sound wave. A monochromatic plane wave source acting on a fluid is depicted in Figure 2.1.

This plot shows the instantaneous position of a vibrating plane source driving the local position of particles in a fluid medium in $x$. This change in position causes a region of the fluid to locally undergo a change in pressure, $\Delta p$. On average the particles of fluid oscillate around a centre point in $x$ with a maximum displacement of the plate and particles proportional to the peak pressure change $\Delta p_\mathrm{max}$. This oscillatory motion has a time period, $\tau$, a frequency, $f = 1/\tau$, and wavelength, $\lambda$. The background pressure for the majority of this work is assumed to be atmospheric pressure, $p_\mathrm{atm} \approx 10^5$ Pa. Note particle size is assumed to be far less than the wavelength of sound and is near point like, neglecting any orientation effects. This simplified example of a compression wave (P-wave) travelling through a fluid is applicable to realistic planar sources within a few wavelengths of the source. As a wave propagates further into a fluid the field becomes complicated by particle-particle interactions and where motion is not confined to one-dimension. This is mainly due to the non-particle-like nature of the molecules.
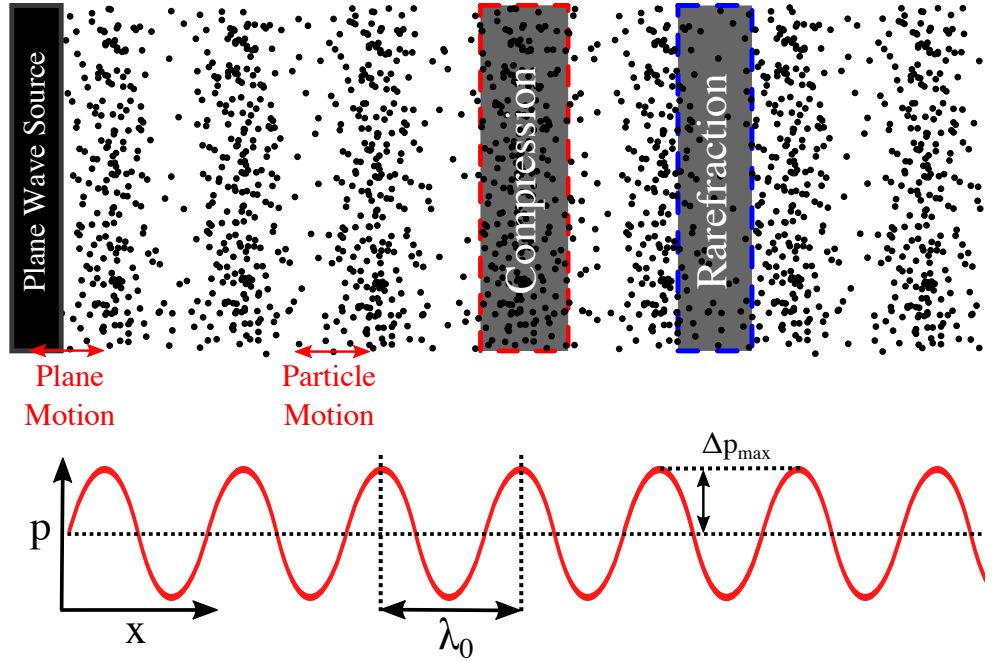
**Figure 2.1:** A 2D graphical representation of a vibrating plane wave (bar) source exciting a sound wave in the $x$ direction. The oscillation of fluid particles responds to changes in relative pressure, $\Delta p$, with maximum pressure, $\Delta p_{\mathrm{max}}$.

This chapter describes how sound waves are further complicated when viscous effects, thermodynamic effects, elastic motion and interface effects are introduced. But first the general form of the wave equation using some common approximations of acoustics in fluids is derived.

### 2.2.2 Equation of State

The first law of thermodynamics states that the change to the internal energy of a system is defined as $dU = dQ \pm dW$. Here $U$ is the internal energy, $W$ is the work done and $Q$ is heat energy. In the acoustic case the work done on the system is related to pressure as $dU = -pdV$, where $p$ is pressure and $dV$ is the change in volume. The internal energy of the system is a function of temperature at a constant volume, $dU = \mathrm{n}C_{\mathrm{v}}dT$, and at a constant pressure, $dU = \mathrm{n}C_{\mathrm{p}}dT$. Here, $C_{\mathrm{v}}$ and $C_{\mathrm{p}}$ are the heat capacities of the fluid at a constant volume and pressure, respectively. Summing the energies obtains:

$$\mathrm{n}C_{\mathrm{v}}dT = \mathrm{n}C_{\mathrm{p}}dT - pdV. \tag{2.1}$$

It is assumed for the purposes of this work that there is no transfer of heat during the elastic collisions between the particles of our fluid. This is called an adiabatic process. The assumption means $pV = $ constant which is equivalent to $p = k'\rho$ where $\rho$ is the

density of the material defined as the mass $m$ contained in a volume $V$ and $k$ is a constant. $k'$ can be defined as $k' = \partial p/\partial \rho$. Equation 2.1 can be expressed in terms more familiar to acoustics:

$$p_{\mathrm{a}} = \left(\frac{\partial p}{\partial \rho}\right)_{\mathrm{S}},\tag{2.2}$$

where acoustic pressure $p_{\mathrm{a}} = \Delta p = p - p_0$, $\rho$ is the density and $S$ is entropy.

The assumption that water is are adiabatic is widely accepted as a good approximation. More complicated models will assume the fluid to be isothermal ($dT = 0$), rather than adiabatic. But the discrepancy between the adiabatic and isothermal bulk modulus is small $(0.1\%)$[9] for the case of water, so thermal effects will be ignored for the majority of this work. Although the thermal properties of acoustic fluids will be revisited in sections 2.2.9.2 and 2.2.11.

### 2.2.3 Continuity Equation

A standard acoustic assumption to make of a fluid medium is conservation of mass or the continuity equation. This relates the motion of the particles in or out of a volume, $V$, to the change in density in that volume over time. This is mathematically described as[60,9]:

$$\frac{\partial \rho}{\partial t} + \boldsymbol{\nabla} \cdot (\rho \boldsymbol{v}) = 0,\tag{2.3}$$

where $\boldsymbol{v}$ is the fluid particle velocity, $t$ is time and $\boldsymbol{\nabla}$ is the gradient operator,

$$\boldsymbol{\nabla} = \frac{\partial}{\partial x}\hat{\boldsymbol{x}} + \frac{\partial}{\partial y}\hat{\boldsymbol{y}} + \frac{\partial}{\partial z}\hat{\boldsymbol{z}}.$$

### 2.2.4 Conservation of Momentum

As stated in section 2.2.1, molecular shape and thus orientation may play a key role in how particles collide. In a many-particle system the vast combination of collisions means that the system is non-trivial to predict. To simplify this, the fluid is treated as a macroscopically flowing elastic medium.

In 1827 Augustin-Louis Cauchy rewrote Newton's second law of motion ($\boldsymbol{F} = m\boldsymbol{a}$) in terms of the effective force acting on a volume,

$$\boldsymbol{f} = \int_V \rho \left(\frac{\partial \boldsymbol{v}}{\partial t} + (\boldsymbol{v} \cdot \boldsymbol{\nabla})\boldsymbol{v}\right) dV.\tag{2.4}$$

Here, $V$ is the volume of the fluid.

This uses the local material time derivative, $\frac{D}{Dt}$, commonly used in fluid dynamics:

$$\frac{D}{Dt} = \frac{\partial}{\partial t} + \boldsymbol{v} \cdot \boldsymbol{\nabla}. \tag{2.5}$$

Cauchy redefined the total momentum equation for a fluid as:

$$\frac{D\boldsymbol{v}}{Dt} = \frac{1}{\rho}\nabla \cdot \boldsymbol{\sigma} + \boldsymbol{g}. \tag{2.6}$$

Here, $\boldsymbol{g}$ is the body force and $\boldsymbol{\sigma}$ is the three-dimensional stress tensor[64]:

$$\boldsymbol{\sigma} = \begin{bmatrix} \sigma_{xx} & \tau_{xy} & \tau_{xz} \\ \tau_{yx} & \sigma_{yy} & \tau_{yz} \\ \tau_{zx} & \tau_{zy} & \sigma_{zz} \end{bmatrix}, \tag{2.7}$$

where $\tau_{ij}$ and $\sigma_{ij}$ are the three-dimensional shear and normal stress.

The measure of friction of force resisting a flow is the viscosity $\eta$[60,61]. Viscous loss is commonly referred to as frictional loss, which scales with the viscosity of the fluid. Like stress, viscosity can also be represented as a tensor[65]. Assuming the fluid is isotropic, the stress forces relate to the viscosity through the form[66,62]:

$$\sigma_{ij} = -p\delta_{ij} - \eta(\boldsymbol{\nabla}_i \cdot \boldsymbol{v}_j + \boldsymbol{\nabla}_j \cdot \boldsymbol{v}_i). \tag{2.8}$$

The result of substituting the viscous stress properties into equation 2.4 is the Navier-Stokes equation, which will be discussed in section 2.2.8. But for the purposes of this section the equation is simplified assuming the fluid medium is Newtonian, there are no viscous forces ($\eta = 0$), the medium is homogeneous and under small disturbances in pressure. The resultant conservation of momentum (from equations 2.4 and 2.6), or Euler's equation of motion is[62]:

$$\rho_0 \frac{\partial \boldsymbol{v}}{\partial t} + \boldsymbol{\nabla}p_{\mathrm{a}} = 0. \tag{2.9}$$

This equation relates the fluid velocity, $\boldsymbol{v}$, to the steady state density, $\rho_0$, and the acoustic pressure, $p_{\mathrm{a}}$, in time, $t$.

### 2.2.5 Bulk Modulus

An intrinsic property of elastic materials in a volume is the bulk modulus[60]:

$$K = -V \left( \frac{dp}{dV} \right)_S. \tag{2.10}$$

Here, $p$ is pressure and $V$ is the volume. $K$ is related to the compressibility of the fluid,

$$\beta = -\frac{1}{V} \frac{\partial V}{\partial p}. \tag{2.11}$$

As compressibility, $\beta$, is a measure of how easy it is to squeeze and object or the change in volume when pressure is applied to the material, a material with a large bulk modulus is near incompressible.

As $\partial p$ is in this analysis the acoustic pressure $p_a$ the equation 2.10 is rearranged to define the acoustic pressure in terms of elastic properties:

$$p_a = K \left( \frac{\rho - \rho_0}{\rho_0} \right), \tag{2.12}$$

where $\rho_0$ is the unperturbed density of the material.

### 2.2.6 The Speed of Sound in Water

Sir Isaac Newton was the first to analytically derive the speed of sound travelling through a fluid in *Principia Mathematica*[4]. His analysis investigated a simple wave depicted in figure 2.1 with a reference pressure, $p_0$. When this travelling wave reaches a point in space the local particles of the medium experience total pressure $p_1$ (equivalent to peak acoustic pressure) leading to a resultant acceleration. As particles outside the pulse are moving at $\boldsymbol{v}_0$ the acceleration is defined as $\boldsymbol{a} = (\boldsymbol{v}_0 - \boldsymbol{v}_1)/dt$. Using $\boldsymbol{F} = m\boldsymbol{a}$ then:

$$p_1 - p_0 = (\rho_0 dx) \frac{\boldsymbol{v}_0 - \boldsymbol{v}_1}{dt} = \rho_0 \boldsymbol{v}_0 (\boldsymbol{v}_0 - \boldsymbol{v}_1). \tag{2.13}$$

Rearranging this obtains:

$$\boldsymbol{v}_0^2 = \frac{\rho_1}{\rho_0} \left( \frac{p_1 - p_0}{\rho_1 - \rho_0} \right). \tag{2.14}$$

Approximating to small perturbations in density this simplifies to:

$$\boldsymbol{v}_0^2 = \frac{p_1 - p_0}{\rho_1 - \rho_0} = \left( \frac{dp}{d\rho} \right) (\rho - \rho_0). \tag{2.15}$$

Combining equations 2.12 and 2.15, Newton derived speed of sound in an elastic fluid[67],

$$c_{\text{fluid}} = \sqrt{\frac{K}{\rho_0}},\tag{2.16}$$

where $K$ is the bulk modulus of elasticity.

Comparisons between the experimentally observed and analytically calculated results in air were 343 m/s and 280 m/s. To correct this Laplace adapted the equation to include an adiabatic index[6] $\gamma = \frac{C_\text{p}}{C_\text{v}}$, saying that, $\gamma K = K'$ and $c_{\text{fluid}} = \sqrt{K'/\rho_0}$. At room tempertaure ($T \approx 293$ K) water's heat capacity $C_\text{p} \approx C_\text{v}$, where the the adiabatic index is $\approx 1$[68,69]. Therefore 2.16 is a valid approximation for underwater use.

A free travelling non-dispersive wave has a speed of $c = f\lambda_0$ where $c$ is a constant. This means that the wave has a constant speed which is frequency independent. Although it is a good approximation for sound in air and water, in reality this is not the case for most elastic media.

The first recorded experimental measurements of the speed of sound in water were performed in Lake Geneva in 1826[9] giving 1435 m/s. But as the speed of sound varies with depth, salinity and temperature, each body of water has a different characteristic speed of sound. For this thesis the speed of sound in room temperature ($\approx 293K$) non-saline water is taken to be 1512 m/s, as will be shown in section 3.6.

### 2.2.7 Acoustic Wave Equation

Combining the effects of the continuity equation, the equation of state and the conservation of mass produces a mathematical description of the nature of propagating acoustic waves called the acoustic wave equation. Here, equations 2.2, 2.3 and 2.9 are incorporated to form the first-order loss-free three-dimensional acoustic wave equation,

$$\boldsymbol{\nabla}^2 p_\text{a} - \frac{1}{c^2}\frac{\partial^2 p_\text{a}}{\partial t^2} = 0,\tag{2.17}$$

where $c$ is the speed of sound. Helmholtz restated this in terms of angular frequency, $\omega$ ($\omega = 2\pi f$) or wavevector, $k = \omega/c$:

$$\boldsymbol{\nabla}^2 p_a + k^2 p_\text{a} = 0.\tag{2.18}$$

For planar and monochromatic acoustic waves, as shown in figure 2.1, the general solution to the wave equation has the form,

$$p_\text{a}(\boldsymbol{r}, t, \boldsymbol{k}) = A e^{-i(\boldsymbol{k}\cdot\boldsymbol{r}-\omega t)},\tag{2.19}$$

where $\omega$ is the angular frequency, $\boldsymbol{k}$ is the wavevector and $\boldsymbol{r}$ is the direction of propagation. The corresponding fluid flow speed for this solution:

$$\boldsymbol{v} = \frac{A}{\rho_0 c} e^{-i(\boldsymbol{k} \cdot \boldsymbol{r} - \omega t)}. \tag{2.20}$$

### 2.2.8 Navier-Stokes Equation

Equating the separate forces acting on a fluid in equation 2.4 and inputting the velocity gradient in equation 2.8 the new effective density force becomes[62]:

$$\nabla \cdot \sigma_{ij} = -\nabla_i p + \eta \left( \Sigma_j \nabla_i \nabla_j v_j + \Sigma_j \nabla_j^2 v_i \right) = -\nabla_i p + \eta \boldsymbol{\nabla}^2 v_i. \tag{2.21}$$

Inserting this into the Cauchy equation of motion results in the Navier-Stokes equation:

$$\frac{\partial \boldsymbol{v}}{\partial t} + (\boldsymbol{v} \cdot \boldsymbol{\nabla})\boldsymbol{v} = -\frac{1}{\rho}\boldsymbol{\nabla}p + \frac{\eta}{\rho}\boldsymbol{\nabla}^2 \boldsymbol{v} + \boldsymbol{g}. \tag{2.22}$$

This form is commonly used to describe the fluid structure interactions. In acoustics, the Cauchy stress tensor must be resated for a compressible fluid as[62]:

$$\sigma_{ij} = -p\delta_{ij} + 2\eta v_{ij}. \tag{2.23}$$

Here $v_{ij}$ is the symmetric velocity gradient,

$$v_{ij} = \frac{1}{2}\left( \nabla_i v_j + \nabla_j v_i - \frac{2}{3}\boldsymbol{\nabla} \cdot \boldsymbol{v}\delta_{ij} \right). \tag{2.24}$$

It is necessary to state this in this form as $v_{ij}$ accounts for the friction between local areas of the fluid, $\nabla_i v_j + \nabla_j v_i$ is the gradient of the fluid and $\frac{2}{3}\boldsymbol{\nabla} \cdot \boldsymbol{v}\delta_{ij}$ accounts for the resistance to compression. Inserting this into equation 2.22 results in the compressible Navier-Stokes equation,

$$\rho \left( \frac{\partial \boldsymbol{v}}{\partial t} + (\boldsymbol{v} \cdot \boldsymbol{\nabla})\boldsymbol{v} \right) = -\boldsymbol{\nabla}p + \eta \left( \boldsymbol{\nabla}^2 \boldsymbol{v} + \frac{1}{3}\boldsymbol{\nabla}(\boldsymbol{\nabla} \cdot \boldsymbol{v}) \right) + \boldsymbol{f}, \tag{2.25}$$

where $\boldsymbol{f}$ accounts for the body and external forces acting on the fluid. As the Navier-Stokes infamously difficult to solve, it is approximated. Acoustics software, such as Comsol Finite Element Method (FEM) modelling[70] used in this work, does this computationally and is further described in section 3.8.

### 2.2.9 Acoustic Attenuation

Until now this study has assumed that acoustic waves undergo lossless propagation, but this is not true as they are subject to attenuation. On a molecular scale, the particles of a system collide with each other in a non-elastic manner and have some associated loss. Using a complex wavenumber $\boldsymbol{k} = -i\boldsymbol{\alpha} + \boldsymbol{\beta}$, now the flow speed (equation 2.20) of the fluid is:

$$\boldsymbol{v_r} = \boldsymbol{v_{r0}} e^{-i(\boldsymbol{\beta} \cdot \boldsymbol{r} - \omega t)} e^{-\alpha \boldsymbol{r}}, \tag{2.26}$$

where $\alpha$ is the unknown coefficient of attenuation to be determined[61].

Acoustic attenuation and losses transfer kinetic energy into thermal energy. In an infinitely large volume all propagating sound energy will eventually convert into thermal energy. In a fluid-based system the majority of loss comes from viscous losses, the form of which is examined in the next section.

#### 2.2.9.1 Viscous Loss

As the fluid is compressible and viscous, the definition of the way in which it reacts to changes in pressure (equation 2.12) must be redefined as[62]:

$$p_{\mathrm{a}} = \frac{K_0}{\rho_0} \Delta\rho - \eta_B \boldsymbol{\nabla} \cdot \boldsymbol{v}, \tag{2.27}$$

where $\eta_B$ is the bulk viscosity of the fluid and $K_0$ is the steady state bulk modulus. Combining this pressure correction, the Navier-Stokes equation 2.25 and the time derivative of the continuity equation 2.3 obtains:

$$\frac{\partial^2 \Delta p}{\partial t^2} = \frac{K_0}{\rho_0} \boldsymbol{\nabla}^2 \Delta\rho + \frac{\eta_B + \frac{4}{3}\eta}{\rho_0} \boldsymbol{\nabla}^2 \frac{\partial \Delta\rho}{\partial t}. \tag{2.28}$$

This has as similar form to the acoustic wave equation 2.18, with the addition of the term on the far right. This term accounts for the viscous attenuation. This equation has phase velocity, $c_0 = \sqrt{\frac{K_0}{\rho_0}}$, and angular frequency,

$$\omega_0 = \frac{K_0}{\eta_{\mathrm{B}} + \frac{4}{3}\eta} = \frac{c_0^2 \rho_0}{\eta_{\mathrm{B}} + \frac{4}{3}\eta}. \tag{2.29}$$

The resulting attenuation is[62]:

$$\alpha = \frac{\omega^2}{2\rho_0 c_0^3} \left( \eta_{\mathrm{B}} + \frac{4}{3}\eta \right). \tag{2.30}$$

This shows that $\alpha \propto \omega^2$, meaning that as frequencies increase viscous losses increase quadratically with that of frequency.

### 2.2.9.2 Thermal Loss

The thermal conductivity of a medium, $\kappa$, is a measure of how long it takes for heat to transfer quantified as the temperature gradient. For simplicity this work has thus far assumed that fluids subjected to sound are adiabatic. This is strictly only true if the thermal conductivity is zero, which is not realistic. As $\kappa$ is finite, heat energy in areas of high pressure (compression) will be transferred to areas of low pressure (rarefaction). This is related to the Fourier equation or the standard diffusion equation[62]:

$$\frac{\partial T}{\partial t} = \kappa \boldsymbol{\nabla}^2 T, \tag{2.31}$$

where the heat diffusivity, $\kappa$, is mathematically described as:

$$\kappa = \frac{k}{\rho_0 C_{\mathrm{p}}}. \tag{2.32}$$

Here, $\kappa$ is the thermal conductivity, $\rho_0$ is the unperturbed density and $C_{\mathrm{p}}$ is the heat capacity at constant pressure. Substituting this into equation 2.30 in the previous section, the attenuation constant is now:

$$\alpha = \frac{\omega^2}{2\rho_0 V_0^3} \left( \frac{4\eta}{3} + \eta_{\mathrm{B}} + \frac{\kappa(\gamma - 1)}{C_{\mathrm{p}}} \right). \tag{2.33}$$

Both thermal and viscous loss have been included in this equation. In water the viscous losses are far more dominant and, as $\gamma \approx 1$. Therefore, in most cases thermal loss is ignored[71].

### 2.2.10 Reynold's Number

In 1883 Osborne Reynolds introduced another intrinsic property of all fluids[72], the Reynolds number,

$$Re = \frac{\rho v L}{\eta}. \tag{2.34}$$

Here, $v$ is the velocity of the fluid, $\eta$ is the dynamic viscosity and $L$ is the characteristic linear dimension (of the system being considered). This is used to predict how a fluid medium will react to flow. This work deals with water.

### 2.2.11  Fluid Mechanic Boundary Layers

Acoustic waves in fluids have the macroscopic property of flow. When flowing liquids come into contact with a boundary they interact dependent on the type of boundary. As was the case for the loss of energy of freely travelling sound waves, the dominant factors are viscous forces and thermal conductivity. These boundary conditions lead to viscous boundary layers and the thermal boundary layers. that fall into two sub-categories that are Reynolds number dependent: laminar and turbulent. This work will only look at low Reynolds number, Laminar flow as only small variations in pressure are considered. In this case, travelling fluid particles interact with a fixed boundary condition, as shown in figure 2.2. This type of boundary is called a no-slip boundary condition as the fluid particles which come into contact with the boundary match the speed of the surface.
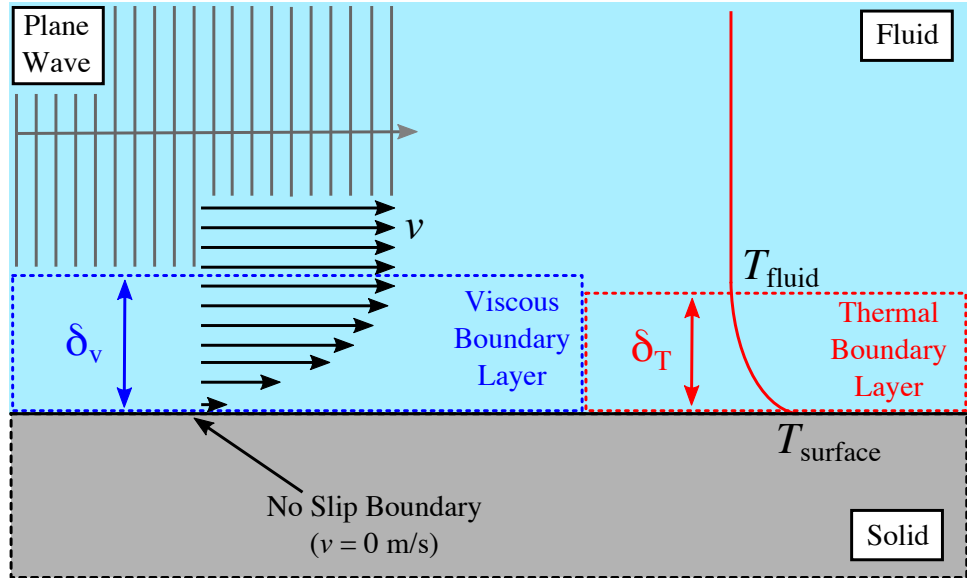


**Figure 2.2:** A 2D illustration of the thickness and effect of viscous and thermal boundary layers over a rigid boundary. The thickness of the viscous and thermal boundary layers are labelled as $\delta_{\mathrm{v}}$ (blue) and $\delta_{\mathrm{T}}$ (red). Both transition from the local velocity and temperature of the surface, $v_{\mathrm{surface}}$ and $T_{\mathrm{surface}}$, to the fluid's temperature and flow speed, $T_{\mathrm{fluid}}$ and $v_{\mathrm{fluid}}$.

The viscous boundary thickness results from the Navier-Stokes equation 2.25, the acoustic boundary condition 2.53, the continuity equation 2.9 at a boundary[73]. For a flat plate flat plate this takes the form[62,73]:

$$\delta_{\mathrm{v}} = \sqrt{\frac{2\eta}{\rho_0 \omega}}. \tag{2.35}$$

Also shown in figure 2.2 is an illustration of the thermal boundary layer. This example shows that the fluid in contact with the surface has a different temperature to that of the bulk liquid, with a temperature gradient in between. The thermal boundary layer thickness $\delta_\mathrm{T}$ is related to the viscous boundary layer thickness, $\delta_\mathrm{v}$, and the Prandtl number[9,62,73] $Pr$ as:

$$\delta_\mathrm{T} = \delta_\mathrm{v} Pr^{-1/3} = \sqrt{\frac{2\kappa}{\omega \rho_0 C_\mathrm{p}}}. \tag{2.36}$$

The Prandtl number is the ratio of the viscous diffusion rate to the thermal diffusion rate (thermal diffusivity), $Pr = \frac{C_\mathrm{p}\eta}{\kappa}$. For water at 293 K the Prandtl number[74] is $\approx 8$. Therefore the thermal viscous layer is half the viscous boundary layer thickness, $\delta_\mathrm{T} = \delta_\mathrm{v}/2$.

## 2.3 Solid Acoustics

Not only can sound waves travel through liquids and gases, they also travel through solid materials with elastic properties. When confined to a solid material, the speed of sound is dependent on the elastic properties: mass density, elastic modulus, and Poisson's ratio. These properties are quantified as extensions of the generalised Hooke's Law and are all metrics of how the material bends, flexes and wobbles in three dimensions as force or pressure is applied to it.

For a solid, the mass density $\rho$ and bulk modulus $K$ take the same form as for the the fluid: $\rho = \frac{m}{V}$ and $K = -V\frac{dp}{dV}$, where $m$ is mass, $V$ is volume and $p$ is the solid pressure. But now a new set of parameters to describe elastic solids are introduced.

### 2.3.1 Poisson's Ratio, Elastic Modulus and Shear Modulus

The Poisson's ratio, $\nu$, is a measure of the Poisson effect, whereby materials tend to expand outwards in one direction when compressed in another direction. The Poisson's ratio is defined as:

$$\nu = d\varepsilon_\mathrm{transverse}/d\varepsilon_\mathrm{axial}, \tag{2.37}$$

where $\varepsilon_\mathrm{transverse}$ and $\varepsilon_\mathrm{axial}$ are the transverse and axial strain ($d\varepsilon_{\boldsymbol{r}} \approx \frac{d\boldsymbol{r}}{\boldsymbol{r}}$). For very small variations in axial length, $\Delta L$, and radial length, $\Delta L'$, the Poisson's ratio is $\nu \approx -\frac{\Delta L'}{\Delta L}$.

Typically, unstructured metals have a positive Poisson's ratio[75] between 0.25 and 0.5. Some more exotic materials have Poison's ratios that vary significantly: cork has a Poisson's ratio of around zero and auxetic materials have negative Poisson's ratio[76].

But this study will only examine materials that have positive $\nu$.

The elastic modulus, $E$, is a measure of how a material responds when force is applied as a compression or contraction normal to the surface of the material. This is commonly defined as[77]:

$$E = \frac{\sigma_{\text{tensile}}}{\varepsilon_{\text{extensional}}}, \tag{2.38}$$

where $\sigma_{\text{tensile}}$ is tensile stress and $\varepsilon_{\text{extensional}}$ is extensional strain.

Measurements of the elastic modulus are performed on rods or bars by applying force to one end and measuring the change in length, approximated as $E = \frac{FL_0}{A\Delta L}$ in the elastic regime. Here $F$ is the force applied, $L_0$ is the initial length of the object, $\Delta L$ is the change in the objects length and $A$ is the area of the object over which force was applied. This will be revisited briefly in chapter 4.

Shear modulus, $G$, is an elastic measure of how a material reacts when force is applied in a direction parallel to a surface. It is usually defined as shear stress, $\sigma_{\text{shear}}$, over shear strain, $\varepsilon_{\text{shear}}$:

$$G = \frac{\sigma_{\text{shear}}(\varepsilon_{\text{shear}})}{\varepsilon_{\text{shear}}}. \tag{2.39}$$

Measurements of the shear modulus are calculated using $G = \frac{FA}{\Delta L/L_0}$.

Although the elastic modulus and shear modulus can alter with strain in materials that are subjected to extreme forces that result in non-linearity. The majority of this work will look at materials that are subjected to weak forces that remain in the linear regime. Therefore these materials have an assumed constant elastic modulus and shear modulus.

### 2.3.2  Related Elastic Properties

The elastic properties of a material can be described using the linear elastic tensor (an expansion on Hooke's Law)[78,79]:

$$\begin{bmatrix} \sigma_{11} \\ \sigma_{22} \\ \sigma_{33} \\ \sigma_{23} \\ \sigma_{31} \\ \sigma_{12} \end{bmatrix} = \begin{bmatrix} C_{1111} & C_{1122} & C_{1133} & C_{1123} & C_{1131} & C_{1112} \\ C_{2211} & C_{2222} & C_{2233} & C_{2223} & C_{2231} & C_{2212} \\ C_{3311} & C_{3322} & C_{3333} & C_{3323} & C_{3331} & C_{3312} \\ C_{2311} & C_{2322} & C_{2333} & C_{2323} & C_{2331} & C_{2312} \\ C_{3111} & C_{3122} & C_{3133} & C_{3123} & C_{3131} & C_{3112} \\ C_{1211} & C_{1222} & C_{1233} & C_{1223} & C_{1231} & C_{1212} \end{bmatrix} \begin{bmatrix} \varepsilon_{11} \\ \varepsilon_{22} \\ \varepsilon_{33} \\ 2\,\varepsilon_{23} \\ 2\,\varepsilon_{31} \\ 2\,\varepsilon_{12} \end{bmatrix} \tag{2.40}$$

Here $C_{ijkl}$ represents the tensor elastic properties of a material (in Voigt notation[80]). Assuming the elastic properties of a material are homogeneous and isotropic this matrix takes the form:

$$\begin{bmatrix} \sigma_{11} \\ \sigma_{22} \\ \sigma_{33} \\ \sigma_{23} \\ \sigma_{31} \\ \sigma_{12} \end{bmatrix} = \begin{bmatrix} C_{11} & C_{12} & C_{12} & 0 & 0 & 0 \\ C_{12} & C_{11} & C_{12} & 0 & 0 & 0 \\ C_{12} & C_{12} & C_{11} & 0 & 0 & 0 \\ 0 & 0 & 0 & \frac{(C_{11}-C_{12})}{2} & 0 & 0 \\ 0 & 0 & 0 & 0 & \frac{(C_{11}-C_{12})}{2} & 0 \\ 0 & 0 & 0 & 0 & 0 & \frac{(C_{11}-C_{12})}{2} \end{bmatrix} \begin{bmatrix} \varepsilon_{11} \\ \varepsilon_{22} \\ \varepsilon_{33} \\ 2\,\varepsilon_{23} \\ 2\,\varepsilon_{31} \\ 2\,\varepsilon_{12} \end{bmatrix} \tag{2.41}$$

Substituting in the elastic properties of the material of Poisson's ratio, $\nu$, elastic modulus, $E$, and shear modulus, $G$. This is commonly represented as the constitutive relation[62,81]:

$$\begin{bmatrix} \varepsilon_{xx} \\ \varepsilon_{yy} \\ \varepsilon_{zz} \\ 2\varepsilon_{yz} \\ 2\varepsilon_{zx} \\ 2\varepsilon_{xy} \end{bmatrix} = \begin{bmatrix} \frac{1}{E} & -\frac{\nu}{E} & -\frac{\nu}{E} & 0 & 0 & 0 \\ -\frac{\nu}{E} & \frac{1}{E} & -\frac{\nu}{E} & 0 & 0 & 0 \\ -\frac{\nu}{E} & -\frac{\nu}{E} & \frac{1}{E} & 0 & 0 & 0 \\ 0 & 0 & 0 & \frac{1}{G} & 0 & 0 \\ 0 & 0 & 0 & 0 & \frac{1}{G} & 0 \\ 0 & 0 & 0 & 0 & 0 & \frac{1}{G} \end{bmatrix} \begin{bmatrix} \sigma_{xx} \\ \sigma_{yy} \\ \sigma_{zz} \\ \sigma_{yz} \\ \sigma_{zx} \\ \sigma_{xy} \end{bmatrix} \tag{2.42}$$

This can be restates simply in a one line equation,

$$E = 3K(1 - 2\nu) = 2G(1 + \nu). \tag{2.43}$$

Importantly, this shows how the different elastic properties of material can be derived from two other elastic properties of the material. In this work, this is used to derive the wavespeeds in solids and is restated using another method in chapter 4.

### 2.3.3 Bulk Wave Speed

The sound velocity of a travelling pressure wave in a solid is a function of the materials' elastic properties. Unlike a fluid, there are a number of different sound wavespeeds in an elastic solid Poisson's ratio and the elastic modulus (due to the extra degrees of freedom related to crystal symmetry). Bulk wavespeeds come in two different varieties:

compressional and shear.

The compressional wave is similar to that of the compressional of an acoustic wave travelling through a fluid. Unlike a fluid, the intermolecular elastic collisions of the solid are not confined to one dimension so are dependent on a combination of the shear and bulk modulus. A first order approximation of the compressional or P-wave wave speed[60]:

$$c_P = \sqrt{\frac{K + \frac{4}{3}G}{\rho}} \tag{2.44}$$

Here $\rho$ is the mass density and $K$ and $G$ are the bulk and shear moduli of the material. The compressional wave is generally the fastest type of wave to travel through a solid. Therefore during seismic events the P-wave are the first type of wave to be detected.

The shear wave speed or S-wave speed is given by[60]:

$$c_S = \sqrt{\frac{G}{\rho}} \tag{2.45}$$

Here $\rho$ is the mass density. Usually $G < K + \frac{4}{3}G$, the S-wave is typically slower in wavespeed than the P-wave.

## 2.4  Acoustic Impedance

To quantify the effects of loss, the most commonly used analogy is to compare an acoustic system to a system made up of masses, springs, resistors and dampers. This assumes that acoustics follows Hookean laws and can be simplified to an LCR circuit[60,61]. Acoustic impedance is a measure of the resistance to a change in pressure of a medium or at a boundary. This term is a common parameter associated with the mechanical-electrical analogy and acoustic impedance is a directly translated with the impedance in an LCR circuit[60]. There are a few different types of acoustic impedance. The specific acoustic impedance is a function of pressure, $p$, and flow speed, $v$:

$$z = \frac{p}{v}, \tag{2.46}$$

measured in $\frac{\mathrm{Pa} \cdot \mathrm{s}}{\mathrm{m}}$. Another type of acoustic impedance is called the characteristic acoustic impedance and is defined as:

$$Z_0 = \rho_0 c, \tag{2.47}$$

where $\rho_0$ is density of the medium and speed of sound travelling through it $c$, which can be split into shear and compressional ($c_\mathrm{S}$ and $c_\mathrm{P}$). A third type of impedance called "normal impedance" is introduced in Section 2.4.3.

### 2.4.1 Particle Displacement

When considering pressure interacting with a fluid, it is useful to picture the particle displacement. For a plane sinusoidal wave particles undergo displacement,

$$\delta(\boldsymbol{r}, t) = \delta \cos(\boldsymbol{k} \cdot \boldsymbol{r} - \omega t + \psi), \tag{2.48}$$

where $\delta$ is the displacement and $\psi$ is the phase shift. Pressure and velocity have equivalent forms:

$$p(\boldsymbol{r}, t) = p \cos(\boldsymbol{k} \cdot \boldsymbol{r} - \omega t + \psi_p), \tag{2.49}$$

$$v(\boldsymbol{r}, t) = v \cos(\boldsymbol{k} \cdot \boldsymbol{r} - \omega t + \psi_v), \tag{2.50}$$

The specific impedance (equation 2.46) states that:

$$z(\boldsymbol{r}, t) = \frac{p}{v} = \frac{\rho c^2 \boldsymbol{k}}{\omega}. \tag{2.51}$$

Consequently, this relates to particle displacement as:

$$\delta = \frac{v}{\omega} = \frac{p}{\omega z(\boldsymbol{r}, t)}, \tag{2.52}$$

where $\delta$ is the spatial displacement. The next section will discuss what happens when materials that significantly differ in impedance respond to sound.

### 2.4.2 Ideal Acoustic Boundary Conditions

Two types of ideal acoustic boundary conditions called acoustically rigid and pressure-release (or acoustically soft), first outlined by Rayleigh[15]. The acoustically rigid boundary condition takes the form:

$$\frac{\partial p_\mathrm{a}}{\partial \boldsymbol{n}} = 0. \tag{2.53}$$

Here $p_\mathrm{a}$ is the acoustic pressure and $\boldsymbol{n}$ is the boundary vector normal the interface. An example of this is the boundary between air and steel.

The acoustic pressure at a pressure-release boundary is:

$$p_\mathrm{a} = 0. \tag{2.54}$$

This condition is sometimes called free boundary. Both of these boundaries reflect sound. But the pressure-release boundary reflects with zero phase shift whereas the rigid boundary reflects with a $\pi$ phase shift.

In reality no interfaces are perfectly acoustically rigid or pressure-release, but somewhere in between. Therefore, waves can propagate through interfaces from one medium to another, without being perfectly reflected. This will be investigated in section 2.4.3.

### 2.4.3  Reflection and Transmission

At the boundary between two media the acoustic impedance changes with the angle of the incident sound. A new definition of impedance must be introduced, the Normal Impedance[60],

$$Z_i = \rho_0 c \cos(\theta_i). \tag{2.55}$$

Here, $\theta_i$ is the angle of incident sound from the normal to the surface.

The proportion of energy transmitted, $T$, and reflected, $R$, are functions of the acoustic impedance of the materials[60]:

$$R = \left( \frac{Z_2 - Z_1}{Z_2 + Z_1} \right)^2, \tag{2.56}$$

$$T = \left( \frac{2Z_1}{Z_2 + Z_1} \right)^2. \tag{2.57}$$

The next section will explore how structuring rigid materials beyond flat surfaces changes the way in which acoustic fields propagate and support resonances.

## 2.5  Acoustic Resonance

Structures can be shaped to support acoustic resonance. Later sections of this chapter will detail how closely spaced coupled resonators can be used to support in-plane acoustic modes, or surface waves. But first, this section gives an overview of acoustic resonance in a single structure, using rigid or pressure-release boundary conditions.

### 2.5.1  A Helmholtz Resonator

One common method of supporting acoustic resonance is that of air blowing over the edge of the rim of an empty bottle. This type of acoustic cavity mode is called a Helmholtz resonator. In the idealised case, Helmholtz created a spherical hollow cavity

made of metal that had a tube connecting the air-filled inner cavity to the outside ambient environment[32]. A typical Helmholtz resonator is shown in figure 2.3.

Helmholtz stated that these devices could be used to select specific tones from a broadband source of noise. That frequency is given by the equation[60]:

$$f_{\text{H}} = \frac{c}{2\pi}\sqrt{\frac{A}{V_0 L_{\text{h}}}}, \tag{2.58}$$

where $c$ is the speed of sound, $A$ is the cross-sectional area of the neck, $V_0$ is the volume of the cavity and $L_{\text{h}}$ is the length of the neck. The motion of air inside the cavity is lossy and, through viscous and thermal damping, can be used to absorb unwanted frequencies. This has been known and used in structural acoustics for some time[82,83,84].
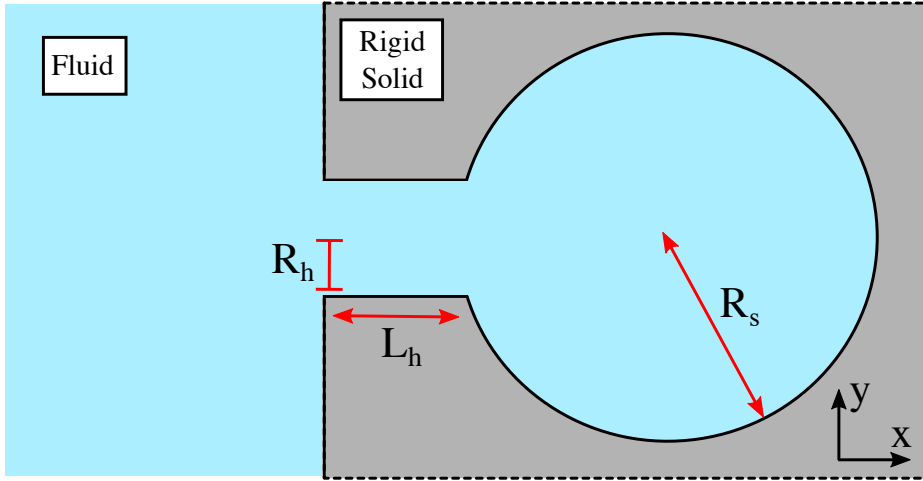


**Figure 2.3:** A cross sectional schematic of a Helmholtz resonator. This type of resonant cavity is defined by it is inner radius $R_{\text{s}}$, the length of the connecting neck $L_{\text{h}}$ and the radius of the neck $R_{\text{h}}$. The resonator is surrounded by an acoustically rigid material (grey).

### 2.5.2 Modes of a Circular Hole

Another simple resonating object is that of a pipe, well studied in music and acoustic physics[32,85,86]. The resonant frequencies of the pipe modes are dictated by its geometric properties of length, $L$, and radius, $R$. For the open-open case, the acoustic pressures ($p_{\text{a}}$) field minima are expected to be at the open ends of the pipe and the maxima at the centre. Therefore, the form of the equation to estimate the $n^{\text{th}}$ mode of an open-open

pipes (ignoring end effects) is simply:

$$f_n(\text{open-open}) = \frac{nc}{2L}, \tag{2.59}$$

where $c$ is the speed of sound, $n$ is the order of the mode (harmonic) and $L$ is the pipes length. When one of the ends is closed the closed, end functions as a maximum in the pressure field amplitude and therefore the harmonics are estimated to be:

$$f_n(\text{open-closed}) = \frac{nc}{4L}. \tag{2.60}$$

In practice there are end effects that are discuss in section 2.5.3. Furthermore, the effect of using multiple open ended pipes in close proximity to each other will be discussed in chapters 6 and 7 .

### 2.5.3   End Corrections

Rayleigh experimentally observed that there is a shift of the frequency of a resonating cavity associated with the radius or width of the entrance and exit of a resonant cavity. This shift was due to the effective length of the structure being longer than predicted and longer than the structure itself. The correction to the length is called the end correction[87], $\Delta L$.

   This study will only discuss simple structures made of open-ended holes. Rayleigh was the first to publish the end correction to an open-closed ended pipe[87] in 1871:

$$\Delta L = 0.6R = 0.3D, \tag{2.61}$$

where $L$ is the length of the pipe, $R$ is its radius and $D$ is its diameter. Therefore open-open ended pipes have an end correction $\Delta L = 0.6D$. Therefore, the pipe equation stated in the section 2.5.2 (equation 2.59) have to be restated as:

$$f_n = \frac{nc}{2(L + \Delta L)} \tag{2.62}$$

for the open-open ended pipe modes. This has been well documented[15,88,89] and most good acoustic computational modelling software will have this correction built in to their analytical calculations[70].

### 2.5.4   Acoustic Cut-off Frequency of a Circular Hole

The pressure-release boundary described in section 2.4.2 is analogues to a Perfect Electric Conductor (PEC) in electromagnetism (EM). A well-known property is that struc-

tures made out of PECs have an associated cut-off frequency, under which EM waves will not propagate through it. Thus, a hole in a pressure-release material has an equivalent acoustic cut-off frequency.

The acoustic cut-off frequency of a circular hole is given as[90]:

$$f_{\text{cut-off}} = \frac{Z_{mn}c}{2\pi R},\tag{2.63}$$

where $R$ is the radius of the hole and $Z_{mn}$ is the $m^{\text{th}}$ and $n^{\text{th}}$ zero of the Bessel's function of a first kind $J_n$. First order Bessel functions have the form plotted in figure 2.4.
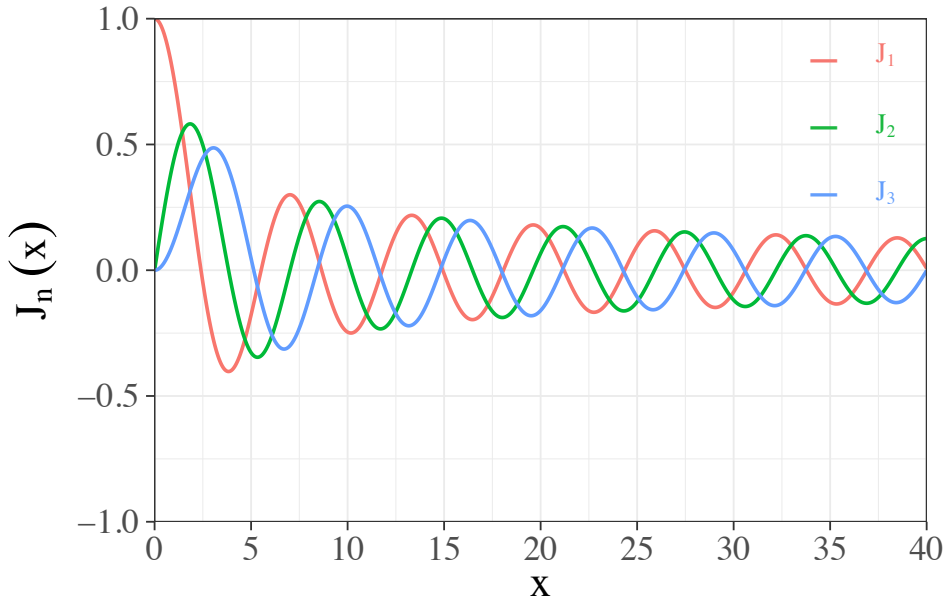


**Figure 2.4:** A graph of the solutions to the Bessel's function from orders 1 to 3. Here the Bessel functions cross the x-axis are called the zeros of the Bessel's function, $Z_{mn}$.

Figure 2.4 shows that first order Bessel's functions have a number of zeros and therefore there are a number of cut-off frequencies associated with a single hole. The first zero is $Z_{01} = 2.4048$ to 5 significant figures[91] and defines the fundamental cut-off. This will be revisited in the final experimental chapter, chapter 8, which investigates and observes the cut-off frequency of arrays of pressure-release holes.

Many resonators in close proximity to one another can support types of modes that depend on the geometry of the array. This will later be investigated in section 2.6.2, but first the modes of a unstructured plate are discussed as the foundation of the in-plane studies.

## 2.6    Surface Waves

Surface waves are waves that are supported at the interface between two or more elastic media. In acoustics there are several different types of surface waves. For a truly "trapped" surface wave, the magnitude of the in-plane wavevector, $|k_x|$, is greater than the maximum bulk wavevector magnitude of the system, $k_0$, where $k_0^2 = k_x^2 + k_z^2$. Here $x$ and $y$ are in the plane of the surface and $z$ is out from the plane. This means that beyond $k_0$, $k_z^2$ is negative and $k_z$ is imaginary. Therefore the wave is localised to the surface and exponentially decays normal to it.

### 2.6.1    Surface Acoustic Waves

Surface Acoustic Waves (SAWs) exist at the boundary between two elastic media and depend on the elastic properties of the material through which they travel. Due to the asymmetry of elastic motion these waves can travel in elliptical motion and have an associated "polarisation". Like all surface waves, the decay length normal to the surface of a SAW is an exponential function of the material properties and is typically less than a free travelling wavelength out of the plane of the surface. SAWs are divided into different sub-classifications, as summarised by Hess[92].
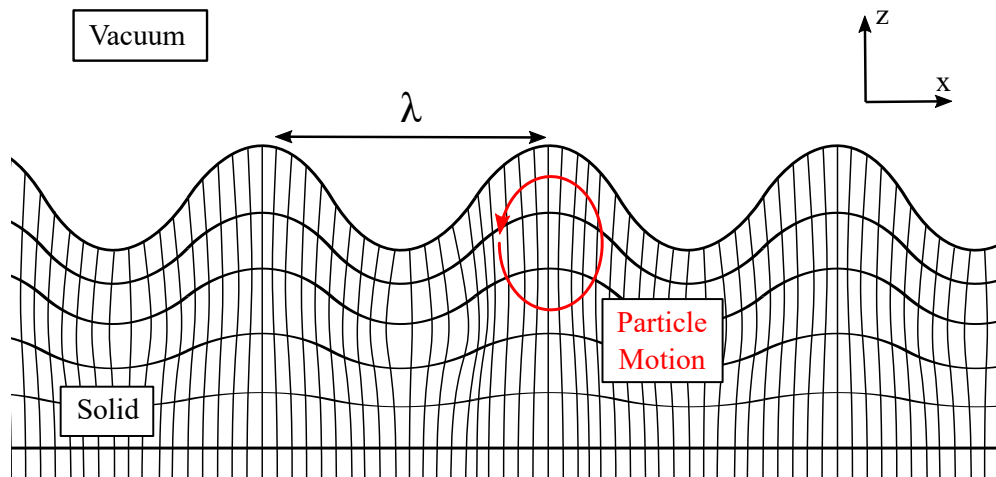


**Figure 2.5:** A diagram of a Rayleigh wave over the surface of an infinitely thick elastic medium beside a vacuum. This type of Rayleigh wave is non-radiative as it cannot couple into the vacuum. Exaggerated particle motion is highlighted in red.

One of the first SAWs to be named was the Rayleigh wave[34]. Generally, this type of wave occurs at the interface between an elastic medium and a near-vacuum. This interface has a high to low impedance mismatch ($Z_1 \gg Z_2$) and can be approximated as with metal to air, with the Rayleigh wave travelling within the metal. A cross section

showing the expected particle motion in a Rayleigh wave in an isotropic medium is shown in figure 2.5.

The atoms in figure 2.5 move in an approximately elliptical motion when a Rayleigh wave propagates across the surface (shown as a red arrow), a motion which decreases in amplitude inward from the surface. These types of waves are supported by the ground and, due the vertical motion of the surface, are some of the most destructive in the event of an earthquake. Therefore, a lot of recent work has been conducted in order to reflect or guide the wave energy of ground supported Rayleigh waves[93,94].

The Rayleigh wavespeed $c_R$ is associated to the shear wavespeed $c_S$. In an infinitely thick linear elastic medium $c_R$ is a fixed and therefore is non-disperive. The Rayleigh wavespeed has been approximated a number of times, each working for a specific bound of Poisson's ratios[95,18,96]. Recently set out, Malischewsky's approximation[97] works for both positive and negative values of Poisson's ratio,

$$c_R = c_S(0.874 + 0.196\nu - 0.043\nu^2 - 0.055\nu^3), \tag{2.64}$$

where $\nu$ is the Poisson's ratio of the material. As the equation shows, the Rayleigh wavespeed is close to the Shear wavespeed $c_S$.
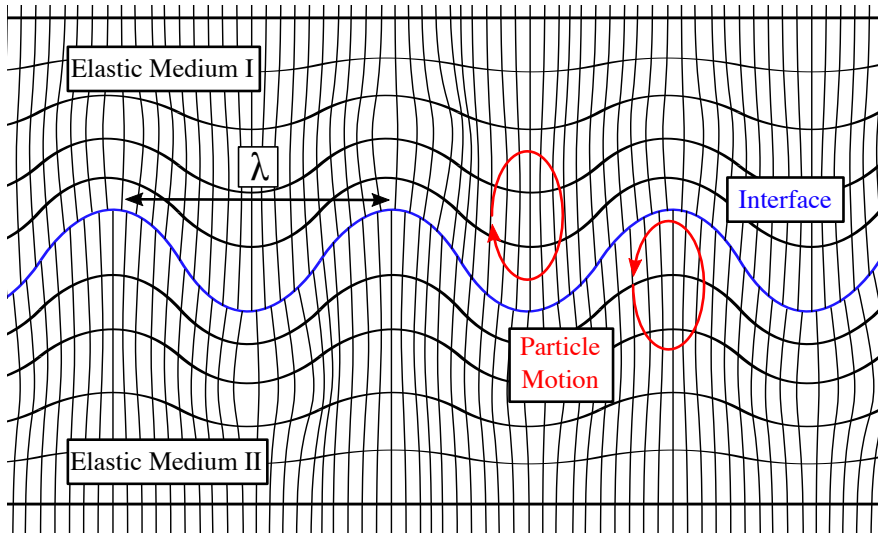


**Figure 2.6:** A diagram of a Scholte-Stoneley wave propagating at the interface between two elastic media. The interface between the two elastic materials is highlighted in blue and the exaggerated particle motion in each medium is highlighted in red.

Another type of SAW occurs at the interface between two elastic media with similar elastic properties. Scholte classified these types as Scholte waves at water-solid interfaces and Stoneley waves at solid-solid interfaces[17,56]. In the literature, these have been grouped together as Scholte-Stoneley Waves (SSWs) as they have very similar

characteristics. In this work they will therefore be referred to as SSWs. A cross-section of a travelling SSW has been depicted in figure 2.6.

Although SSWs travel in much the same way as Rayleigh waves, they travel at a slower group velocity. However, they are also non-dispersive in infinitely thick media. Underwater, SSWs are very important as many of the elastic properties of common metals are similar to that of water and therefore support SSWs.

So far this work has only discussed elastic media where thickness $L \gg \lambda$. When the thickness of the medium is finite and is near the wavelength of sound ($L \approx \lambda_0$) the medium will support types of SAWs called Lamb waves. There are two families of Lamb waves: Symmetric ($S_n$) and Asymmetric ($A_n$)[16]. Example shapes of these categories are shown in figure 2.7. There is theoretically an infinite number of Lamb modes, only limited by the elastic properties of the material. Unlike the Rayleigh and SSW modes, Lamb modes are highly dispersive.
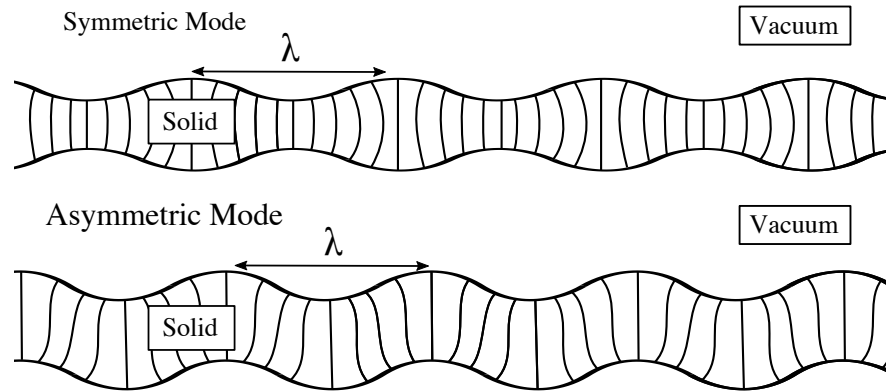


**Figure 2.7:** A diagram of the two different classes of Lamb wave. These are general shapes to show the symmetry of the symmetric and asymmetric modes, which have wavelength $\lambda$.

### 2.6.1.1  Finite Element Method SAWs

It is possible to use Finite Element Method (FEM) models to visualise acoustic waves travelling within media. A broadband monopole point source exciting the flat interface between water and aluminium is shown in figure 2.8. Here, is an instantaneous picture of the different SAWs propagating over the surface as well as the bulk waves travelling through the water and the aluminium 0.03 ms after the single cycle pulse was launched. Each of the labelled modes has a different wavespeed. Therefore at 0.03 ms the Rayleigh, SSW and bulk waves have all travelled different distances from the point of excitation. Note that figure 2.8 has introduced "leaky" Rayleigh waves that exist at

the interface between most metals and water. This will further be explained using the help of SAW dispersion in the section 2.6.1.2.

Compressional, shear, Lamb, Rayleigh, Schote-Stoneley waves can all exist in material at the same time[98]. It can become very hard to discern and characterise one wave from one another in time and frequency domains. A way to separate and label these modes is by plotting the dispersion relation, which will be covered in section 2.6.1.2.
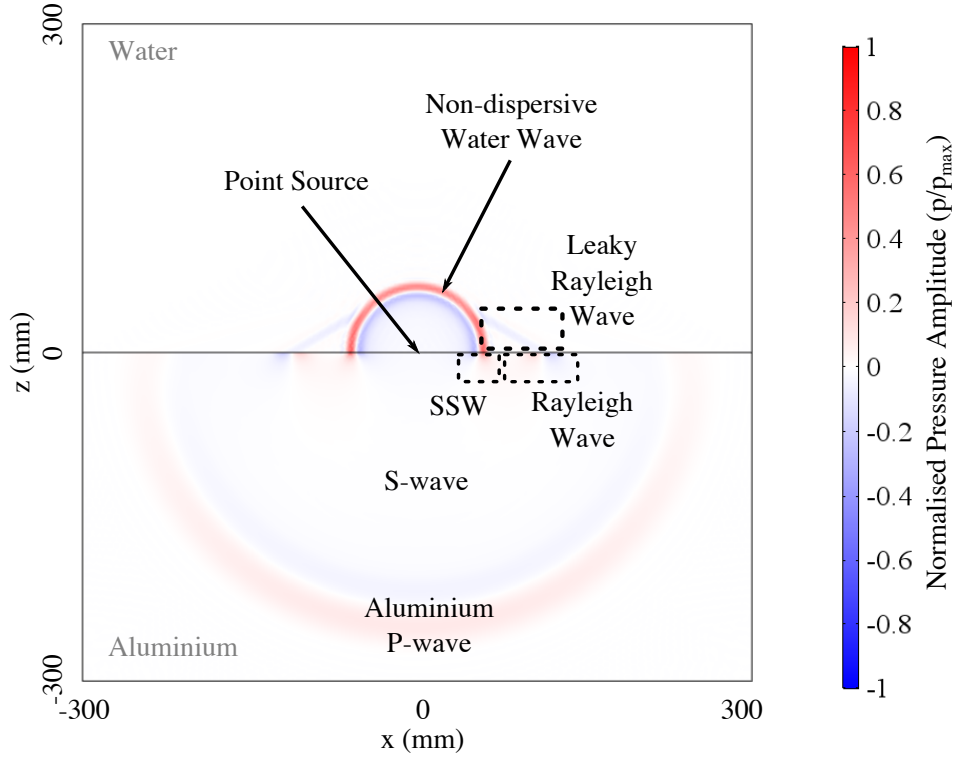


**Figure 2.8:** Comsol modelled instantaneous pressure arising from a single cycle Hanning-windowed pulse from a point source on the surface of a submerged elastic solid (Aluminium) in space ($x$ and $z$) at 0.03 ms after the pulse was launched. The propagating SAWs present in both materials are labelled. As the positions of each wave shows, each SAW has a different wavespeed.

#### 2.6.1.2   SAW Dispersion Relation

The dispersion of a wave represents how its phase and group wavespeed ($v_{\mathrm{p}} = 2\pi f/k$ and $v_{\mathrm{g}} = 2\pi \frac{\partial f}{\partial k}$) changes with frequency $f$ and wavevector $k$. A wave is non-dispersive when the group velocity and phase velocity are the same ($v_{\mathrm{g}} = v_{\mathrm{p}}$) at every frequency. As SAWs come in many different forms that are difficult to characterise in the time and frequency domain, it is helpful to show how the dispersion relation. This shows how each different type of wave evolves and overlaps over a range of frequencies and wavevectors,

and is widely used in condensed matter, photonics, phononics and acoustics[99,100].

Figure 2.9 shows a simplified example of the dispersion of different plate modes. This plot shows frequency, $f$, plotted against the wavevector component parallel to the surface of a plate in one direction, $k_x$. The modes themselves are eigenfrequencies of the finite thickness plate, the Lamb modes. These fall into two categories antisymmetric $A_n$ and symmetric $S_n$, as was previously outlined. Similar plots are exhibited in several works on elastic plates[18,101,22].
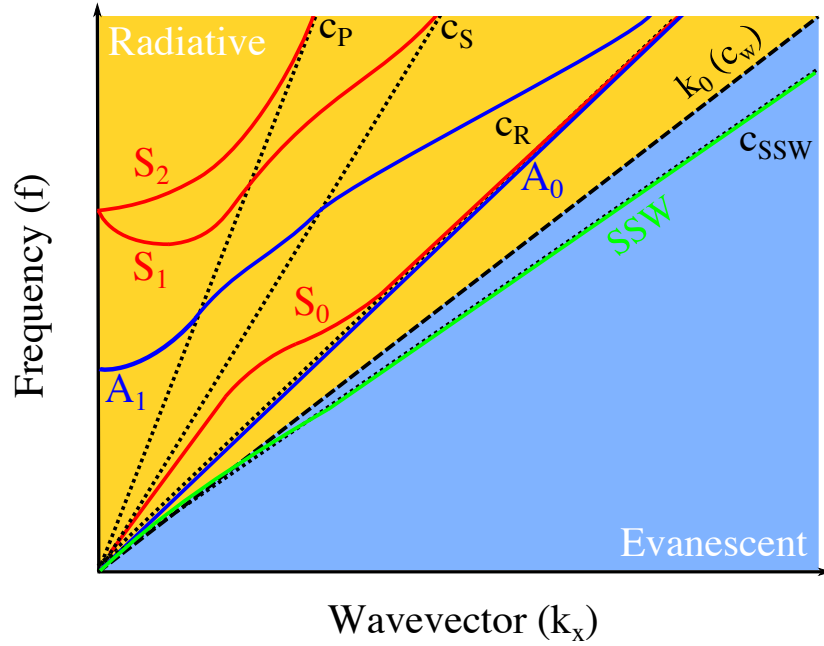


**Figure 2.9:** An example dispersion plot of the acoustic wave transmission through a solid plate immersed in water. The wavespeed limits have been plotted as the Rayleigh wavespeed $c_R$, the S-wave speed $c_S$, the P-wave speed $c_P$ and the SSW speed $c_{SSW}$. This example includes a sound line, $k_0$, which represents a typical sound line for water. As such, most acoustic modes fall into the radiative regime, whereas SAW modes are in the evanescent regime. In this case, the SSW mode is an SAW.

A common feature of dispersion plots is the sound line defined as $k_0 = \frac{2\pi f}{c_w}$ where $c_w$ is the non-dispersive speed of sound in the surrounding water. This is shown as a black dashed line in figure 2.9. $k_0$ defines the maximum wavevector which a freely propagating wave can have ($|k| < |k_0|$) in the chosen direction. $k_0$ also defines the point at which a mode is radiative or evanescent. When $|k_x| < |k_0|$ the mode is radiative as it can couple to the surrounding medium and radiate away from the surface. In contrast, when $|k_x| > |k_0|$ the mode is evanescent, trapped within the medium and exponentially decaying into the surrounding medium. Experimentally, the range of $k_x$ values detected is a function of the field that excites them $k_x = k_0 \sin \theta_i$. Here $\theta_i$ is the

angle of incidence of sound. This will be discussed in detail in the methods chapter 3 and investigated much further in experimental chapters 4 and 5.

In figure 2.9, the dotted black lines show the compressional, shear, Rayleigh and Scholte-Stoneley wavespeeds ($c_P$, $c_S$, $c_R$ and $c_{SSW}$). As can be seen the different Lamb modes, plotted in blue (asymmetric) and red (symmetric), follow these wavespeed lines as function of frequency and wavevector. For small values of $f$ and $k$, the $S_0$ and $A_0$ modes have very different phase velocities $v_p$ and group velocities $v_g$, but at higher values the two modes disperse similarly, and are one and the same mode can be seen. This linear region is where the $A_0$ and $S_0$ modes are now Rayleigh waves. For the purposes of this work, the Rayleigh wavespeed is defined as the limit at which the $A_0$ and $S_0$ modes become degenerate and linear will be referred to. This will be explored much further in the experimental chapters of this thesis.

In the underwater example of figure 2.9, most of the Lamb and Rayleigh waves exist inside the radiative regime and therefore not bound to the surface. This means that they are "Leaky Rayleigh" and "Leaky Lamb" waves that couple into the surrounding medium and are not surface waves. Leaky waves radiate from the plate and can be detected at large distances from the plate[102]. This was mentioned and depicted in figure 2.8. On the other hand, the one SSW mode depicted exists beyond the sound line in the evanescent domain, which means that this wave is non-radiative and SSW acoustic energy is confined close to the surface of the plate.

### 2.6.2 Acoustic Surface Waves

Another type of surface wave is that of the non-radiative, trapped, highly localised, evanescent decaying waves supported by near-acoustically-rigid periodically structured surfaces called Acoustic Surface Waves (ASWs). These waves are sometimes referred to as "spoof surface waves" or "coupled Rayleigh waves". Usually, they are excited over surfaces periodically patterned with sub-wavelength sized cavities (sections 2.5.1 and 2.5.2) integrated into a solid material.

Analytical theory of these systems varies depending on the medium supporting the ASW, the shape of the cavity and the size of the unit-cell. The most common method to derive the radiative transmission and plot the evanescent dispersions of such structures is modal-matching. This method uses approximations of the diffraction[55,50] from perfectly rigid cavities and Bloch periodicities to calculate the eigenfrequencies of the system. This method is commonly used in plasmonics and photonics. It is a useful but somewhat inexact method and many studies have opted to use Finite Element Method (FEM) models to model ASW supporting systems[51,103].

A cross-section of an example ASW-supporting rigid grating is shown in figure 2.10.

The pictured system is periodic with a repeated "unit-cell" of the structure outlined in purple with pitch $\lambda_g$. Each unit cell contains a single water-filled rigged-walled cavity that has length, $L$, width, $w$, and material spacing, $d$. As mentioned before, each of these cavities will have an associated end-correction $\Delta L$ that will change the resonant frequency of the Fabry-Perot ($f_{FP} = c/\lambda_{FP}$) modes of the system. But the short periodicity of $\lambda_g \ll \lambda_{FP}$ between each cavity changes the end correction due to the coupling between each cavity, and an associated overlap integral[55,104]. Through evanescent diffracted coupling, the system will support ASWs over very narrow frequency ranges where $k_x > k_0$ and $k_z$ is purely imaginary above the grating, with the magnitude of $p_a$ shown in figure 2.10 inside the red dashed box.
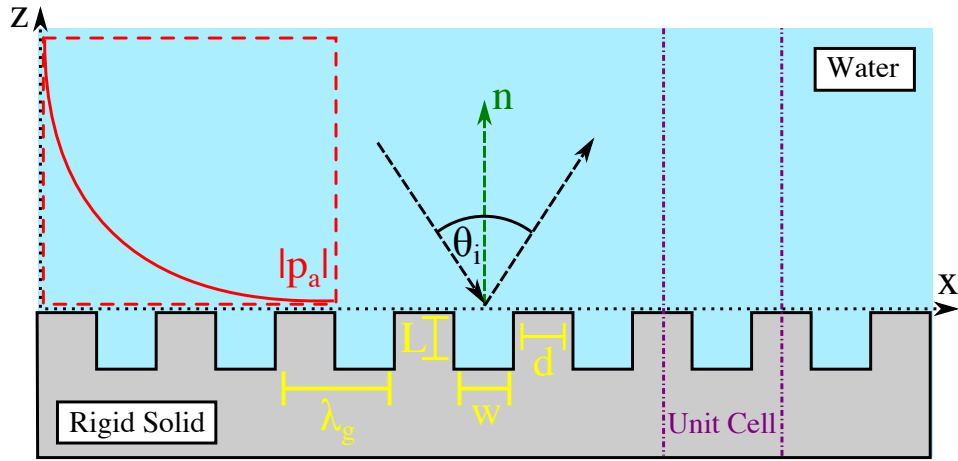


**Figure 2.10:** An illustration of an underwater acoustically rigid grating with pitch $\lambda_g$, cavity width $w$, cavity length $L$ and material spacing $d$. The grating is periodic with a unit-cell of width $\lambda_g$ (bounded by purple dotted-dashed lines). Also shown is the incident angle of sound $\theta_i$. The exponentially decaying magnitude of $p_a$ is plotted in red.

### 2.6.2.1   Finite Element Method ASWs

Again this is modelled using an FEM. Figure 2.11 shows an instantaneous time-domain pressure field plot of a Hanning-windowed pulse point excitation travelling over the surface of an ASW supporting 6 mm pitch grating in a perfectly rigid solid at 0.12 ms after the pulse launched. A scaled up view of this system is shown in the top of figure 2.11. Here the free travelling wave has moved through the fluid at the speed $c_w \approx 1500$ m/s and behind it there are later arriving waves. As these fields interact with the resonant cavities these cavities then act as secondary sources that couple into the water, diffracting radiating fields. Unlike the unstructured case, there is the presence

of a slowly travelling wave close to the surface. These are the ASW waves. As the model uses a Hanning-windowed pulse containing many frequencies, there are a range of excited wavelengths.
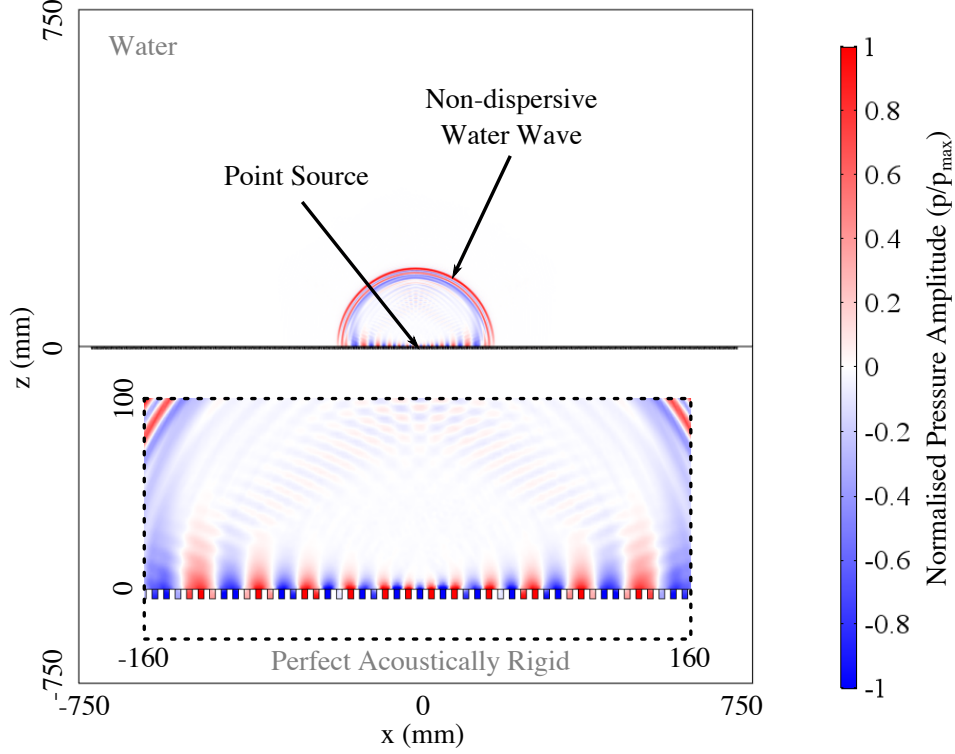


**Figure 2.11:** The Comsol modelled instantaneous pressure arising from an approximately single-cycle Hanning-windowed pulse from a point source on the surface of a submerged perfectly rigid array of cavities in space plotted as normalised pressure amplitude ($p/p_{max}$). These cavities have pitch $\lambda_g = 6$ mm and width $w = 3$ mm.

First observed in air by Ivanov-Shits and Rozhin[105] in 1959, ASWs have been the focus of a large body of work as they can be supported by air and water systems to direct and manipulate in-plane acoustic waves. They have been shown to support surface waves with near-infinite in-plane decay lengths due to the impedance matching between periodic features of the systems at specific frequencies which can be "tuned" by varying the size and pitch of the ASW supporting grating. Most of the work on ASWs was performed in air as it is easier to experimentally observe them. Underwater the situation is more complex due to the similar velocities of sound in water to that in patterned solids, which may be treated as imperfectly rigid.

### 2.6.2.2 ASW Dispersion Relation

Figure 2.12 shows an example dispersion of an ASW in $k_x$. This example is that of a typical short pitch ($\lambda_g \ll \lambda_{FP}$) ASW supporting system similar to that of the grating pictured in figure 2.10. Shown are two ASW modes being excited at two different frequencies. The asymptotic frequencies of both these modes is approximately defined by the length of the coupled resonant features, as in the case of Fabry-Perot resonances. As can be seen in the figure, the gradient and therefore group velocity is not constant, so these modes disperse. This plot is bounded in $k_x$ by the BZ, $k_{BZ} = k_g/2 = \pi/\lambda_g$. If the $\lambda_g$ was increased, the second mode would eventually surpass the diffraction edge and would be found on the sound line.
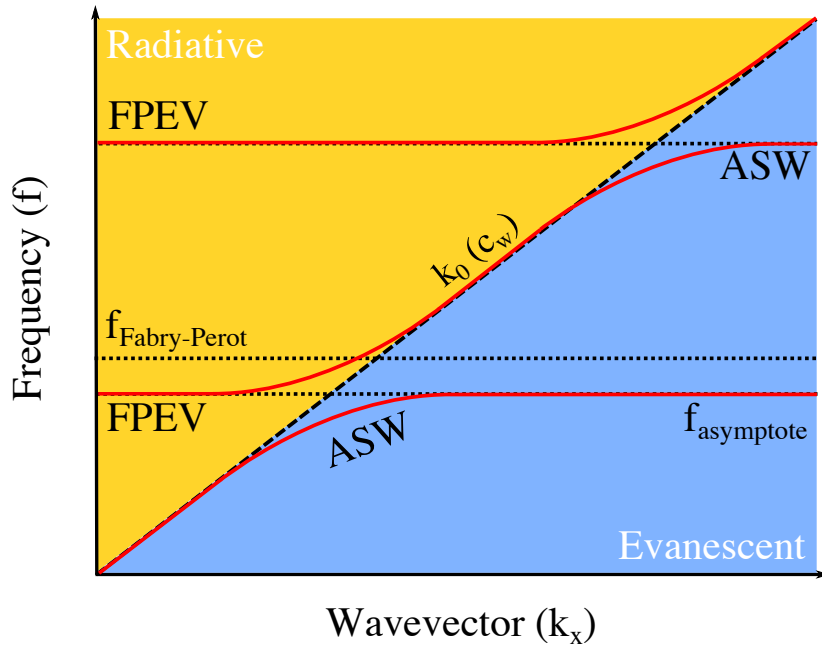


**Figure 2.12:** The dispersion plot of Acoustic Surface Waves (ASWs), plotted between $k_x = 0$ and $k_x = k_g/2$. The wavespeed limit of the non-dispersive wave $k_0$ has been plotted as the black dashed line. The Fabry-Perot frequencies $f_{FP}$ and the asymptotic frequencies $f_{asymptote}$ are plotted as black dotted lines. The ASW eigenmodes of the system are plotted as red lines.

Note that in figure 2.12, there are two regions defined by $k_0 = \pm\frac{2\pi f}{c_{water}}$. Modes with $|k_x| < |k_0|$ are radiative and modes with $|k_x| > |k_0|$ are evanescent. All the ASW modes of this system are evanescent, meaning that they are trapped at the surface. In the radiative regime the modes have a small enough wavevector to couple into the water with an associated angle of incidence, $\theta_i$. This relates to the wavevector as $k_x = k_0 \sin(\theta_i)$, which at normal incidence ($\theta_i = 0°$) has zero amplitude $k_x = 0$ and at

grazing ($\theta_i = 90°$) $k_x = k_0$. This type of dispersion will be experimentally plotted in chapters 6 and 7.

In figure 2.12, the radiative regime includes the presence of so called "Fabry-Perot Evanescent-Waves" (FPEVs). The radiative transmissive properties of structured plates are the focus of many studies as they can be designed to enhance or absorb the SAWs[106,107,108,109].

### 2.6.3 The Extended Zone Scheme

The last section looked at the ASW dispersion with $0 < k_x < k_g/2$. Values outside of this range were ignored, to avoid confusion. However, the periodicity, $\lambda_g$, is the reason the ASW mode can be supported and it is instructive to also look outside of the range of the first BZ. There are three common ways to represent the extended dispersion relation[100]

- A "repeated-zone" scheme, where every eigenfrequency band is drawn within every Brillouin zone.

- A "reduced-zone" scheme, where only the first Brillouin zone is included, this time with every mode "band-folded" back and represented between $0 < k_g/2$.

- An "extended-zone" scheme, where the band structure is extended from the origin to higher $k$ without repeats in each zone.

It is of course possible to plot the dispersion in more than one direction, but this work is primarily concerned with the dispersion in one-dimension. Therefore an example of repeated-zone scheme dispersion is plotted for a structure similar to that of the one-dimensional periodic grating, similar to that in figure 2.10, in figure 2.13.

There are a few important features to note. At the edge of the first Brillouin Zone (BZ) $|k_x| = |k_g/2|$ the first standing wave condition is met. At these points the gradient and therefore the group velocity of the ASW modes is zero and in practice it is impossible to excite this mode at the BZ boundary. Beyond this at $|k_g| > |k_x| > |k_g/2|$ the waves shown are Bragg-scattered with negative group and phase velocities, these regions are referred to as the diffracted regions.
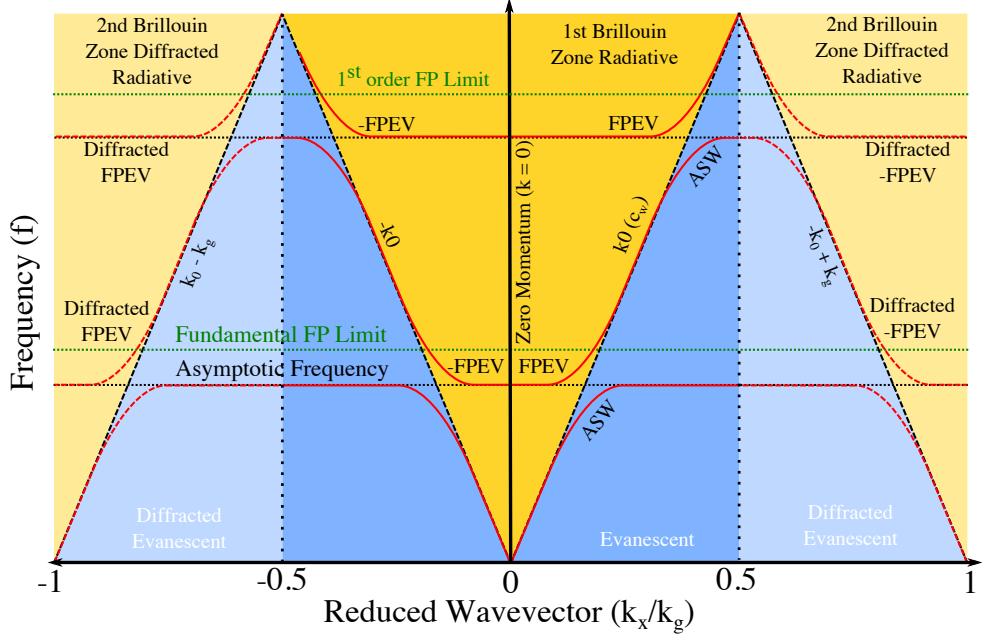
**Figure 2.13:** A plot of an example extended zone scheme of an ASW supporting structure. Here, the first and second Brillouin zones in the forward and backward propagating directions. Labelled are the ASW modes and the FPEV modes. Shaded are the radiative and the evanescent regimes.

### 2.6.4 Bloch Theorem

It is useful to use a mathematical description of a physical system whenever possible. Felix Bloch's thoerem describes wave interactions with periodic systems, such as the ones explored in two of the experiemental chapters of this work. For lattice structures Bloch theorem states that a wavefunction takes the form[100],

$$\psi_{n,\boldsymbol{k}} = e^{i\boldsymbol{k}\cdot\boldsymbol{r}}u_{n,\boldsymbol{k}}(\boldsymbol{r}) = \sum_{\boldsymbol{G}} C_n(\boldsymbol{k}+\boldsymbol{G})e^{i(\boldsymbol{k}+\boldsymbol{G})\cdot\boldsymbol{r}}. \tag{2.65}$$

Here $\boldsymbol{k}$ is the wavevector in the band $n$, $\boldsymbol{G}$ is the reciprocal lattice vector of the periodic structure and $C_n$ is the band dependent amplitude. Bloch theorem is a useful analytical method of quantifying the effects of structure on a waveform $\psi(\boldsymbol{r})$, which is analogous to $p(\boldsymbol{r})$. Although, for complicated structures it becomes much harder to specify and solve for $\boldsymbol{G}$. This will be revisited in chapters 6 and 7.

### 2.6.5 The Effect of Elasticity

The descriptions of the nature of Acoustic Surface Waves have so far only looked at periodic structures which are perfectly rigid. Underwater metamaterials and metamaterial-like structures must include the elastic properties of the structures to be studied. The

bridge between metamaterial-like concepts and elastic plate theory is where the research presented in this thesis will focus.

In figures 2.14 and 2.15 shows a 6 mm pitch grating made out of aluminium, the same as the structure described in the previous section, excited with the same Hanning-windowed shaped single-cycle pulse at 0.12 ms after the pulse was first sent. Figures 2.14 shows the full time-domain model where the wave is travelling through both the aluminium and the water. Like the unstructured surface (section 2.6.1), the compression and non-dispersive wave within the water have travelled away from the origin the furthest. But unlike the unstructured surface the proceeding waves are a mix of all the resonating cavities, making it a far more complicated field map to identify the Rayleigh, Leaky Rayleigh and SSWs.
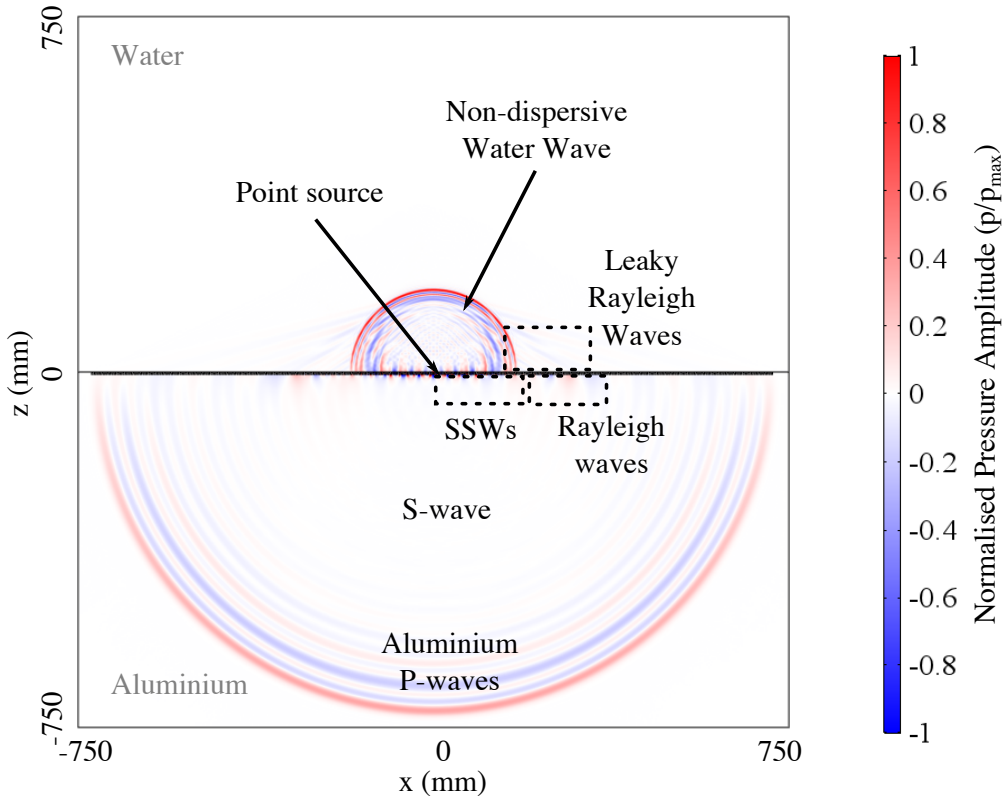


**Figure 2.14:** The Comsol calculated instantaneous pressure arising from a single-cycle Hanning-windowed pulse from a point source on the surface of a submerged aluminium sample with a patterned array of cavities on it's surface in space, plotted as normalised pressure amplitude ($p/p_{max}$) at 0.12 ms after the pulse was first sent. These cavities have pitch $\lambda_g = 6$ mm and width $w = 3$ mm.

Figures 2.15 shows the comparison between the complicated elastic and the simpler rigid case. This highlights how even though it may be possible to analytically determine

the modes of the rigid case, the waves become further complicated by the presence of an elastic structure. A large part of this work concerns experimentally detecting ASWs over submerged metal plates that have been structured to support ASWs. This thesis investigates how ASWs and elastic modes of the plate interact. This will be further discussed and investigated in experimental chapters 6 and 7.
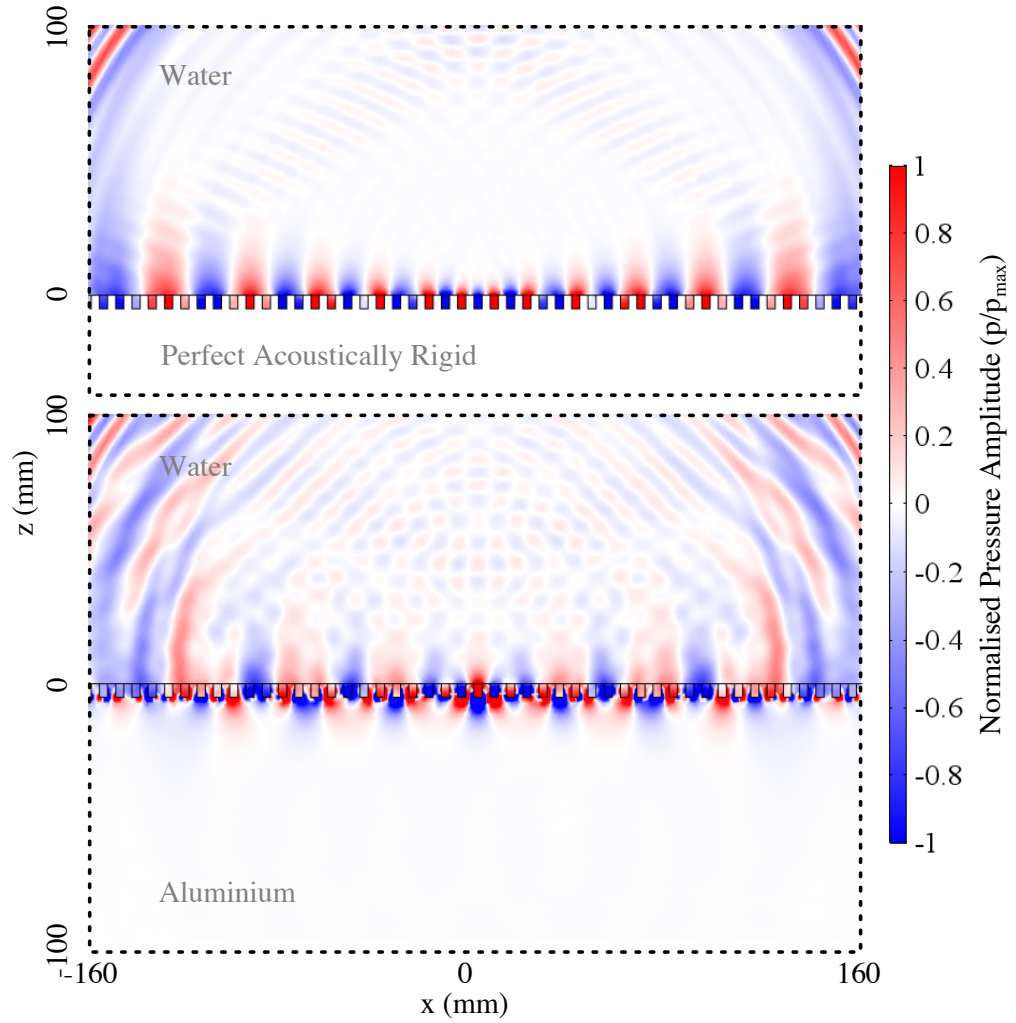


**Figure 2.15:** A comparison between the surface of a perfectly rigid vs an elastic aluminium patterned surface using Comsol to plot the normalised pressure ($p/p_{\max}$). These cavities have pitch $\lambda_{\mathrm{g}} = 6$ mm and width $w = 3$ mm.

## 2.7 Conclusion

This chapter covered fundamental concepts of the acoustics of fluids and solids including the loss-free acoustic wave equation, impedance, elastic properties, losses and resonant structures. Importantly, this chapter looked surface wave phenomena at the interface between two elastic materials, which is particularly common underwater. Further to this, the idea of acoustic resonance and how arrays of closely packed resonators support surface bound waves was outlined. To help understand and characterise acoustic fields, the dispersion relations of each type of wave was plotted and showed how it is useful for identifying the different radiative and evanescent modes of a system. Experimental results outlined later in this work will reflect on the theory set out here with the final results set out as dispersion diagrams. The next chapter will outline the experimental techniques used to detect sound underwater and the work expands on some of the analytical theory and computational modelling of sound propagating over periodically structured surfaces.

# Chapter 3

# Methods

## 3.1  Introduction

In this chapter the experimental, computational and analytical methods used throughout the subsequent chapters are presented. Firstly the details and reasoning for the choice of materials from which samples are made is described. Then the experimental pulse techniques used to acoustically excite the samples are described, including the equipment used to send and receive ultrasound and the methods used to analyse the data produced. Two types of experiment are detailed; the first setup with the source in the far field, used to acoustically excite the plate in the radiative regime, and the second setup with the source in the near field used to excite the evanescent fields of the modes of a structure. Finally, the computational analysis of the systems is described. Many of the methods of the work discussed in this chapter can be found in textbooks by Xavier Lurton[110], Allan D. Pierce[9] and Earl G. Williams[111].

## 3.2  Material Selection

There are a vast array of solid materials that can be cut, drilled and shaped to create patterned surfaces. For experiments in air there is little dependence on the material properties as most will closely approximate to being acoustically rigid[15], described in section 2.4.2. These types of boundary conditions have been used to create "exotic" acoustic structures using additive manufacturing techniques[58,112]. However, these techniques use polymer-based materials, which may be unsuitable for underwater work (section 2.6.1) as the speed of sound in polymers can be slower than in water and it may also be quite lossy. As discussed in section 2.6.1.2, the speed of sound underwater sets the limit between the radiative and the evanescent regimes. However, solids support wavespeeds (Rayleigh, shear and compressional) that are close to, and slower than, the

speed of sound underwater and so certainly may not be treated as perfectly rigid. This was briefly discussed in section 2.6.1.2 and will be further investigated in chapter 4.

Another point of interest is that generally the most common boundary found in air is the rigid boundary condition as most solid materials have a large impedance mismatch from low to high characteristic impedance, $Z$, previously described in section 2.4. In contrast to this it is difficult to find a material that fulfils the role of being a perfect pressure-release material in air as the high to low characteristic impedance mismatch would need to be satisfied. Aerogels are one possible candidate but are notoriously hard to cut and shape as they are brittle[113]. Underwater it is easier to achieve this boundary condition, as most thin walled air-filled cavities act as pressure-release materials. Thus, underwater novel experiments on pressure-release boundaries may be conducted which cannot readily be undertaken in air.

### 3.2.1 Underwater Pressure-release Materials

The majority of fluids have a far greater characteristic acoustic impedance than light gases such as air. For example, the characteristic impedance of room temperature water[114] is $Z_{\text{water}} \approx 1.5 \times 10^6 \ \frac{\text{Pa} \cdot \text{s}}{\text{m}^3}$ and air[115] has $Z_{\text{air}} \approx 4 \times 10^2 \ \frac{\text{Pa} \cdot \text{s}}{\text{m}^3}$. As $Z_{\text{water}} \gg Z_{\text{air}}$ a material such as a closed cell foam can be used as a pressure-release material underwater.

There are a numbers of different foams available[116,117,118]. They fall into two categories: open-cell foams or closed-cell foams. A comparison between open-cell and closed-cell foam microscope images is shown in figure 3.1. As shown, open-cell foams consist of a series of open walled cells that are interlinked. Common open-cell foams are widely used as dish sponges, bedding and packing foams. These foams will quickly fill with liquid when submerged as a result of having interconnected cells. This makes them unsuitable as a candidate for constructing pressure-release structures underwater. By contrast, closed cell foams usually consist of a polymer-based substance that is cured using an active agent that produces gas whilst it cures. Once cured, these materials have the majority of their cell walls intact and are not primarily interconnected. In general, closed cell foams are not as malleable as open-cell foams, which makes them easier to cut and drill. This makes them ideal candidates for a pressure-release material underwater. This work will use the closed-cell foam pictured on the right of figure 3.1, the Ethylene Vinyl-Acetate (EVA) foam to construct a foam adapter described in section 3.5 and the sample examined in chapter 8.
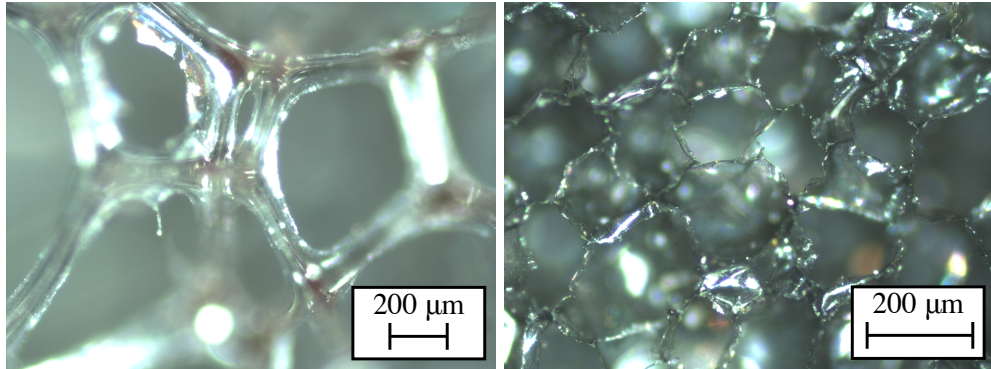
**Figure 3.1:** $10\times$ magnification microscope images of open (left) and closed (right) cell foams. The pore sizes of the closed-cell foam ranges from $d_{\mathrm{pore}} \approx 50$ $\mu$m to $d_{\mathrm{pore}} \approx 200$ $\mu$m. The open cell foam does not have pores, but strands of polymer that connect throughout.

Ethylene Vinyl Acetate, Ethylene Polymer Acetate and Polyurethane foams are closed cell foams that have a variety of applications, from the sports to the aerospace industry. The main criteria that determines the effectiveness of a pressure-release material is the acoustic wavelength, $\lambda$, compared to pore size, $d_{\mathrm{pore}}$. Note that when these materials are machined the outer surface of these materials will have a range of intact and compromised pores.

### 3.2.2 Underwater Elastic Materials

Many common metals have a similar impedance to that of water and therefore cannot be classed as acoustically rigid when submerged. Therefore, the metals studied in this work are treated as elastic materials.

This work investigates simple resonating structures integrated into these elastic materials. In order to structure these metals, they will be drilled and cut. Metals such as steel and aluminium are ideal candidates to be cut and shaped. The majority of the experiments in this thesis will investigate the properties of aluminium alloy as flat unstructured and structured plates. Cutting and drilling was performed using a CNC (Computer Numerical Control[119]) machine to pattern the surfaces with arrays of holes in one-dimensional or two-dimensional geometries.

Underwater, there are several issues that need to be addressed before using metals. Galvanisation and oxidization become issues that are heightened by impurities present within the water, as water bubbles form on metal surfaces scattering acoustic waves and acting as secondary sources. This problem is of course more of an issue with longer scan times. In this work, many experimental scan times fell in the $8 - 34$ hours range. There are techniques to reduce this such as the use of sacrificial metals[120], but the simplest technique is just to remove all other metals from within the water tank and if

other metals are needed for construction purposes then choose the same alloy, removing the potential difference between the two.

## 3.3 Experimental Setup

The experiments discussed in this work are performed underwater in a $3.00 \pm 0.05$ by $1.75 \pm 0.05$ by $1.20 \pm 0.05$ m fibreglass water tank in the lab. This tank is filled with tap water up to 1 m deep, with the addition of a minimal amount of chlorine ($\approx 1$ ppm) to keep the water free of fouling. The water has no flow and the ambient temperature stays similar to that of the room, varying from 291.0 to 295.0 K. The assumed ambient pressure of the room is that of the air pressure in the room that is $p_0 \approx 1$ atm. The water tank is pictured and graphically rendered in figure 3.2. The size of the setup makes it hard to photograph without obscuring parts of the tank, so graphical renders are utilised to help visualise it and to later visualise the in-water experiments.
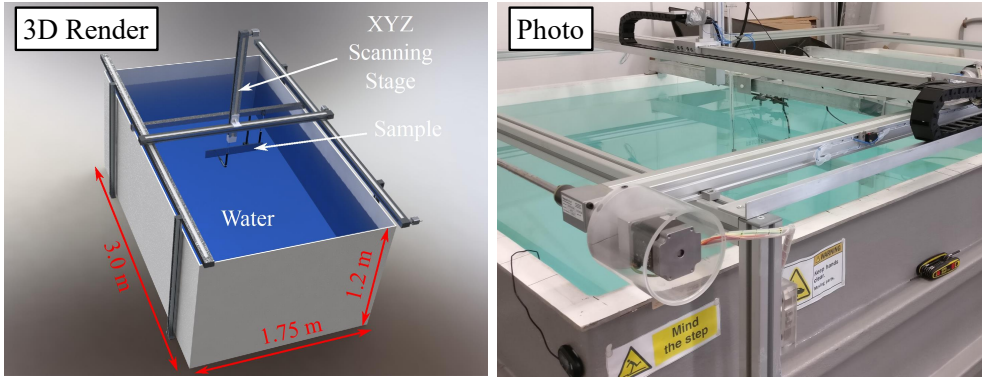


**Figure 3.2:** The water tank used for experiments outlined in this thesis. The right figure is a photo of the water tank and the left is a scale 3D render of the water tank with the addition of a scanning stage that will be later explained.

### 3.3.1 Ultrasound Sources

A Neptune Sonar D70 transducer[121] is used as an acoustic source. The transducer is a $3.4 \pm 0.1$ cm diameter ball made of a black polyurethane outer shell with an inner core made of a piezoelectric (lead zirconate titanate or PZT) that generates ultrasound through an applied voltage, $V$. An image of the transducer is shown in figure 3.3. This source has a nominal resonant frequency of 70 kHz and has an omni-directional beam pattern (quoted[121] up to 80 kHz). The typical transmission response for the D70 transducer is shown in figure 3.4[121], calibrated up to 150 kHz, but as will be discussed in section 3.5, the source can be driven outside of this range.

**Figure 3.3:** Photos and renders of the two sources. Top is the normal Neptune Sonar D70 transducer and bottom is the EVA foam wrapped D70 transducer. Left are photos of the devices on a 1 by 1 cm grid and right is the graphical representations of these devices with the dimensions given. Measurements of the diameter of the ball D70 has $\pm 0.1$ mm error and the dimensions of the wrapped D70 has $\pm$ 0.5 mm error.

To use the D70 transducer in the near field, a purpose-built $10.0 \pm 0.5$ mm thick pressure-release foam (Ethylene-Vinyl Acetate or EVA) source adapter was built. It was fashioned into the shape of a box with a $0.50 \pm 0.01$ mm walled $6.00 \pm 0.01$ mm diameter aluminium tube linking the outside to the water filled cavity containing the transducer. In making this device it was necessary to fulfil two criteria: maintain the broad usable frequency spectrum that the source outputs and reduce the apparent size of the source by varying the radial aperture to the end of the narrow tube. This is designed to make the modified source more point-like and directional to excite modes supported by samples that are examined. Figure 3.3 shows the source in the bottom two plots. More details about the construction of this source is explained in appendix A and the output of this source is given in section 3.5.
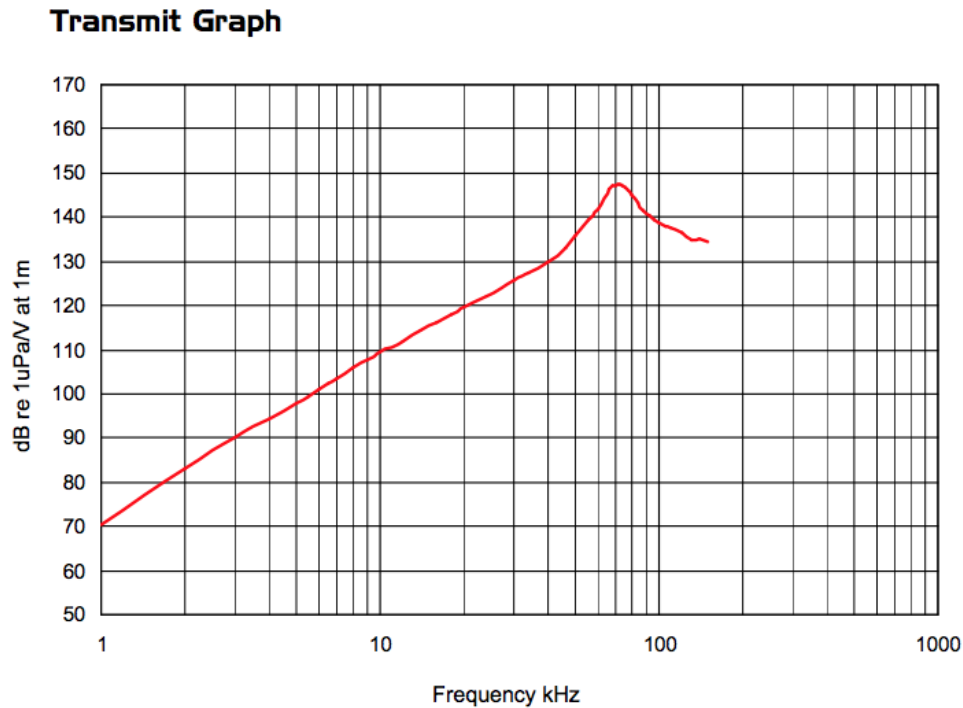
**Transmit Graph**



**Figure 3.4:** A typical transmissivity calibration of a Neptune Sonar D70 transducer. Peak nominal frequency of 70 kHz, although it has a broad output usable down to 1 kHz and up to 150 kHz. This data was taken from the Neptune Sonar public web page[121].

### 3.3.2 Ultrasound Detectors

Hydrophones are used to detect underwater pressure fields. This type of detector converts local pressure into electrical current using piezoelectric crystals[110]. In this work two different types of hydrophone are used: a Precision Acoustics (PA) 1 mm diameter needle hydrophone[122] and a Brüel & Kjær 8103 hydrophone[123]. These are pictured in figure 3.5 as well as their 3D rendered images, showing the dimensions of the two detectors. The hydrophone is gold plated, to make it inert underwater, and encloses a 28 $\mu$m thick gold electrode Polyvinylidene fluoride (PVdF) detector film at the tip of the 1 mm extrusion. This means it is a relatively point-like detector at the frequencies that are investigated in this work.
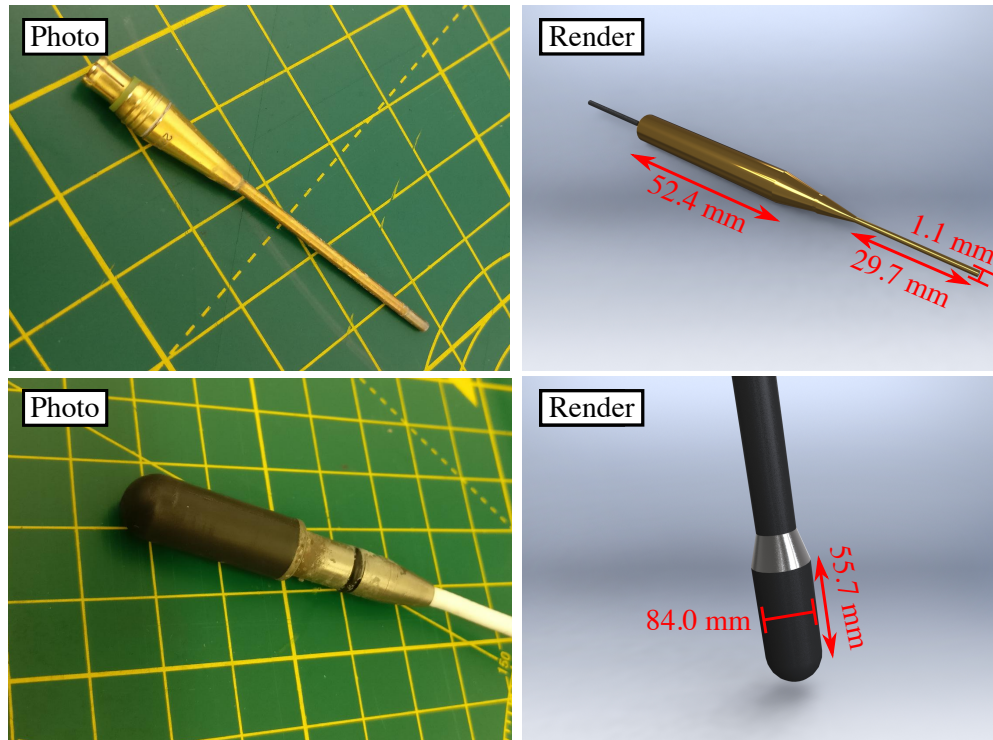
**Figure 3.5:** Photos and renders of the two detectors. Top is the Precision Acoustics 1 mm needle hydrophone and bottom is the Brüel & Kjær foam 8103 hydrophone. The left photos are of the devices on a 1 by 1 cm grid and right is the graphical representations of these devices with the dimensions given. The PVdF detector is positioned is at the tip of the measured 1.1 mm diameter extrusion. Measurements of the dimensions of both detectors have ± 0.1 mm error.

Calibration data for the two detectors is shown separately in figures 3.6 and 3.7. The two plots show the receiving sensitivity of the two detectors. The Brüel & Kjær hydrophone has a broad non-zero receiving sensitivity in the frequency range between 0 and 300 kHz with a peak response at ≈ 250 kHz. Shown in figure 3.7, the needle hydrophone is not calibrated in the frequency range that will be studied. Experimental results here use the spatial mean and maximum values in order to avoid minima in the output amplitude of the source, when normalisation takes place, and to visualise the detected signals, further explained in section 3.5. The results are collected and analysed using and normalised using a reference or self-normalisation technique described further in section 3.5. Therefore, it is only important that the source-detector setup has a usable range that is suitable for acoustically probing the samples in this work.
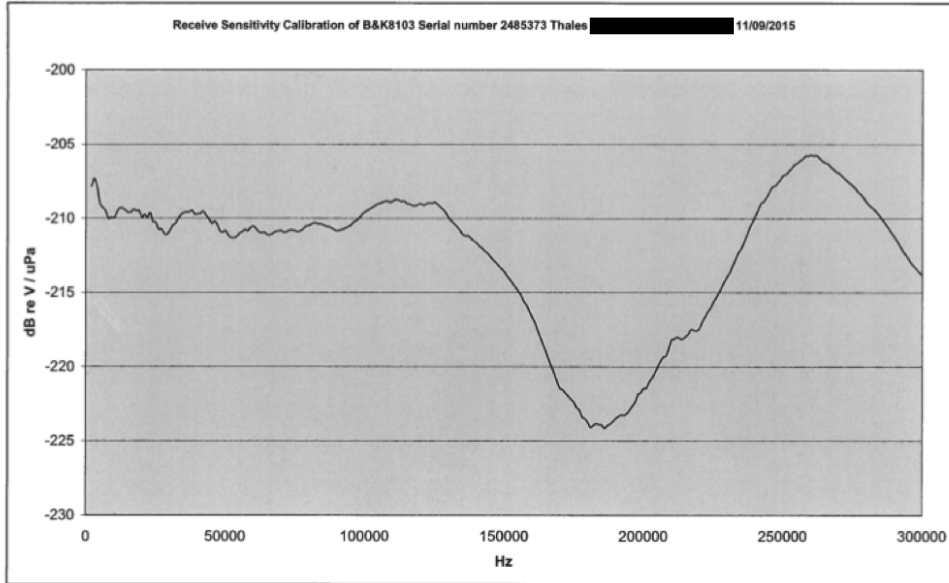
**Figure 3.6:** The measured receiving sensitivity of the Brüel & Kjær 8103 hydrophone. This graph shows that the receiving sensitivity, $\frac{V}{\mu Pa}$, is generally flat between 0 and 300 kHz with a minimum at 190 kHz. This measurement was taken by Thales.



**Figure 3.7:** The measured receiving sensitivity, $\frac{mV}{MPa}$, of the Precision Acoustics needle hydrophone. The sensitivity drops off at the higher frequencies. But as this work will show, it is usable in the range of 50-150 kHz.

## 3.4 Other Equipment

The experimental system is run computationally using a LabView code that defines the output pulse shape as voltage, $V$, over time, $t$, and reads the detected signal using a USB linked digital oscilloscope[124] (Picoscope 5442D). This also synchronises the sending, from the waveform generator, and detecting of signals. The Picoscope runs at 14-bit dynamic range, but to improve the signal to noise and take advantage of the full dynamic range of the Picoscope it is necessary to use a wideband signal amplifier (pre-amp), which will be further detailed in section 3.5. A full schematic of the experiment is presented in figure 3.8.
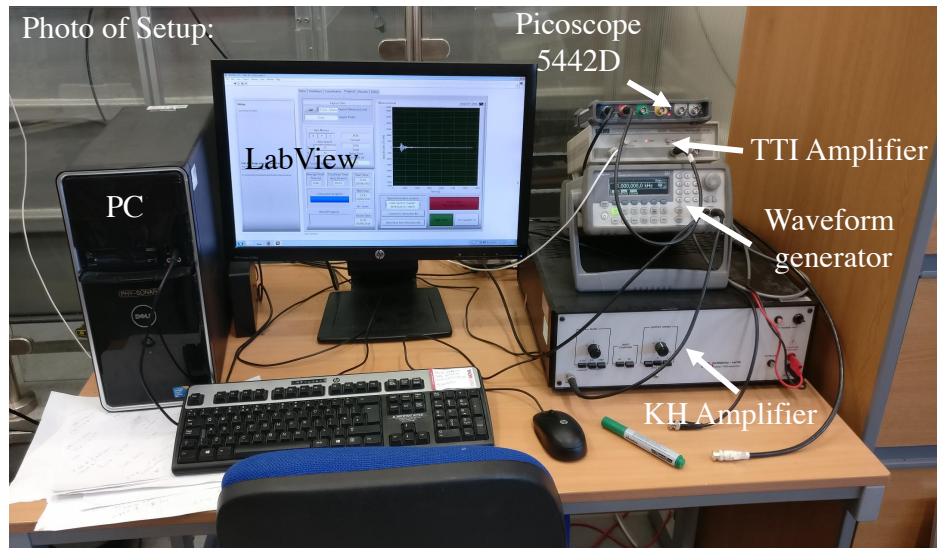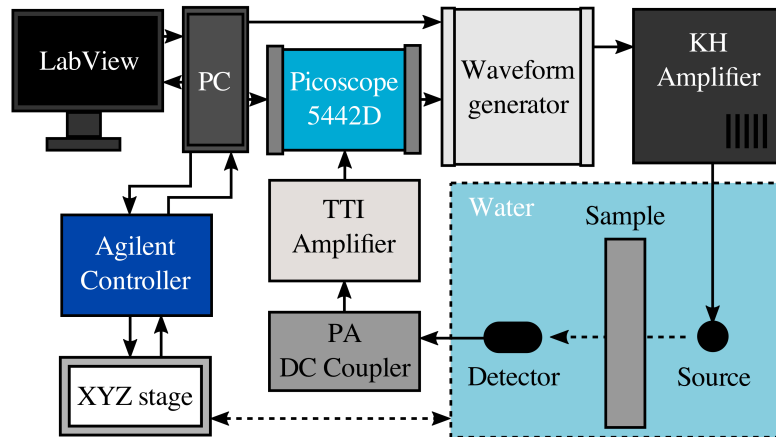


**Figure 3.8:** Top is a photograph of the full experimental setup used to run experiments. Bottom is a schematic of the setup, including the in-water equipment. The source and detector can be interchanged as to best suit the sample and the frequency range being scanned.

To scan the fields spatially, a LabView controlled XYZ scanning stage is used. The hydrophone detectors are mounted to the stage using bespoke acrylic and 3D printed mounts that allow the detector to be positioned with precision with reference to the sample. Further details about this and the process used to analyse the data is discussed in section 3.7.

## 3.5 Pulse Measurement Technique

There are several different types of pulse shapes used to extract the response function of a sample: Continuous Wave (CW), chirped and broadband pulses are commonly used in material evaluation techniques to excite acoustic systems with single frequency or a range of frequencies[25,125].

The interface between two different impedance materials is a source of acoustic reflections, scattering and diffraction (section 2.4.3). As experimentation takes place in 1.00 m deep water and the speed of sound in water is, $c_w \approx 1500$ m/s (experimentally measured in section 3.6), detected signals may include significant reflections from the sides of the tank. There are two ways to deal with these reflections. The first method is to cover any reflecting surfaces in an absorbing material. This method is commonly used in air[126,127], but underwater this method is very costly as it is necessary to use specialist syntactic rubber which is limited to a usable frequency range[128]. The second method is to remove the reflected signal in post-processing by time-gating the results. This time-gating of the signal is by the far the simplest and most cost-effective method. Reflections in the tank also mean that for repeat pulses, the time-gap between each pulse must be large enough for all reverberations to dissipate. Therefore experimentation is gathered over 120 $\mu$s recording times, time-gated at 65 $\mu$s, when necessary, and with a pulse rate of 1 every 0.3 s. In summary, the experimentation in this thesis uses the broadband pulse technique that uses approximately double-cycle Hanning windowed pulses centred around ultrasonic frequencies that are then time-gated to remove reflections.

A comparison of different Hanning shaped pulses centred around the same carrier frequency is shown in figure 3.9. Changing the length of the pulse changes the number of oscillations contained within the pulse and changes the frequency bandwidth of the pulse. The Fourier analysis used here will be discussed in detail in section 3.7. Unlike CW experimentation, this pulse technique can then be used to test a broad frequency range of acoustic signals.
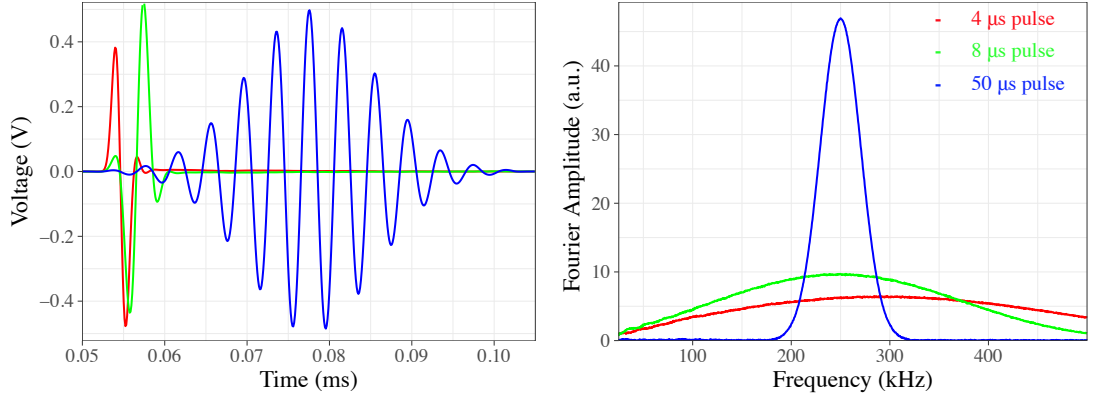
**Figure 3.9:** Example pulses centred at 250 kHz with 4 $\mu$s, 8 $\mu$s and 50 $\mu$s pulse length output from a waveform generator. On the left the time domain data for each pulse and on the right is the frequency spectra of the detected electrical signals.

Pulses can be changed to alter the central frequency of the Fourier analysed frequency spectrum, as evidenced in figure 3.10. In this work, the experiments are performed with pulses centred at 60 (chapters 6 and 7) and 250 kHz (chapters 4, 5 and 8). These are excited with double-cycle Hanning pulses, chosen as they output higher power and can be centred on the chosen frequency, figure 3.9.
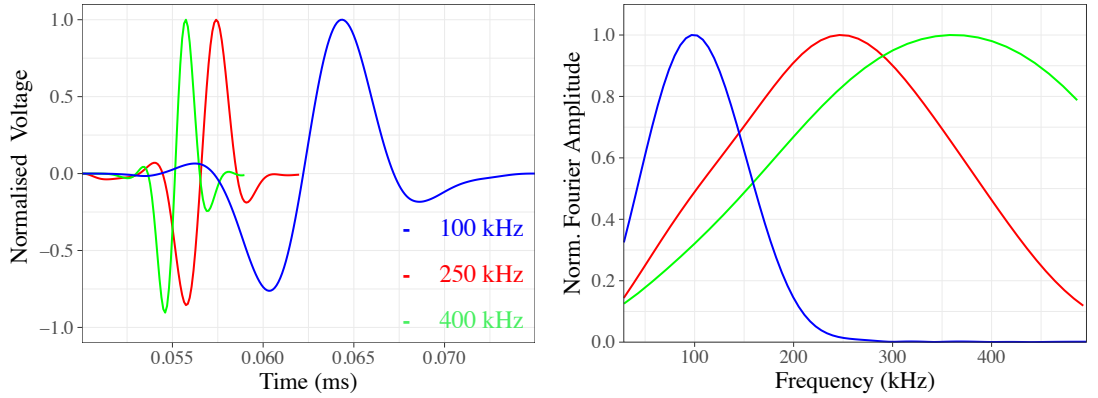


**Figure 3.10:** Example pulses centred at 100, 250 and 400 kHz output from a waveform generator. On the left the time domain data for each pulse and on the right is the frequency components of the detected electrical signals.

The signal to noise ratio is improved for this setup by pulsing, recording and then averaging temporally, by taking $\frac{\Sigma_N V(t)}{N}$. Here $N$ is the number of repeats averaged. The majority of scans in this work are performed using an average of 50 pulses.

The dynamic range of a measurement sets the minimum possible signal that can be detected. The Picoscope settings set the dynamic range of this work. Generally the range is set to 500 mV at 14-bits. This means the minimum voltage (V) that can be recorded is $V_{\min} = \frac{0.5\text{V}}{2^{14}} = 30.5~\mu\text{V}$. In order to take advantage of the full dynamic-range

of the Picoscope, the output signal is amplified along with the input signal. To do this two amplifiers are used: a Krohn Hite (KH) 7500 power amplifier for the input [129] and a Thurlby Thandar Instruments (TTI) wideband WA301 amplifier [130] for the output. Figure 3.11 shows the signal of a double-cycle Hanning pulse centred at 250 kHz sent with use of both amplifiers. The gain on the KH amplifier was set to $\approx \times 70$ and the gain on the TTI amplifier was set to $\approx \times 10$. The results in fact show that the pulse was amplified by $Amp_{KH} \approx \times 10$ (due to being below the flat banded range of the amplifier) and $Amp_{TTI} \approx \times 8$.
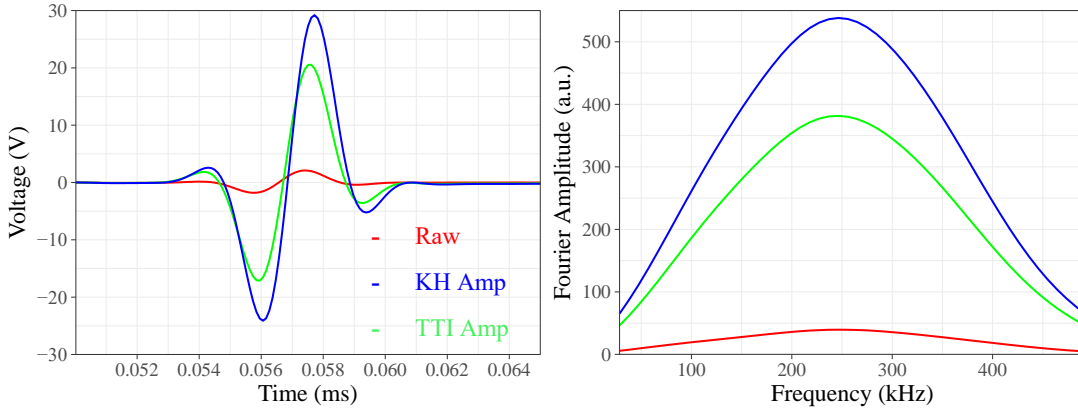


**Figure 3.11:** The output 8 ms waveform pulse (red) centred at 250 kHz and amplified voltage detected from the Krohn-Hite (blue) and the TTI amplifiers (green).

The plots in figures 3.9 and 3.11 show mostly clean well-defined signals that are Fourier transformed into broadband peaks containing many frequencies. Experimentally detected signal between the D70 source and the 8103 hydrophone are shown in figure 3.12. When this signal excites the Neptune Sonar D70 source, the results is a transfer function of the input signal with response of the device. The same is also true for the detector. Here the results show the 50 pulse signal centred at 250 kHz, showing that the signal "rings down" over time quite significantly, but the frequency spectrum remains broad and non-zero around the central frequencies of the pulse.

To excite a sample using a broadband pulse, the source is positioned some distance away from the sample. Each source used will also have a characteristic beam pattern which may mean that the source has increased amplitude signal in a certain direction. The next section will describe how the wrapped and unwrapped D70 transducer sources are employed.

**Figure 3.12:** Experimentally detected in-water example measurements, showing the detected time domain and frequency domain output after 8 ms Hanning pulses centred at 100, 250 and 400 kHZ are projected and detected using the D70 transducer to Brüel & Kjær hydrophone.

### 3.5.1 Radiative Excitation and Detection

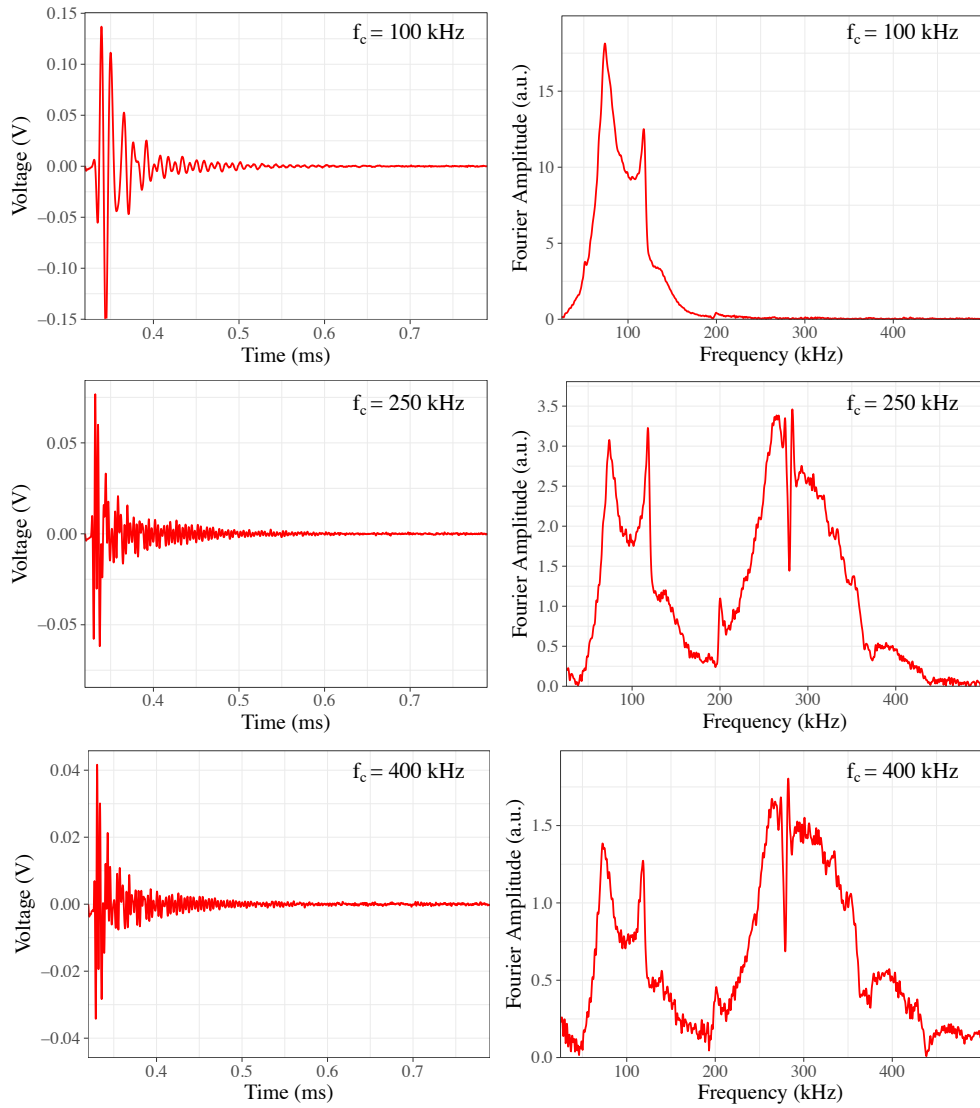In this work both structured and unstructured plates are explored using acoustic pulse excitation with a range of incident angles and therefore a range of in-plane wavevector, $k$, values. The radiative regime is that where $k < k_0$. In order to excite these modes, the source must be positioned some distance away from the sample. But given the finite size of the sample it is clear that larger source-sample distances reduces the incidence angles possible, therefore the source distance is dictated by the range of angles and wavevectors necessary to excite the modes of the system. In this work the sample is positioned $40.0 \pm 0.5$ cm from the unwrapped omnidirectional source i.e. in the "far-field" when scanning the radiative modes of the plates.

Although this experiment can be used to scan the reflected radiative modes of a material, this work mainly uses transmission measurements. This means that the detector (Brüel & Kjær hydrophone) is positioned on the opposite side to the source (Neptune Sonar D70 transducer) and detects the signal transmitted through the samples. By scanning the detector spatially, parallel to the plate, the different angular components of the fields ($\theta_i$) can be probed to characterise the acoustically excited modes within the plate. This method is used in chapters 4, 5 and 8 to excite the acoustic response of different materials. In these chapters the source is positioned $400 \pm 10$ mm away from the sample and the detector positioned $10 \pm 1$ mm from the opposite side of the samples.

The Brüel & Kjær 8013 hydrophone is used to spatially scan the fields transmitted through the plate. To do this the hydrophone is mounted on the scanning stage described in section 3.3. This Aerotech controller device allows the detectors to be accurately positioned and moved spatially with $\pm$ 30 $\mu$m minimum precision. Scanning takes place in a plane or a line parallel or normal to a sample surface.

In this work results are normalised using reference scans and self normalisation. A spatial scanned empty tank measurement (reference) of the D70 transducer is shown in figure 3.13. For this, the detector was scanned in a plane at $z = 400 \pm 1$ mm with a double-cycle Hanning pulse centred at 250 kHz. Perhaps naively, it might be expected that the most intense signal is recorded at the centre of the area. However, the bottom row of figure 3.13 shows this maximum in other positions, which are dependent on frequency. This is the reason the reference data is recorded spatially for every frequency step. The maximum value of the spatial reference data is used as the data set used to normalise the experimental frequency absolute amplitude ($A$) data, where $|A_{\text{result}}(f)| = \frac{|A_{\text{experiment}}(f)|}{|A_{\text{reference}}(f)|}$. Whereas wavevector data is self normalised, $|A_{\text{result}}(k)| = \frac{|A_{\text{experiment}}(k)|}{|A_{\text{max}}(k)|}$.
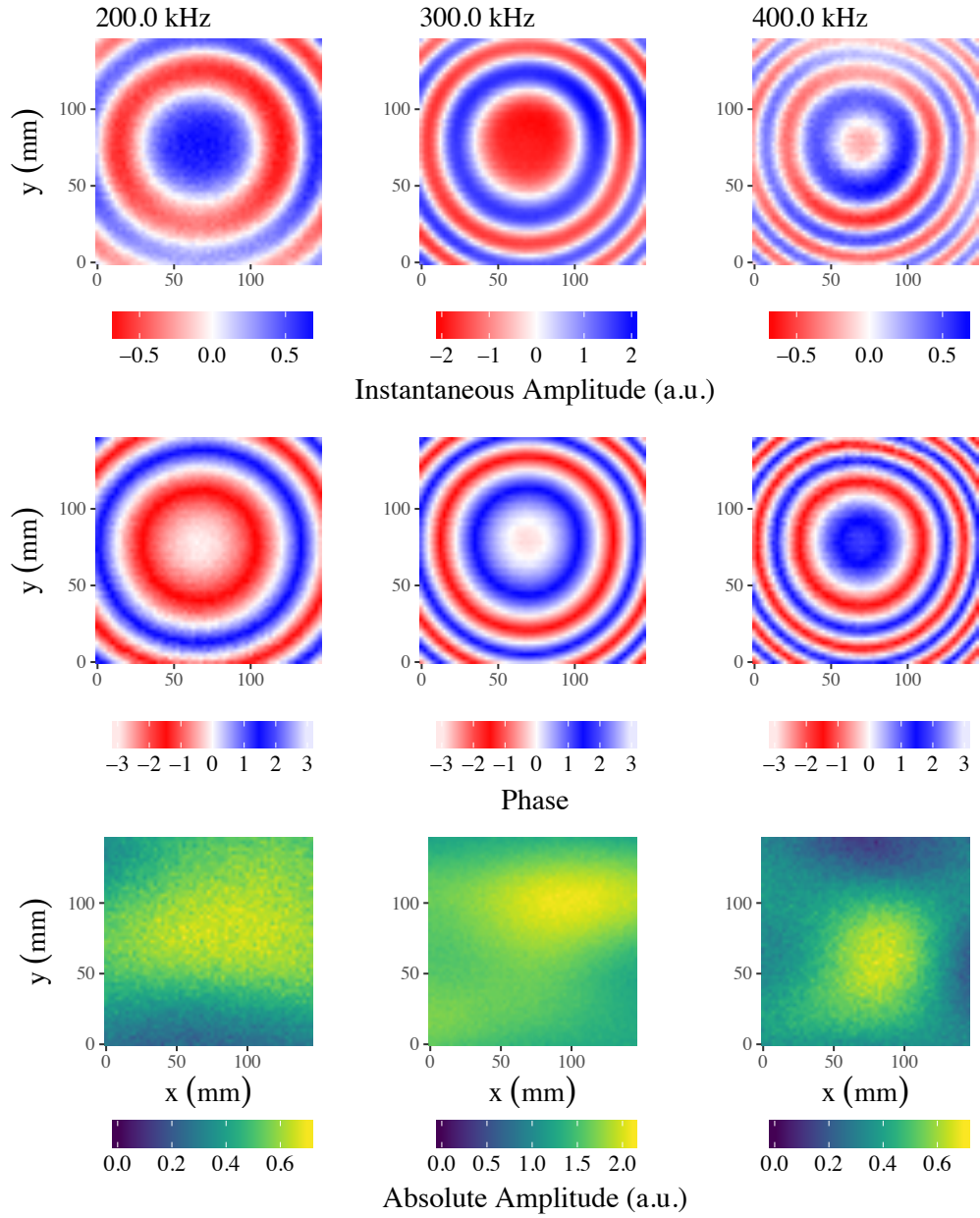
**Figure 3.13:** Spatial field-maps of the instantaneous amplitude (top), the phase (middle) and the absolute amplitude (bottom) of a freely travelling sound wave excited by an approximately double-cycle Hanning pulse from the Neptune Sonar D70 transducer and detected using the 8103 hydrophone, $41.0 \pm 0.5$ mm from the source.

### 3.5.2   Evanescent Excitation and Detection

As discussed in section 2.6.1, surface waves are "trapped" acoustic fields that propagate at the interface between two elastic media. As these types of evanescent fields exponentially decay normal to the surface it is necessary to acoustically excite the sample close to the surface and with high wavevector along the surface. This is undertaken using the point-like D70 foam-wrapped transducer positioned $\approx 3$ mm from the sample surface.

It is also necessary to scan close to the sample surface, within the near field $(< \lambda)$. But this also introduces the complication of detector-to-sample reflections that may influence the measured data. Therefore it is best to use of a point-like detector. Experimentation is performed using the PA 1 mm diameter needle hydrophone described in section 3.3. The evanescent field experiments are performed by scanning spatially and Fourier transforming the signal in $x$, $y$ and $z$. To do this, the needle hydrophone is mounted on the scanning stage described in section 3.3. This allows the detector to be accurately positioned and moved spatially with $\pm$ 30 $\mu$m precision. Generally scans are taken in a plane parallel to the surface of the sample 0.500 mm from the sample surface to detect the evanescent acoustic fields.

Again these results are normalised using reference scans without a sample and self normalisation. Spatially scanned reference data for foam-wrapped D70 transducer is shown in figure 3.14. This scan area has the closest point to the source here is at the centre of the plot and $z = 0.50 \pm 0.01$ mm using a double-cycle Hanning pulse centred at 60 kHz. The scanned data shows that the source works well as a localised point source, which is needed to excite the structured samples in chapters 6 and 7. This source-detector setup is usable from 40-150 kHz. The upper limit of the source is shown in the right row plots of figure 3.14. Here the signal is weaker and the background "noise" is clearly visible. Again, this data is used to normalise the experimental frequency absolute amplitude data, where $|A_{\text{result}}(f)| = \frac{|A_{\text{experiment}}(f)|}{|A_{\text{reference}}(f)|}$ and any wavevector data is self normalised, $|A_{\text{result}}(k)| = \frac{|A_{\text{experiment}}(k)|}{|A_{\text{max}}(k)|}$.

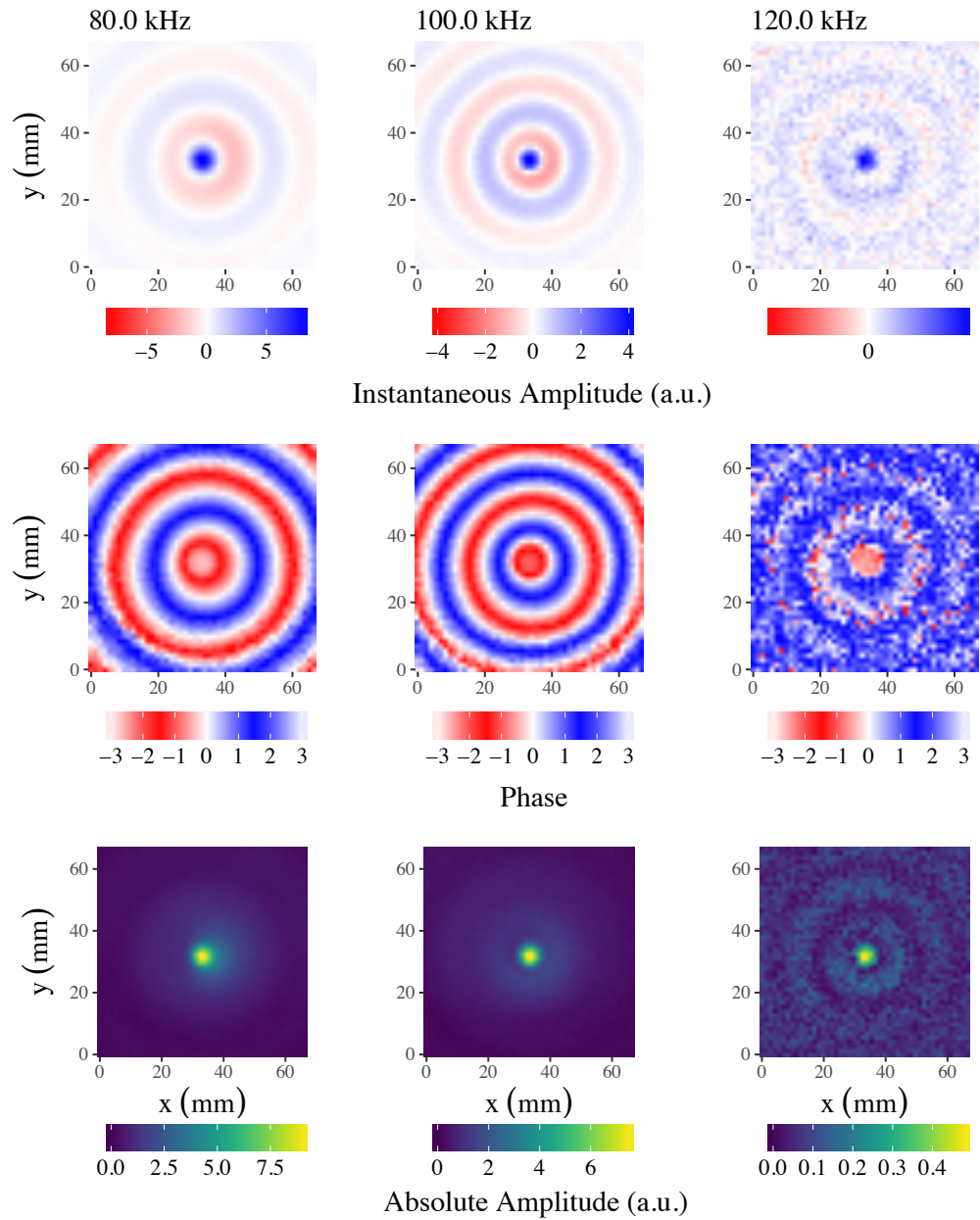**Figure 3.14:** Spatially plotted frequency domain data of the instantaneous real pressure (top), the instantaneous phase (middle) and the absolute amplified (bottom) of a freely travelling sound wave excited by an approximately double-cycle Hanning pulse from the EVA foam wrapped Neptune Sonar D70 transducer and detected using the PA 1 mm needle hydrophone, positioned $5.0 \pm 0.1$ mm from the source.

## 3.6 Measuring the Speed of Sound in Water

Chapter 2 explained that it is common to use in-the-field measurements of the speed of sound in a body of water as the speed significantly depends on the salinity and impurities of the water[9]. As unperturbed sound in water is non-dispersive, the speed is extracted by tracking the phase fronts of a broadband pulse travelling through water by scanning a line moving away from the transducer (foam wrapped D70), as shown in figure 3.15.
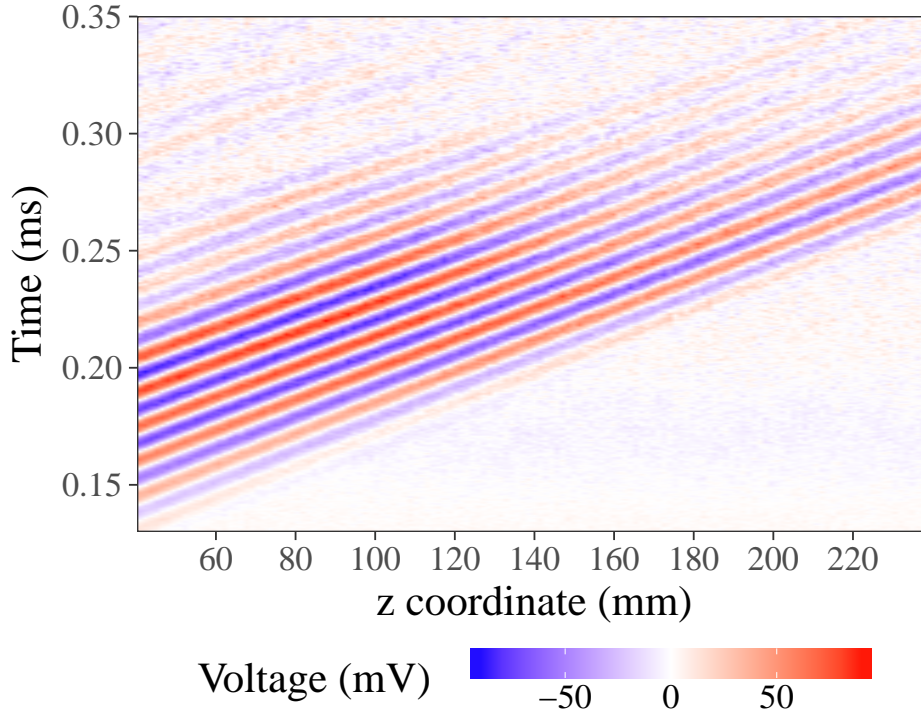


**Figure 3.15:** The line-scan time-domain data of a freely travelling sound wave excited by an approximately double-cycle Hanning pulse from the wrapped D70 transducer.

The experimental results in figure 3.15 were obtained by scanning the PA 1 mm needle hydrophone from $60.0 \pm 0.1$ mm from the source to $220 \pm 0.1$ mm from it, with $2.5 \pm 0.1$ mm step size of the scan. At each point of the scan a 8 ms long broadband pulse, was sent and received 50 times and averaged. The speed of sound is extracted from the experimental results by taking the gradient of phase ($c_{\text{water}} = \Delta x/\Delta t$) over multiple phase fronts in the region pictured in figure 3.15. The average result of measuring the speed of sound is $c_{\text{w}}(293.5 \pm 0.5K) = 1512 \pm 6$ m/s. This speed of sound does not significantly depend on the water temperature, therefore this value is used in all experimental work throughout this thesis.

## 3.7 Fourier Acoustics

This section will elaborate the method used to extract the frequency, $f$, and wavevector, $\mathbf{k}$, components of the recorded time-domain data. The Fourier acoustic method set out here is commonly used in other acoustics research [25,111,57].

### 3.7.1 Time Domain

In the following example, an FFT algorithm is used to extract the frequency and wavevector components, performed using a computational R-code [131]. Data is collected by scanning the detectors spatially, for example in $x$ and $y$ with total scan lengths $x_{max}$ and $y_{max}$ (section 3.3). Here the spatial resolutions of the scan are $\Delta x$, $\Delta y$ and $\Delta z$. At each point in space the voltage, V, over time, t, is collected and then averaged over 50 or 250 repeats. Results at each point have a time resolution of $\Delta t = 0.104 \ \mu$s.
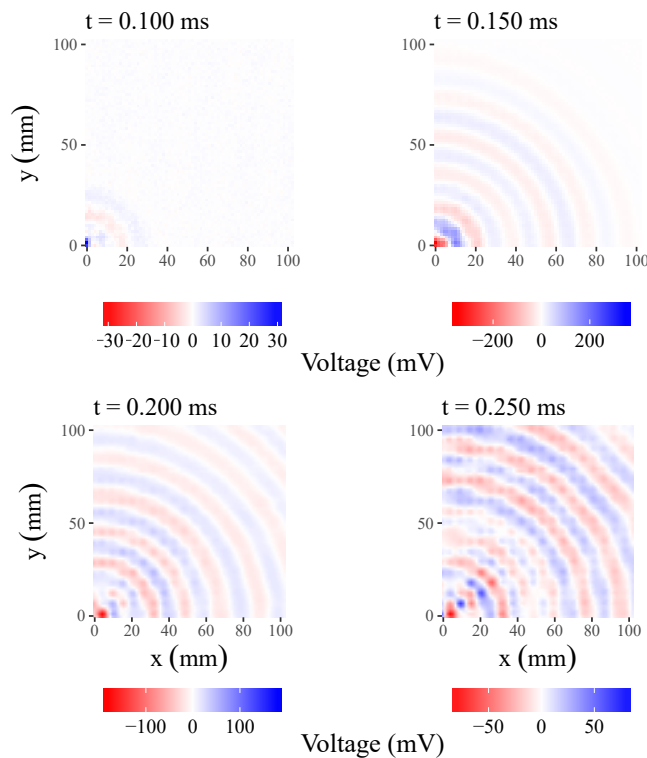


**Figure 3.16:** An example of the Instantaneous voltage above the 6.4 mm thick plate at three different points in time: 0.100, 0.150, 0.200 and 0.250 ms after the source first projects a signal. Voltage (mV) is shown as blue (positive) and red (negative).

An example of a scanned time domain results for a square array of holes in aluminium alloy, discussed in chapter 7, is shown in figure 3.16. This figure depicts four instantaneous snapshots of the voltage detected spatially at 0.100, 0.150, 0.200 and

0.250 ms, after the electrical pulse was launched. This source is located at $x = 0$ mm, $y = 0$ mm and $z \approx 3$ mm from the sample.

### 3.7.2 Frequency Domain

By Fourier transforming the time-domain data in time using an FFT($t$) (a discrete Fourier transform algorithm) the frequency, f, dependent complex Fourier amplitudes present within a signal are extracted at each point in space.

An example frequency domain set of plots for the two-dimensional data in figure 3.16 is shown in figure 3.17.



**Figure 3.17:** Example plots of three different frequency dependent $xy$ spatial plots showing the instantaneous real amplitude (top), which shows the phase and amplitude, and normalised absolute amplitude (bottom) of the excited field of the square array of holes at 80.0, 82.4 and 85.0 kHz.
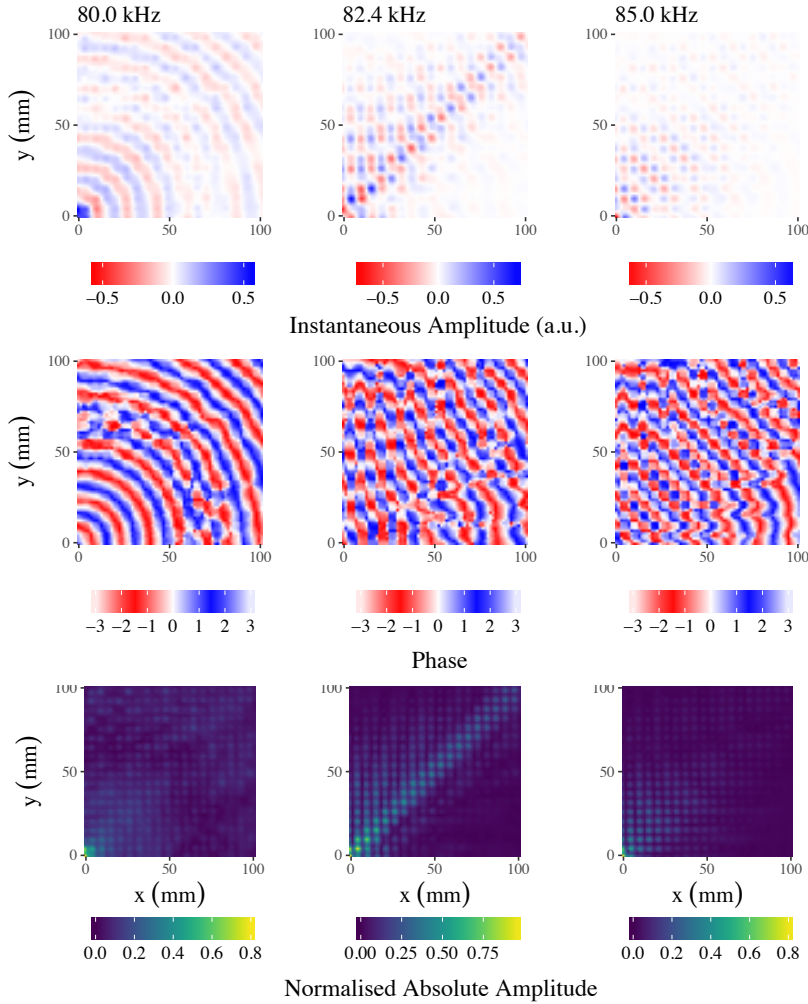
Figure 3.17 is taken from a data set for a 6.4 mm thick square array of holes chapter 7. Here the data shows the three outputs of the FFT as real instantaneous amplitude, phase and then normalised absolute amplitudes at 80.0, 82.4 and 85.0 kHz.

The maximum frequency resolution of these scans is dictated by the length of the window, $t_{\text{window}}$, where $\Delta f = 1/t_{\text{window}} = 833$ Hz with $t_{\text{window}} = 1.2$ ms. The highest frequency value accessible is set by the Nyquist limit [132] of $f_{\text{max}} = \frac{1}{2\Delta t} = 4.8 \times 10^6$ Hz.

### 3.7.3 Reciprocal Space

The work here will eventually explore structured surfaces, like the square array example in the previous section. Through Fourier analysis the wavevector components of the fields ($k_x$, $k_y$ and $k_z$) the effect of the periodicity can be visualised in reciprocal space. This is analysed using a two-dimensional spatial FFT of the complex amplitude of the frequency components, $\text{FFT}(x, y, z)$. An example set of k-space plots is shown in figure 3.18, which are also taken from chapter 7.
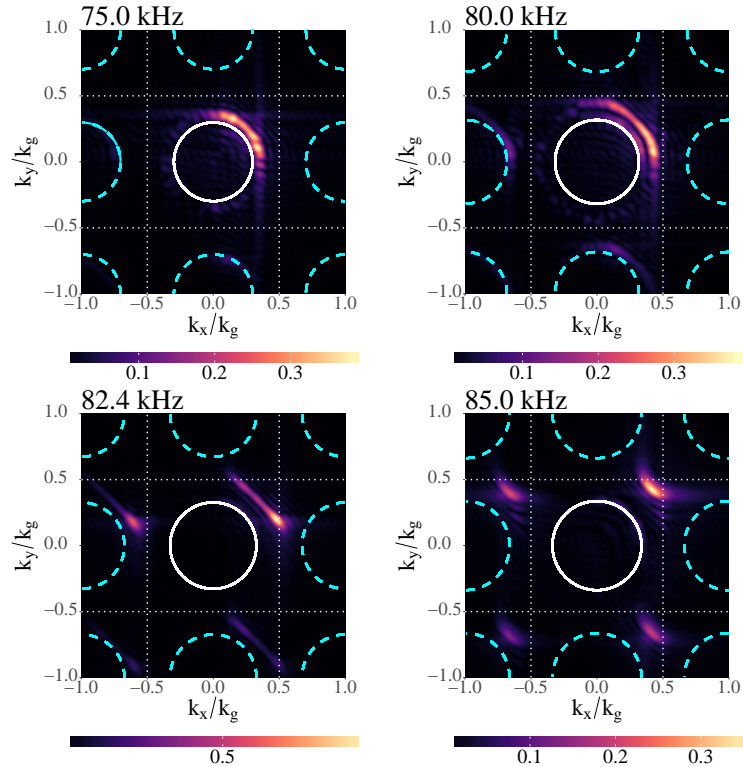


**Figure 3.18:** Example wavevector plots of the field propagating over a 6.4 mm thick square array of holes at four different frequencies: 75.0, 80.0, 82.4 and 85.0 kHz These plots show directional components of the fields as the Fourier amplitude of the signal propagating in the $x$ and $y$ directions as $k_x$ and $k_y$ components. The sound line is represented as a white continuous circle with the diffracted sound lines as dashed circles. The white dotted lines are the Brillouin zone boundaries in $x$ and $y$.

61

These results are essential in determining the directionality of the excited modes. The maximum measurable wavevector component in a given direction is determined by the step size $\Delta x$, $\Delta y$ or $\Delta z$, through the relation $k_{\max} = \frac{2\pi}{\Delta x}$ etc. The maximum resolution of the wavevector components, $\Delta k$, is determined by the total scan length, $x_{\max}$, as $\Delta k = \frac{2\pi}{x_{\max}}$.

### 3.7.4 Extracting the Dispersion

To plot the dispersion relation of the data both the wave vector and frequency components are taken at selected value of $k_x$, $k_y$ or $k_z$. An example dispersion is shown in figure 3.19, resulting from the k-space plots in the previous section. This example shows the dispersion plotted between the points of high symmetry in reciprocal space $\Gamma$, $X$ and $M$. As previously mentioned in 2.6.3, the points of high symmetry are dictated by the intersection of Bragg planes in reciprocal space that in this example is a simple square. $\Gamma$, $X$ and $M$ are indicated in the insert in the top right corner of the figure. For the majority of this work, dispersion plots will be plotted in only one wavevector direction ($k_x$, $k_y$ or $k_z$).
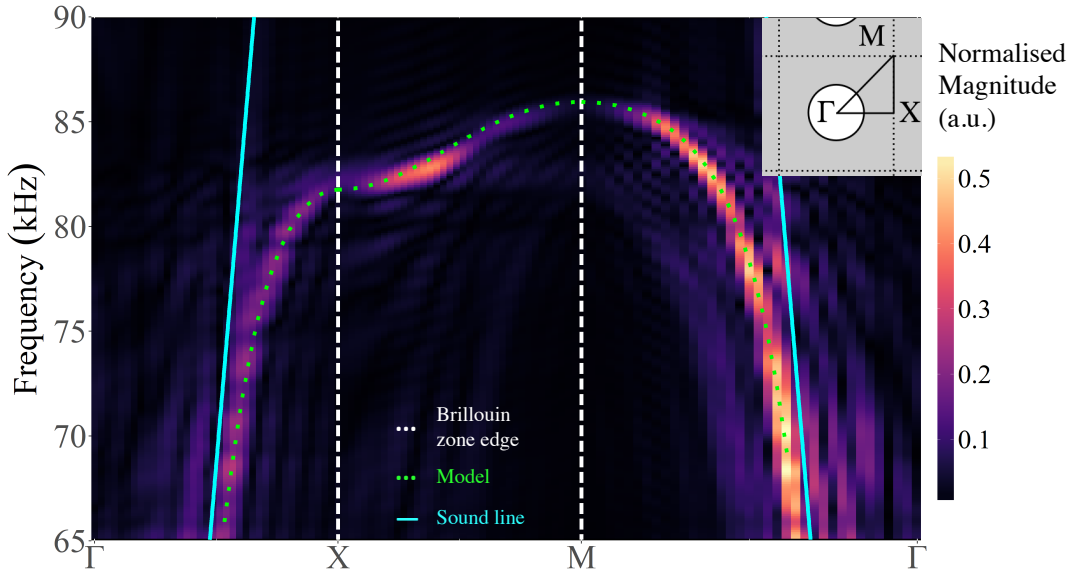


**Figure 3.19:** An example dispersion of a square array of holes plotted along lines of high symmetry $\Gamma - X - M - \Gamma$. $X$, $M$ and $\Gamma$ are defined by the shape of the array and the wavevector of the grating, $k_g/2$. Modelled data (green dotted line) is the result of computationally calculated FEM modelling to be explained in section 3.8.

### 3.7.5 Zero-padding and Window Functions

Fourier results can be modulated by artefacts that are entirely related to the finite size of the data, the resolution and any non-zero components at the ends of the windowed data. One of the most important tasks is to match the phase components at the edge of the scanned data, temporally and spatially. Fast Fourier Transforms (FFTs) assume periodic data sets and therefore the edges of the data window must match temporally and spatially. This can be done by simply setting the amplitude to zero using a window function. Windows such as Hanning windows are widely used to remove these artefacts[133]. A Tukey window commonly used throughout this work is shown in figure 3.20.
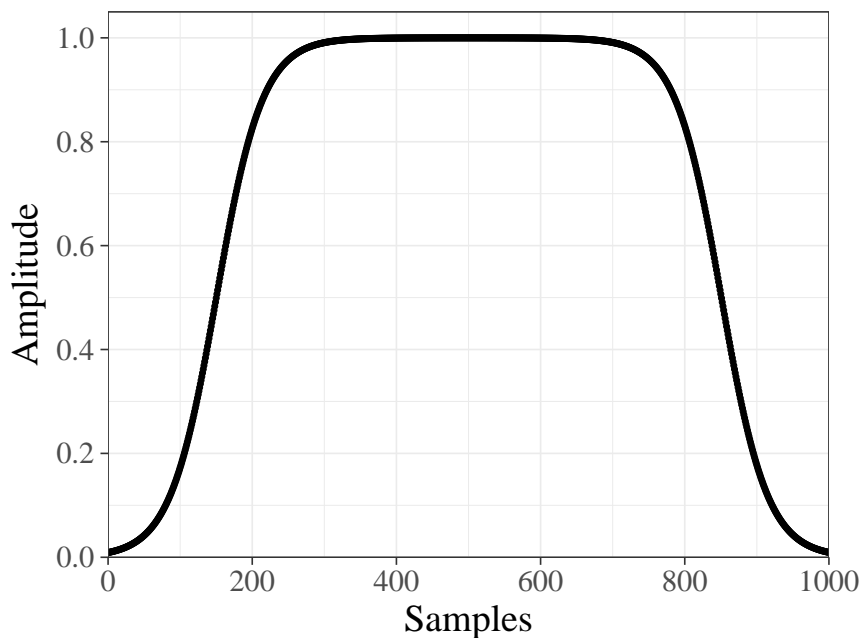


**Figure 3.20:** An example Tukey window which is centred around the 500 samples. This window is multiplied with a list of data of length $N$, where in this case $N = 1000$.

A comparison between the raw and Tukey windowed and zero-padded dispersion relations of the surface modes of a single line of resonating holes is shown in figure 3.21 and is discussed further in chapter 6. These results show that some features are enhanced and some features removed using a Tukey window, which has changed the result. Therefore, spatial windows will not be employed in chapter 7.
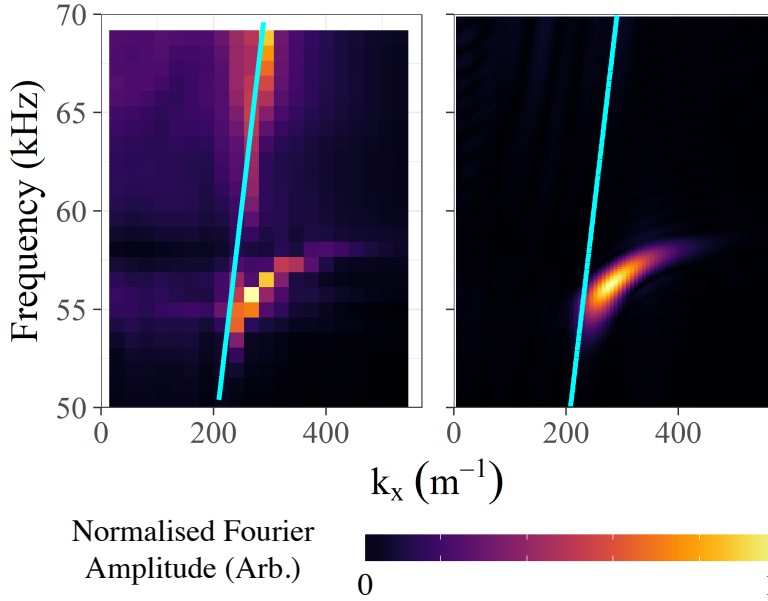
**Figure 3.21:** An example data set from chapter 6 of the surface mode of a single line of holes plotted as the dispersion between $k_x = 0$ and $k_x = k_g/2$. Here, the left-hand plot has not been post processed and the right hand plot has been zero padded to three times the length in time and space with a Tukey window applied. The cyan blue line is the sound line for water, $c_w$.

Zero padding is used throughout this work to interpolate in frequency and wavevector space. Zero padding three times the data length (temporal and spatial) was used to produce the data presented in figures 3.17, 3.18 and 3.19.

## 3.8 Finite Element Method Modelling

As this work will examine both the pressure-acoustic and the elastic properties of different media, any software packages used to model these systems will need to be able to model both as coupled domains. Comsol multiphysics 5.3a [70] is a Finite Element Method (FEM) software that is widely used to solve these types of systems. This is used throughout this thesis to verify results as the software can be used to model our systems with multiple types of coupled regions, using different fundamental physics in each and results can be extracted in time and frequency space in up to three dimensions.

One way of representing the FEM method is in acoustic matrix form:

$$\boldsymbol{M} \cdot \boldsymbol{p} = \boldsymbol{b}, \tag{3.1}$$

where $\boldsymbol{M}$ is the matrix representation of the governing equations of the system, $\boldsymbol{p}$ is the

unknown pressure matrix and $b$ is the matrix form of the source function. For further details please view the Comsol handbook[70].

FEM modelling involves a four step process:

- The geometry being examined is built and the physics in each region set.

- The geometry is meshed.

- The appropriate wave equations are solved within and at the boundaries of each region.

- The quality of the solutions are assessed (whether the solutions converge to a reasonable solution).

Setting up the models means building a 2D or 3D system that consists of the whole model or uses a unit cell with periodic conditions to describe an infinitely repeated system. These models are then meshed using tetrahedral components and rectangular layers as shown in the example 3D system in figure 3.22, used in chapter 7.
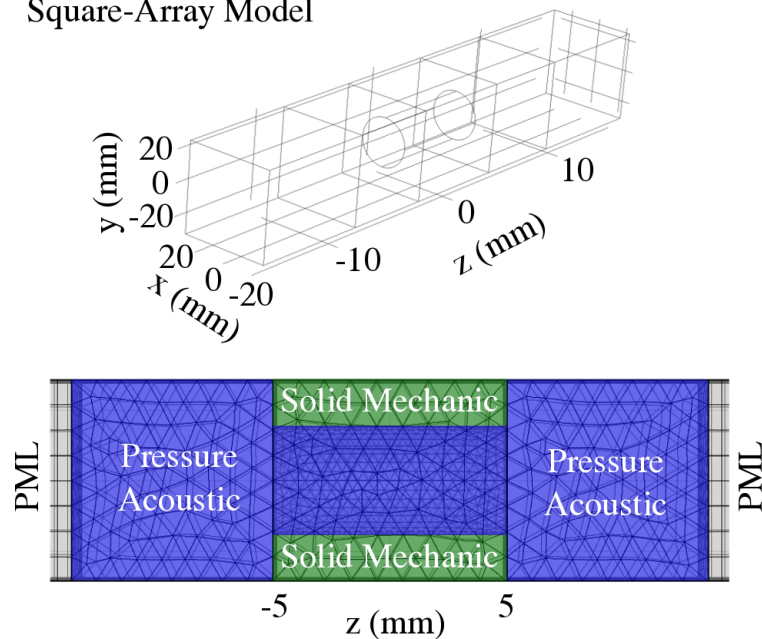


**Figure 3.22:** An example 3D Comsol model of a 2D array of holes in an aluminium plate. The top plot shows the geometry of the system being studied and bottom is a side-on $xz$ view of the system with each domain labelled.

Figure 3.22 shows the different component parts of a 3D model used to extract the eigenfrequencies of a geometry. This model consists of six domains which are made of either water or aluminium. Regions containing water are governed by pressure acoustics

and regions containing aluminium are governed by solid mechanics (elastic waves). The model is bounded in the $z$ direction by Perfectly Matched Layers (PMLs) that work as absorbers. This section will use this example to describe how FEM models are used to calculate the eigenfrequencies of a system.

### 3.8.1 Meshing

Once the geometry is selected and built, the first step is to construct a mesh that fills it in order to calculate transmission, reflection or eigenfrequencies of a specific modelled system. This dictates where the software solves the governing physics equations. Note that because the wavelength of sound in any of the solids being investigated is typically smaller than that in water and this dictates $\lambda_{\min} = c_w/f$. Here $c_w$ is the speed of sound in water. For the purposes of this work we used a $\lambda_{\mathrm{mesh}} = \frac{\lambda_{\min}}{16}$.

The two different mesh types used in this work are the tetrahedral and swept meshes. Tetrahedral meshes are more commonly used to mesh geometries as they can effectively fill most shapes. Importantly, the region defined as the Perfectly Matched Layer (PML) cannot be meshed using the tetrahedral method as PMLs rely on a method of extending the mesh infinitely, which cannot be performed computationally on a triangular face. PMLs use swept meshing as there are no infinitesimally narrow regions associated when approximated infinitely. Swept meshes use rectangular shaped elements normal to the boundaries of the region being meshed. Both methods of meshing have been used in figure 3.22.

### 3.8.2 Solving the Acoustic Wave Equation

Time evolved, frequency domain and eigenfrequency analysis solving methods are used in order to model the systems presented in this work. These models either use a well-defined source of acoustic waves (a point, line, face or domain source) or solve the steady state solutions of the system. At each intersecting element of the meshed system, Comsol solves an adapted Helmholtz equation to obtain $p(\mathbf{x}, \omega)$. In the absence of the source components, this Helmholtz wave equation has the form[70]

$$\boldsymbol{\nabla}^2 \left( -\frac{p}{\rho_c} \right) - \frac{\omega^2 p}{\rho_c^2 c_c^2} = 0, \tag{3.2}$$

where $\omega$ is the angular frequency and $c_c$ is the complex speed of sound, governed by the viscosity of the water and accounts for the loss within the system:

$$c_c = c_0 \left( 1 + i\omega \frac{\left( \frac{4\eta}{3} + \eta_B \right)}{\rho c^2} \right)^{\frac{1}{2}}. \tag{3.3}$$

Here, $c_0$ is the compressional speed of sound within that medium, $\eta$ is the dynamic viscosity, $\eta_B$ is the bulk viscosity and $\rho_c$ is the complex density, which is related to complex density:

$$\rho_c = \frac{\rho_0 c^2}{c_c^2},$$
(3.4)

where $\rho_0$ is the initial density of the medium. These equations are the same as those described in chapter 2. During processing, the software tries to minimise equation 3.2. The simulation solves this equation at every mesh element at the vertices contained within the model. For large models there are thousands of mesh elements that need to be solved and this requires a great deal of processing power.

### 3.8.3   Periodicity and Symmetry

To reduce the processing power needed to run these models, periodic or symmetric boundary conditions are used. Symmetric and axis symmetric systems simply mirror or rotate the model at a symmetric boundary or about a symmetric axis. The axial symmetric results being output as $p(r, \theta, z)$. There are fewer mesh elements in these models. By mirroring the mesh in one plane the computational power used is approximately halved and it is even further reduced by rotating the mesh around an axis, as shown in the example in figure 3.23. This example is used to model the modes within a single layer of aluminium alloy in chapters 4 and 5.
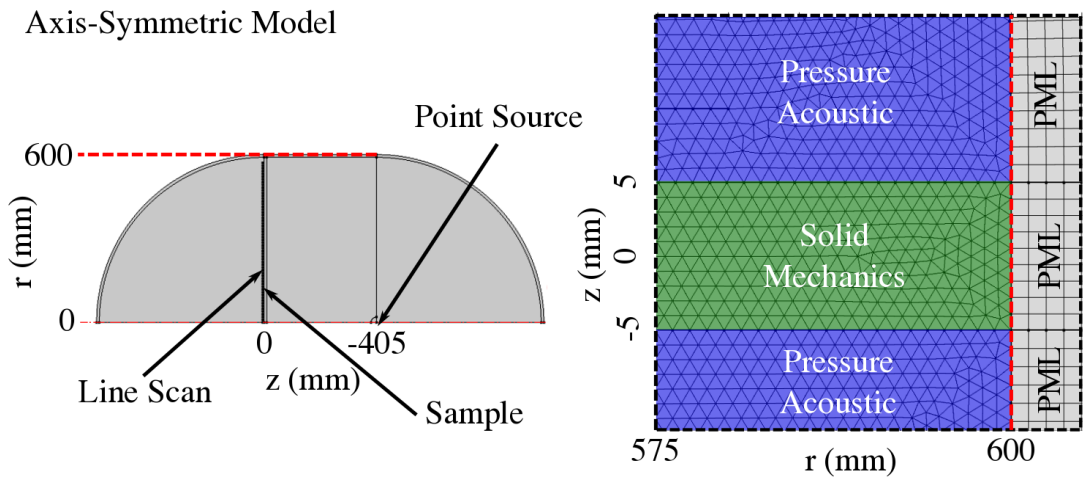


**Figure 3.23:** An example axisymmetric used in chapter 4. The model used pressure acoustics and elastic physics with the entire model surrounded by a layer of PML.

Another condition used in this work is Floquet periodicity. In the previously examined figure 3.22, the model is bounded in the $x$ and $y$ directions by Floquet periodicity,

simulating an infinite array of unit cells in those directions. In this simulation the pressure is now redefined as:

$$p = pe^{-k_{\text{Floquet}} \cdot r}. \tag{3.5}$$

Here $k_{\text{Floquet}}$ is the wavevector of the periodicity. This is used in chapters 6, 7 and 8.

### 3.8.4 Results

Typical FEM results are extracted as spatial plots or global evaluations of the eigenfrequencies of a system. Both types results are used throughout this work to verify experimental results. Figure 3.19 shown in section 3.7 shows the eigenfrequencies of the a square set of holes overlaid on top of the experimental data for a square array of holes, with a unit cell 6.0 by 6.0 mm and 6.4 mm thick.

Figure 3.24 shows example plots of the spatially calculated transmission, as normalised absolute pressure, through a $9.0 \pm 0.5$ mm thick array of pressure-release holes, which will be further discussed in the final experimental chapter, chapter 8. These types of results are useful for visualising the pressure inside a material or structure, as this cannot be easily extracted without damaging the sample or altering it in a non-trivial way, and was used to test a system before fabricating it.
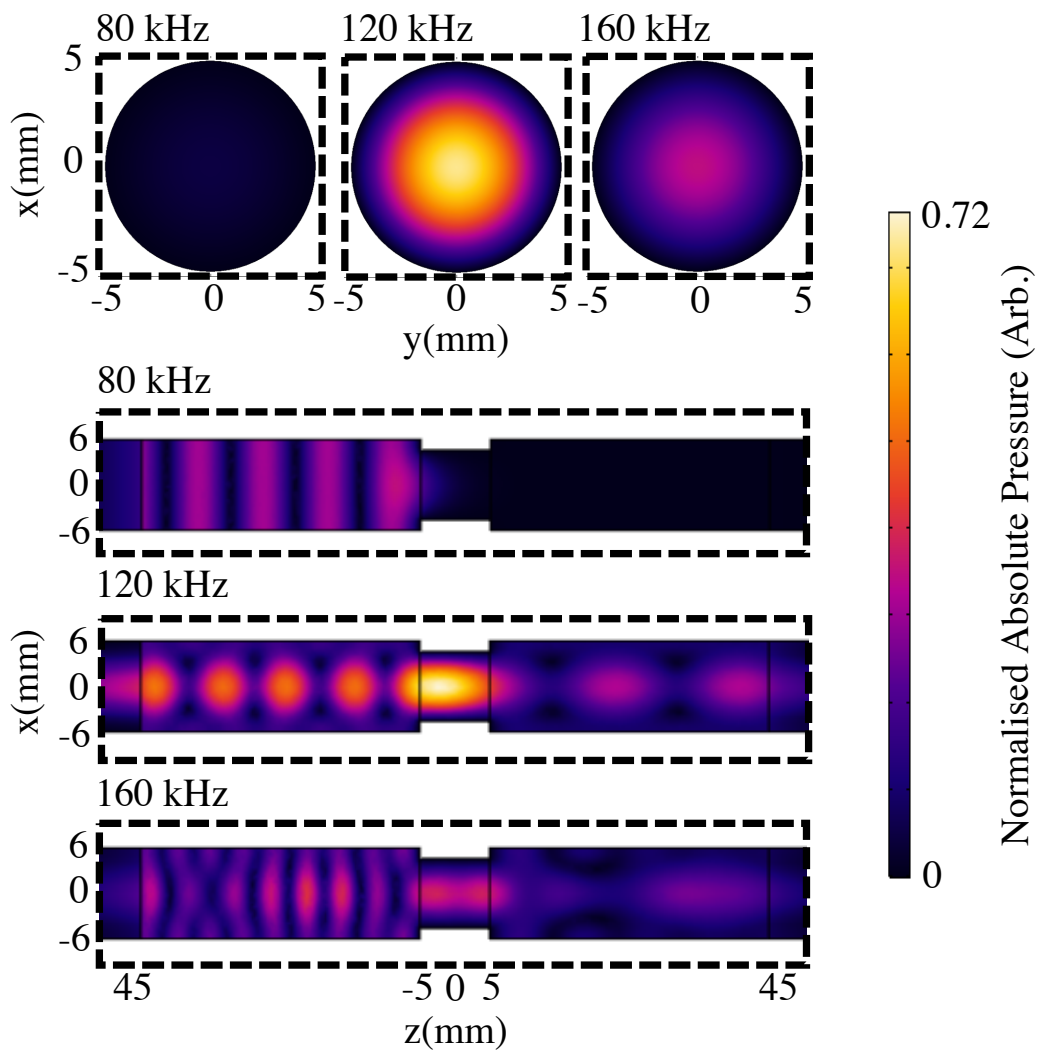
**Figure 3.24:** Example Comsol multphysics 5.3a modelled spatial data of the normalised absolute pressure in and around a unit cell of the square array of pressure-release holes. Cross-sections of the absolute amplitude of the fields at the centre of the hole in all three dimensions are shown.

## 3.9  Summary of methods

To clarify the methods used to Fourier transform and remove artefacts from the data, here is a list of the steps involved:

- Raw data is recorded as voltage, measured in $V$, over time, measured in $s$, in space, $x, y, z$.

- Raw data is time-windowed to remove reflected and diffracted signals.

- This data is then windowed using a Hanning function in time.

- Data is then Fast Fourier Transformed (FFT) in time at each spatial coordinate.

- Frequency dependent data is then windowed using a Tukey window in space, $x, y, z$.

- The frequency domain data is then FFT'd in space to produce the k-space data.

- Lastly, the k-space data is windowed to remove regions that are not of interest (past the first or second Brillouin zone boundary).

This method is used throughout the following work.

## 3.10  Conclusion

This chapter outlined the experimental and computational methods used throughout this thesis to extract, analyse and characterise the acoustic fields of the original work detailed in later chapters. Firstly, this chapter reasoned the choice of the materials used to fabricate the samples made of metals and closed-cell foams. Then the experimental setup was described and how a pulse measurement technique is used to excite the response of the samples. Furthermore, the method of collecting these results spatially was outlined and a method of computationally extracting the dispersion relation of these results was outlined. Finally, the Finite Element Method (FEM) was detailed, which will be used throughout this work to verify the results. The next chapter is the first experimental chapter, exploring a method of elastically characterising flat solid plates by extracting the dispersion relation of their acoustic responses.

# Chapter 4

# Underwater Acoustic Tomography of Flat Plates

## 4.1 Introduction

This chapter explores the dispersive properties of modes within flat plates submerged in water. Using pulsed broadband ultrasound signals from a point-like source, multiple elastic modes of plates are simultaneously excited. By Fourier analysing the transmitted fields temporally and then spatially, the detailed dispersion relations of the transmitted ultrasonic signals through the plates are obtained. Experimental data is plotted against models developed from analytic theory and compared to determine the elastic properties of the solids. The experimental results agree well with analytic models. The properties of the resonant modes depend on the plate thickness and material parameters and therefore may be readily controlled. This work investigates the spatial components of focussing and direction sound and has implications on both the radiative and non-radiative regime. Therefore, this work has applications in acoustic energy harvesting[134] (focussing of surface waves[135] onto piezoelectric microelectromechanical systems), acoustic imaging (lens-like characteristics further explored in chapter 5), enhanced sound transmission and absorption over narrow bands, non-destructive testing and defect detection[28,30].

## 4.2 Background

First studied at the end of the eighteenth century, Rayleigh and Lamb waves are two types of wave that are supported in solids[34,16]. As described in chapter 2, Rayleigh waves are a type of Surface Acoustic Wave (SAW) bound to an interface of an elastic medium that exponentially decay in amplitude outwards from the boundary (i.e. decay

away from the interface). These non-radiative Rayleigh waves have been well studied in air and there has been a substantial amount of work undertaken in seismology [136,137]. When the wavelength of sound inside the material is near the thickness of the elastic medium, Rayleigh-like waves become redefined as Lamb modes [16]. Lamb modes are highly dispersive and dependent on the elastic material properties of the plate.

A submerged elastic material responds differently to that of one in a near-vacuum, like air. For most metals their acoustic waves have a speed faster than that of water, thus they become radiative and are referred to as "Leaky Rayleigh" or "Leaky Lamb" waves. The dispersive nature of these modes (section 2.6.1) shows enhanced transmission or absorption over specific wavevector and frequency ranges and has been looked at in varying degrees of detail recently [19,20,21,22,23,24]. Mapping the dispersive properties of elastic solids is a method of acoustic tomography or Non-Destructive Testing (NDT). This has been an emerging technique whose use ranges from material characterisation to defect identification [25,26,27,28,29,30,31]. Most of this work has been done temporally or in the frequency domain and is yet to take advantage of Fourier acoustics and consequential fitting to the dispersion of Lamb modes to extract the material properties [138].

In this study of acoustic tomography, ultrasonic pulsed signals are used to excite modes in plates of different thickness and dispersive properties, detecting the transmitted fields from which are used to obtain the elastic properties: elastic modulus, $E$, and Poisson's ratio, $\nu$. The results are then compared against a model of Lamb mode transmission and for one metal compared to standard measurement technique to obtain $E$.

## 4.3   Experimental Method

Flat plates made of solid cast aluminium alloy, cast steel and rolled acrylic are fabricated and immersed in water. These materials were chosen as they have a range of elastic properties that can be used to test the characterisation method outlined in this chapter. The list of materials with their typical and range of industry-estimated elastic properties are shown in table 4.1. These solid materials are assumed to be isotropic, homogeneous and linearly elastic. In plate form these materials support acoustic Rayleigh and Lamb modes.

The experiments described in this chapter are performed in a water tank with all samples in plate form. The centre points of these plates are held in place using a perspex frame $62.0 \pm 0.5$ cm by $74.0 \pm 0.5$ cm submerged in $\approx 100$ cm deep water. The water is static and left to settle after samples are positioned. The ambient temperature of experiment was approximately $293.0 \pm 0.5$ K. The density of water was estimated to

| Medium | E (GPa) | $\rho$ ($\frac{\text{kg}}{\text{m}^3}$) | $\nu$ |
|---|---|---|---|
| Aluminium alloy | 68 - 82 | 2550 - 2800 | $\approx 0.34$ |
| Acrylic (PMMA) | 2.24 - 3.80 | 1150 - 1190 | 0.35 - 0.40 |
| Mild Steel | 200 - 215 | 7800 - 7900 | 0.28 - 0.30 |

**Table 4.1:** Estimated ranges of the elastic bulk properties of aluminium alloy, mild steel, acrylic (PMMA)[139,140,141,142,143].

be $\rho_w = 997\frac{\text{kg}}{\text{m}^3}$ and the measured speed of sound $c_w = 1512 \pm 6$ m/s.

Approximately single-cycle Hanning-windowed ultrasonic pulses were projected at the samples using a ball shaped Neptune-Sonar D70 transducer positioned $40.0 \pm 0.5$ cm away from the surface of each plate, as seen in figure 4.1. Exciting the plate at this distance means the source excites over a range of incident angles, $\theta_i$, and a range of wavevectors, $k_r$. The maximum angle is $\theta_{max} = \tan(d_x/d_r)$, where $d_r$ is the source to detector distance and $d_x$ is the distance between the position of the source and the origin of the excited field, radially. This defines the maximum wavevector $k_{max} = k_0 \sin(\theta_{max})$. Bringing the source closer to the plate would increase the value of $k_{max}$ but it would also mean the source appears less point-like, which would broaden the plate modes in k-space. A pulse measurement technique was used to avoid late arriving reflected and refracted waves that would interfere with the primary wave in a Continuous Wave (CW) experiment (section 3.5). This method is an updated method of that presented by Castaings and Hosten[144].
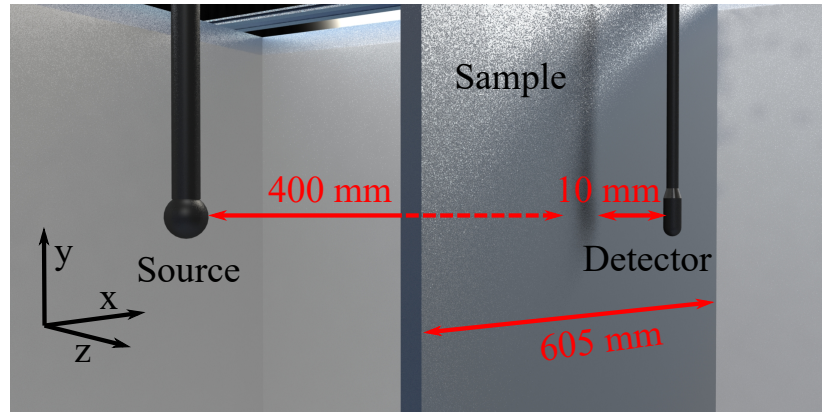


**Figure 4.1:** A 3D rendered image showing the source-sample-detector setup used in the experiment. Source to sample and detector to sample distances are shown ($\pm$ 0.1 mm).

A Brüel & Kjær 8013 hydrophone[123] positioned $10.0 \pm 0.1$ mm from the sample surface on the opposite side to the transducer was used to detect acoustic transmission through the plates. The hydrophone is scanned spatially, using an $xyz$ scanning stage, to obtain the spatial dependence of the transmitted fields. At each point of a scan the

results are averaged over multiple pulses to improve the signal-to-noise ratio. For a line scan, results are collected as voltage, $V$, which is equivalent to acoustic pressure, $p_a$, and time, $t$, over a line scan with spacing, $\Delta x$, and total length, $x_{max}$. For an area scan, repeat lines are scanned with steps in $y$, $\Delta y$, or for $z$, $\Delta z$. This method detects a range of angles, which contain a range of transmitted wavevectors $k_x$. The usable frequency range of this setup is between 50-500 kHz, as detailed in chapter 2. Scans take around 2 hours.

Using the Fourier acoustic method[111] (section 3.7), the time and spatially dependent pressure is used to extract the frequency, $f$, and in-plane wavevector, $k_x$, components of the transmitted fields. The frequency resolution of the scan is limited by the total time length of the signal recorded at each point $t_{max}$. The k-space values are limited by the minimum step of $\Delta x$ (maximum wavevector $k_{max} = 2\pi/\Delta x$) and the k-space resolution $\Delta k = 1/x_{max}$. Finally, plotting frequency, $f$, against the k-space data, $k_x$, produces the dispersion of the family of modes of the plate. To reduce the pixelation of the data and to remove artefacts that result from Fourier transforming, the results were zero-padded, three times the length of the data set, and then had a Hanning-like window applied in both space and time[145,133].

## 4.4 Theory of Waves in Layered Media

The transmission of acoustic waves through layered media has been theorised and approximated using known formulae set out by Leonid Brekovskikh[18]. This splits a multi-layered system into constituent regions.

This chapter will focus on a solid plates surrounded by water. Figure 4.2 sets out the spatial parameters of the parameters used in the theory: the angle of incidence is $\theta_1$, the plate thickness is $L$ and the angle of the transmitted signal at the second interface is $\gamma_2$. Each region of this system has elastic properties defined by the acoustic impedance, $Z$, density, $\rho$, elastic modulus, $E$, and Poisson's ratio, $\nu$. This theory assumes that all regions are linear, homogeneous, isotropic and obeys the LCR analogy outlined in section 2.4.
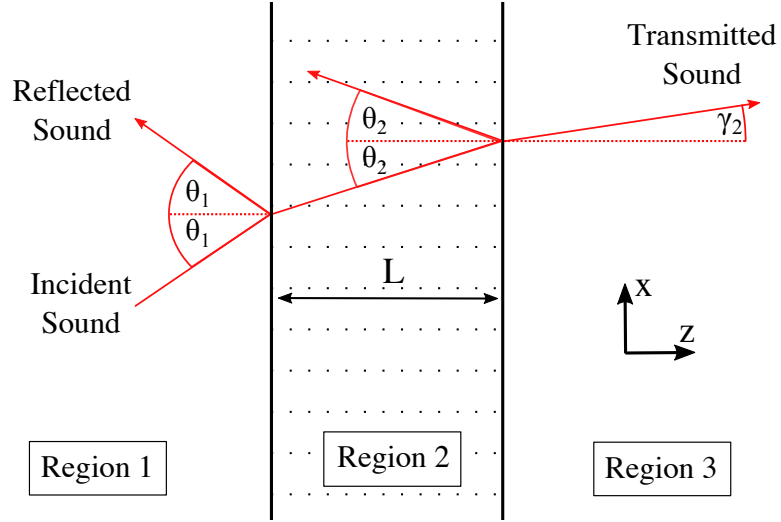
**Figure 4.2:** An illustration outlining the spatial parameters used to calculate the coefficients of transmission and reflection for a three-layered elastic system. In this example sound is incident at an angle $\theta_1$ and transmitted at an angle $\gamma_2$. Elastic medium 2 has a finite thickness $L$ whereas regions 1 and 2 are infinite in there half spaces.

For a three-layered system the impedance of each region of this three-layered system is a function of the angle of incident or transmitted sound at each interface. The acoustic impedances in each region are:

$$Z_1 = \rho_1 c_1 / \cos(\theta_1), \tag{4.1}$$

$$Z_2 = \rho_2 c_2 / \cos(\theta_2), \tag{4.2}$$

$$Z_3 = \rho_3 c_3 / \cos(\theta_3). \tag{4.3}$$

$$\tag{4.4}$$

With the transverse impedance in the second region given by:

$$Z_{2\mathrm{t}} = \frac{\rho_2 c_{s2}}{\cos(\gamma_2)}. \tag{4.5}$$

Here $\rho_1$, $\rho_2$ and $\rho_3$ are the densities of the materials in each region and $c_1$, $c_2$ and $c_3$ are the compressional wavespeeds. $c_{s2}$ is the shear wavespeed in region 2 that is function of the elastic properties,

$$c_{s2} = \sqrt{(E_2/(2(1+\nu_2)\rho_2))}. \tag{4.6}$$

Here $E_2$ and $\nu_2$ are the elastic modulus and the Poisson's ratio of the second region. There is no transverse wave in water, regions 1 and 2 in the systems studied in this

chapter.

Brevoskikh's generalised theory uses a matrix that includes all the elastic properties of the system to derive the transmission and reflection coefficients. Using Brekhoskikh's notation $P = ad$ and $Q = \alpha\beta$, which relate the loss coefficients $\alpha$ and $\beta$ and variables $d_n$, the thickness of the layers of order $n$ (the sum of which is $L$), and $a_{nm}$, which corresponds to the matrix amplitude of $A$ (see Waves in Layered Media[18] for full derivation). For our system, we can write

$$P = \frac{2\pi f \cdot L \cos(\theta_2)}{\sqrt{E_2(1 - \nu_2)/(1 + \nu_2)(1 - 2\nu_2)\rho_2}}, \tag{4.7}$$

and

$$Q = \frac{2\pi f \cdot L \cos(\theta_2)}{L \cos(\gamma_2) \cdot \sqrt{E_2/2(1 + \nu_2)\rho_2}}. \tag{4.8}$$

Here $E_2$ is the elastic modulus of material 2, $f$ is the acoustic frequency and $\nu_2$ the Poisson's ratio of the second region (section 2.3). $P$ and $Q$ both affect the amplitude of acoustic transmission and reflection. These may be combined together as $N$ and $M$:

$$N = \frac{Z_2}{Z_1} \frac{\cos^2(2\gamma_2)}{\sin(P)} + \frac{Z_{2t}}{Z_1} \frac{\sin^2(2\gamma_2)}{\sin(Q)}, \tag{4.9}$$

and

$$M = \frac{Z_2}{Z_1} \cos^2(2\gamma_2) \cot(P) + \frac{Z_{2t}}{Z_1} \sin^2(2\gamma_2) \cot(Q), \tag{4.10}$$

where $\gamma_2$ is the angle of transmitted sound. The resultant transmission coefficient $T$ and the reflection coefficient $R$, and then given by:

$$T = \frac{4N^2}{4M^2 + (N^2 - M^2 + 1)^2} \tag{4.11}$$

and

$$R = \frac{(N^2 - M^2 - 1)^2}{4M^2 + (N^2 - M^2 + 1)^2}. \tag{4.12}$$

Using Brekovskikh's theory, the percentage transmitted and reflected fields propagating through layered elastic media can be calculated. One thing to note is that this model is equivalent to a steady state solution and the primary affect of loss is just a reduction in the amplitude of $T$ and $R$.

Calculated example dispersion diagrams for transmitted sound through plates are

plotted in figure 4.3. These results show that the dispersion of the plates depends strongly on the elastic properties of the plate. As discussed in section 2.6.1, these modes fall into two categories: symmetric and asymmetric ($S_n$ and $A_n$). These analytical results show both ranging from $A_0$ and $S_0$ up to higher symmetric modes in thicker steel. Unlike metals, acrylic plate modes are much less defined and they overlap far more as they are more lossy.
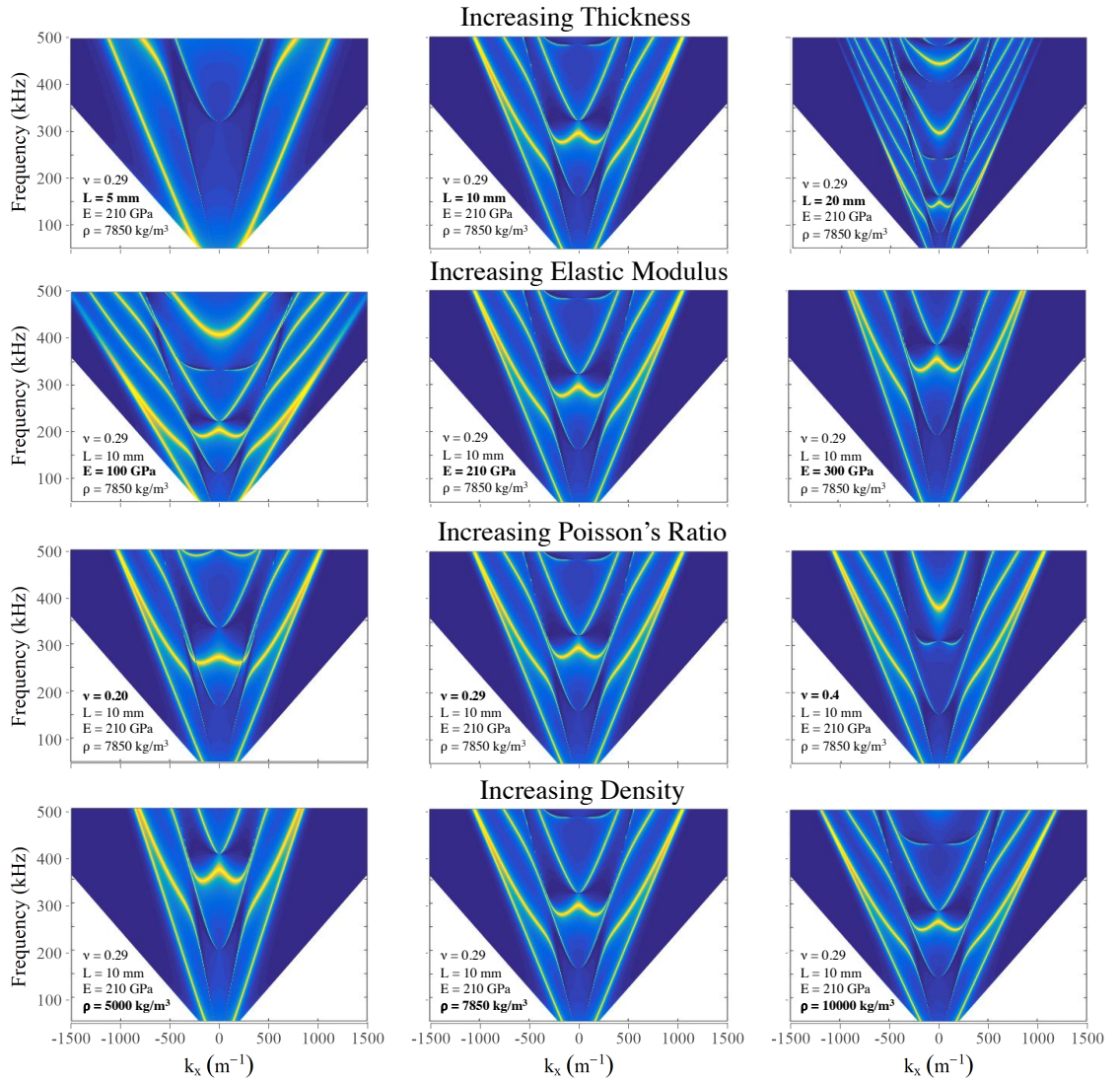


**Figure 4.3:** Plots of the calculated transmission coefficient from 0 (blue) to 100 % (yellow) transmission. They are plotted as dispersions varying thickness, $L$, elastic modulus, $E$, Poisson's ratio, $\nu$, and density, $\rho$. The middle plot of each row is the same and typical of the dispersion of steel.

This elastic model is used to define the Rayleigh, compressional (P) and shear (S) wave speeds of a material: $c_R$, $c_P$ and $c_S$. In Brekovskikh's theory, they are defined as:

$$c_P = \sqrt{\frac{E_2(1 - \nu_2)}{((1 + \nu_2)(1 - 2\nu_2)\rho_2))}}, \tag{4.13}$$

$$c_S = \sqrt{\frac{E_2}{(2(1 + \nu_2)\rho_2}}, \tag{4.14}$$

$$c_R = c_S \frac{0.862 + 1.14\nu_2}{1 + \nu_2}. \tag{4.15}$$

These wave speeds limit the dispersive properties of the modes in the plate, as will be shown experimentally and through modelling in the next section.

## 4.5 Results

Experimentation was performed by pulsing identical singe cycle pulses underwater at the 605 by $605 \pm 1$ mm area plates, shown in figure 4.4, with the source positioned at $400 \pm 5$ mm from the sample surface.
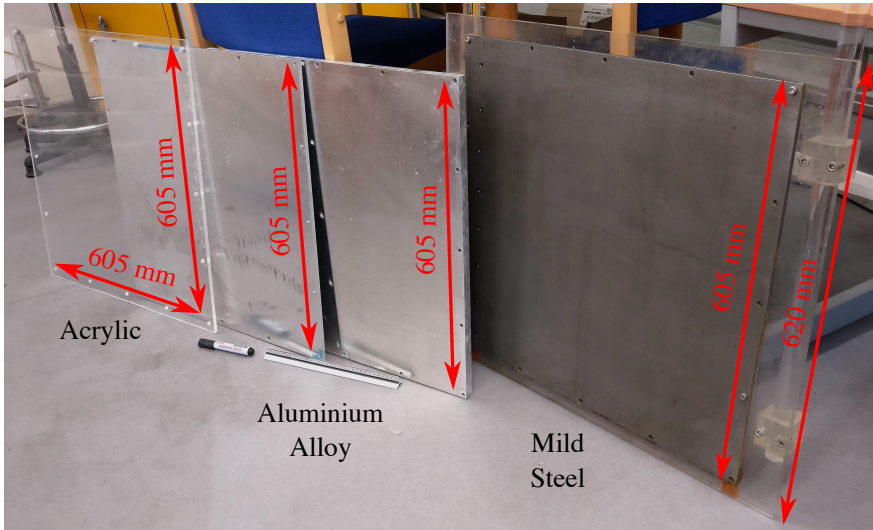


**Figure 4.4:** The four samples examined in this chapter. Left to right: one acrylic, two aluminium alloy samples and one mild steel. Each sample has holes at the edges to mount them to the acrylic frame shown in the picture attached to the mild steel plate. A 35 cm ruler and a whiteboard marker are present for scale.

Transmitted signals were detected at points along a line parallel to the surface of the sample, in the $x$ direction, the nearest part of the hydrophone being $10.0 \pm 0.1$ mm from the surface. The samples are offset so that propagating signal first hits at $50 \pm 2.5$ mm from the sample edge, to increase the maximum x-coordinate accessible

up to $x \approx 550$ mm (giving a maximum k-space resolution of $\Delta k = 11.4$ m$^{-1}$ in the absence of zero padding). Spatial scans are performed over 400 mm with $\Delta x = 2.5$ mm. At each point in space the voltage, $V$, over time, $t$, is recorded by averaging over 250 identical pulses with a pulse every 0.3 s and averaged in time with sample rate $\Delta t = 0.104$ $\mu$s and maximum time $t_{max} = 1.2$ ms. The following results are for four different samples using the same experimental and analytical technique to determine their elastic properties.

### 4.5.1 Mild Steel

Time domain results for the $9.4 \pm 0.1$ mm thick mild steel (low carbon steel) plate are shown in figure 4.5. Depicted is the transmitted pulse as voltage, time and spatial coordinate, $x$, in mm. Time domain data of the scan swept between 0 mm and 400 mm (chosen to avoid the edges of the samples where the plate modes are damped) shows the shape of the wavefront transmitted through the plate, first arriving at the detector at $t = 0.32$ ms at $x = 0$ mm ($50 \pm 2.5$ mm from the edge of the sample). The presence of diffracted signals originating at the edges of the plate are visible in the time domain data at $x = 0$ mm when $t = 0.36$ ms and at $x = 400$ mm when 0.45 ms. These are independent of the Lamb modes of the plate.
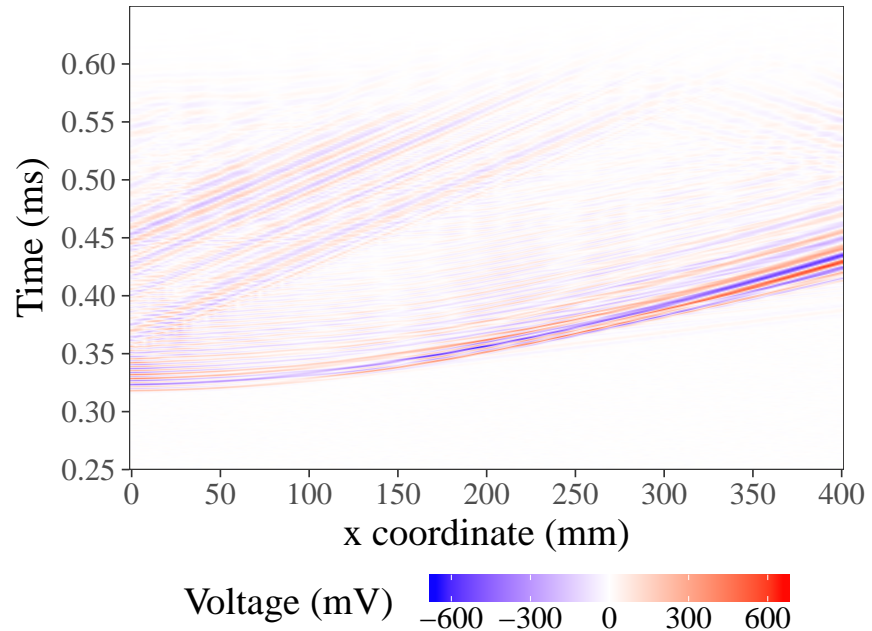


**Figure 4.5:** Detected signal transmitted through a 9.4 mm thick steel plate, plotted as spatial coordinate $x$ in mm against voltage over time at a distance of $10.0 \pm 0.1$ mm from the sample surface. Propagating signal is first detected at 0.32 ms at $x = 0$ mm.

The time domain results are time-windowed between 0.25 and 0.70 ms to remove significant reflections that originate from the sides of the water tank. These results are then zero-padded (three times the sample length), have a Hanning-like window applied and are Fourier analysed in time. Applying an FFT to the data in time produces the frequency components of the fields, shown in figure 4.6. These results indicate that there is a significant spatial dependence of the normalised fields travelling through the steel plate. Note that the transmission is above 100%, peaking at $\approx 175\%$. This feature will be explained in chapter 5.
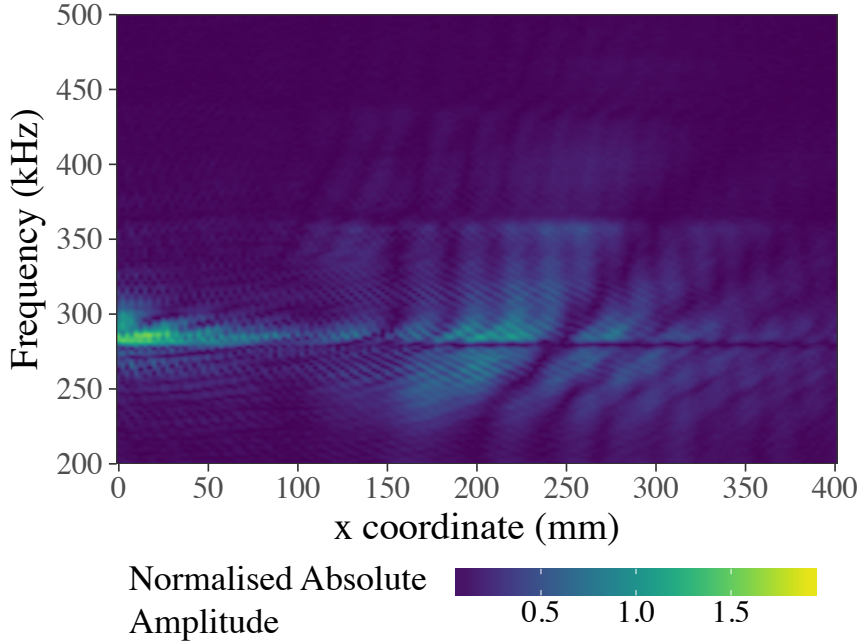


**Figure 4.6:** Normalised absolute amplitude data for the 9.4 mm thick steel plate plotted against frequency, $f$, and spatial coordinate in $x$.

Applying an FFT to the data spatially in $x$ produces the wavevector components, $k_x$, of the transmitted fields. Plotting $f$ against $k_x$ produces the dispersion relation, presented in the top plot of figure 4.7. These results show the dispersion of the independent symmetric, $S_n$, and asymmetric, $A_n$, Lamb modes excited within the plate, coupled to plane waves and transmitted. By comparing this to the model data it is possible to fit using by-eye comparisons to the experimental data through varying the elastic moduli. Castaings and Hosten[144] use a similar characterisation method whereby they plot the phase velocity at selected frequencies and compare their results against theory. But here we present an updated full description, which plots multiple bands at the same frequency (not shown by Castaings and Hosten).

Empirically measured constants of the mass density of steel $\rho_{\text{steel}} = 7850 \pm 10 \text{ kg/m}^3$

and thickness 9.4±0.1 mm are input into Brekovskikh's theory to allow fitting the model to the data and thereby attaining the elastic modulus, $E$, and the Poisson's ratio, $\nu$. A plot of the fitted model is shown in the bottom figure of 4.7. To fit this model to the data the maximum 5% transmission coefficient is first fitted at $k_x = 0$ by adjusting $E$ and then the shape of the dispersion is fitted by varying $\nu$. The extracted values for steel are $E = 210 \pm 2$ GPa and $\nu = 0.30 \pm 0.02$. These values are within the expected values of steel (table 4.1). The fit matches the shape and position of the experimentally observed Lamb modes well, although the results could be improved through the use of computational fitting algorithm. This is not in the scope of this work. Also depicted in the figure are the compression (P), shear (S) and Rayleigh wavespeed limits. The data shows that all Lamb modes have, as expected, wavespeed faster or equal to the Rayleigh wave speed, $c_{\mathrm{R}}$.
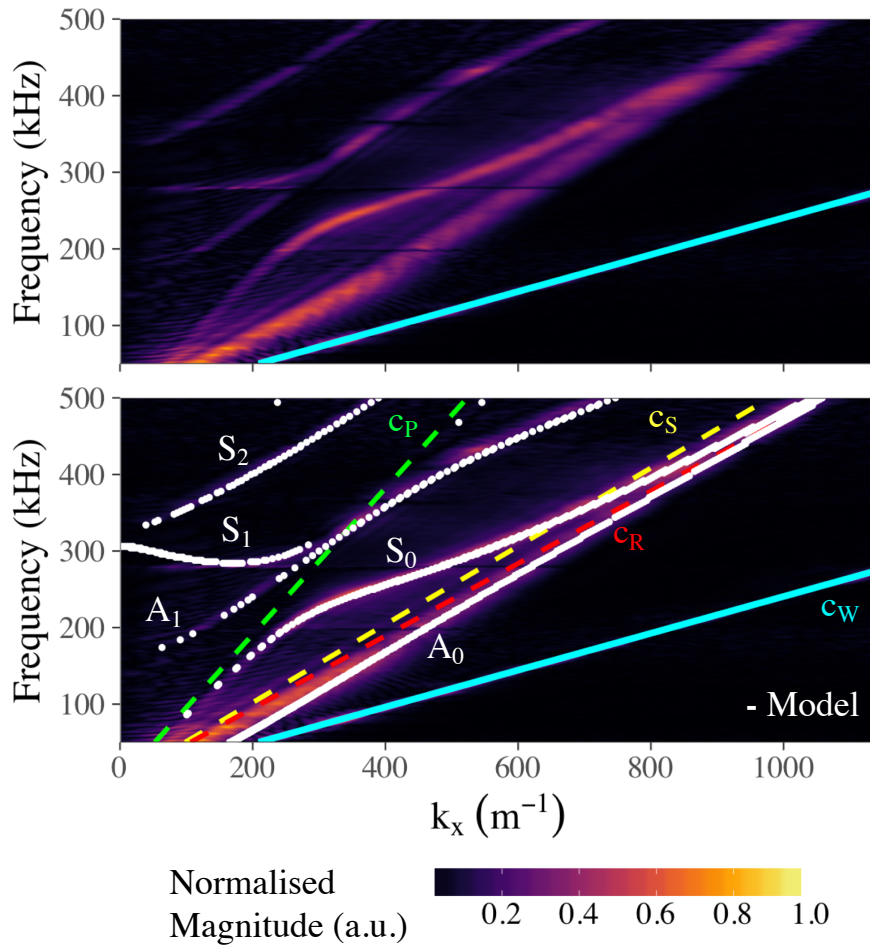
**Figure 4.7:** The 9.4 mm thick steel plate dispersion plotted as normalised magnitude. Top is the uncharacterised data and the bottom has an overlaid fitted model which uses $E = 210.0$ GPa and $\nu = 0.30$. Also shown are the Rayleigh (red dashed line), S (yellow dashed line) and P (green dashed line) wave speed limits and the water sound line (cyan line). The labels show the different symmetric and asymmetric modes of the plate, $S_n$ and $A_n$).

### 4.5.2 Aluminium Alloy

To confirm that the parameter ($E$) extraction method can be used for a range of materials, the extraction method is applied to aluminium alloy (grade 5083) sample. Additionally, to test that the extracted properties do not depend on sample thickness, two samples of thickness 9.8±0.1 mm and 19.98±0.02 mm are studied. Experimentation is performed using samples offset as before with the same pulse measurement technique used on the mild steel plate.
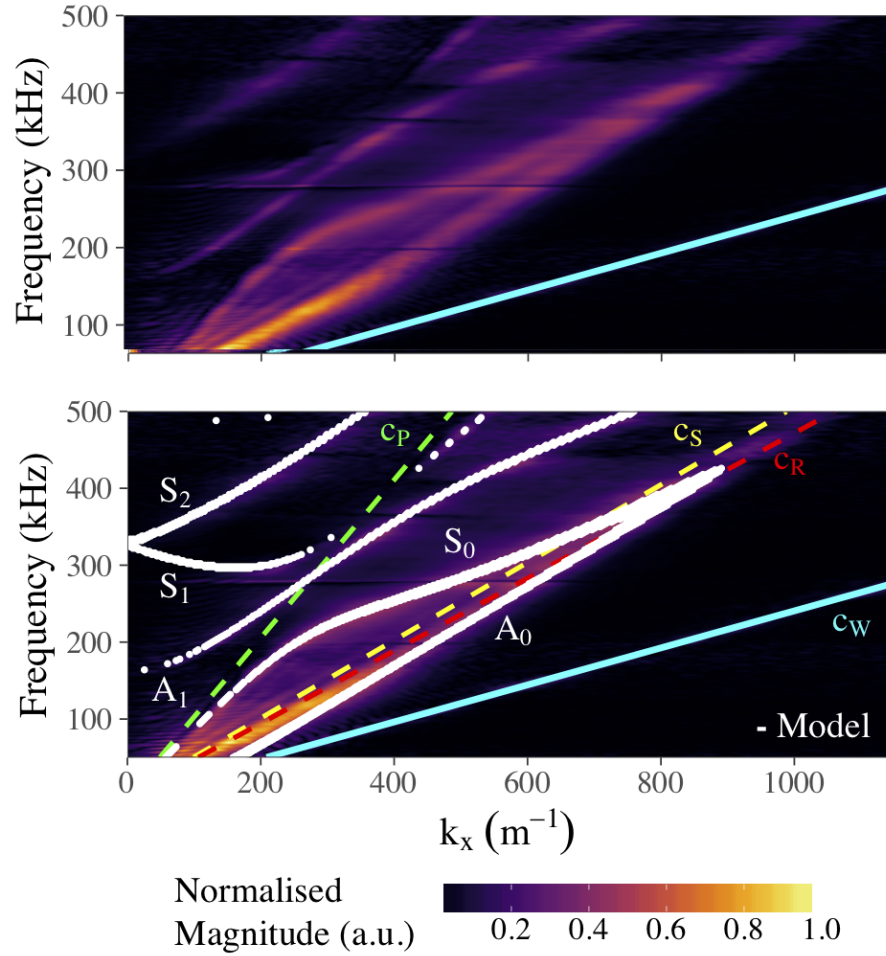


**Figure 4.8:** The extracted dispersion of the modes support by a 9.8 mm thick aluminium alloy plate calculated from the measured transmitted fields. Top is the dispersion plotted as Fourier amplitude with frequency and wavevector in $x$ direction. The bottom plot is the same data with an model fit overlaid. Also shown are the Rayleigh $c_R$ (red dashed line), shear $c_S$ (yellow dashed line) and compression $c_P$ (green dashed line) wave speeds and the water sound line (cyan line). The labels show the different symmetric and asymmetric modes of the plate, $S_n$ and $A_n$.

Figure 4.8 shows the resultant dispersion of the $9.8 \pm 0.1$ mm thick aluminium alloy plotted alongside the fitted data with the Rayleigh, shear and compressional wave speeds shown and the different asymmetric and symmetric modes labelled ($A_n$ and $S_n$). The measured density for this material is $\rho = 2660 \pm 10$ kg/m$^3$. Using $L$ and $\rho$ the extracted elastic modulus and Poisson's ratio are $E = 72 \pm 2$ GPa and $\nu = 0.34 \pm 0.02$. These values also fall within the expected bounds of other aluminium alloys in table 4.2.

Performing the same experiment on the $19.9 \pm 0.1$ mm thick plate produced the results shown in figure 4.9.
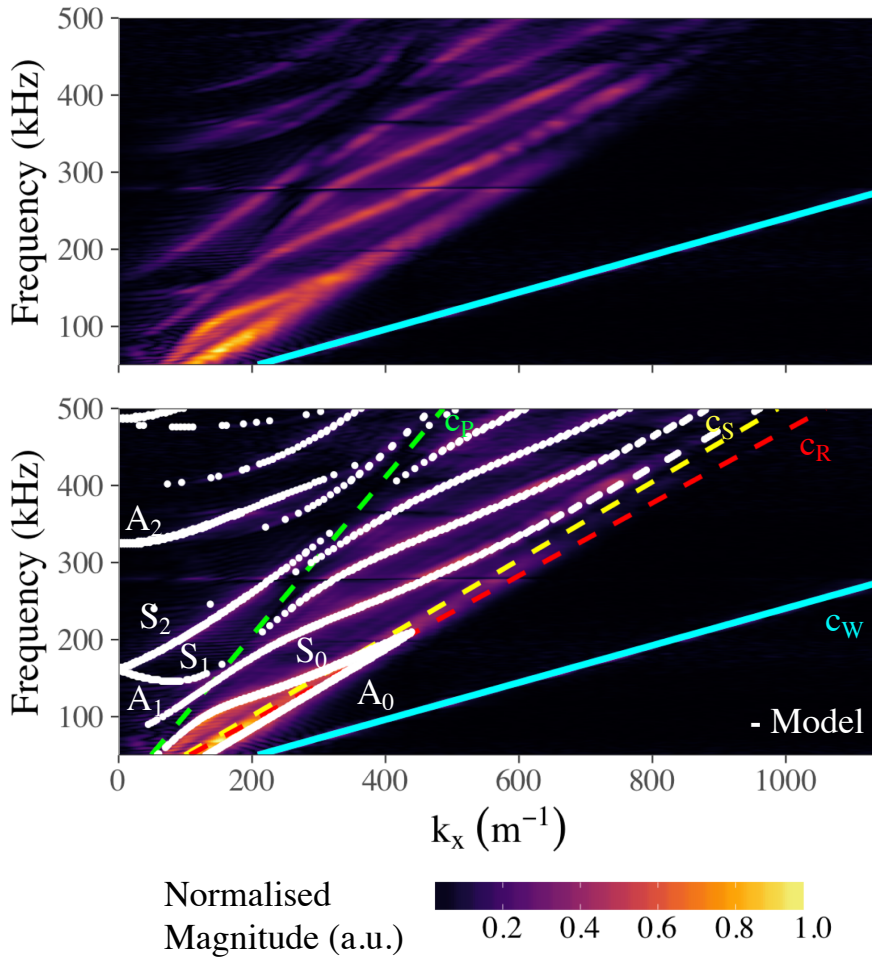


**Figure 4.9:** The extracted dispersion of the modes support by a 19.9 mm thick aluminium alloy plate calculated from the measured transmitted fields. Top is the raw dispersion and on the bottom is the data with an model fit overlaid. Also plotted are the Rayleigh $c_R$ (red dashed line), shear $c_S$ (yellow dashed line) and compression $c_P$ (green dashed line) wave speeds and the water sound line (cyan line). Labelled are the symmetric and asymmetric modes of the plate ($S_n$ and $A_n$).

Figure 4.9 shows the dispersion plotted next to the fitted data with the wave speeds and Lamb modes labelled ($A_n$ and $S_n$). Approximately doubling the thickness means that the modes at $k_x = 0$ are excited at half the frequencies and between 50 and 500 kHz higher order symmetric and asymmetric modes now exist. The measured density for this material is the same as the thinner sample, $\rho = 2660 \pm 10$ kg/m$^3$. Again, $L$ and $\rho$ are used to extract the elastic modulus and Poisson's ratio. These are the same as the extracted values for the 9.8 mm thick plate with $E = 72 \pm 0.1$ GPa and $\nu = 0.34 \pm 0.02$. The excellent agreement between deduced elastic properties confirms the method of extraction is independent of the thickness of the plate.

#### 4.5.2.1 Tensile Testing Aluminium

To verify the results measured using the ultrasonic testing above, the results will now be compared using a standard method of measuring the elastic modulus done by using a tensile test.
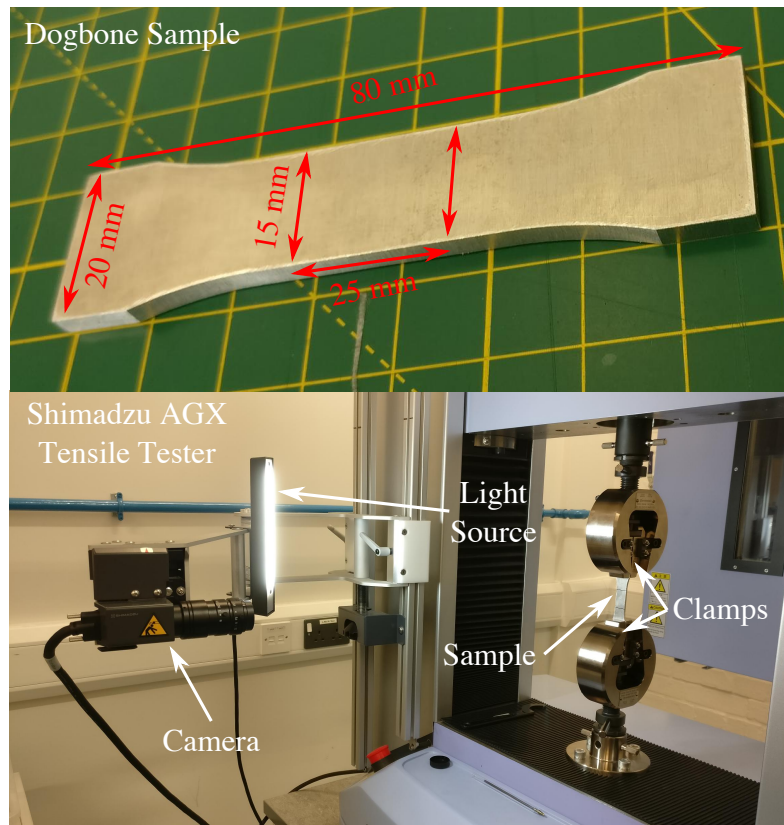


**Figure 4.10:** Top is a picture of a single aluminium alloy dogbone sample of thickness $2.9 \pm 0.1$ mm, length $80.0 \pm 0.1$ mm and a $\approx 25$ mm gauge length. Bottom is a picture of the sample positioned in the in the Shimadzu AGX tensile testing machine[146].

Using the Shimadzu tensile testing machine[146] pictured in figure 4.10, the elastic modulus of a material is extracted by clamping a "dogbone" shaped sample and pulling with force, $F$, both ends (with maximum force $F_{max} \approx 6500$ N). Whilst this is performed the extension of the central region of the sample is tracked using a camera-extensometer.

Ten samples cut from the same sheet of aluminium alloy 5083 using a CNC to have thickness $2.9 \pm 0.1$ mm, length 80.0 mm and a $\approx 25$ mm gauge length. The tensile test was ran in reference to the ASTM E8[147] using a 0.375 mm/min tensile rate up to a maximum extension of 0.125 mm. Out of the ten samples six failed the test due to early slipping and deformation leaving no linear region to extract the value of the Elastic modulus. The results for the four remaining samples are shown in figure 4.11.
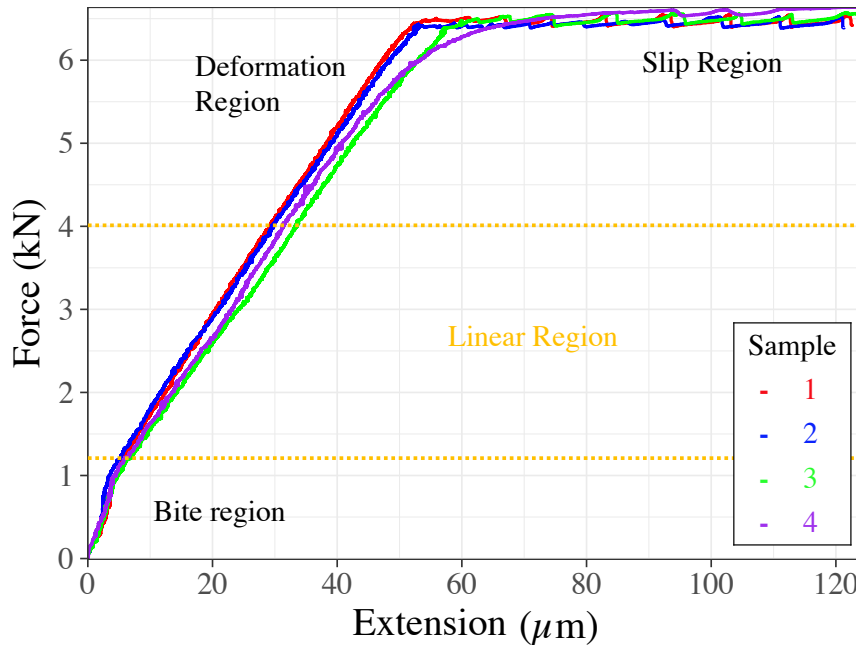


**Figure 4.11:** The results of the tensile test of the four aluminium alloy 5083 dog-bone samples.

The results show four labelled regions:

- Bite region, where the frictional forces result in the sample moving within the clamps and the patterned surface of the clamps cut into the sample.

- Linear region, the usable elastic regime where the tensile properties are extracted.

- Deformation region, where samples deform in a random manner.

- Slip region, where the sample becomes too thin within the clamps under the force applied and slips out of them.

Averaging the results the elastic modulus was measured to be $E = 65.35 \pm 4.26$ GPa, with error being 11.4% of the range.

Even though the elastic modulus measured using the ultrasonic technique developed for this work does not fall in the range of $65.35 \pm 4.26$ GPa, the result is still within a reasonable error of the acoustically extracted result. Also, typically the elastic modulus of materials are lower under in tension than compression. The method also is very dependent on the subjective choice of linear region of the data. Choosing a linear region below 1250 kN in the "bite region" of figure 4.11 would result in a higher value of $E$.

### 4.5.3 Acrylic

This study has so far only looked at metals that have well-specified estimates of their material properties. Other materials have properties that will vary significantly from sample to sample. Acrylics are such materials. Now the ultrasonic tomography method, used to characterise mild steel and aluminium alloy, is employed to estimate the elastic properties of a $7.4 \pm 0.1$ mm thick acrylic plate.

Figure 4.12 shows the Fourier extracted dispersion of the acoustic transmission through the $7.4 \pm 0.1$ mm thick acrylic plate. In contrast to the aluminium and steel models, the model of the acrylic data is fitted using the well-defined minima (lowest 15%) rather than maximum in intensity. This is because the modes in the acrylic are lossy and therefore broadened. The fitted analytical data is shown in the bottom plot of figure 4.12. Using the measured density of the plate of $\rho = 1180 \pm 10$ kg/m$^3$, the elastic modulus and Poisson's ratio are extracted as $E = 5.2 \pm 0.2$ GPa and $\nu = 0.33 \pm 0.02$ by fitting the model to the experimental dispersion. The value of the $\nu$ is slightly outside expected for acrylic, but still within a reasonable 0.02 of the lower limit. However the elastic modulus, $E$, is outside the range stated in table 4.1. This is probably due to the specific make of the manufactured material.
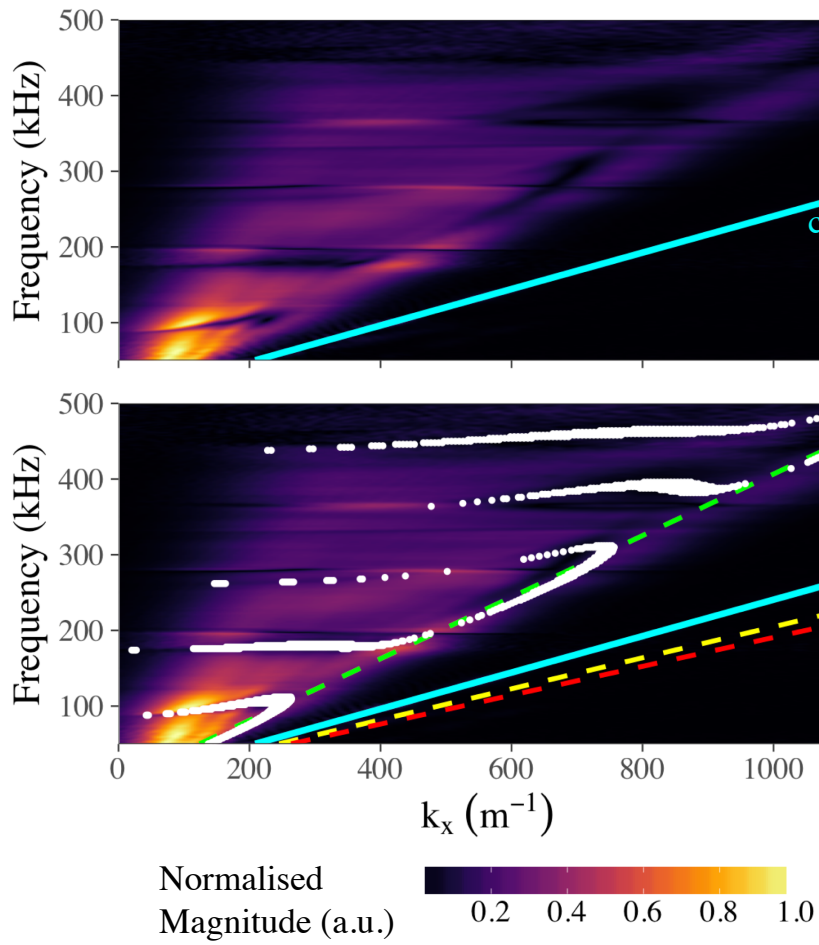
**Figure 4.12:** The dispersion of the transmitted sound through a 7.4 mm thick acrylic plate. Top is the experimental dispersion and on the bottom is the data with an model fit of the minimum transmission coefficient overlaid. Also plotted are the Rayleigh $c_R$ (red dashed line), shear $c_S$ (yellow dashed line) and compression $c_P$ (green dashed line) wave speeds and the water sound line (cyan line).

### 4.5.4 Summary

Table 4.2 shows the complete list of material properties extracted using by-eye fitting of the dispersion curves. The extracted results are mostly within the error expected for the general elastic properties of these materials, set out in table 4.1.

| Medium | $L$ (mm) | E (GPa) | $\rho$ (kg/m$^3$) | $\nu$ |
|---|---|---|---|---|
| Aluminium Alloy (5083) | $19.9 \pm 0.1$ | $72 \pm 2$ | $2660 \pm 10$ | $0.34 \pm 0.2$ |
| Aluminium Alloy (5083) | $9.8 \pm 0.1$ | $72 \pm 2$ | $2660 \pm 10$ | $0.34 \pm 0.2$ |
| Acrylic | $7.4 \pm 0.1$ | $5.2 \pm 0.2$ | $1180 \pm 10$ | $0.33 \pm 0.2$ |
| Mild Steel | $9.4 \pm 0.1$ | $210 \pm 2$ | $7850 \pm 10$ | $0.30 \pm 0.2$ |

**Table 4.2:** The measured results for the four different plates.

The benefit of this simple ultrasonic method for determining plate elastic modulus is that it is non-destructive and easy to implement on large plates. However there are limitations. Firstly, this can only be performed in a fluid environment as there needs to be acoustic power transmitted through the sample and the fields can be spatially scanned. The impedance mismatch in air is too great to perform this method for most solid materials. It is also necessary to use a source-detector setup that has a large frequency range to obtain an accurate fit of the model to experimental data. Other limitations of the value of the Poisson's ratio for which this method will work were outlined briefly in section 2.3.1[75].

## 4.6 Conclusions

This chapter has shown that it is possible to extract the elastic properties of solids using underwater broadband ultrasonic pulses between 50 and 500 kHz together with Fourier acoustics. The method employed a point-like source positioned 400 mm from the samples to excite the modes with in-plane wavevectors, $k_x$. Four samples made of aluminium alloy, mild steel and acrylic were scanned and characterised using Brekhovskikh's analytical theory. Results for the elastic modulus, $E$, and Poisson's ratio, $\nu$, were mostly in the expected region of elastic properties, with the acrylic being the one outlier with $E = 5.2 \pm 0.2$ GPa beyond the expected value. This method can be used to extract $E$ and $\nu$ of a range of metals, plastics and other homogeneous materials. It may be possible to use other liquids and source-detector setups to expand the range of materials that can be characterised using the same acoustic tomographic method. This work has obvious applications in material characterisation and defect detection. The next chapters will use the characterised aluminium alloy (5083) to examine the out of plane properties and the detailed dispersion of the 9.8 mm thick sample.

# Chapter 5

# Ultrasonic Focussing Through Coupled Excitation of Symmetric Lamb Modes

## 5.1 Introduction

This chapter concerns further investigations into the properties of the symmetric and antisymmetric Lamb modes within a thin flat aluminium plate submerged in water and excited using pulsed broadband ultrasound from a point-like source. By Fourier analysing the transmitted fields in time and space, the dispersion of the excited Lamb modes is acquired. Experimental data is compared against computational Finite Element Method (FEM) modelled data. Acoustic power beaming for a small frequency band supported by a 9.8 mm thick aluminium alloy plate is observed. This is attributed to collimation of acoustic energy to the coupling between the first and second order symmetric plate modes leading to negative dispersion and zero in-plane group velocity. The properties of the acoustic focussing depend on the plate thickness and material parameters and may be readily controlled. The experimental results agree well with computational models.

## 5.2 Background

Lamb acoustic waves are a type of bulk wave that propagate through solids and were first studied at the start of the nineteenth century[16]. Lamb modes are supported by elastic plates when the wavelength, $\lambda$, of sound is near the thickness, $L$, of the medium ($\lambda \approx L$). These modes are highly dispersive and are dependent on the elastic

91

material properties of the plate. They are classified into two families of symmetric and asymmetric modes. The interactions between thin plates and shells are significant in guided wave applications, such as acoustic energy harvesting, acoustic absorption and transmission.

Narrowing of the acoustic field emitted from these plates has been widely observed and classified as a feature of the "Negative Group Velocity" (NGV) or "Zero Group Velocity" (ZGV) mode[148]. This mode is the first order symmetric mode of the plate and previous theories have show the gradient of the dispersion of this mode in the in-plane direction switches from positive to negative. Prada et. al. have shown that it is possible to focus in-plane waves using this ZGV mode whilst exciting the plate from a free edge[22,149,150]. Further work recently evidenced the shape of the fields inside the plate[151,152]. In addition, it has also been observed that the ZGV mode affects the radiated acoustic waves whereby the beam pattern of fields is directionally dependent over narrow frequency ranges[153]. These effects are similar to those seen on structured plates using bulleye or arranged resonators in order to enhance acoustic transmission[154,155].

This chapter will investigate the NGV/ZGV mode and observe its focussing effect. The experimentally derived frequency and dispersion data is compared to a computationally modelled system to verify the method of extraction and the validity of the results. There is excellent agreement between the two. Using the FEM models the computationally calculated dispersion of the modes inside the plate is observed, showing how the NGV/ZGV mode propagates.

## 5.3 Experimental Method

The experiment described in this chapter is performed using the same experimental technique as described in chapter 4. Experiments are performed in a water tank with an aluminium alloy (5083) plate which is 9.8±0.1 mm thick and 605±1 by 605±1 mm in area. The centre point of the plate is held in place using a perspex frame approximately 620±1 mm by 740±1 mm submerged ≈ 50 cm in approximately ≈ 100 cm deep water. The water is static and left to settle after samples are positioned.

Approximately single-cycle Hanning-windowed ultrasonic pulses are projected at the samples using a ball-shaped Neptune-Sonar D70 transducer positioned $40.0 \pm 0.5$ cm away from the surface of the plate. Exciting the plate at this distance means the source excites over a range of incident angles, $\theta_i$, and a range of wavevectors, $k_x$. A Brüel & Kjær 8103 hydrophone[123] placed $10.0 \pm 0.1$ mm from the surface of the sample is used to measure acoustic transmission. For a line scan the hydrophone is scanned in space, using an $xyz$ scanning stage. The data is recorded as voltage, $V$, and time, $t$,

over a linear scan with spacing $\Delta x$ and total length $x_{\max}$ and for an area scan repeat lines are scanned with steps in $y$, $\Delta y$, or for $z$, $\Delta z$. The usable frequency range of this setup is between 50 and 500 kHz. The results at each spatial point are averaged over multiple pulses to improve the signal-to-noise ratio.

Using Fourier acoustic methods[111] (section 3.7) the temporally and spatially dependent pressure is used to extract the frequency, $f$, and in-plane wavevector, $k_x$, components of the transmitted fields. The frequency resolution of the scan is limited by the total time length of the signal recorded at each point $t_{\max}$. The k-space values are limited by the minimum step of $\Delta x$ (maximum wavevector $k_{\max} = 2\pi/\Delta x$) and the k-space resolution $\Delta k = 1/x_{\max}$. Finally the dispersion of the modes is plotted as frequency, $f$, against in-plane wavevector, $k_x$. To visualise the results and to remove artefacts that result from Fourier transforming, the results were zero-padded and then had a Hanning-like window applied[145,133].

## 5.4   Results

In chapter 4, the dispersion of a 9.8 mm aluminium alloy plate, in figure 4.8, was shown to have Lamb modes at $k_x = 0$, where two of these modes intersected at 300 kHz. These two modes are characterised as the $S_1$ or $S_2$ modes. In this chapter, the plate dispersion is explored with the source exciting central to the sample and no longer offset. This symmetrically excites the plate around $k_x = 0$ more effectively. In-plane experimentation on the 9.8 mm thick aluminium alloy (5083) plate are performed by pulsing identical singe-cycle pulses underwater at a 605 by $605 \pm 1$ mm area plate with the source positioned at $400 \pm 5$ mm from the sample surface. Transmitted signals are detected at points along a line parallel to the surface of the sample, in the $x$ direction. The nearest part of the hydrophone is $10.0 \pm 0.1$ mm from the surface. Spatial scans are performed over 400 mm with the centre of the plate at $x = 200$ mm and with spatial resolution $\Delta x = 2.5$ mm. At each point in space the voltage, $V$, over time, $t$, is recorded over 250 identical pulses with a 0.3 ms pulse rate and averaged in time with sample rate $\Delta t = 0.104$ $\mu$s until maximum time $t_{\max} = 0.65$ ms.

### 5.4.1   Time Domain

Time domain data for the centred 9.8 mm aluminium alloy sample are shown in figure 5.1. At $x = 0$ there appears to be a faint concentration of fields which may be attributed to the overlapping $S_1$ and $S_2$ modes. These results also show diffraction from the edges as straight diagonal phase fronts appearing at the edges, $x = -180$ and $x = 180$ mm at 0.47 ms.
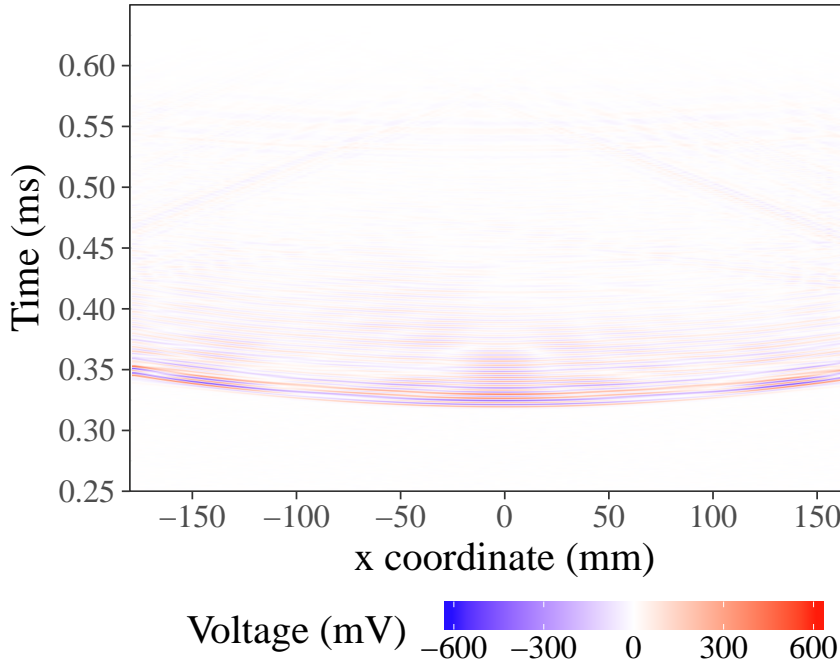
**Figure 5.1:** Voltage, $V$, over time, $t$, of the averaged detected signal propagating through a centred 9.8 mm thick aluminium alloy plate.

### 5.4.2 Frequency Domain

Fourier transforming the time domain data using an FFT temporally produces the frequency domain data presented in the top plot of figure 5.2. The transmission amplitude is $\approx 130\%$ at the centre of the plate ($x = 0$ mm). It is unclear from this data as to why this is occurring, but it suggests some form of focussing of power.

To verify the results a FEM Comsol 5.3a model of the system is employed. The model shows the results of an equivalent system, where the source is a point source positioned 400 mm away from the sample surface, the plate is equivalent to the 9.8 mm thick aluminium alloy with elastic properties of elastic modulus $E = 72$ GPa, Poisson's ratio 0.34 and density 2660 kgm$^{-3}$ (measured values from chapter 4). The model is an axis-symmetric frequency domain analysis of the system swept through frequency calculating the field projected through the plate. The model is used to extract the transmitted complex acoustic pressure, $p_a$, to create a like-for-like data set. In figure 5.2 the comparison between the modelled (bottom) data and the experimental data (top) is shown. These results are in reasonable agreement with the major difference being that the minima seen in the experimental data at 280 kHz, associated with the source-detector response functions, are not seen in the modelled data. Both sets of data show concentrated power at $f \approx 300$ kHz at $x = 0$ mm.
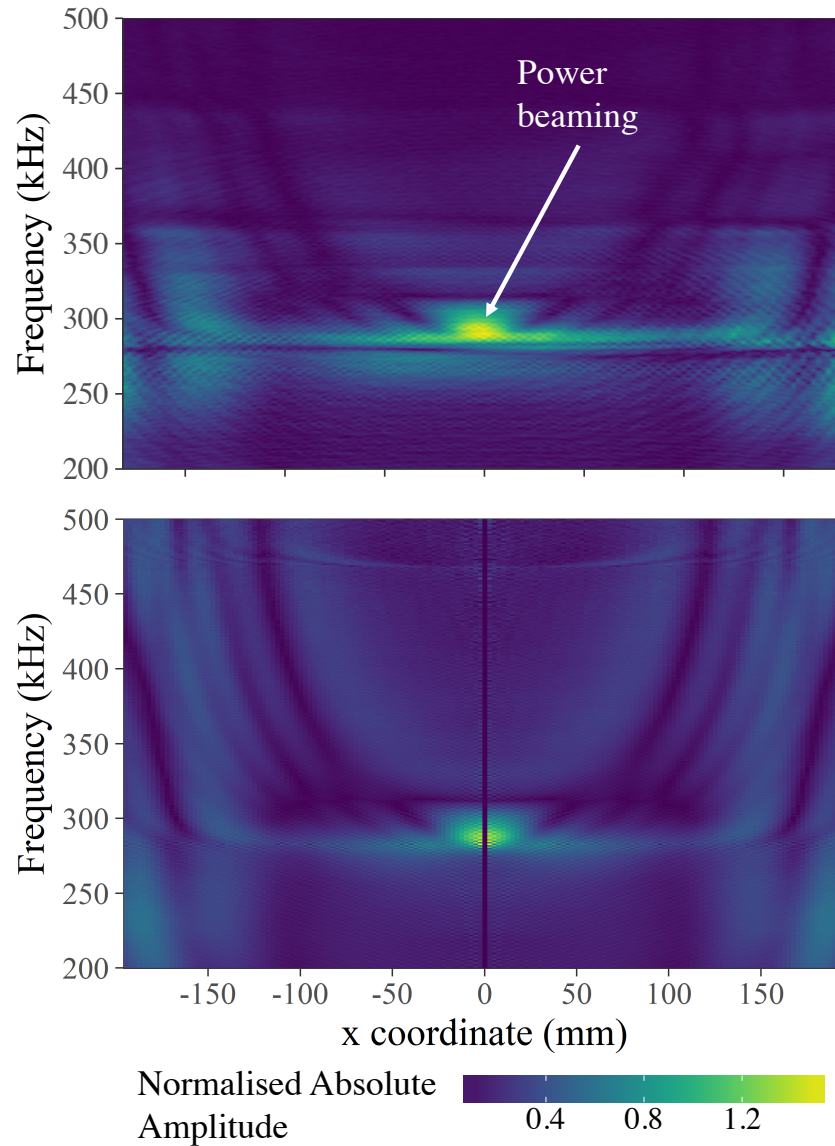
**Figure 5.2:** The normalised Fourier amplitude of transmitted fields through the centred 9.8 mm thick aluminium alloy plate plotted in frequency, $f$, and x coordinate. Top is experimental data; bottom is model data. The amplitude of the model at x = 0 mm have been set to zero to remove necessary data, which will be further explained in section 5.4.4.

### 5.4.3 Dispersion

Fourier transforming spatially produces the wavevector components in $x$. From this the dispersion in $k_x$ is produced, figure 5.3.
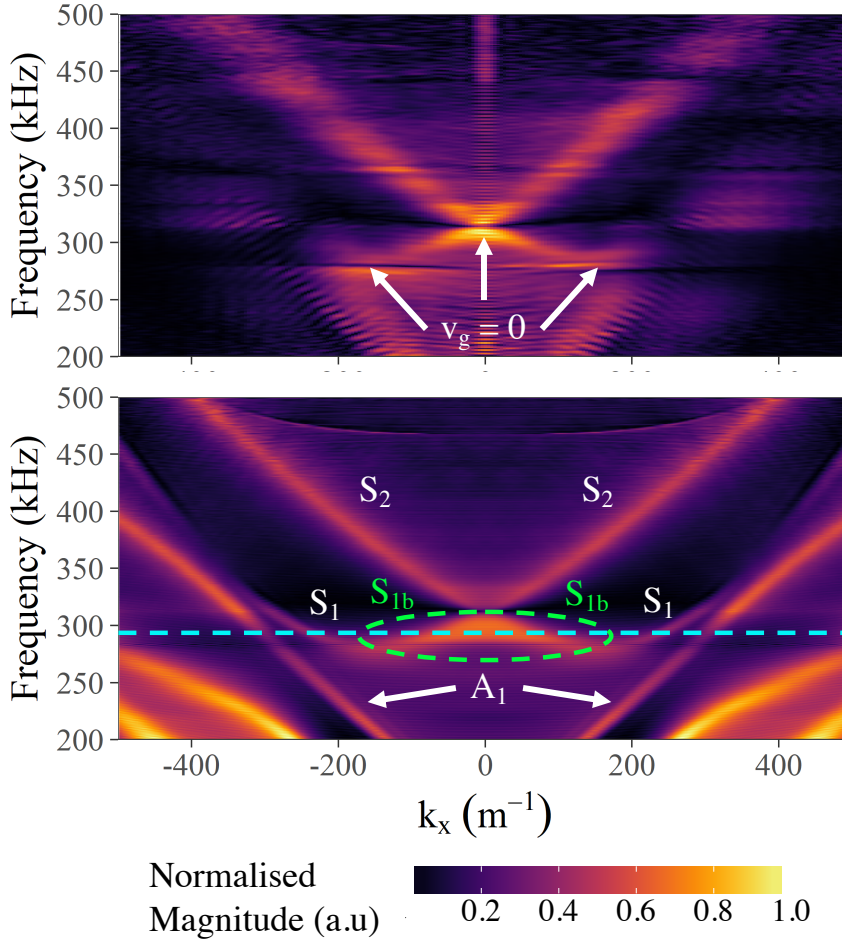


**Figure 5.3:** The dispersion of the transmitted signal through the centred 9.8 mm thick aluminium alloy plate. Experimental results are plotted top and Comsol modelled data is shown for comparison bottom. Labelled are the different Lamb modes and areas where the group velocity is zero ($v_g = 0$).

Figure 5.3 shows the region where the first order ($S_1$) and second order ($S_2$) symmetric modes form a band-gap. Moving away from $k_x = 0$ along the $S_1$ mode, an area of "negative" dispersion is seen as the phase velocity ($v_p$) is negative for positive group velocities ($v_g$). This region of the $S_1$ dispersion is labelled the $S_{1b}$ mode in accordance with the literature[22,149,150]. At the points where the group velocity is zero, $v_g = 0$, both the model and experimental data show an eigenmode of the system. This is because $v_g = 0$, the wave cannot propagate in $x$ so there must be an out-of-plane component

to the wave normal to the plate. For values of negative phase velocity, the wave is
"focussed" inwards with in-plane energy projected back towards $x = 0$ over narrow
frequency ranges resulting in the beaming of acoustic energy at $\approx 300$ kHz. This effect
is also visible in figure 5.2 and is the reason for the "above 100 %" transmission.

### 5.4.4 XZ Two-dimensional Spatial Scan

A 2D plane normal to the surface in $x$ and $z$ is scanned to picture acoustic focussing
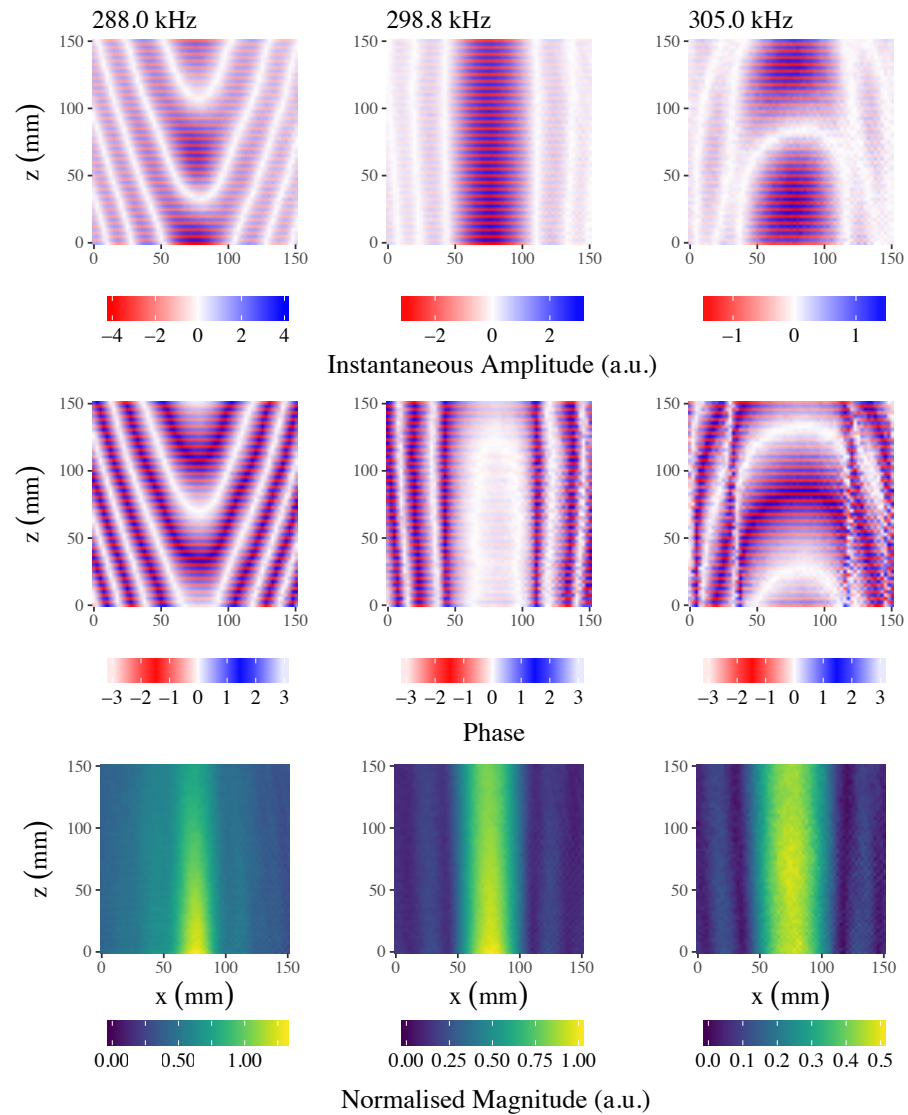in radiative fields of the plate is shown in figure 5.4.



**Figure 5.4:** 2D scanned results for the plane normal to the surface of a 9.8 mm thick
aluminium alloy plate. The results are for frequencies 280.0, 298.8 and 305.0 kHz,
where the acoustic focussing is visible.

## 5. Ultrasonic Focussing Through Coupled Excitation of Symmetric Lamb Modes

Figure 5.4 shows the experimental results for the 2D area in front of the plate at 280.0, 298.8 and 305.0 kHz. The effect of acoustic beaming through the plate is seen at all of the frequencies depicted. This effect is visible at 280.0 kHz, where the beaming is localised within the scanned area, and 305.0 kHz, where the beam is wider and projects beyond the scanned area. Note that the maximum Fourier magnitude drops as the results go up in frequency.

In addition to the acoustic beaming, there is also a beat pattern in the $z$ direction in the phase and instantaneous real amplitude plots of figure 5.4. The cause of this is the presence of two oscillating waves in $z$ with two values of $k_z$. The surface wave, $\psi_1$, and the plane wave, $\psi_2$, can be represented by the equations:

$$\psi_1 = A\sin(k_\parallel x - \omega t)e^{-k_z z}, \tag{5.1}$$

$$\psi_2 = B\sin(k_\perp z - \omega t). \tag{5.2}$$

The resultant intensity of the fields, fully derived in appendix B, is:

$$\psi_t^2 = \frac{1}{2}(A^2 + B^2) + AB(\cos(k_\parallel x - k_\perp z),$$

Here the factor of $\cos(k_\parallel x - k_\perp z)$ gives the modulation that is seen in the phase of figure 5.4.

### 5.4.5　FEM Plate Modes

It is very difficult experimentally to probe the fields inside the plate. But using the FEM model the predicted fields inside the plate are plotted. Using this the solid acoustic pressure of the fields inside the plate are plotted in figure 5.5. In this there are distinct regions of pressure within the plate, which shift in $x$ position dependent on frequency. These regions help to identify the different modes of the plate that are depicted in the dispersion diagrams of figures 5.5 and 5.6: $S_0$,$A_0$,$A_1$, $S_1$ and $S_{1b}$.
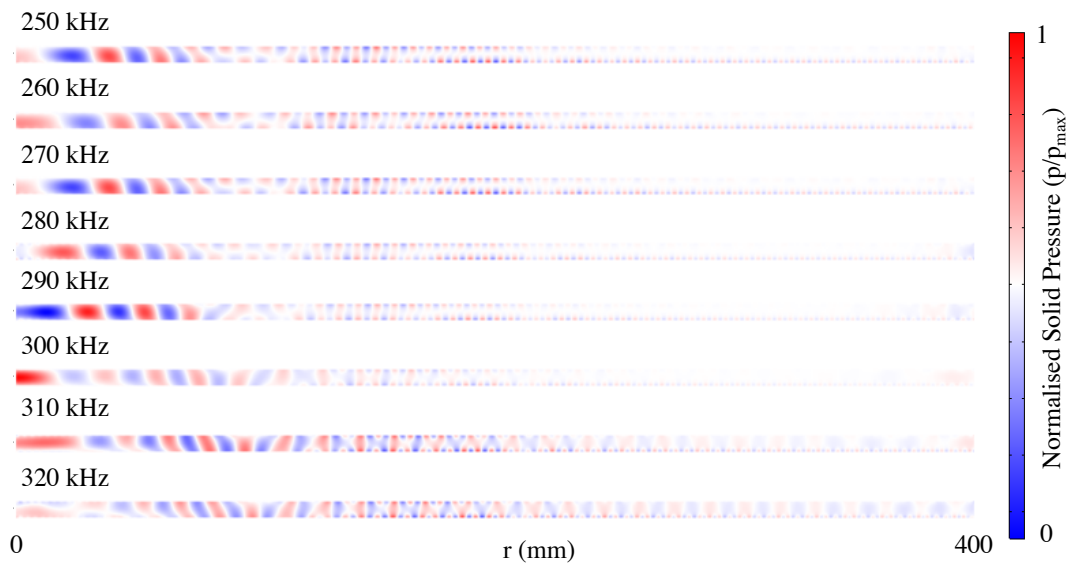


**Figure 5.5:** The normalised modelled instantaneous pressure fields within the solid $L = 9.8$ mm thick aluminium alloy plate plotted at individual frequencies.

In figure 5.6 the five different Lamb mode regions of the plate have been identified. Here the five spatial regions are subjected to an acoustic field with a range of $k_x$ values, as identified as the cyan dashed line in figure 5.3. Thus, each region represented here depicts a mode identified in the plate dispersion. Importantly, the region between the $S_1$ and $S_{1b}$ mode shows the switching of the direction of the phase fronts. This is the cause of this acoustic focussing, where acoustic energy is directed back towards $x = 0$ mm.
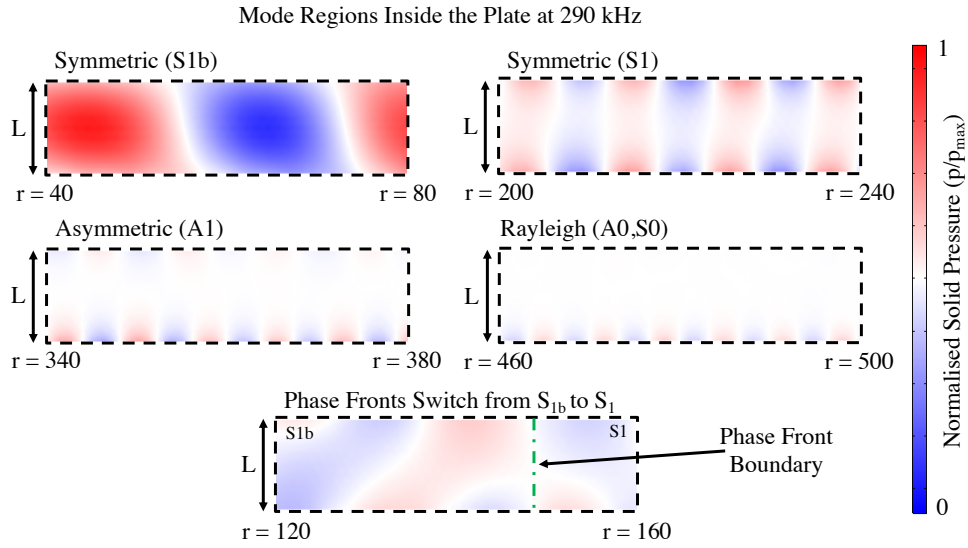
**Figure 5.6:** A close-up visualisation of the modelled $L = 9.8$ mm thick aluminium plate with pressure fields at 290 kHz. Shown are the five different modes contained within the excited fields.

## 5.5   Conclusions

In this chapter, the coupling between symmetric $S_{1b}$ Lamb modes were shown to focus acoustic energy at $\approx 300$ kHz for a $9.8 \pm 0.1$ mm thick aluminium alloy plate. Comsol 5.3a was used to show that it is possible to extract the equivalent dispersion results from the modelled data. Further use of modelled data was employed to investigate the modes within the plate, showing that the phase fronts of sound within the plate are refracted inwards towards the centre of the plate. Additionally, an explanation for the beat pattern in the radiated fields of the scanned data was shown analytically. This was a combination of a surface wave and plane wave acoustic waves of the same frequency component with different wavevector components, adding together to give a time averaged spatially periodic wave. The next chapter investigates aluminium alloy plates that are patterned with lines of holes.

# Chapter 6

# Underwater Acoustic Surface Waves on Straight Parallel Lines of Regularly Spaced Holes

## 6.1 Introduction

This chapter details a method of supporting underwater Acoustic Surface Waves (ASWs) using straight lines of equally spaced holes in aluminium alloy plates. One, two and three parallel lines of open ended holes will be utilised to support multiple degenerate or non-degenerate ASW modes. This work includes a method of pulsing broadband ultrasound close to the surface of the samples to excite high momentum surface waves and detect their propagating fields using an $xyz$ scanning stage mounted hydrophone. Fourier analyses of the two-dimensionally scanned data, in time and in space, is used characterise the ASWs in frequency and reciprocal space. In addition, interactions between ASWs and Scholte-Stoneley Waves (SSWs) are shown. Fully modelled acoustic-elastic computational data will be used to verify the experimental results. This work has applications in acoustic communications, acoustic energy harvesting, defect detection and acoustic circuitry.

## 6.2 Background

Surface acoustic waves are supported at the boundary between two differing mediums and they come in several distinct varieties[92]. ASWs are a type of surface wave that are non-radiative, highly localised and evanescently decaying normal to, and propagate over, an acoustically rigid periodically patterned surfaces, discussed in sec-

tion 2.6.2. Similar non-radiative surface waves were first observed in photonic and airborne phononic systems[45,46,47,48], but there has been significant recent interest in acoustics. Periodically patterned elastic media also support ASWs, the nature of which depends on the elastic properties of the plate and is yet to be fully investigated.

ASWs are supported by one-dimensional periodic arrays of simple resonators. First hypothesised by Scholte, one-dimensional periodic underwater structures influence both the evanescent and radiative fields[156,157,158,159]. Recently it has been shown that 1D arrays of metal rods can support ASWs or so-called spoof surface waves[160,161,162]. Most underwater studies of spoof surface waves and ASWs have been very recent and there is still much to investigate.

The following chapter examines the acoustic excitation of periodically structured lines of holes, which through the coupled diffraction of simple patterned resonators supports surface bound ASWs. A hole in a solid is a simple diffracting object and therefore solid flat plates patterned with a periodic array of holes are expected to support ASWs. Through diffraction and nearest neighbour coupling, acoustic fields in these resonating cavities interact in a way that is dependent on the spacing between features or the pitch, $\lambda_g$. Briefly mentioned in chapter 2, in 1D this type of array should have an adapted waveform,

$$\psi(x) = \sum_n \psi_n e^{i(\mathbf{k_x}+\mathbf{G})x} \tag{6.1}$$

Here the acoustic wavevector is $\boldsymbol{k_x}$ and $\boldsymbol{G}$ is the reciprocal lattice vector of the array. For a single row of holes $\boldsymbol{G} = k_g = (2\pi/\lambda_g)$. For two and three lines of holes, the structure will have additional degrees of freedom and will support additional modes.

Experimentally, this work will begin by looking at the simplest case of the single row of holes and finish with the more complicated three row samples. But first, sample fabrication and the experimental method will be discussed.

## 6.3 Sample Fabrication

This study investigates the coupling of diffracted fields from water filled circular open ended holes in solid aluminium alloy (5083). The arrays are patterned into the four plates with a fixed $150 \pm 1$ by $600 \pm 1$ mm area. The alloy's mechanical properties are defined by the Poisson's ratio $\nu = 0.34 \pm 0.2$, elastic modulus $E = 72 \pm 2$ GPa and mass density $\rho = 2660 \pm 10$ kgm$^{-3}$ (chapter 4). A CNC (Computer Numerical Control) machine is used to pattern the plates with lines of holes. These lines have a fixed pitch $\lambda_g = 6.00 \pm 0.01$ mm, radius of holes $R = 1.50 \pm 0.01$ mm and thickness $L = 9.7 \pm 0.1$ mm, as they were fabricated using the same sheet of alloy. The results in this chapter are

Fourier analysed using triple zero-padding and a Hanning-like window fit. Frequency domain results are presented as reference normalised data and k-space data is presented as self normalised amplitude (section 3.5). Figure 6.1 shows the four line samples with one row of holes, two mirror-symmetric rows of holes, two glide-symmetric rows of holes and three psuedo-glide-symmetric rows of holes.
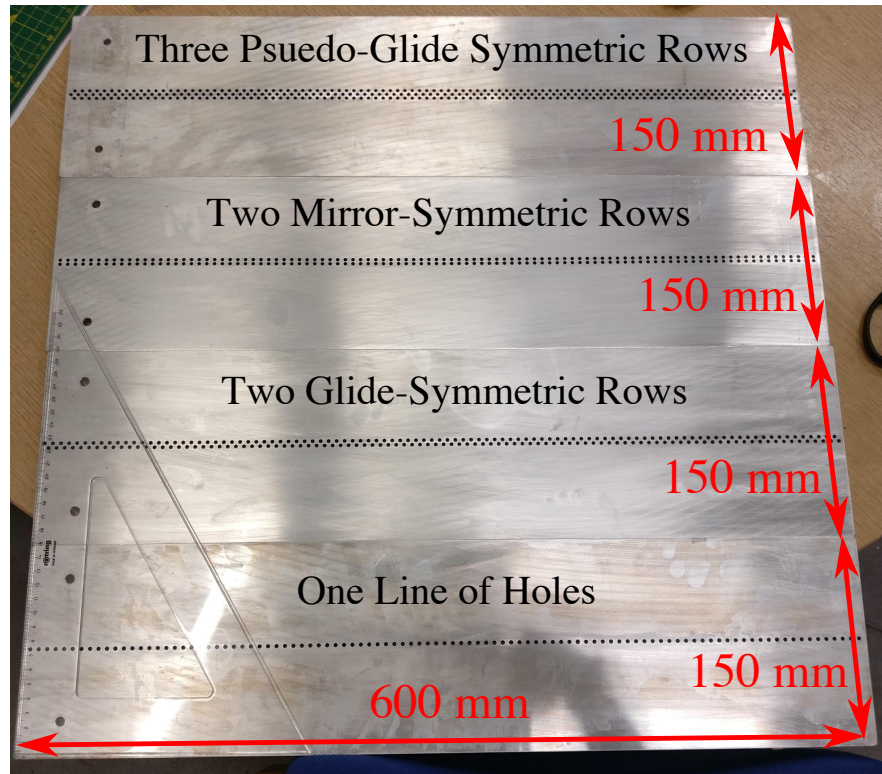


**Figure 6.1:** The four $9.7 \pm 0.1$ mm thick aluminium alloy (5083) samples that are investigated in this chapter.

## 6.4  Experimental Method

Experimentation is performed on the samples that are fully submerged underwater in $\approx 100$ cm deep water contained in a fibreglass water tank (described in section 3.3). A $3.0 \pm 0.1$ cm diameter acrylic arm is used to suspend samples underwater, centred at $\approx 50$ cm above the bottom of the tank. The plate is fixed to this arm using flat pieces of perspex threaded with nylon screws. Sample and support materials were chosen to be inert underwater, to avoid galvanisation during the scanning process that can take up to 8 hours.

The experiment uses the foam-wrapped Neptune Sonar D70 transducer (described in section 3.5). The transducer emits approximately double-cycle Hanning-windowed

pulses projected at the $150 \pm 1$ by $600 \pm 1$ mm area plates. The source is positioned above one of the holes of the sample at a point $\approx 10$ cm from the edge of the sample to limit edge reflections and $\approx 3$ mm from the samples surface as shown in figure 6.3. The exit of the source is a $6.00 \pm 0.01$ mm diameter $0.05 \pm 0.01$ mm thick steel tube. This source is directional and uses its own diffraction plus that from one of the open-ended holes of the sample to excite surface waves.
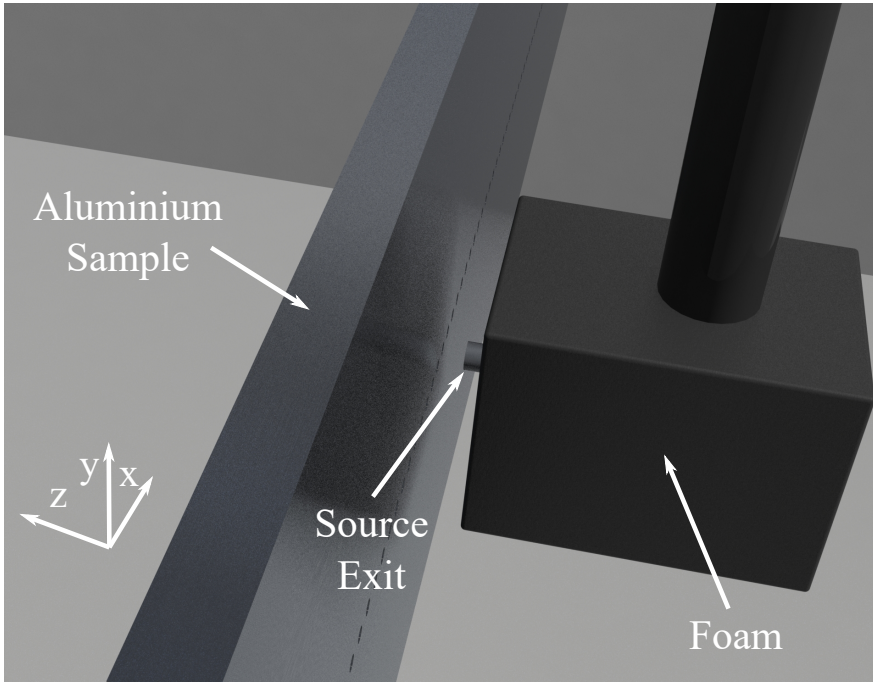


**Figure 6.2:** A 3D render of the foam-wrapped D70 source positioned in front of a singe line of holes in a 9.7 mm thick aluminium alloy plate. The exit of the source is approximately 3 mm from the surface of the sample and is positioned over one of the holes.

Transmitted signals are detected spatially by scanning a Precision Acoustics $1.00 \pm 0.01$ mm diameter needle hydrophone in an $xy$ plane. Results are collected as spatial $xy$ maps of the time averaged voltage, $V$, over time, $t$. Spatial scans are acquired detecting $0.50 \pm 0.01$ mm from the surface in a $21.21 \pm 0.03$ mm by $128.70 \pm 0.03$ mm area with a non-commensurate $\Delta x = \Delta y = 0.707 \pm 0.003$ mm. At each point in space the voltage, $V$, over time, $t$, is recorded over 50 identical pulses with a 0.03 s pulse rate and averaged in time with $\Delta t = 0.104$ $\mu$s and $t_{\max} = 1.20$ ms.
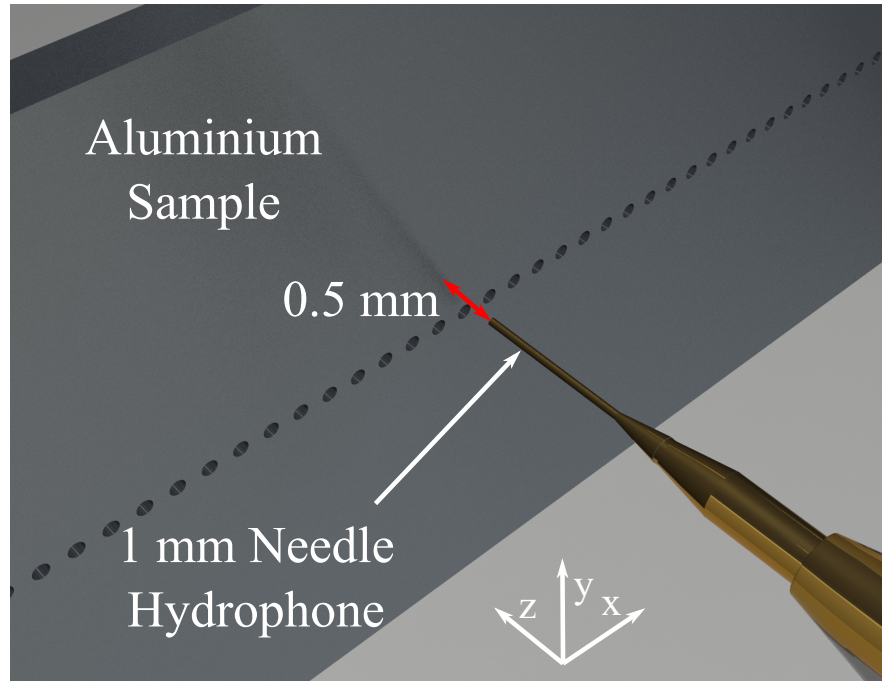
**Figure 6.3:** A 3D render of the gold plated Precision Acoustics 1.00 mm diameter needle hydrophones positioned in front of a line of holes in a 9.7 mm thick aluminium alloy plate. This needle is positioned 0.50 mm from the sample's surface as it is spatially scanned.

The 2D scanned results are Fourier analysed using a computational FFT in time, $t$, and space, $x$ and $y$, to produce the frequency, $f$, and wavevector components of the fields, $k_x$ and $k_y$. The resolution in frequency is limited by the total time of the signal recorded at each point $t_{\max}$. The k-space values are limited by the maximum wavevector ($k_{\max} = 2\pi/\Delta x = 2\pi/\Delta y$) and the k-space resolution $\Delta k = 2\pi/x_{\max}$. This method has been widely applied to scanning fields in acoustics, electromagntism and optics[111] as field maps allow easy attribution and characterisation of fields that contain multiple interacting surface waves.

## 6.5 One Row of Holes

The first sample examined is the one-dimensional line of holes fabricated in a $9.7 \pm 0.1$ mm thick aluminium alloy (5083) plate, depicted in figure 6.4. The row of holes is central to the plate in $y$, with pitch $\lambda_\mathrm{g} = 6.00 \pm 0.01$ mm and radius $R = 1.50 \pm 0.01$ mm. The aluminium plate was machined using a CNC device to drill 100 open-ended holes along its length. The sample is then submerged underwater with the holes being entirely water filled whilst experimentation took place.
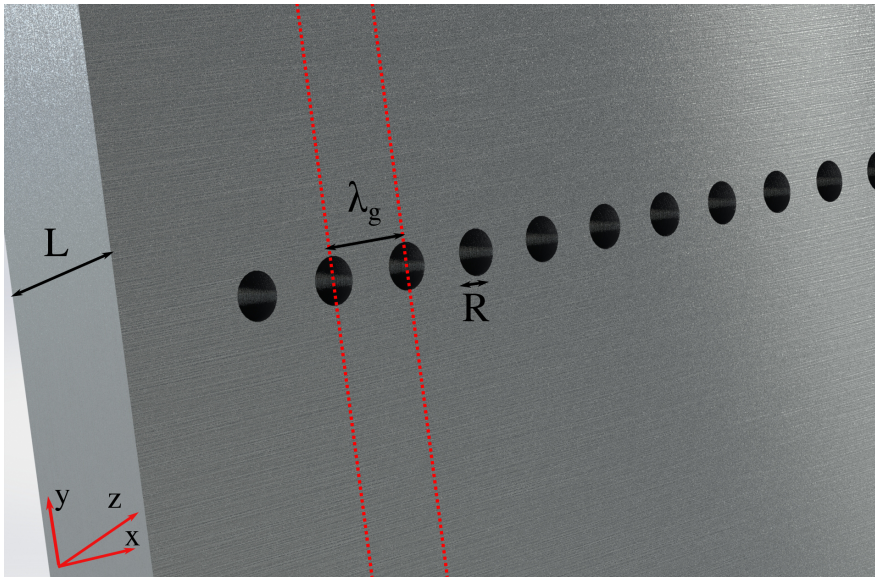


**Figure 6.4:** A scale 3D rendered image of the single row of holes in the aluminium alloy plate. Labelled is the pitch $\lambda_\mathrm{g} = 6.00 \pm 0.01$ mm, radius of the holes $R = 1.50 \pm 0.01$mm and thickness $L = 9.7 \pm 0.1$ mm. The holes are open-ended and the entire sample is submerged underwater during experimentation.

### 6.5.1 Time Domain

Scanning in a $21.21 \pm 0.03$ by $128.70 \pm 0.03$ mm area the field components containing the ASWs are collected. Unfiltered time-averaged results of the instantaneous fields are shown in figure 6.5, as voltage, $V$, in space. The excited acoustic waves travel from left, $x = 0$ mm, to right. In this figure, four instances in time are plotted at 0.100, 0.150, 0.200 and 0.250 ms after the pulse was launched. These results show the propagating fields that are predicted to contain the ASW, SAW and free wave components. To characterise the modes of the plate, this data is Fourier analysed to produce the frequency and k-space components, $k_x$ and $k_y$, of the acoustic fields.
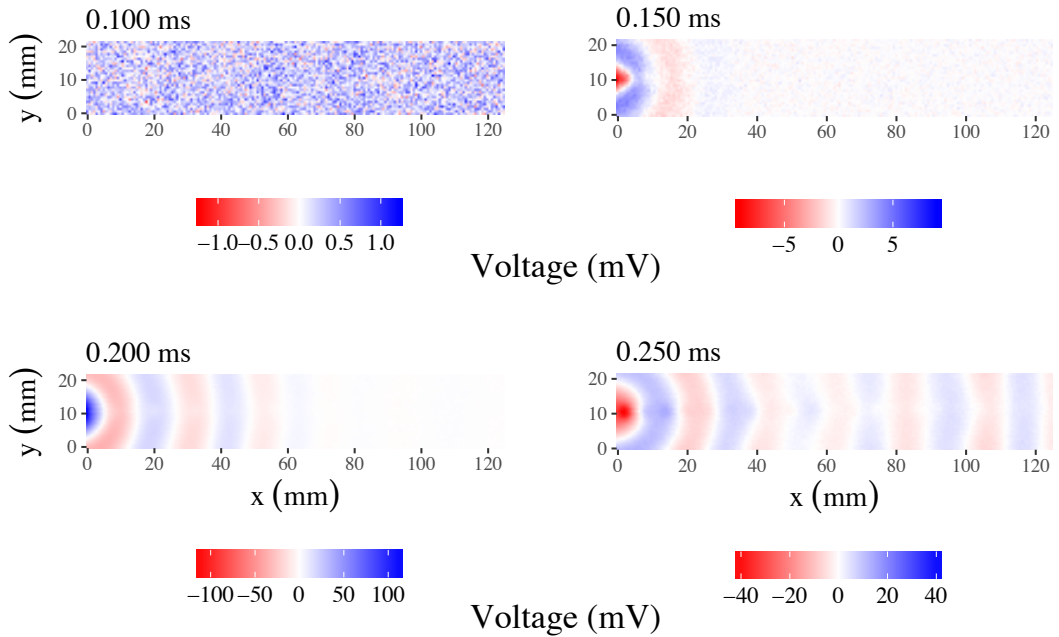
**Figure 6.5:** The instantaneous voltage fields of acoustic waves propagating over the surface of a single row of holes in the flat aluminium alloy sample. These plot show the instantaneous voltage at 0.100, 0.150, 0.200 and 0.250 ms after the pulse was launched.

### 6.5.2 Frequency Domain

The diffracted coupling between neighbouring holes of a structure that supports ASWs means that at the BZ boundary there is only one possible excitation for the single row of holes. The predicted phase map of this mode is shown in figure 6.6. As depicted, the fields in neighbouring holes are $\pi$ out of phase at the BZ boundary.
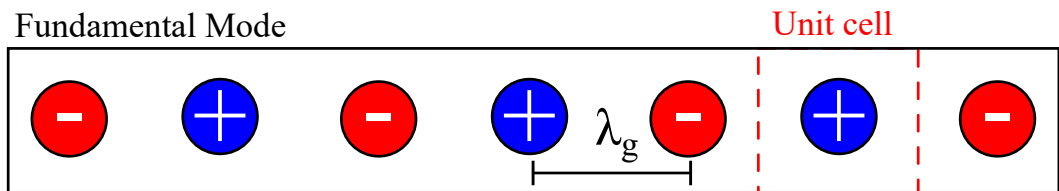


**Figure 6.6:** The only predicted excitable ASW mode of a single line of acoustically coupled holes at the BZ boundary. The colour represents the phase of each hole, where blue is positive phase ($\pi/2$) and red is negative phase ($-\pi/2$).

Time domain results are computationally Fast Fourier Transformed (FFT), in time $t$, to produce the frequency components of the fields. The instantaneous amplitude, absolute amplitude and phase experimental results are shown in figure 6.7, figure 6.8 and figure 6.9, respectively. The results are plotted at 50.0, 52.5, 55.0, 57.5, 59.0 and 60.0 kHz frequencies. Instantaneous amplitude plots contain both the phase and

amplitude content present in figure 6.8 and figure 6.9. Although, they are plotted independently for visualisation of the power and the structure of the fields.
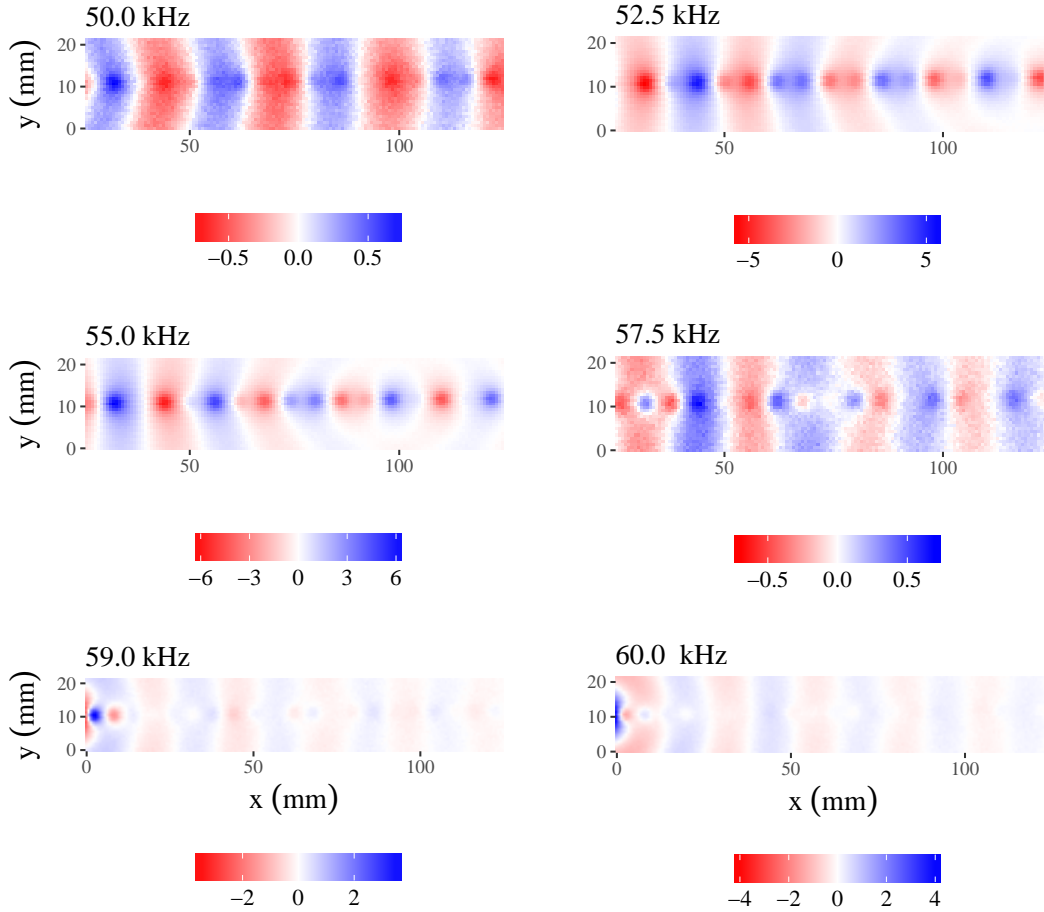


**Figure 6.7:** The experimental instantaneous amplitude above the single line of holes at 50.0, 52.5, 55.0, 57.5, 59.0 and 60.0 kHz. Field amplitude at 55.0 and 57.5 kHz increases as the propagating ASW mode is present.

These frequency results show the nature of the ASW mode over the range of 50.0 to 60.0 kHz. As can be seen in the phase plots, at 55.0 kHz the curvature of the field at $x \approx 95$ mm suggests the presence of more than a single signal, resulting in interference. In both figures 6.7 and 6.8, at 59.0 and 60.0 kHz the ASW mode is not present. Instead the result contains the free travelling water wave and the SSW scattering from the structure, leaving an absence of amplitude where the holes of the array are positioned.
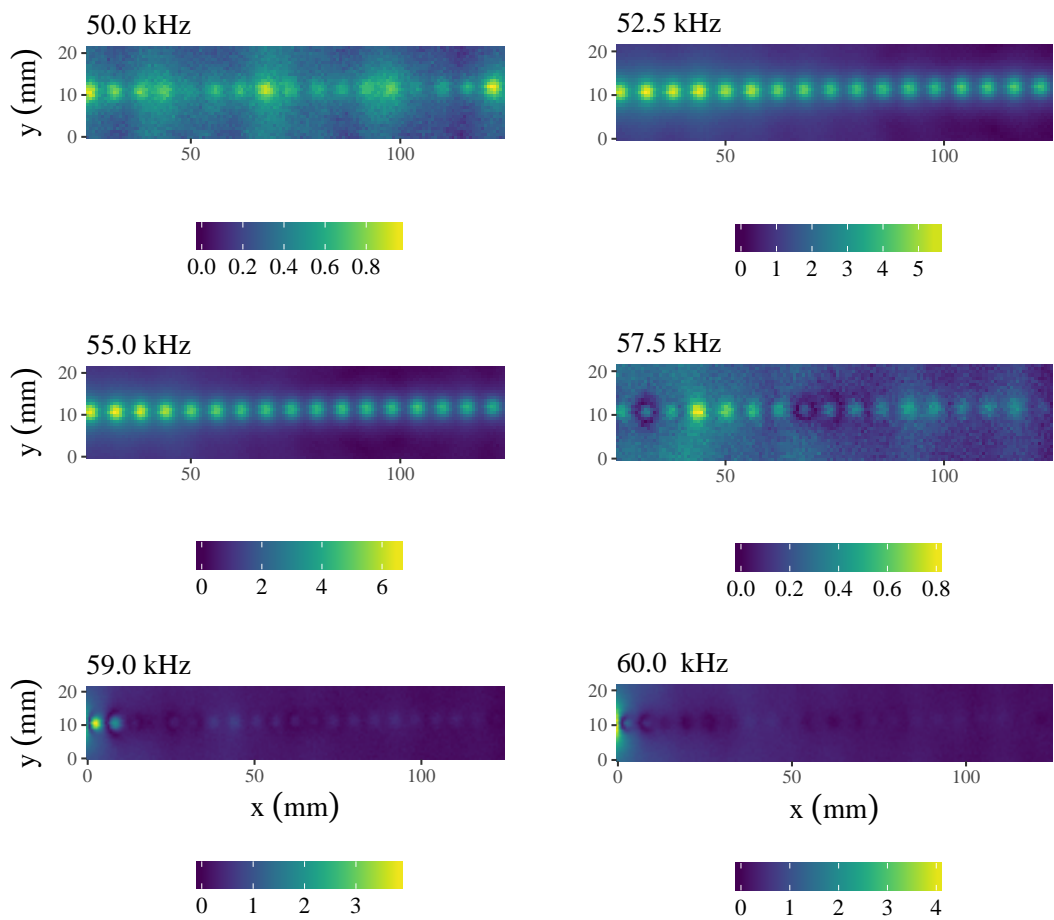
**Figure 6.8:** The experimental absolute amplitude results of the fields over the line of holes at 50.0, 52.5, 55.0, 58.0, 59.0 and 60.0 kHz. At 55.0 and 57.5 kHz the field amplitude and the propagation distance increases, as the propagating ASW mode is present.
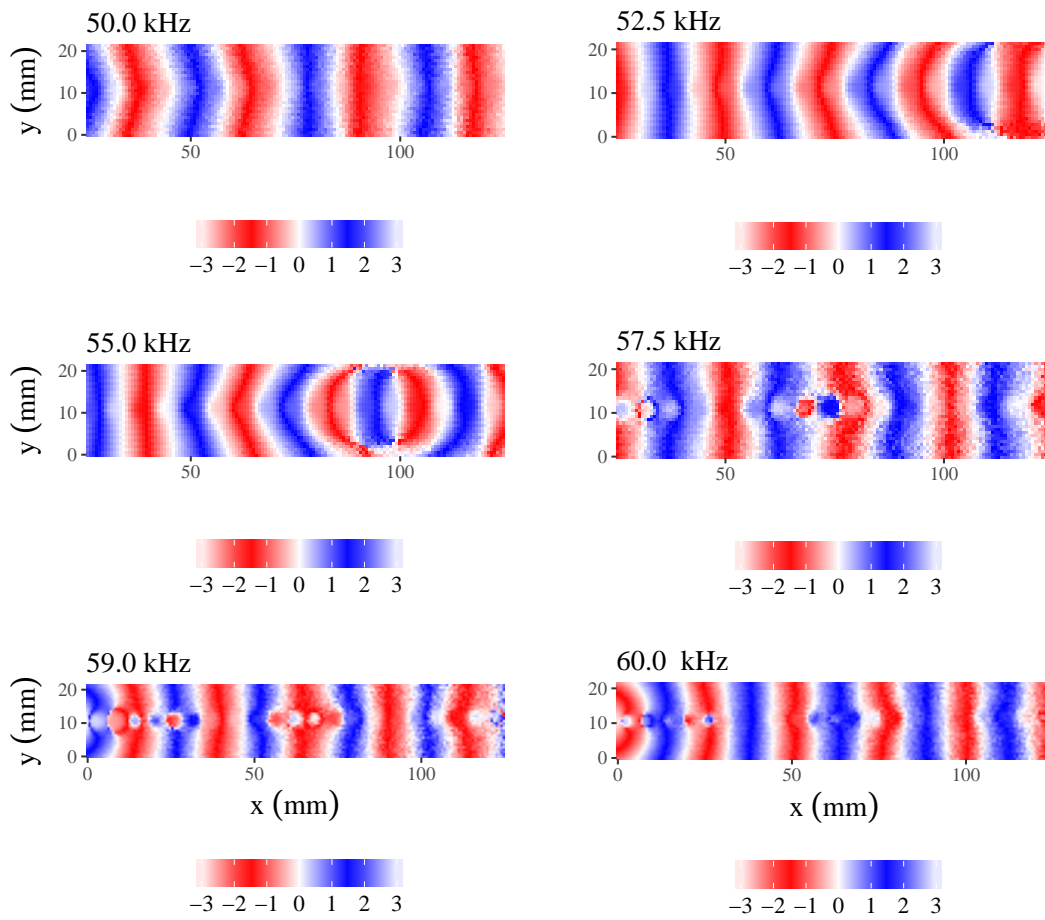
**Figure 6.9:** The experimental phase results above the line of holes at 50.0, 52.5, 55.0, 58.0, 59.0 and 60.0 kHz plotted between $-\pi$ and $+\pi$. The curvature of the field spatially at $x \approx 95$ mm at $f = 55$ kHz suggests multiple interfering in-plane travelling acoustic signals.

### 6.5.3 Wavevector Components

To obtain the directionality, investigate the source of the spatial quantisation and confirm our initial characterisation of the ASW, it is necessary to examine the wavevector components of the fields. Processing the frequency components using a spatial FFT, in $x$ and $y$, produces the wavevector components of the fields, $k_x$ and $k_y$. Two-dimensional wave vector results of the excited fields of the one-dimensional single line of holes at 52.0, 54.0, 56.0 and 58.0 kHz frequencies are shown in figure 6.10.
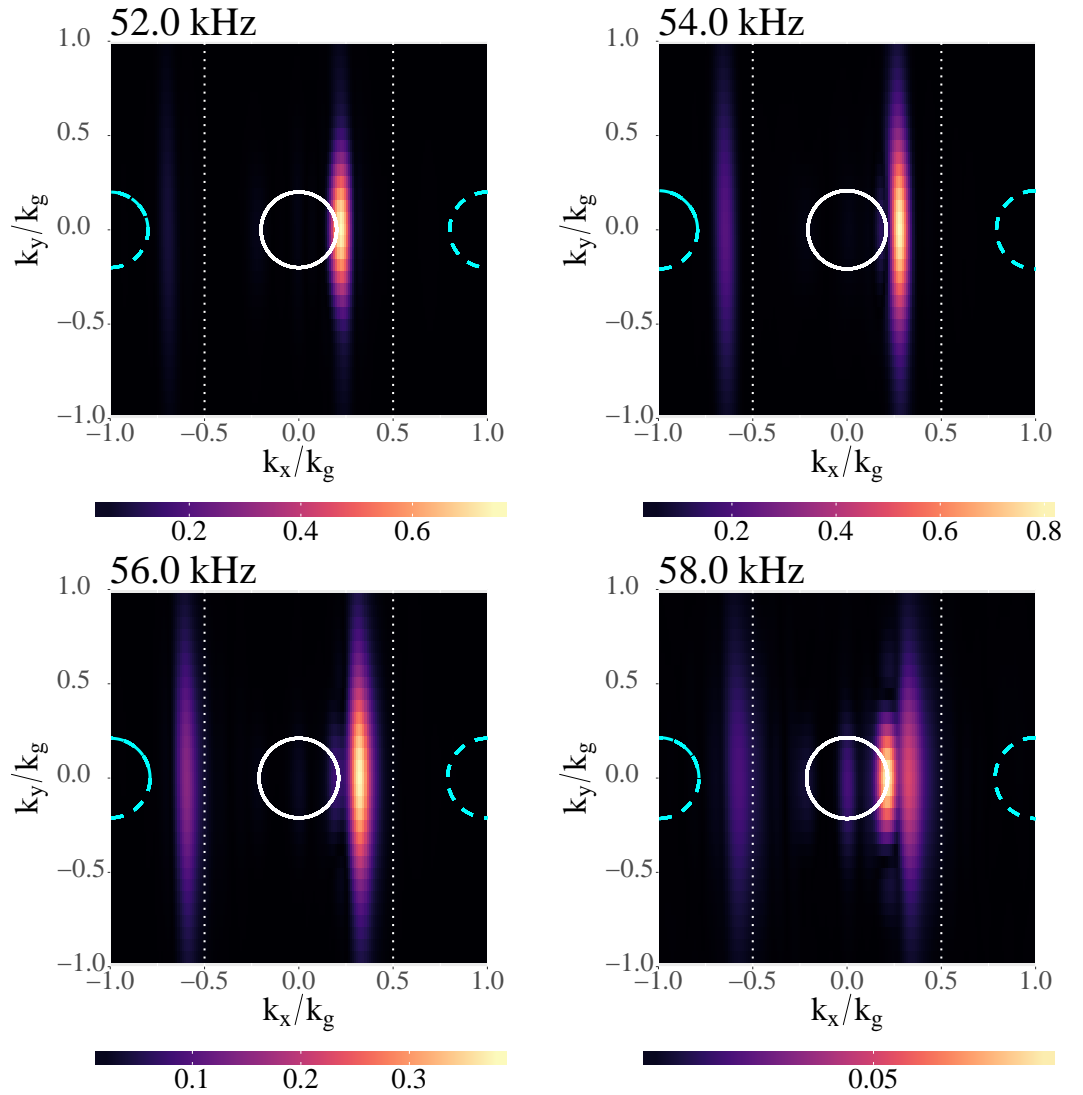


**Figure 6.10:** The experimental wavevector components of the excited fields above a single row of holes, plotted as self normalised magnitude in $k_x$ and $k_y$ at 52.0, 54.0, 56.0 and 58.0 kHz. Data is plotted beyond the BZ boundaries, white dotted lines, in the $k_x$ direction.

## 6. Underwater Acoustic Surface Waves on Straight Parallel Lines of Regularly Spaced Holes

These results are plotted as normalised magnitude, with high amplitude components representing eigenmodes of the system at these chosen frequencies. The k-space results are plotted beyond the BZ, showing the diffracted components of the fields beyond the BZ boundary. The BZ lies at $k_{\text{BZ}} = \frac{k_{\text{g}}}{2} = \pi/(6\text{mm}) = 523\text{m}^{-1}$. Also shown is the corresponding frequency dependent sound lines, defined by the compressional speed of sound in the water, $c_{\text{w}} = 1512$ m/s.

The results in figure 6.10 show the ASW dispersing from the sound line until the mode weakens at 58.0 kHz. At 56.0 and 58.0 kHz a weak mode bound to the sound line and propagating in the $x$ direction at all frequencies is present. This is characteristic of an SSW or water sound line bound mode. Both the SSW mode and ASW modes appear as straight lines perpendicular to $k_x$ as the propagate only in the $x$ direction. The diffracted order ASW has the same shape and symmetry as the mode in positive $k_x$ region.

### 6.5.4 Dispersion

Figure 6.11 shows the dispersion at the chosen wavevector $k_y = 0 \text{ m}^{-1}$ (a cross section of figure 6.10).
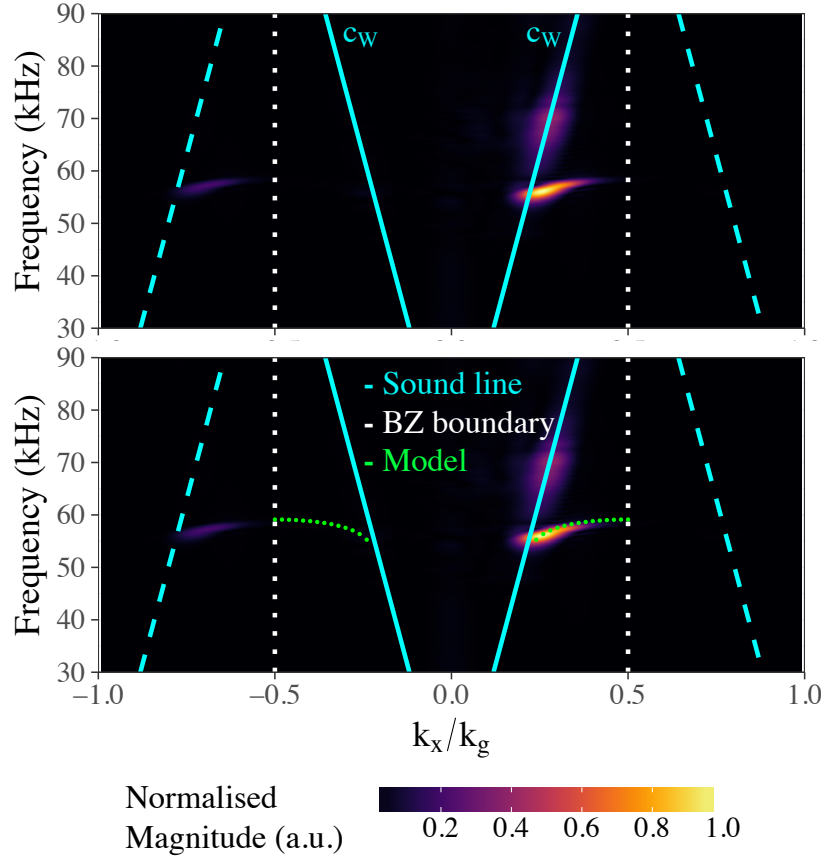


**Figure 6.11:** The experimentally observed dispersion of a single line holes in 9.7 mm thick aluminium alloy. Top is the experimentally extracted dispersion of the single line of holes. Bottom is the dispersion compared to overlaid Comsol multiphyics 5.3a modelled eigenfrequencies of an equivalent system with $L = 9.7$ mm, $\lambda_g = 6.0$ mm and $R = 1.5$ mm. This was modelled as an elastic solid with elastic properties Poisson's ratio, $\sigma = 0.32$, elastic modulus, $E = 72.0$ GPa, and density, $\rho = 2660 \text{ kg/m}^3$.

Figure 6.11 shows the ASW dispersing from the sound line between 55 and 65 kHz. As it approaches the BZ boundary the mode weakens in amplitude. This is where the group velocity of the ASW is near zero and the wave therefore does not propagate far enough to be measured. The mode on the sound line is evident at all frequencies in this range explaining the interference signal. The diffracted portion of the dispersion shows the presence of the diffracted orders of this sound line. The results here are plotted against the results of a Comsol multiphysics 5.3a model pressure acoustic-elastic model of the system.

### 6.5.5 A Rigid vs Elastic Comparison

This study has uncovered that it is essential to model the eigenfrequencies of the single row of holes treat the plate as an elastic medium. Here, Comsol multiphysics is used to demonstrate the difference between the FEM rigid plate and elastic plate computed eigenvalues of an ASW mode in figure 6.12.
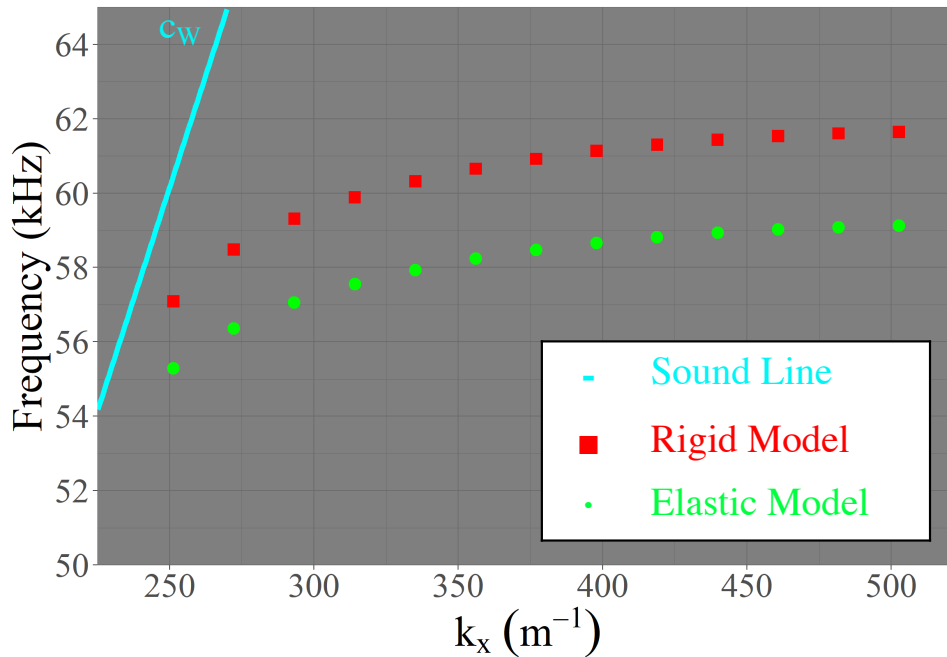


**Figure 6.12:** Comsol multiphysics modelled eigenfrequency results of a single line of holes for open in an elastic aluminium alloy plate (green dots) and a perfectly rigid plate (red squares). The geometry of the array is 6.00 mm pitch, 1.5 mm radius and 9.7 mm thick.

The results in figure 6.12 shows that there is a significant difference between the produced dispersion of the perfectly acoustically rigid solid (red squares) and that of an elastic solid (green dots). The difference in the value of the asymptotic final eigenfrequency is $\Delta f = 2.53$ kHz at $k_x \approx \frac{k_g}{2}$. The agreement between the modelled and experimental results in figure 6.11 show that it is necessary to factor in the elastic properties of the plate when modelling their evanescent modes.

## 6.6    Two Rows of Holes with Mirror Symmetry

The second sample examined has two parallel lines of holes drilled into a $L = 9.7 \pm 0.1$ mm thick aluminium alloy (5083) plate with spacing between the centre lines of the holes $d = 3.50 \pm 0.01$ mm, $\lambda_\mathrm{g} = 6.00 \pm 0.01$ mm and $R = 1.50 \pm 0.01$ mm. The holes in rows are aligned with a mirror plane between the lines. This sample is depicted in figure 6.13. The Brillouin zone boundary of this sample remains at $k_\mathrm{BZ} = 523$ m$^{-1}$, the same as for the single row as the pitch has not changed.
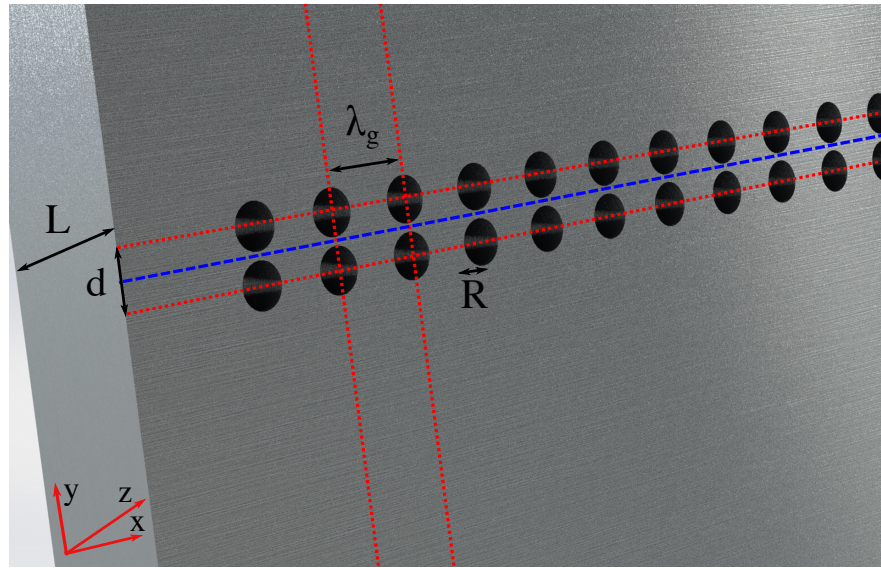


**Figure 6.13:** A to scale 3D rendered image of the two symmetric rows of holes in the aluminium alloy sample. Labelled are the pitch $\lambda_g = 6.00$ mm, radius of the holes $R = 1.50$ mm, thickness $L = 9.7 \pm 0.1$ mm and spacing between the centre of both rows $d = 3.5$ mm. The holes are open-ended and the entire sample is submerged underwater during experimentation.

Due to the extra degree of freedom, it is expected that there are two excitable ASW modes of this sample at the BZ boundary, as shown in figure 6.14. These modes are labelled the symmetric and antisymmetric modes after the associated field in the $y$ direction symmetry. At the BZ boundary both the these modes can exist independently. To excite these two modes, the source is positioned off-centre of the two lines of holes, over one of the holes. This will give the field plots an asymmetry, but is necessary to excite the antisymmetric mode.

## 6. Underwater Acoustic Surface Waves on Straight Parallel Lines of Regularly Spaced Holes
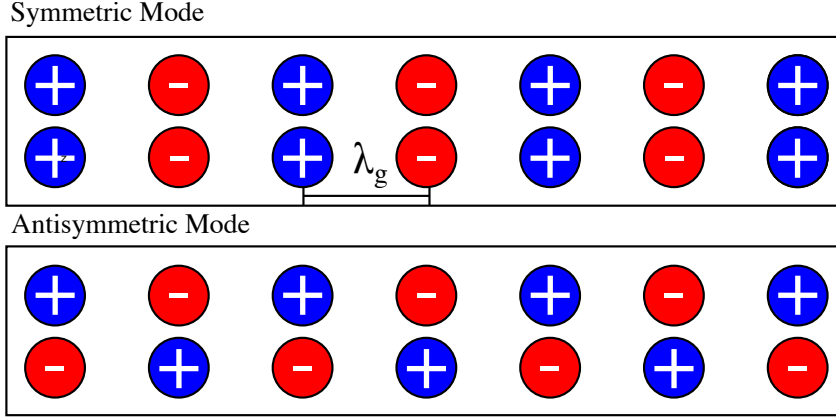
Symmetric Mode



Antisymmetric Mode



**Figure 6.14:** The two excitable ASW modes of two mirror symmetric lines of coupled resonating holes at the BZ boundary. The colour represents the phase of each hole, where blue is positive phase ($\pi/2$) and red is negative phase ($-pi/2$).

Taken from the generalised Floquet theorem, this system has the glide operator:

$$G = \begin{cases} x \to x \\ y \to -y \\ z \to z \end{cases} \qquad (6.2)$$

### 6.6.1 Frequency Domain

Time domain data is collected $0.50 \pm 0.01$ mm from the surface in a $21.21 \pm 0.03$ mm by $128.70 \pm 0.03$ mm area as voltage over time. These results are Fourier transformed in time using an FFT to produce the instantaneous amplitude, absolute amplitude and phase, presented in figures 6.15, 6.16 and 6.17. The four frequencies depicted are 53.6, 55.0, 56.4 and 59.0 kHz illustrating the two supported ASW modes.

At 53.6, 55.0, 56.4 and 59.0 kHz the presence of the ASW modes are seen, shown by the significant increase in power in figures 6.15 and 6.16. They split into two distinct modes as the BZ is approached, figure 6.14. The lower frequency mode shown at 53.6, 55.0 and 56.4 kHz is the symmetric mode of the sample and the the antisymmetric mode is clearly visible in figures 6.15 and 6.16 at the higher frequency of 59.0 kHz. In addition, note that three plots at 59.0 kHz show the expected null in the field at the centre of the two rows of holes.

In addition, the frequency plots show a presence of the modulation, as seen previously in the single row of holes, at $x \approx 60$ mm at 55.0 kHz in the phase plots of figure 6.17. This feature is associated with the overlapping ASW and SSW modes. It is expect that these features disperse independently when the wavevectors and dispersions are plotted.
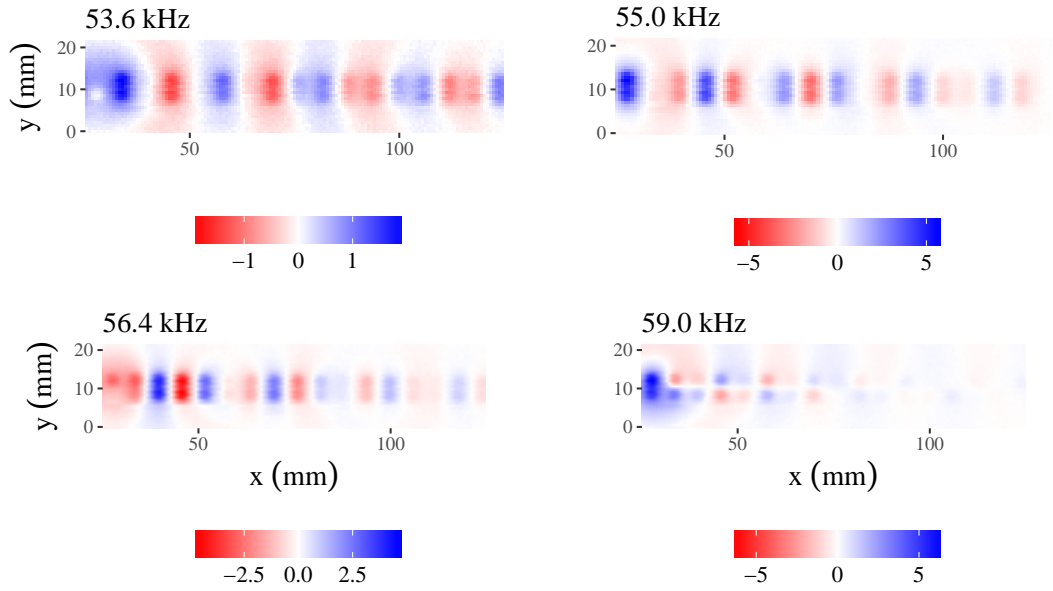
**Figure 6.15:** The experimental instantaneous signal of the fields above two rows of symmetrically aligned holes in the 9.7 mm thick aluminium alloy plate. Shown are the results at 53.6, 55.0, 56.4 and 59.0 kHz.



**Figure 6.16:** The absolute amplitude results of the fields above two rows of symmetrically aligned holes in the 9.7 mm thick aluminium alloy plate. Shown are the results at 53.6, 55.0, 56.4 and 59.0 kHz.

**Figure 6.17:** The experimentally measured results of the phase of the fields above two rows of symmetrically aligned holes in the 9.7 mm thick aluminium alloy plate. S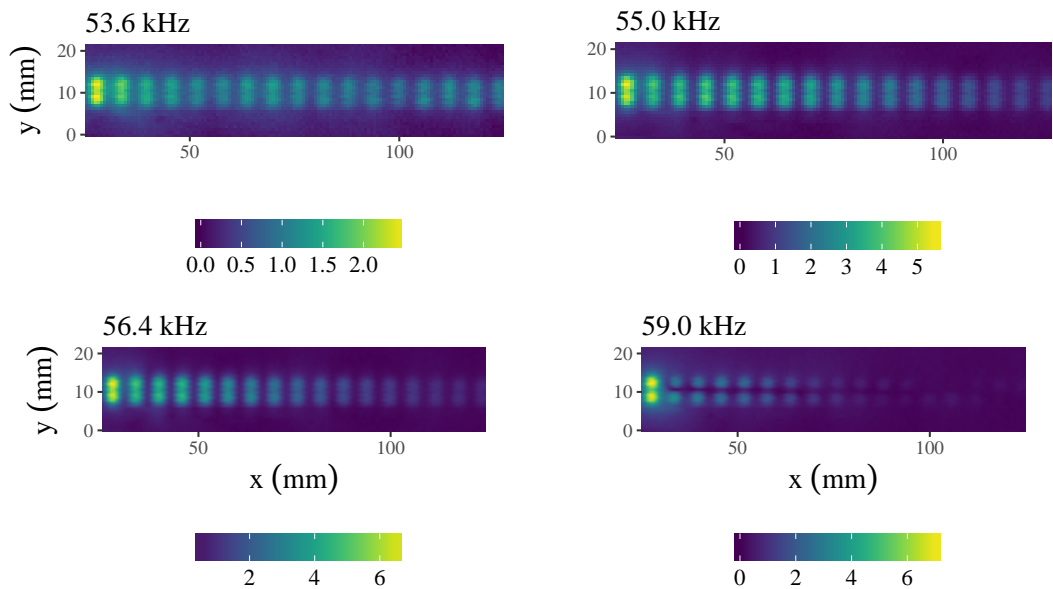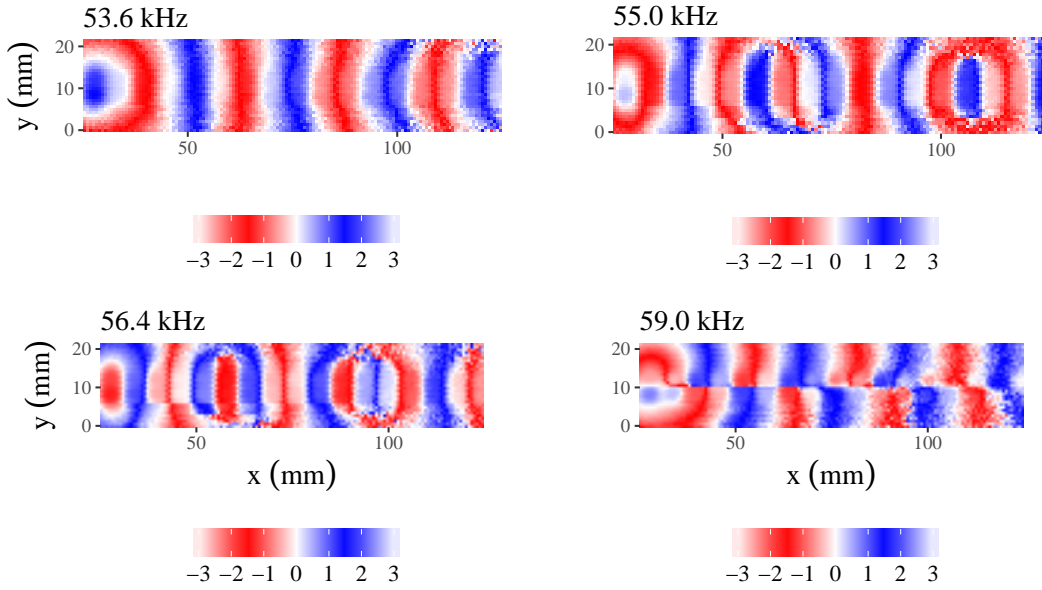hown are the results at 53.6, 55.0, 56.4 and 59.0 kHz. Here blue represents positive phase $+\pi/2$ and red is negative phase $-\pi/2$.

### 6.6.2 Wavevector Components

The frequency results are now Fourier transformed spatially in $x$ and $y$ to produce the wavevector components of the detected fields, shown in figure 6.18. These results depict the wavevector components at 53.6, 55.0, 56.4 and 59.0 kHz as Fourier magnitude in wavevector space, $k_x$ and $k_y$.

The propagating symmetric ASW mode has a symmetric amplitude distribution similar to the fundamental mode of the single line of holes at 53.6 and 55.0 kHz in figure 6.10. There is a second forward-propagating ASW mode that appears at larger $|k_y|$ at 59.0 kHz. This antisymmetric mode is split in amplitude with a minimum at $k_y = 0$. The slight asymmetric intensity of this order mode is due to the fact that the excitation is at one side of the structure. Note that the diffracted modes have the same intensity distribution with regard to the $y$-axis as the forward-propagating modes.
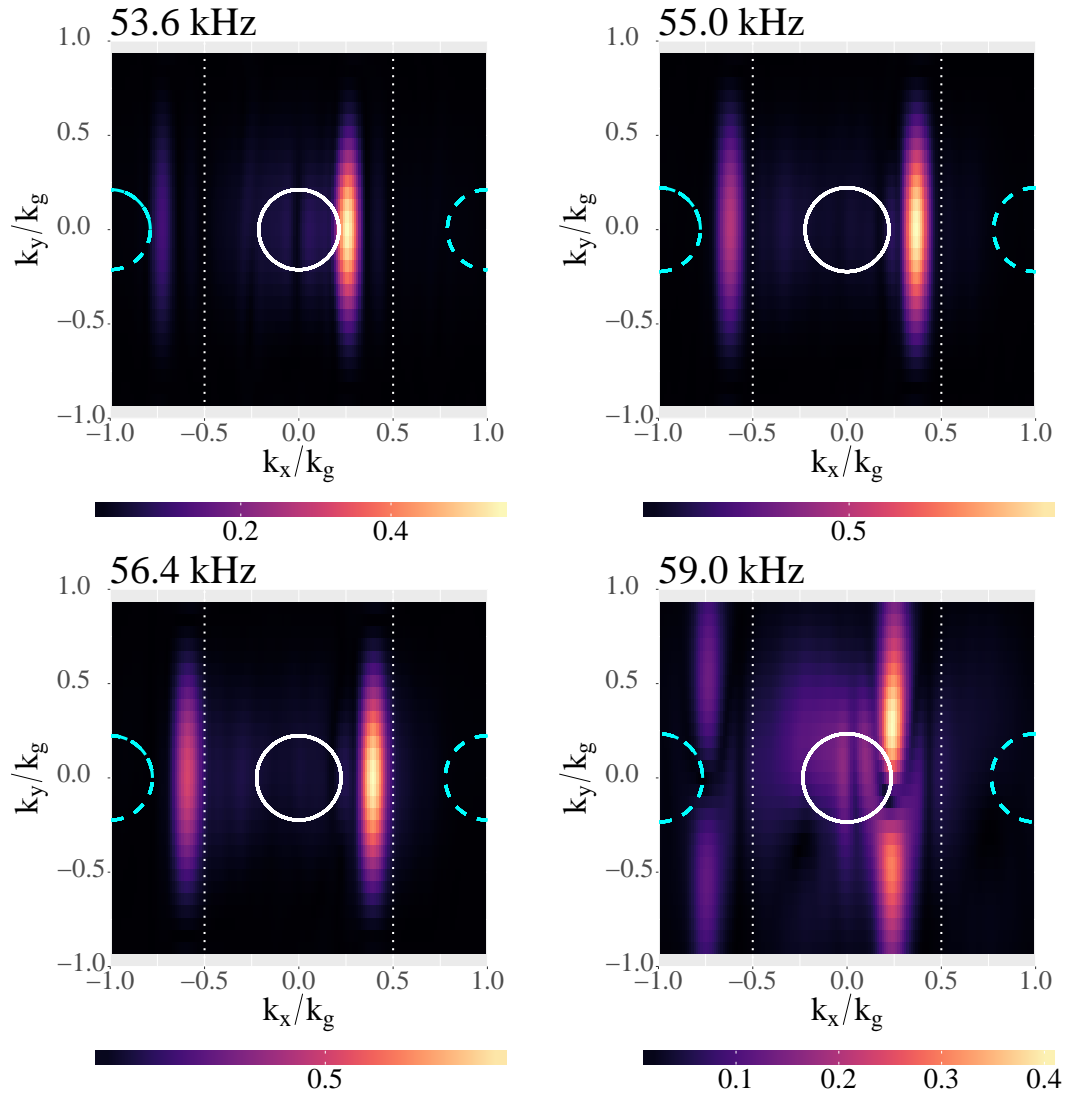
**Figure 6.18:** The experimentally extracted wavevector plots for the two mirror symmetric rows of holes at 53.6, 55.0, 56.4 and 59.0 kHz. Each plot shows the normalised magnitude of signal in a given direction, with high amplitude features characterised as the ASW modes.

### 6.6.3    Dispersion

Plotting frequency, $f$, against wavevector, $k_x$, at $k_y = 0$ produces the dispersion depicted in figure 6.19. As highlighted in figure 6.18, the second order antisymmetric ASW has zero amplitude at $k_y = 0$. Therefore when plotting the dispersion at $k_y = 0$, results show that the forward-propagating and negative wavevector diffracted order of the antisymmetric mode does not exist. To visualise the fundamental antisymmetric mode, the dispersion at finite $k_y$ is plotted, choosing $k_y = \frac{k_g}{2} = 523$ m$^{-1}$ in figure 6.20. The group velocity of this mode is significantly lower than that for the symmetric mode and it decays more quickly in the propagation direction, making it harder to detect, but now both modes are visible in the diffracted side of the dispersion diagram with a gap between the two at the BZ boundary.
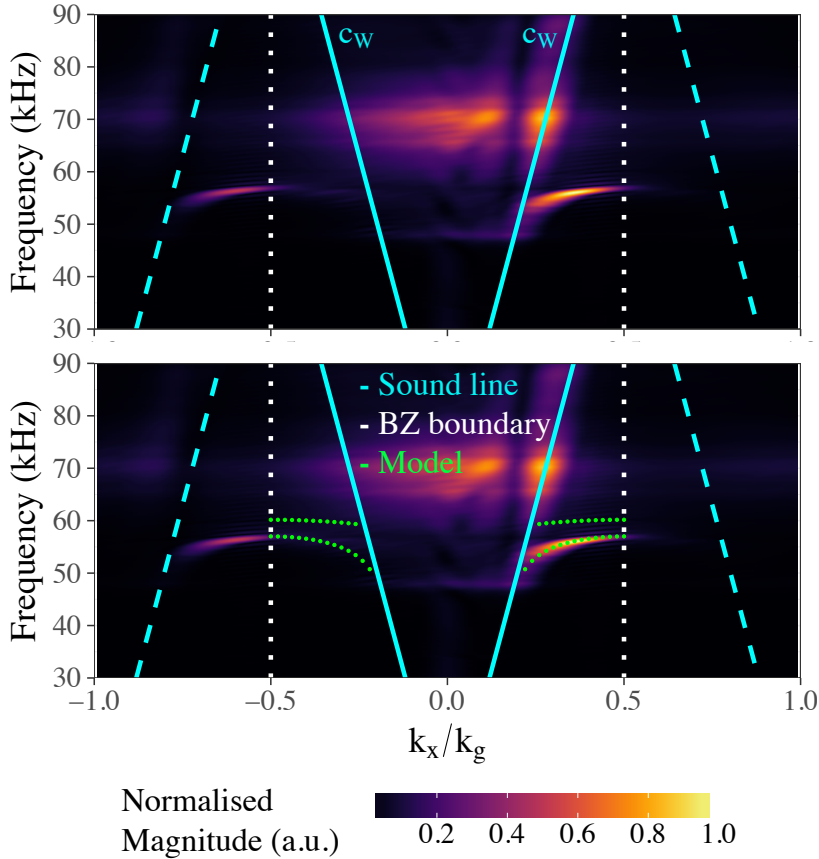


**Figure 6.19:** The experimentally-measured and Comsol-calculated (green dots) dispersion of the detected fields over the 9.7 mm thick aluminium sample with two mirror-symmetric rows of holes drilled into it. The top plot is the data at a cross-section in wavevector space at $k_y = 0$ and the bottom plot has the elastic-acoustic model superposed for the comparison.

Plotted against the experimental data is the Comsol pressure acoustic-elastic dispersion curve results of the system in figures 6.19 and 6.20. The dispersion curves of the model are overlaid onto the experimental eigenvalues and are in excellent agreement. Shown in the modelled data, the two modes are separate at the BZ boundary as they do not overlap. Experimentally the results do not reach the BZ boundary because as the group velocity of these modes decreases to zero there is progressively less signal to detect. The band gap between the upper and lower mode at the BZ is 3.1 kHz.
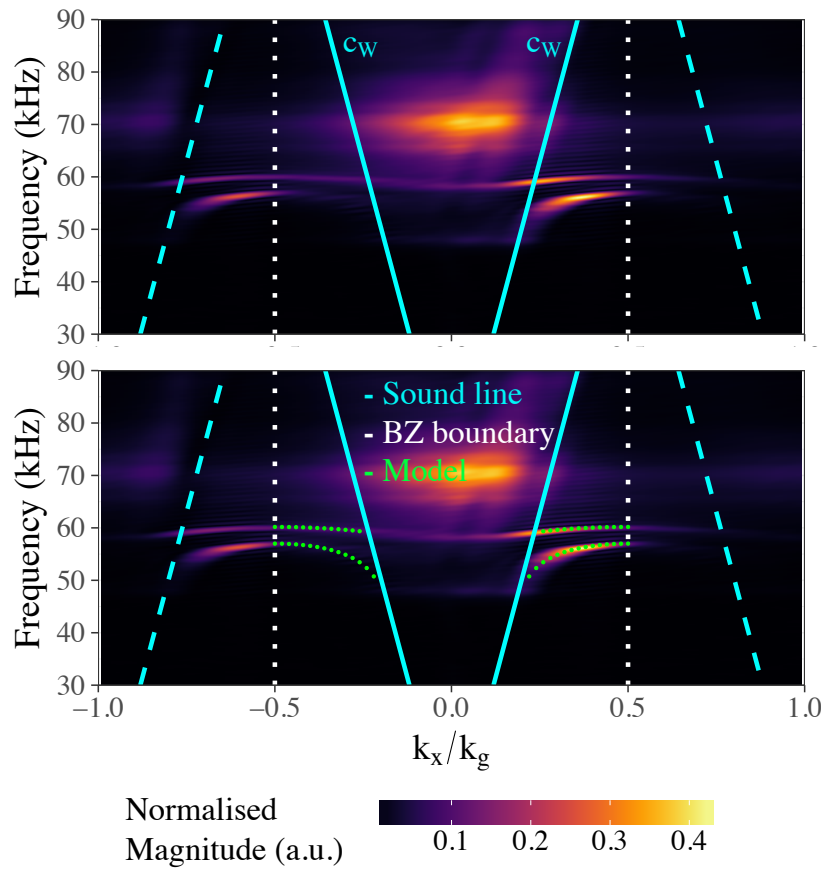


**Figure 6.20:** The experimentally-measured and Comsol-calculated (green circles) dispersion of the detected fields over the 9.7 mm thick aluminium sample with two mirror symmetric rows of holes. The top plot is taken at a cross-section in wavevector space at $k_y = \frac{k_g}{2}$ and the bottom plot has the elastic-acoustic model superposed for the comparison. The backwards-propagating diffracted orders are present between $k_x < -k_g/2$ and the forward-propagating waves exist in the range $0 < k_x < \frac{k_g}{2}$.

## 6.7 Two Glide-symmetric Rows of Holes

The third sample studied is composed of two parallel lines of holes having glide-symmetry drilled fabricated in a $9.7 \pm 0.1$ mm thick aluminium alloy (5083) plate with spacing between the centre points of each row $d = 3.5 \pm 0.1$ mm, $\lambda_{\mathrm{g}} = 6.0 \pm 0.1$ mm and $R = 1.5 \pm 0.1$ mm, as shown in figure 6.21. The BZ boundary in the $x$ direction is again $k_{\mathrm{BZ}} = 523$ m$^{-1}$.
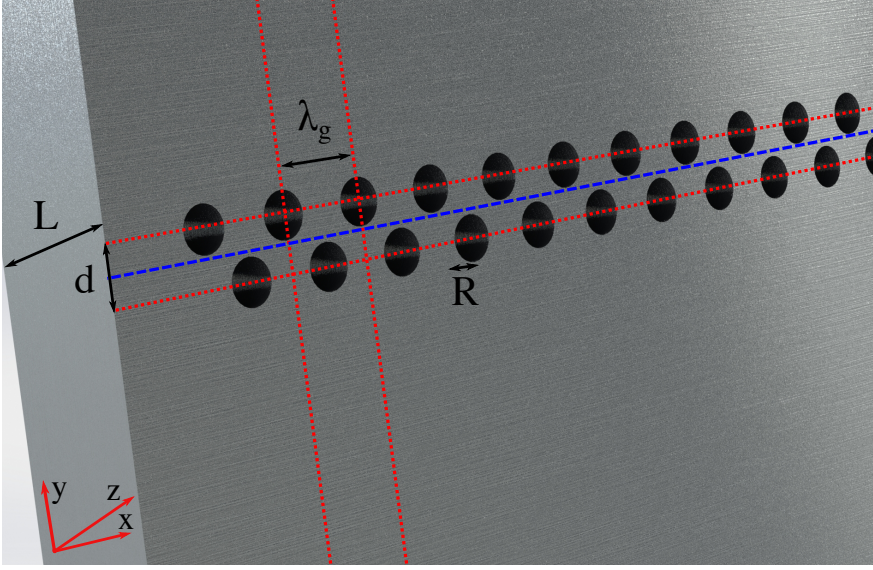


**Figure 6.21:** A 3D rendered image of the two glide-symmetric rows of holes sample in a $9.7 \pm 0.1$ mm thick aluminium alloy plate. Labelled is the spacing between the centre of the rows, $d$, pitch, $\lambda_{\mathrm{g}}$, radius of the holes, $R$, and thickness, $L$.

The sample pictured in figure 6.21 is similar to the symmetric sample but one of the rows has been translated by $3.0 \pm 0.1$ mm in the $x$ direction. This system has the glide operator:

$$
G = \begin{cases} x \to x + \frac{\lambda_{\mathrm{g}}}{2} \\ y \to -y \\ z \to z \end{cases}
\tag{6.3}
$$

Here $\lambda_{\mathrm{g}}$ is the spacing between holes, the lattice period, in $x$ and $k_{\mathrm{g}}$ is the fixed wavevector component of the glide symmetric array, $k_{\mathrm{g}} = 2k_{\mathrm{BZ}} = 2\pi/\lambda_{\mathrm{g}}$. This type of symmetry has been well studied in electromagnetism[163].

The glide symmetry of the system means that there is no band-gap between the higher and lower frequency branches of the dispersion curve at the BZ boundary, unlike for the mirror symmetric rows of holes. At the BZ boundary there is only two allowed

degenerate excitable modes, with the expected phase maps shown in figure 6.22. The figure shows the two modes at the BZ boundary, which are independent of each other, but can exist at the same time.
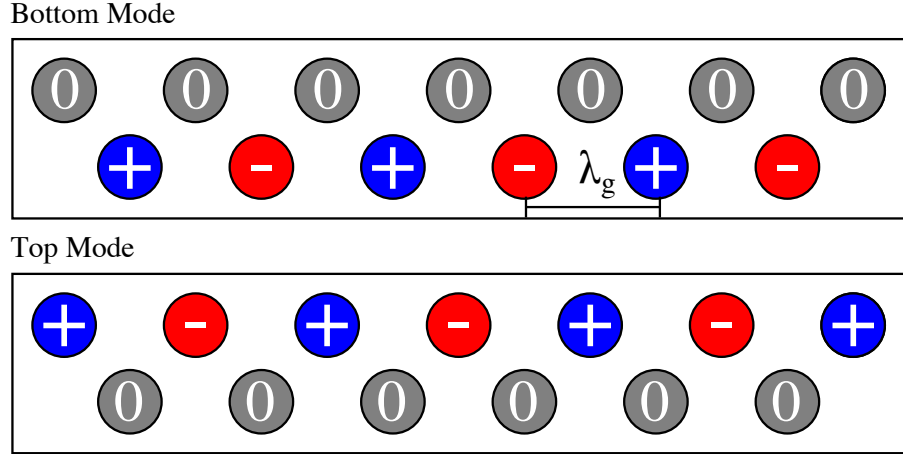
Bottom Mode



Top Mode



**Figure 6.22:** The excitable ASW modes of the two row glide symmetric sample made of coupled resonating holes and the two modes at the BZ. They are fully degenerate in energy. The colour represents the instantaneous phase of each hole. Here blue is positive phase $(+\pi/2)$ and red is negative phase $(-\pi/2)$.

### 6.7.1 Frequency Domain

Spatially scanned time averaged data is fast Fourier transformed in time to extract the frequency plots of the fields above the glide-symmetric sample. Instantaneous amplitude, absolute amplitude and phase plots of the fields are shown in figures 6.23, 6.24 and 6.25, respectively. Plotted in each are the components at 53.6, 55.0, 56.4 and 59.0 kHz. These frequencies are chosen to illustrate the essential mode behaviour. It is anticipated that there are two degenerate solutions at the BZ boundary depicted in figure 6.22.

In figures 6.23 and 6.24, at all frequencies depicted the field amplitude increases where the ASW is present. At 53.6, 55.0 and 56.4 kHz the field has the antisymmetric intensity distribution of the long wavelength excitation. At 59.0 kHz this is seen along with the symmetric short wavelength intensity distribution of the higher frequency mode. The absolute pressure plots in figure 6.24 shows that the field of the antisymmetric mode propagates further than the mode at 59.0 kHz. The 55.0 kHz field is modulated by the SSW-ASW interaction at $x \approx 60$ mm.
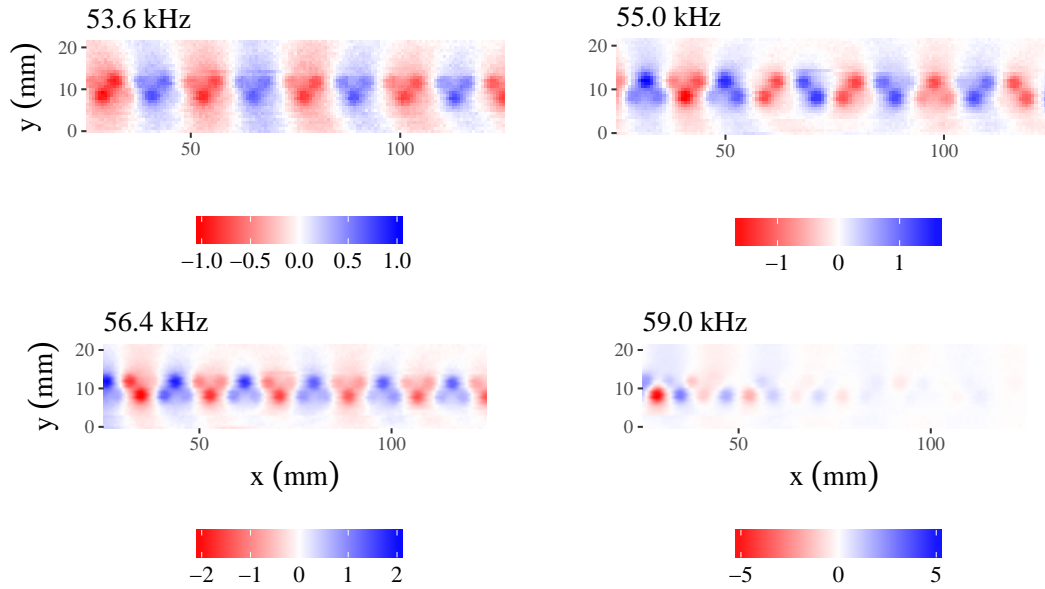
**Figure 6.23:** The experimental instantaneous signal of the fields above the two row glide-symmetric sample at 53.6, 55.0, 56.4 and 59.0 kHz.
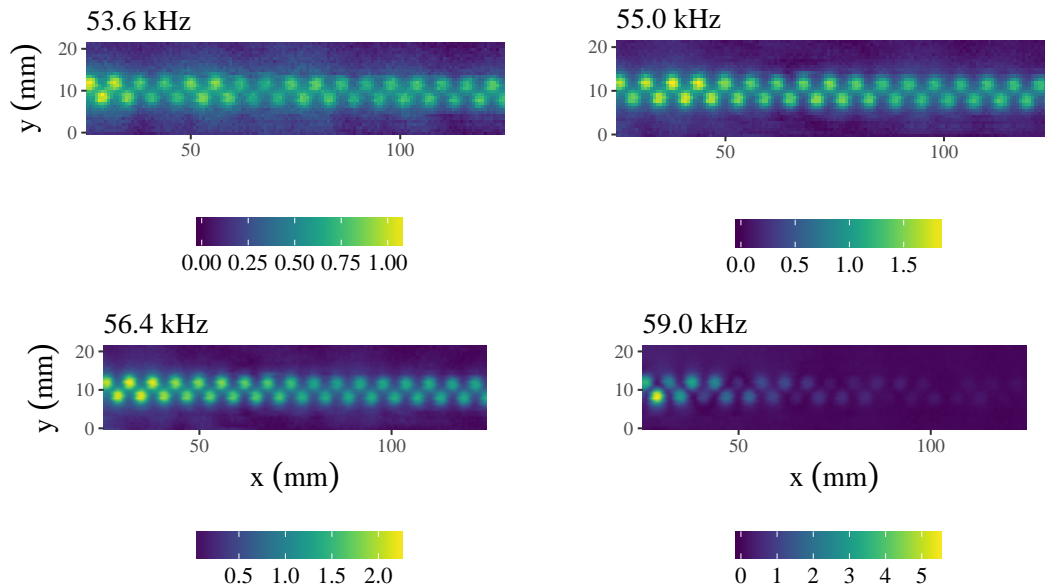


**Figure 6.24:** The experimental absolute amplitude of the fields above the two row glide symmetric sample at 53.6, 55.0, 56.4 and 59.0 kHz.

In figure 6.25, there is a "zig-zag" pattern of the mode of the field at 59.0 kHz as the mode appears to propagate along the array as if reflecting from the edges of a waveguide.
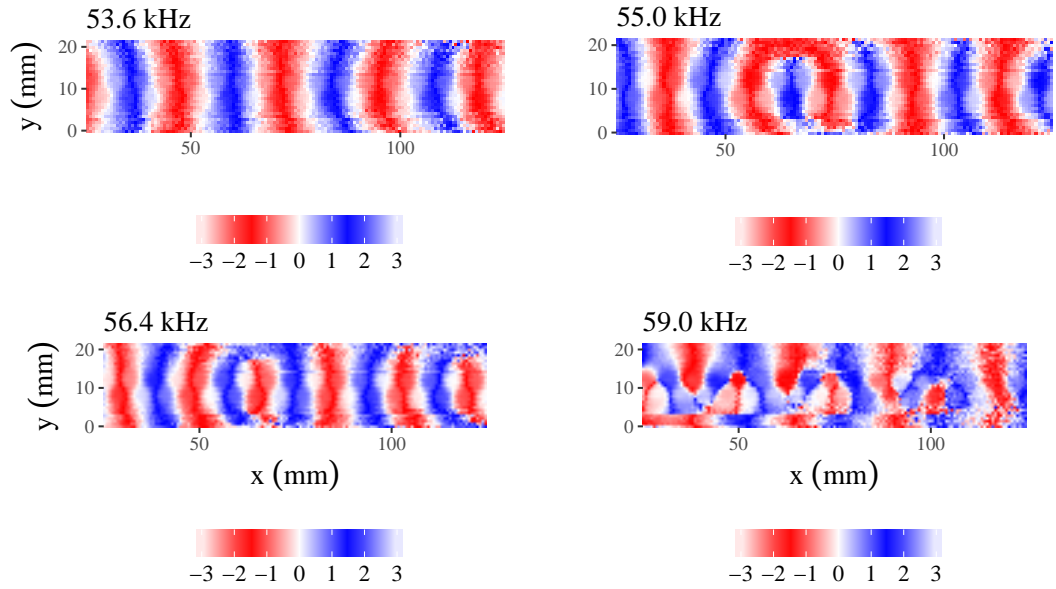


**Figure 6.25:** The experimental phase above the two row glide symmetric sample at 53.6, 55.0, 56.4 and 59.0 kHz. The phase is plotted between $-\pi/2$ as red and $+\pi/2$ as blue.

### 6.7.2 Wavevector Components

Fourier transforming frequency dependent spatial data in $x$ and $y$ produces the wavevector component plots of the detected fields above the glide symmetric sample, shown in figure 6.26.
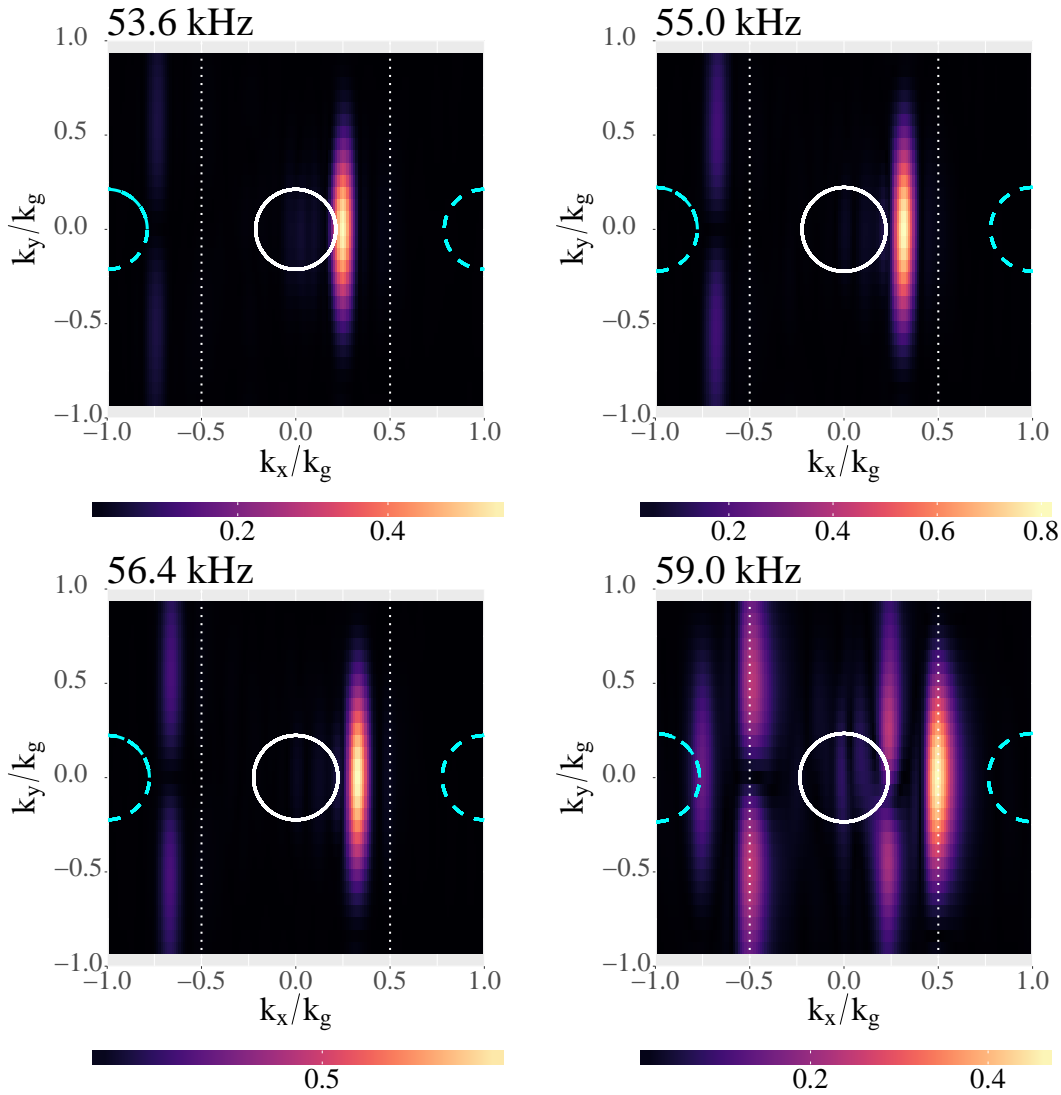


**Figure 6.26:** The wavevector components of the fields over the two row glide-symmetric sample plotted as Fourier magnitude in reciprocal space at 53.6, 55.0, 56.4 and 59.0 kHz. The solid white ring represents the sound line at each frequency and the blue dashed lines are the diffracted sound lines. The Brillouin zone boundaries are marked by the dotted white lines.

Figure 6.26 shows the fundamental mode at 53.6, 55.0 and 56.4 kHz in the forward propagating direction. The diffracted fundamental has negligible amplitude at $k_y = 0$. This shows that the coupling between the forward-propagating ASW. This is also seen

in the higher frequency mode at 59.0 kHz, where there is negligible amplitude of the mode in the forward propagating direction at $k_y = 0$.

### 6.7.3 Dispersion

Comparing the dispersion in $k_x$ at both $k_y = 0$ and $k_y = \frac{k_g}{2}$, as shown in figures 6.27 and 6.28, the higher frequency mode is not excited at $k_y = 0$ but is present at $k_y = \frac{k_g}{2}$.
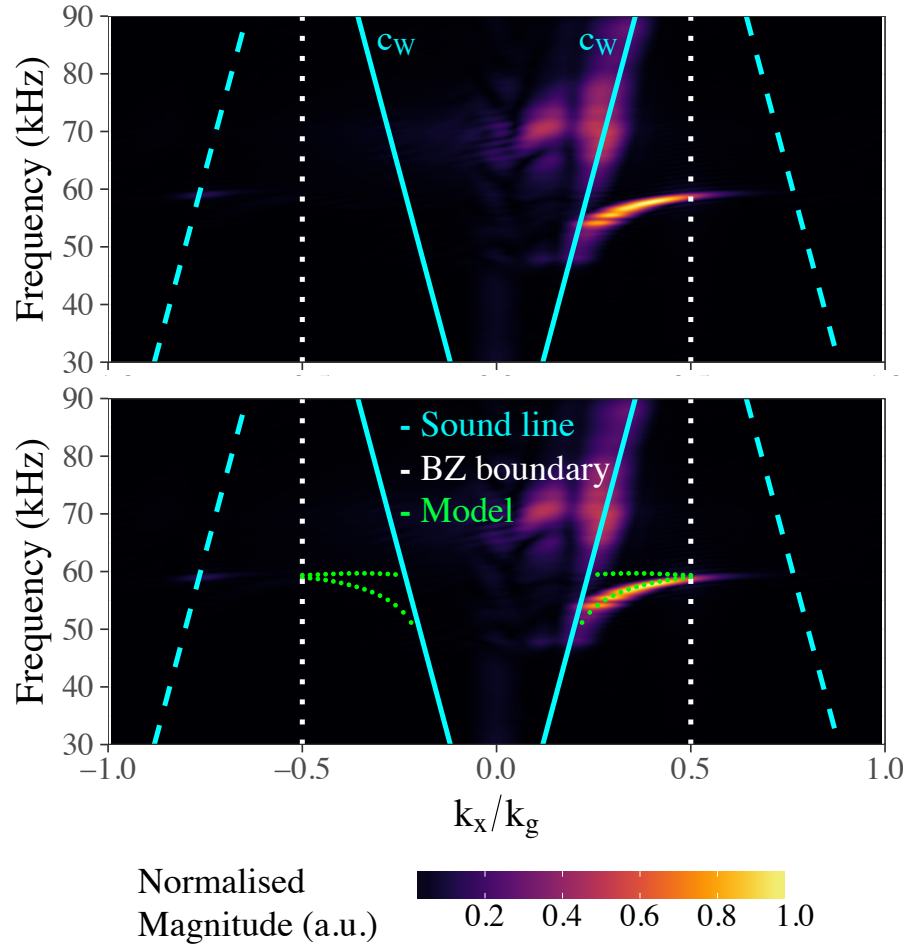


**Figure 6.27:** The experimental dispersion at $k_y = 0$ plotted between $-k_g$ and $+k_g$ with the model in the bottom plot and without the model in the top plot. The full elastic-pressure acoustic Comsol model is plotted as green dots between $-k_g/2$ and $+k_g/2$.

Because there is no mode gap at the BZ, here the group velocity no longer becomes zero and the wave propagates further over the sample at higher $k_x$. This high wavevector overlap region has a low group velocity, making this a method of supporting "slow" surface waves. Unlike in the mirror symmetric case, the diffracted modes are negligible, but not zero amplitude, at $k_y = 0$. This is due to the change in symmetry of the sample.
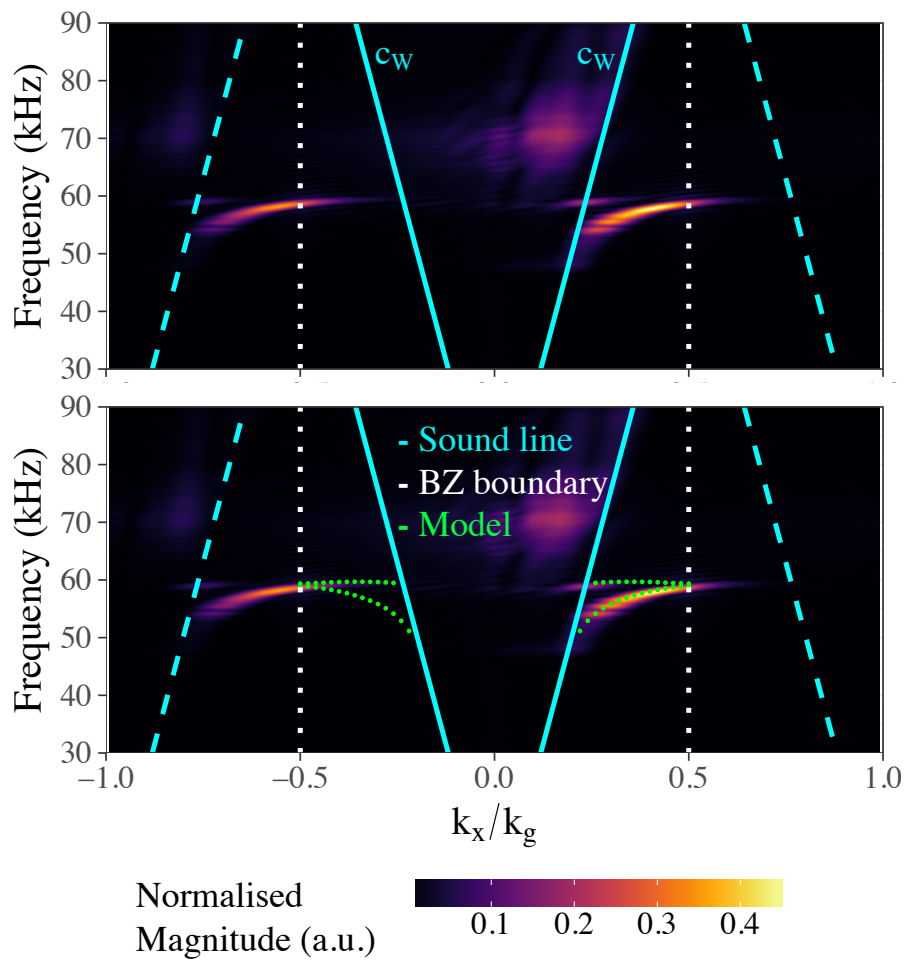
**Figure 6.28:** The experimental dispersion at $k_y = \frac{k_g}{2} = 512\text{m}^{-1}$ plotted between $-k_g$ and $+k_g$ with the model in the bottom plot and without the model in the top plot. The full elastic-acoustic Comsol model is plotted as green dots between $-\frac{k_g}{2}$ and $+\frac{k_g}{2}$.

## 6.8 Three Pseudo-glide Symmetric Rows of Holes

The final sample investigated in this chapter is the Pseudo-Glide Symmetric (PGS) sample composed of three rows of holes drilled in a $9.7 \pm 0.1$ mm thick aluminium alloy plate in an array depicted in figure 6.29. This has space between the centre points of the rows $d = 3.50 \pm 0.01$ mm, $\lambda_g = 6.00 \pm 0.01$ mm and $R = 1.5 \pm 0.01$ mm. This array is not glide symmetric, but it does share similarities in the geometry of neighbouring rows to the previous glide symmetric sample.
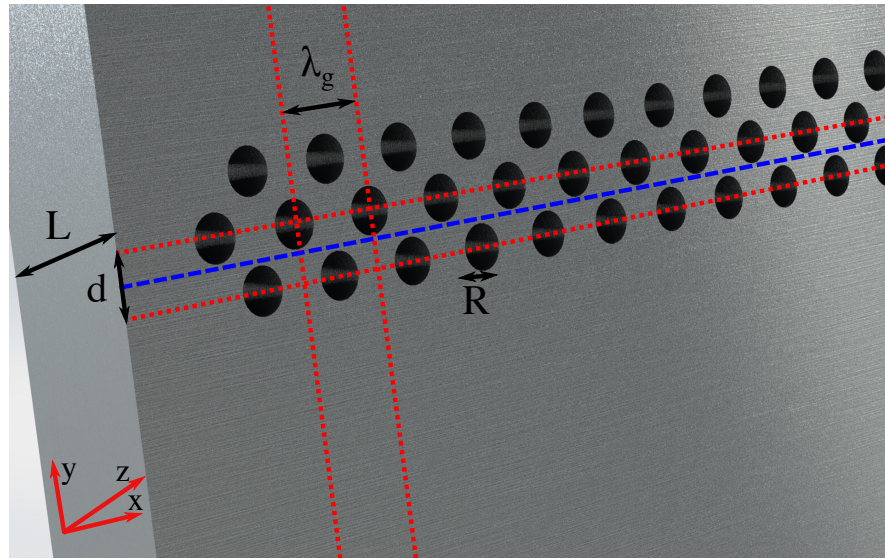


**Figure 6.29:** A 3D rendered image of the sample with three PGS rows of holes. Labelled is the pitch, $\lambda_\mathrm{g}$, radius of the holes, $R$, thickness, $L$, and the spacing between the centre of the rows, $d$.

This system is expected to support three different fundamental ASWs that are represented at the BZ in figure 6.30. These modes are labelled the inner and outer symmetric and the outer antisymmetric modes after their associated phase symmetry. As the figure shows, there is a null at the centre of the first two modes. This means that to excite either of these modes the point-source should be positioned over one of the holes at the edge of the array. The inner and outer symmetric modes occur at the same frequency: they are degenerate since the coupling between the outer rows is negligible.

Outer Antisymmetric Mode



Outer Symmetric Mode

Inner Symmetric Mode
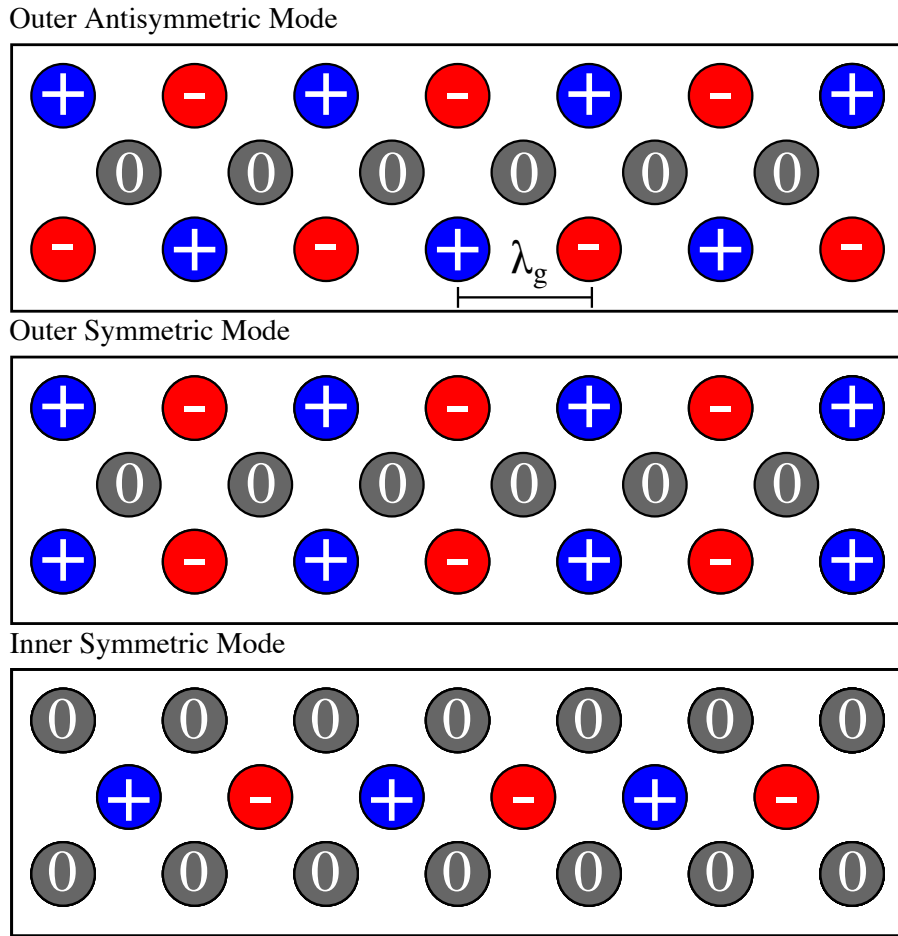
**Figure 6.30:** The three excitable ASW mode of three glide translated lines of coupled resonating holes and the allowed glide-symmetric mode, outlined in red. The colour represents the phase of each hole. Here blue is positive phase $(\pi/2)$, red is negative phase $(-\pi/2)$ and grey is a null.

### 6.8.1 Frequency Domain

Instantaneous and absolute amplitude plots, figures 6.31 and 6.32, show the ASW fields excited above the sample. The lowest order frequency at 53.6 kHz shows the symmetry of lowest order ASW. At 55.0 and 56.4 kHz the fields "zig-zag", also seen in figure 6.33, as the wave propagates as if confined to a waveguide reflecting from the edges of the array. This is similar to the low-to-high impedance acoustic reflections seen in 2D phononic devices[164]. At 59.0 kHz the field begins to weaken and becomes localised near the point of excitation.
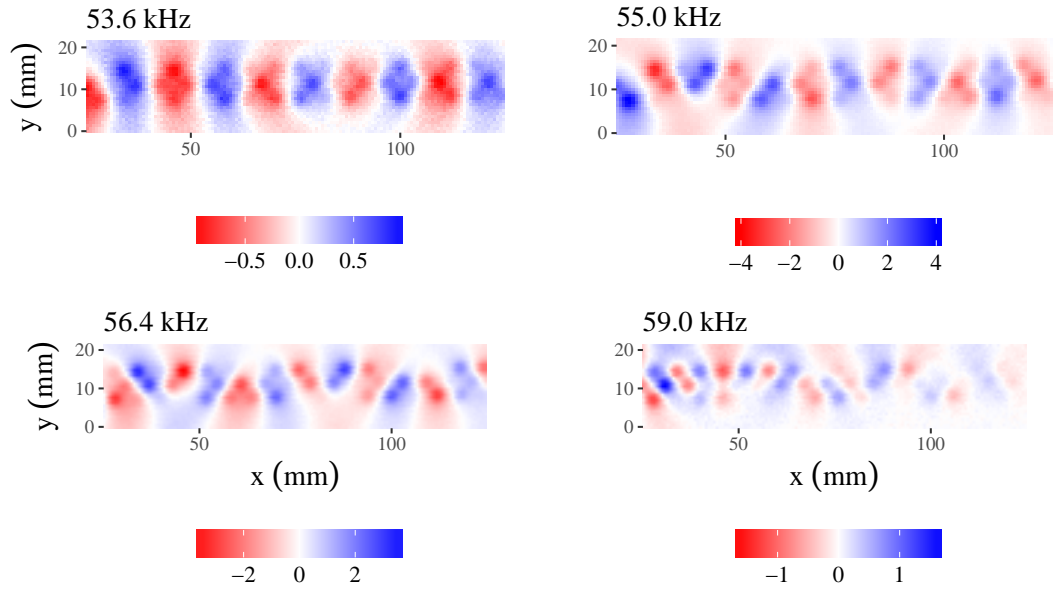
**Figure 6.31:** The experimental instantaneous amplitude of the fields above the three row PGS sample at 53.6, 55.0, 56.4 and 59.0 kHz.
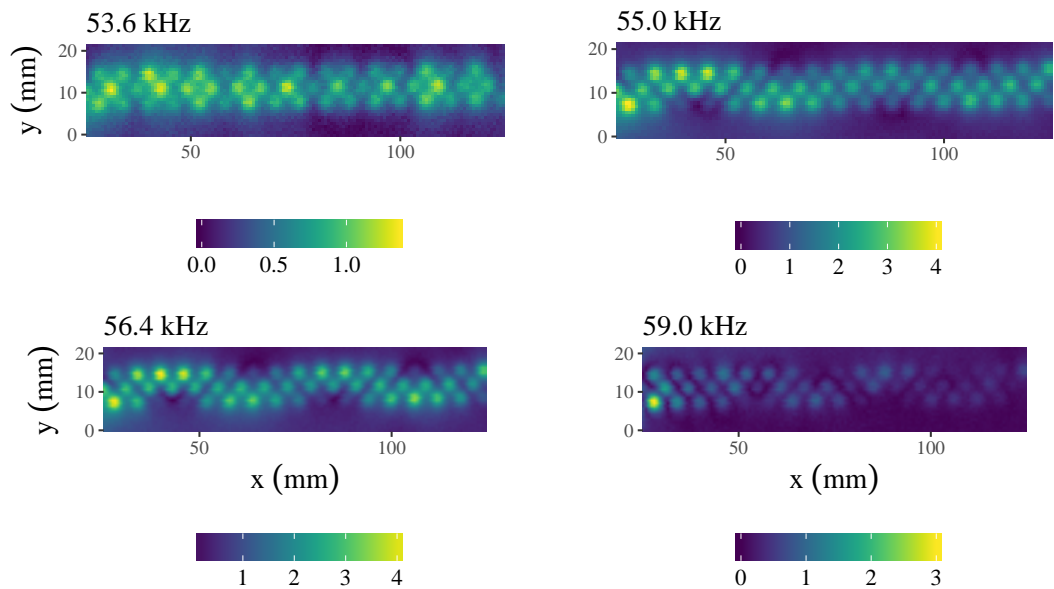


**Figure 6.32:** The experimental absolute amplitude of the fields above the three row PGS sample at 53.6, 55.0, 56.4 and 59.0 kHz.
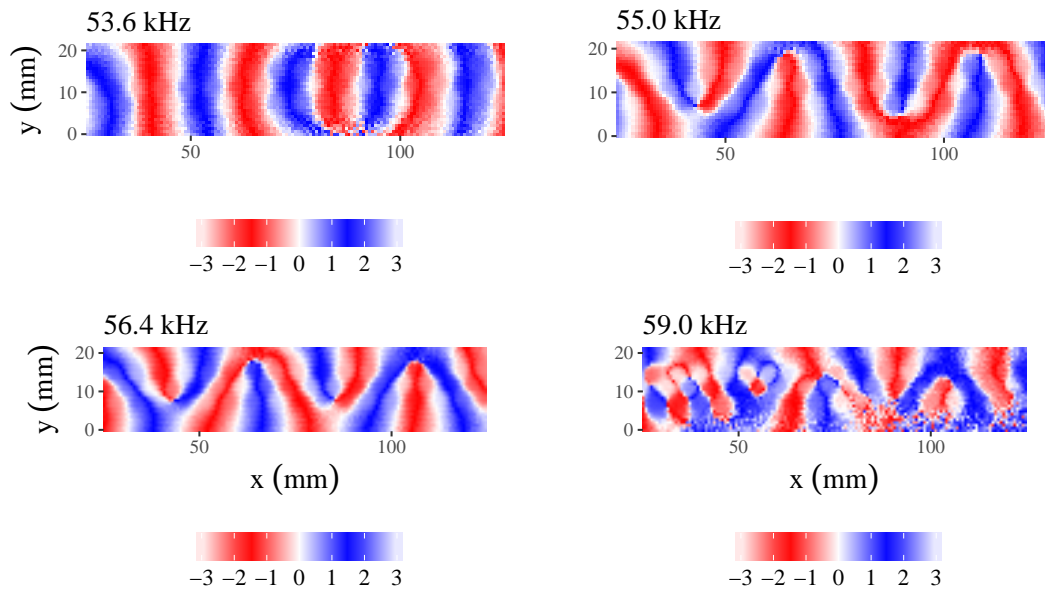
**Figure 6.33:** The experimental phase of the fields above the three row PGS sample at 53.6, 55.0, 56.4 and 59.0 kHz. The phase is plotted between $-\pi$ and $+\pi$, where red is negative and blue is positive.

### 6.8.2 Wavevector Components

Wavevector plots of the three row PGS array are shown in figure 6.34. The outer and inner symmetric modes are visible at 53.6, 55.0 and 56.4 kHz. At the higher frequency of 56.4 kHz, the outer antisymmetric mode is apparent. At the even higher frequency of 59.0 kHz, the modes become blurred and it becomes difficult to identify the highest frequency mode.
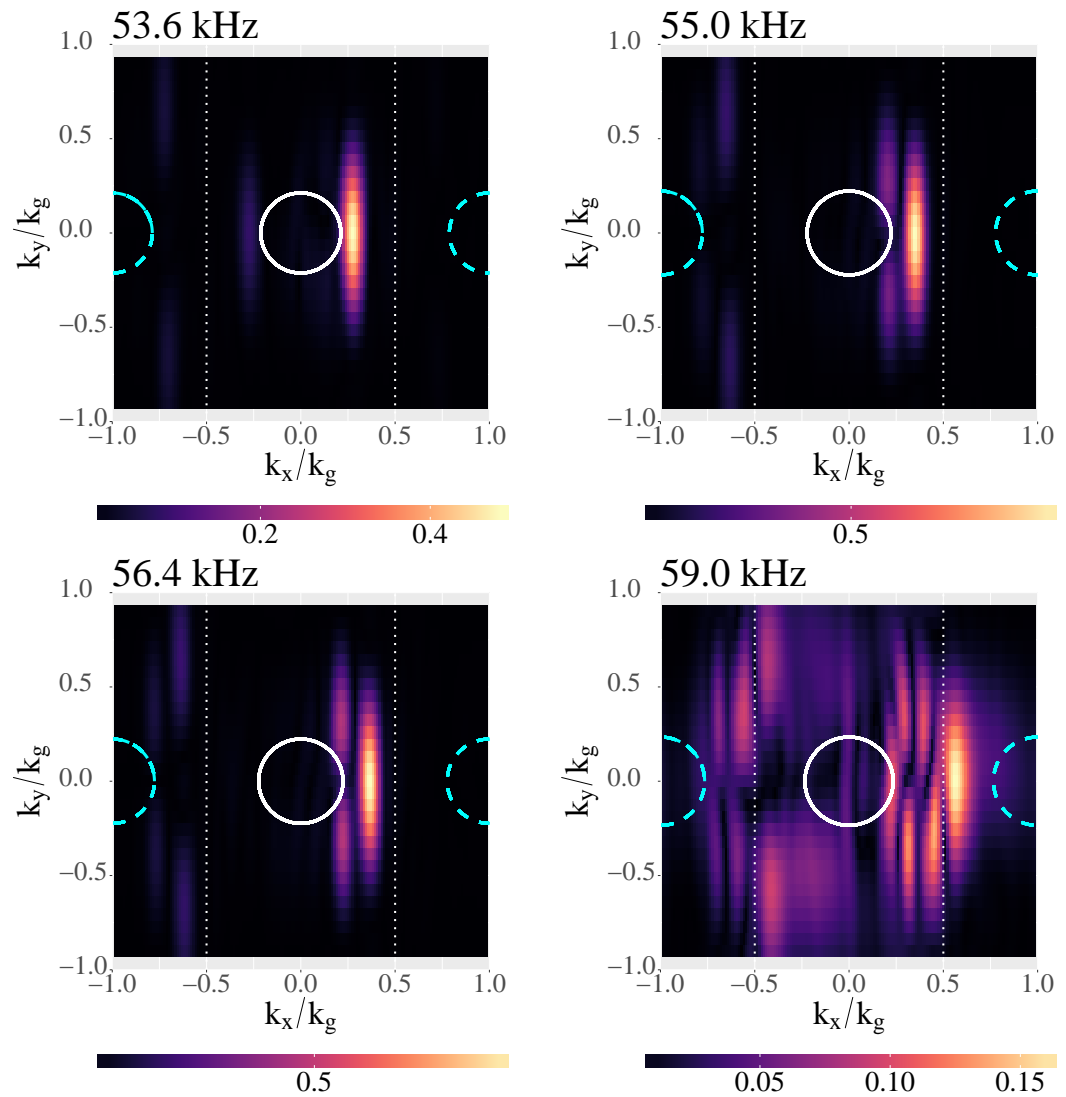


**Figure 6.34:** The wavevector components of the fields over the three row PGS sample plotted as Fourier magnitude in reciprocal space at 53.6, 55.0, 56.4 and 59.0 kHz. The white circle represents the sound line and the blue dashes are the diffracted sound lines. The BZ boundaries are marked by the dotted white lines.

### 6.8.3 Dispersion

The dispersion at $k_y = 0$ and $k_y = \frac{k_g}{2}$ is shown in figures 6.35 and 6.36. Again, the antisymmetric mode is not excited at $k_y = 0$. This time, just like the two row glide-symmetric sample, there are no diffracted orders excited at $k_y = 0 \text{ m}^{-1}$. But now there is expected be three modes dispersion at $k_y = \frac{k_g}{2}$. Again, the dispersion extend up to and through the BZ boundary as there is finite group velocity at the BZ boundary.
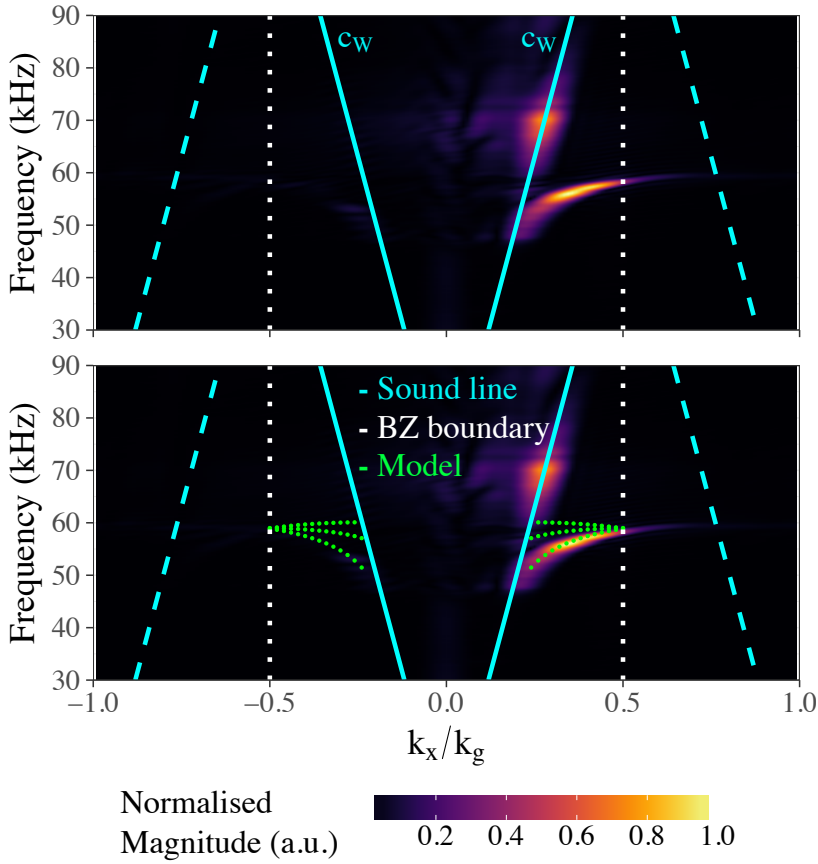


**Figure 6.35:** The experimental dispersion of the 3 PGS sample at $k_y = 0$ plotted between $-k_g$ and $+k_g$ with the model in the bottom plot and without the model in the top plot. The full elastic-acoustic Comsol model is plotted as green dots between $-\frac{k_g}{2}$ and $+\frac{k_g}{2}$. The backwards-propagating diffracted orders are present between $k_x < -k_g/2$ and the forward-propagating waves are represented as $0 < k_x < \frac{k_g}{2}$.

The cross section at $k_y = \frac{k_g}{2}$ shows only two distinct modes in the forward propagating direction. Looking at the diffracted (negative) side of the plots, all modes that appear in the positive $k_x$ appear on the left hand side of the plots. Although the model predicts three modes, the results only show two. This is because there is essentially only nearest neighbour coupling, so the "inner" and "outer" modes are degenerate.
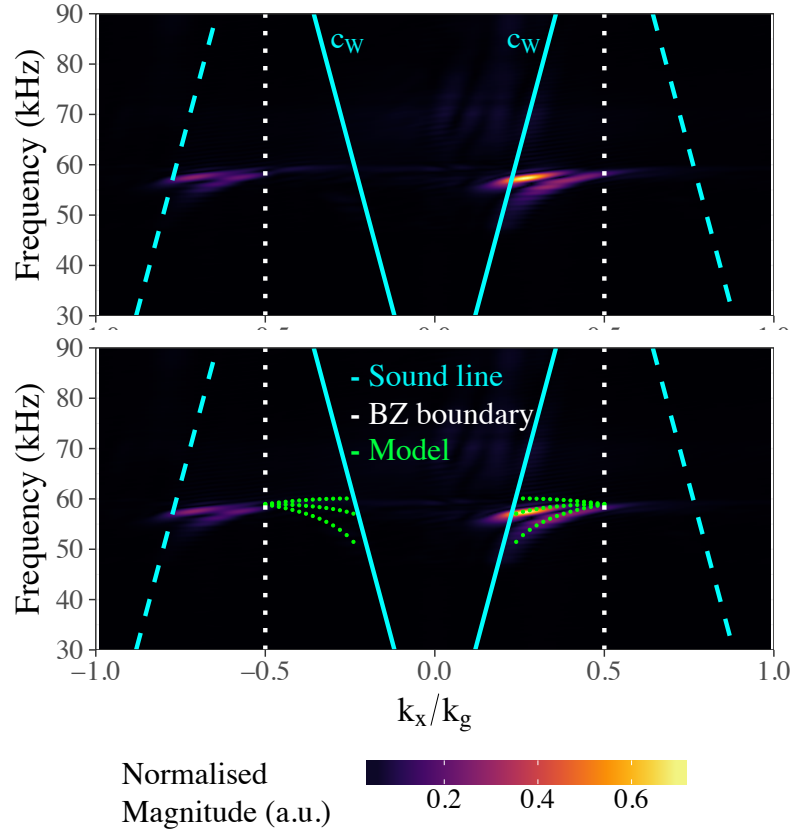
**Figure 6.36:** The experimental dispersion of the 3 PGS sample at $k_y = \frac{k_g}{2}$ plotted between $-k_g$ and $+k_g$ with the model in the bottom plot and without the model in the top plot. The full elastic-acoustic comsol model is plotted as green dots.

## 6.9 Conclusions

This chapter presented original results on the ASWs supported by rows of holes in aluminium alloy underwater. Through the visualisation of time, frequency and wavevector components of the fields, the different excited ASWs were characterised and dispersion relations mapped. Looking at the frequency domain, results were used to identify these modes propagating over narrow frequency ranges with little loss. Importantly data showed how it is possible to create degenerate ASW modes at the BZ boundary through the imposition of glide-symmetry. Interestingly for the three row pseudo-glide-symmetric sample, because of nearest neighbour coupling, only supports two modes that are degenerate. Additionally, it was shown that there is a significant 2.53 kHz difference between the asymptotic eigenfrequencies of a 1D array of holes in a perfectly rigid solid and the case of an elastic solid. Results also showed that there is modulation of the fields associated with the ASWs and the sound line bound SSWs. The next chapter will explore two-dimensional ASWs.

# 6. Underwater Acoustic Surface Waves on Straight Parallel Lines of Regularly Spaced Holes

# Chapter 7

# Underwater Acoustic Surface Waves on Two-dimensional Arrays of Holes

## 7.1 Introduction

Surface waves occur at the boundary between two differing elastic materials. There are several different classifications of surface wave phenomena in acoustics[34,16,17,165], as discussed in chapter 2. In addition, periodically structured surfaces that support non-radiative surface waves are well documented in many photonic, phononic and air-borne phononic systems[45,46,47,48]. These non-radiative waves, here Acoustic Surface Waves (ASWs), are highly localised, evanescently decaying in a direction normal to the surface on which they are supported. They are found on surfaces patterned with near-wavelength sized cavities integrated into a solid material. Unlike Rayleigh and Lamb bulk waves which propagate through a material, ASWs do not penetrate far into the material to which they are bound. Surfaces between solids and fluids support ASWs that are excited in the same frequency regime as Scholte-Stoneley Waves (SSWs). These propagate along the interface between two elastic media and may overlap, and thus interfere with ASWs.

Research into structures that support SSWs and ASWs are areas which have gained attention as these structures can be easily tailored to change their useable frequency ranges simply by changing their geometry. A highly localised and slow travelling ASW has potential applications in acoustic sensing, energy harvesting, signal processing and material characterisation. Most research into ASWs has been undertaken in air[51,52,53] with some studies underwater of two-dimensional structured materials that support

surface waves. These include grooves[54,55] and 2D arrays that have been modulated using material-filled arrays of holes[56].

This chapter details the quantification of the direction dependent dispersions of underwater ASWs bound to two different thickness 2D square arrays of water-filled holes in aluminium alloy plates. Results will be Fourier analysed two-dimensionally using scanned data to characterise ASWs and to show how they mix with SSWs. In addition, directional in-plane beaming at a particular frequencies is observed. A fully pressure-acoustic-elastic computational model of the systems is used to confirm and compare to the experimental results. There is good agreement between experimental and computationally calculated data for the full dispersion.

## 7.2 Experimental Method

Periodically structured arrays produce, by diffraction, localised ASWs that are non-radiative. A water-filled hole in a solid is a simple diffracting object and by patterning a solid plate with a periodic array of holes it possible to create a structure that supports ASWs. This chapter considers square arrays of open-ended holes with a radius of $R = 1.50 \pm 0.010$ mm and pitch of $\lambda_g = 5.50 \pm 0.01$ mm in finite thickness solid plates, as shown in figure 7.1.
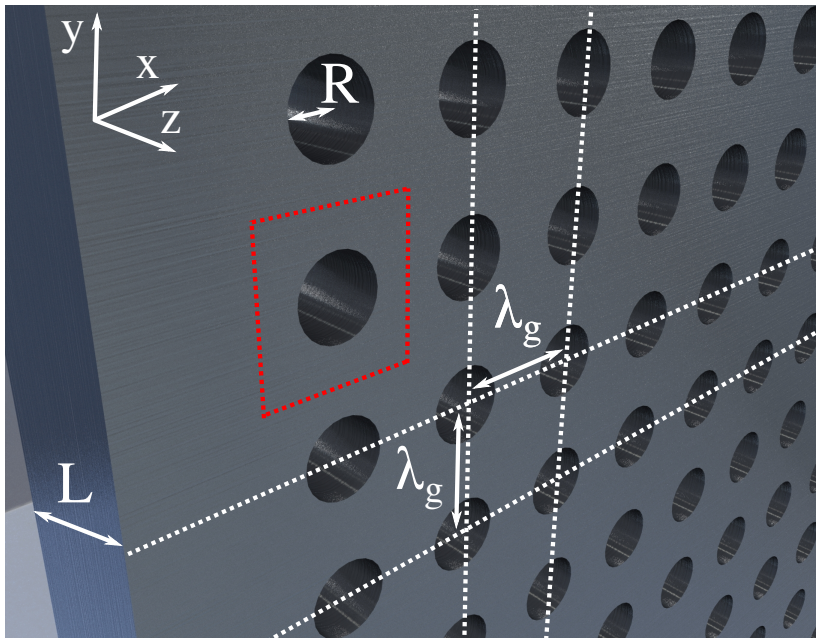


**Figure 7.1:** A 3D rendered image of the two-dimensional square array of holes examined in this chapter. The parameters shown are the radius of the holes, $R$, the pitch of the array, $\lambda_g$, and the plate thickness, $L$. A unit cell of the array is outlined by the red dotted box.

Two-dimensional square arrays of open-ended holes were drilled through both the $L = 6.4 \pm 0.1$ mm and $L = 9.9 \pm 0.1$ mm thick plates of aluminium alloy (5083). The plate is $400 \pm 1$ mm by $400 \pm 1$ mm in area and has 4900 holes, in a 70 by 70 square array. Scanning these arrays takes up to 36 hours.

Experiments are performed underwater with the aluminium alloy plate fixed in position. 8 ms wide approximately Hanning-windowed ultrasonic pulses (double-cycle) centred at 70 kHz are projected at the sample using a foam-wrapped D70 source with an exit diameter of $6.0 \pm 0.1$ mm. This narrow source is positioned directly over one of the holes and $\approx 3$ mm from the sample surface. Projecting at such close proximity to the sample with a small source excites locally, confining the mode, and gives the pulse high wave momentum in the plane of the surface. The excited fields are detected in the near-field using an $xyz$ spatial scanning stage mounted Precision Acoustics 1 mm needle hydrophone. The tip of the detector is positioned on the opposite side of the plate to the source, 0.5 mm from the face of the sample. This is well within the decay length, $\delta_P$, of the expected ASW fields ($\delta_P \approx 40$ mm[60]) . The usable frequency range of this source-detector arrangement is between 40 and 100 kHz. A render of the underwater setup is shown in figure 7.2.



**Figure 7.2:** A 3D rendered image of the square array submerged in the water tank. Acoustic pulses are projected from the foam-wrapped Neptune Sonar D70 hydrophone with a $d = 6.00 \pm 0.01$ mm diameter exit and detected by the Precision Acoustic $1.0 \pm 0.1$ mm diameter needle hydrophone, which is scanned spatially using an $xyz$ stage.

## 7.3 Computational Analysis

FEM Comsol modelling is used to run an eigenfrequency model for the arrays of holes, with the solid treated as elastic and 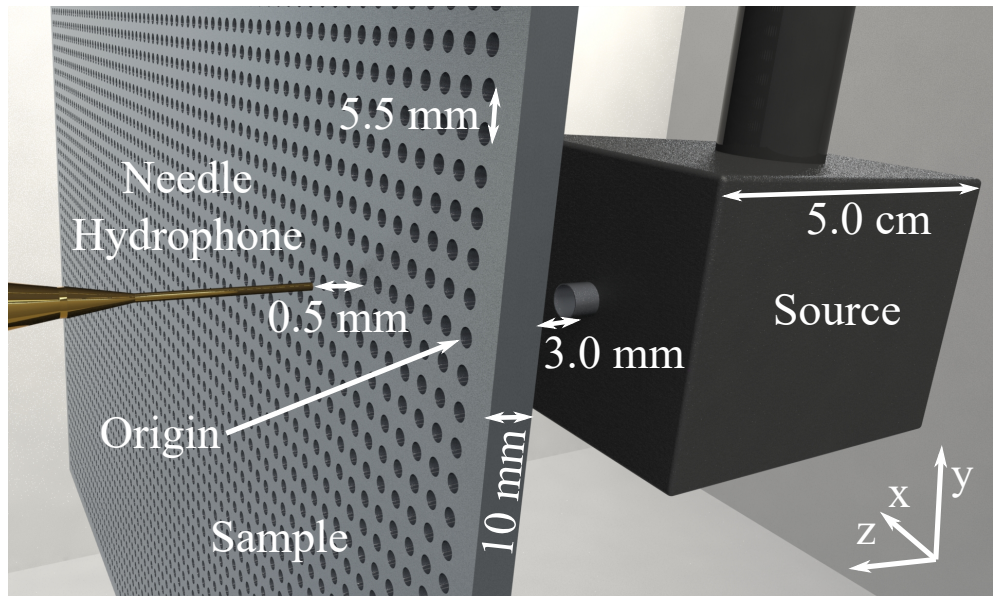water as viscous. The elastic and viscous acoustic parameters of each medium are listed in table 7.1[166,167]. These figures are the experimentally derived values for aluminium alloy from chapter 4 and estimates of the properties of water.

| Medium | $E$ (GPa) | $\rho$ (kgm$^{-3}$) | $\sigma$ | $\eta_\text{B}$ (Pa.s) | $\eta$ (Pa.s) | $c$ (m/s) |
|---|---|---|---|---|---|---|
| Water | - | 997 | - | 2.47 $\times 10^{-3}$ | 8.88 $\times 10^{-4}$ | 1512 |
| Aluminium alloy | 72 | 2660 | 0.34 | - | - | - |

**Table 7.1:** Elastic and viscous acoustic parameters for water and aluminium alloy 5083.

These models use a single hole unit cell and are bounded by Floquet periodicities in the $x$ and $y$ directions and by Perfectly Matched Layers (PMLs) in $z$. From this the eigenfrequencies of the system are derived, as detailed in section 3.8.

## 7.4 Results

This section details the results of experimental data, acquired by scanning the detector over a $106.05 \pm 0.01$ by $106.05 \pm 0.01$ mm area, $0.50 \pm 0.01$ mm from the surface of the sample in the $xy$ plane with signals being averaged at each point over 50 repeated pulses to improve the signal to noise ratio. The resolution of the scan is $\Delta x = 0.707 \pm 0.01-$ mm and $\Delta y = 0.707 \pm 0.010$ mm. The source is positioned at a hole at the edge of the sample, position $(0, 0)$ in the data, and results are thus attained for one of four symmetric quadrants in reciprocal space ($+k_x, +k_y$ only). This avoids high amplitude plate modes that are present when exciting the plate at the centre of the plate. For this, the Hanning-like window function is, used to soften the edges spatially, is removed as this would limit the amount of data along the $x$ and $y$ axes but the data is still zero padded to three times the data length.

### 7.4.1 6.4 mm Thick Two-dimensional Square Array

Unfiltered instantaneous voltage field maps of the wave travelling across the surface of the $6.4 \pm 0.1$ mm thick plate are presented in figure 7.3, shown as detected voltage, $V$, in space, $x$ and $y$.
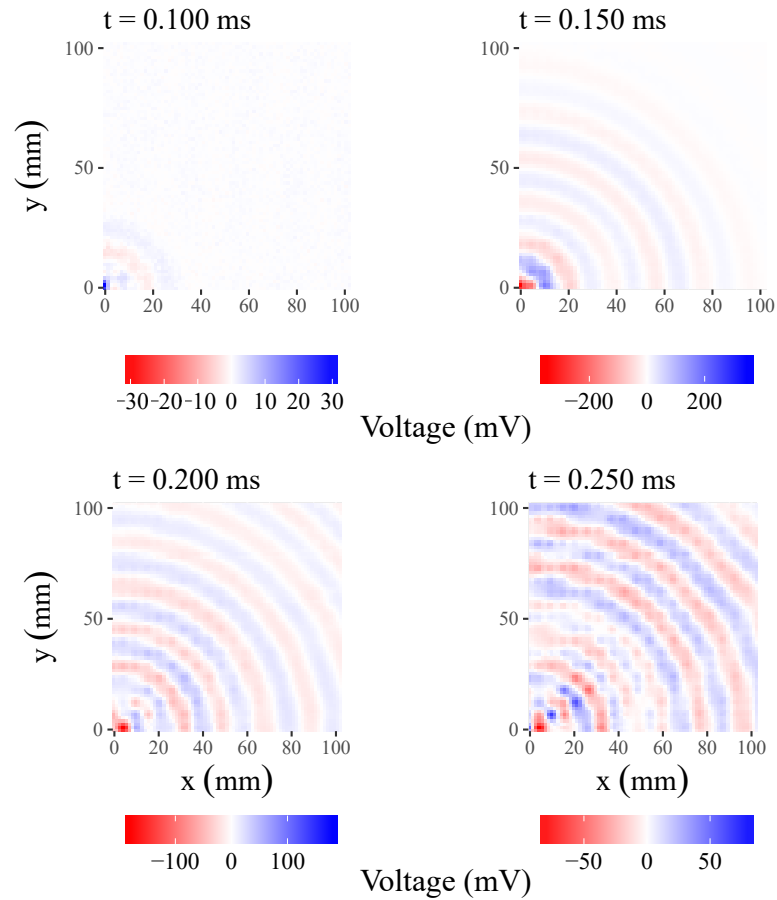
**Figure 7.3:** Instantaneous voltage above the 6.4 mm thick plate at three different points in time: 0.100, 0.150, 0.200 and 0.250 ms after the source first projects a signal. The scale shows the voltage in mV as red (positive) and blue (negative). The max voltage varies significantly as the driving signal positioned at the origin is included in the scan area.

Figure 7.3 shows the acoustic field propagating across the square array of holes, starting nearest the source at 0.100 ms after the pulse was sent until 0.250 ms. At 0.250 ms the results clearly show the holey structure of the plate diffracting as well as the freely propagating wave.

Fourier analysis of these results in time, $t$, reveals the individual frequency components in 2D. Three sets of frequency plots are depicted in figure 7.4 as Fourier amplitude, phase and absolute Fourier amplitude. At 82.4 kHz results show highly directional ASW power beaming at an angle of 45° from the $x$ and $y$ axes.
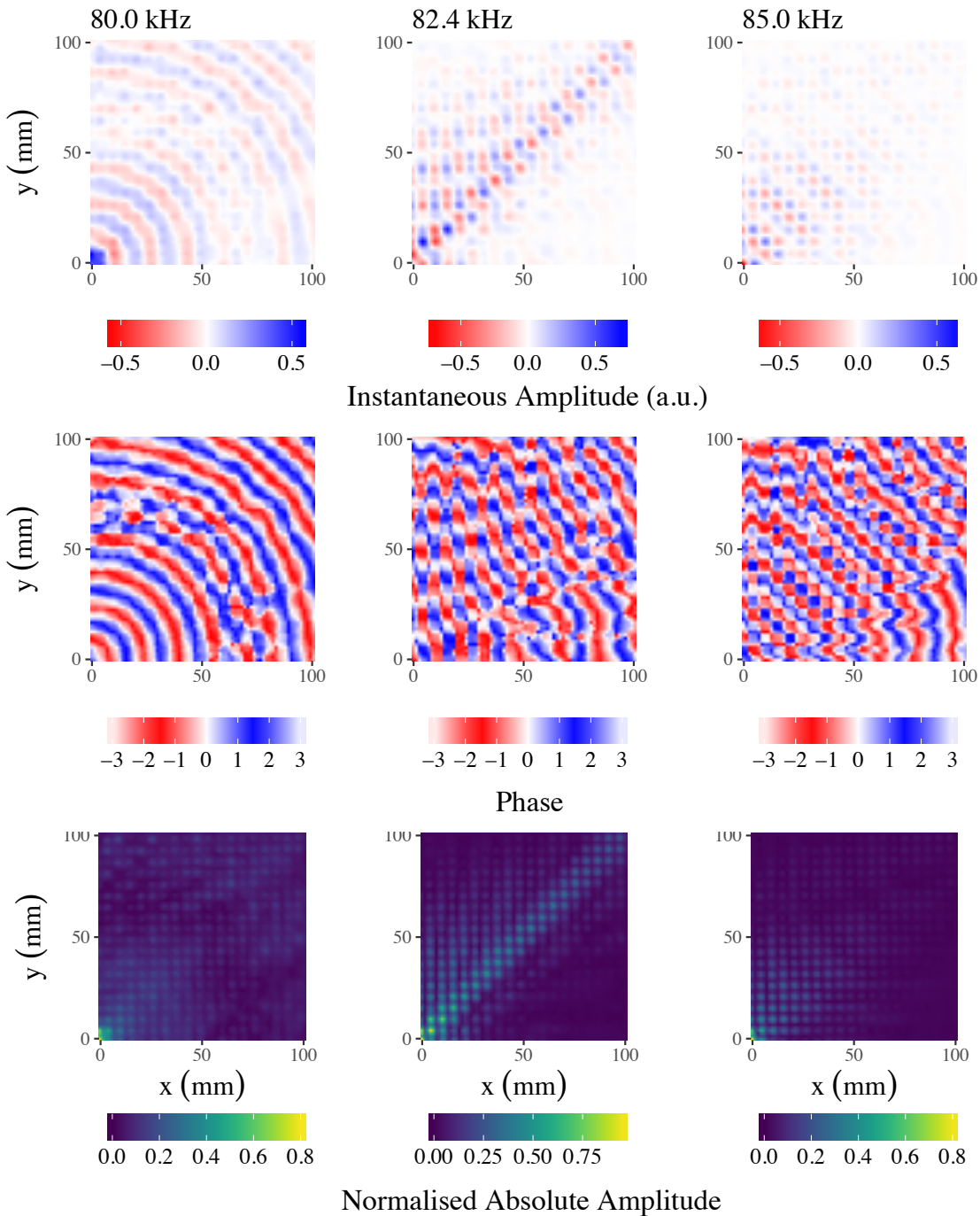
**Figure 7.4:** Three different frequency dependent 6.4 mm thick plate $xy$ spatial plots showing the instantaneous amplitude (top), phase (middle) and normalised absolute amplitude (bottom) of the excited field of the square array of holes at 80.0, 82.4 and 85.0 kHz. Acoustic beaming is clearly shown at 82.4 kHz at 45° off the $x$ axis.

Further, Fourier transforming the 2D frequency data spatially in $x$ and $y$ produces the frequency dependent wavevector components, $k_x$ and $k_y$. Figure 7.5 shows the

experimental k-space results for frequencies: 75.0, 80.0, 82.4 and 85.0 kHz. The overall trend shows that from 75.0 to 85.0 kHz the ASW disperses away from the sound line defined by $k_0 = 2\pi f/c$ (where the measured $c = 1512$ m/s) and changes shape as it approaches the Brillouin zone boundary, $|k_x|, |k_y| = \frac{k_g}{2}$. At 82.4 kHz the isofrequency contour has clearly flattened at the frequency that results showed beaming across the sample in the frequency domain in figure 7.4. A bound mode SSW is visible, close to the sound line, at 80.0 kHz in figure 7.5 along with the ASW.



**Figure 7.5:** Wavevector plots of the field propagating over the 6.4 mm thick square array of holes at four different frequencies: 75.0, 80.0, 82.4 and 85.0 kHz. These plots show directional components of the fields as the Fourier amplitude of the signal propagating in the $x$ and $y$ directions as $k_x$ and $k_y$ components. The sound line is represented as a white circle line with the diffracted sound lines as dashed circles.

# 7. Underwater Acoustic Surface Waves on Two-dimensional Arrays of Holes

### 7.4.1.1    Dispersion Relation
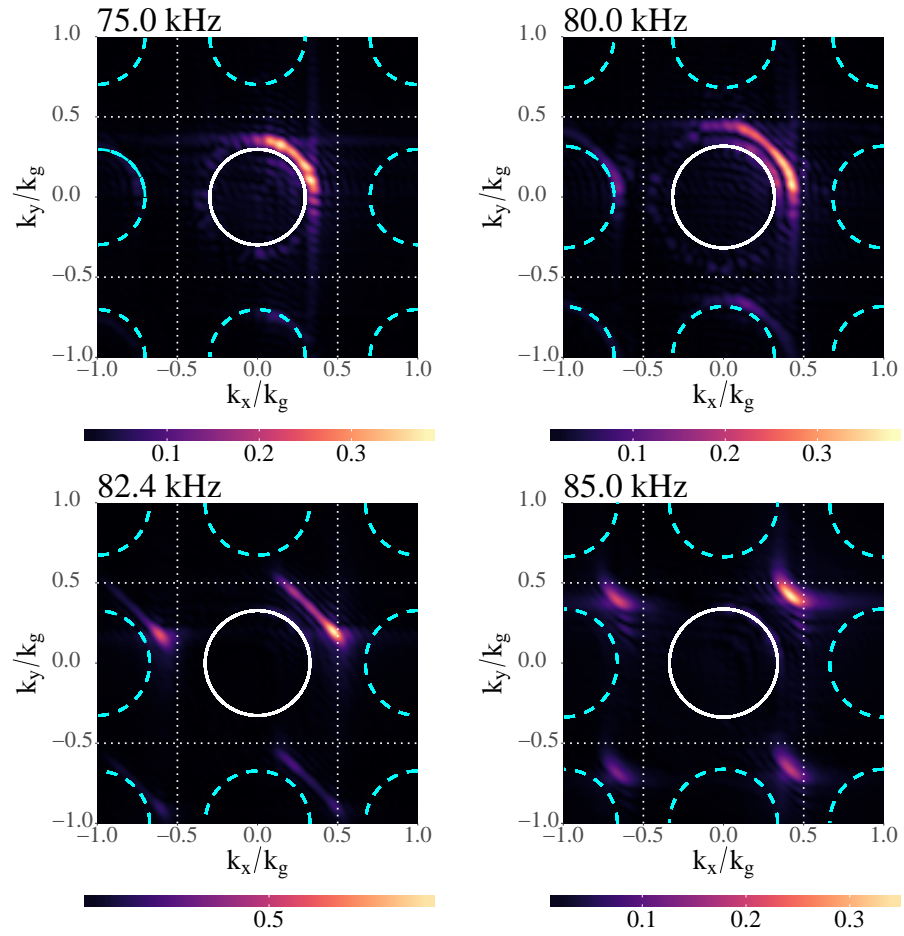
The modelled dispersion is plotted against experimental results in Figure 7.6. It shows data along lines of high symmetry $\Gamma$ to $X$, $M$ to $X$ and $M$ to $\Gamma$, at the zone boundary, indicated in the top right corner of figure 7.6. The computationally predicted ASW mode lies between 60 and 85 kHz, the $X$ point at $k_x = \frac{k_g}{2}$ and $k_y = 0$ is at 82.4 kHz and the $M$ point $k_x = \frac{k_g}{2}$ and $k_y = \frac{k_g}{2}$ is at 85.0 kHz. There is clear agreement between the experimental and the model data.
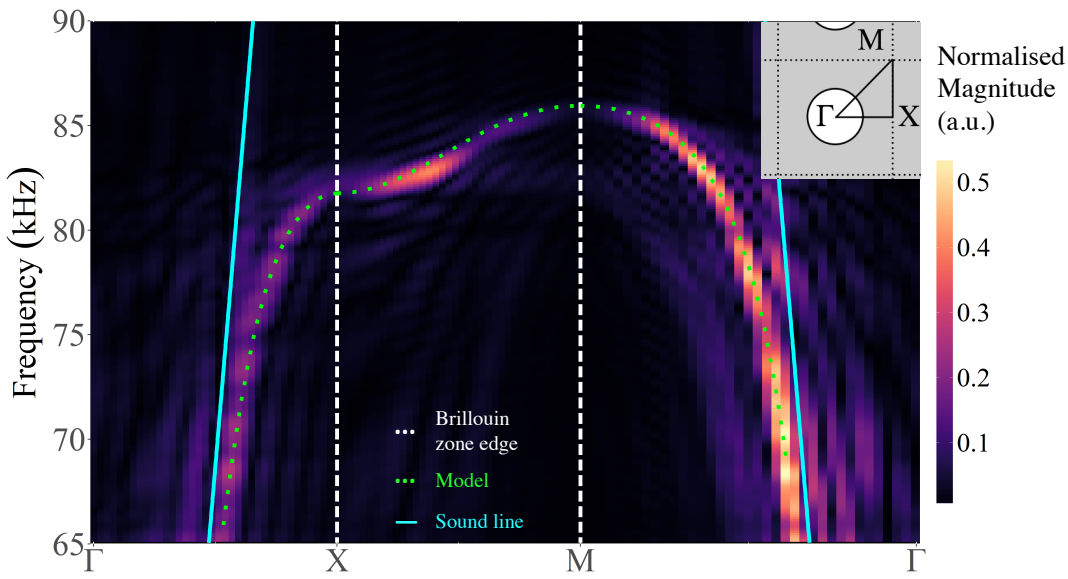


**Figure 7.6:**    The directional dispersion between along lines of high symmetry $\Gamma - X - M - \Gamma$ of the 6.4 mm thick square array of holes. $X$, $M$ and $\Gamma$ are defined by the shape of the array and the maximum wavevector of the grating, $\frac{k_g}{2}$. Modelled data (green dotted line) is the result of computationally calculated FEM modelling.

The enhanced amplitude of the signal between $X$ and $M$ is due to an interference effect between the ASW and reflected signal from the edge of the finite size sample, which can also be seen in the $x$ direction of Figure 7.5. Results also show evidence of a weak mode bound to the sound line in Figure 7.6 that is another source of interference.

### 7.4.1.2    Acoustic and Elastic Mode Shapes

To investigate the interaction between the elastic plate and the acoustic pressure field, the computationally calculated deformation of the plate is now investigated. Figure 7.7, shows the mode shapes at maximum pressure inside the holes of the array and the maximum deformation of the surrounding elastic solid at $X$ and $M$, enhanced by a factor of $10^9$ to visualise it. The maximum pressure in all plots falls at the centre of

the holes, which is characteristic of the fundamental mode within the hole.
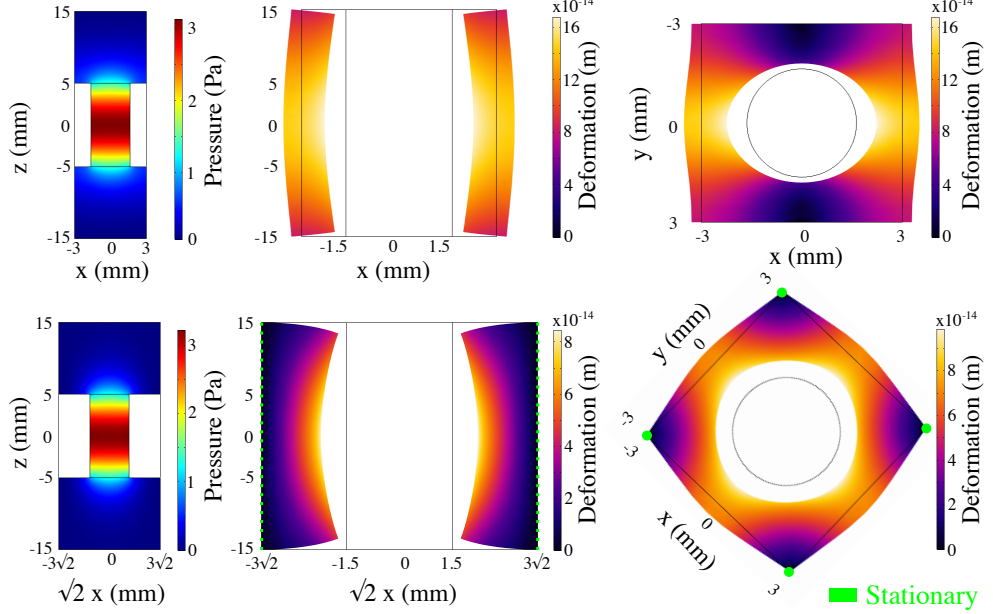


**Figure 7.7:** The computationally calculated mode shapes inside one unit cell of the square array. Shown are the surface acoustic pressure plots, left, and the elastic displacement plots, middle and right at $X$, top row, and $M$, bottom row. Graphically, the displacement has been enhanced by $\times 10^9$ to allow visualisation.

The asymptotic frequencies found for the dispersion of the elastic solid are $\approx 3$ kHz lower than predicted for the same geometry in a perfectly rigid solid. It was posited by Biot[168] that the speed of sound in the hole is slower in the case of the elastic plate, as plate deformation changes the effective compressibility $\beta$ of the fluid. As compressibility $\beta$ is related to the bulk modulus $B$ as $\beta = B^{-1}$ and as $c = \sqrt{\frac{B}{\rho}}$ where $\rho$ is the density then the speed of sound in the water inside the hole must decrease, reducing the asymptotic frequency of the ASW. A 3 kHz change in the frequency would equate to a $\approx 5\%$ change in the bulk modulus of water.

### 7.4.2    9.9 mm Thick Two-dimensional Square Array

To demonstrate the tuneability of these surfaces, to test the limits of ASW mode propagation and to verify the method, results will also be taken for a sample made of a $9.9 \pm 0.1$ mm thick aluminium alloy. The radius and pitch of the array remain the same at $R = 1.50 \pm 0.01$ mm and $\lambda_g = 6.00 \pm 0.01$ mm.

Figure 7.8 shows the voltage field maps of the acoustic pressure wave travelling across the $9.9 \pm 0.1$ mm thick array.
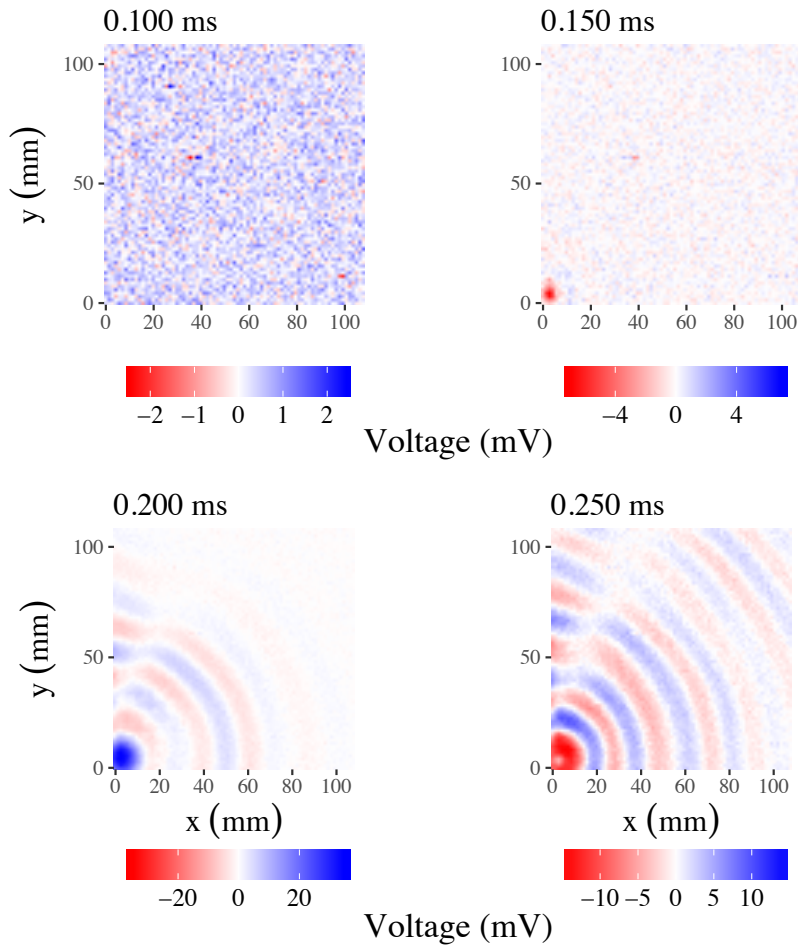
**Figure 7.8:** Instantaneous voltage above the 9.9 mm thick samples at four points in time: 0.100, 0.150, 0.200 and 0.250 ms after the source first projects the pulse. Voltage is shown as blue (positive) and red (negative).

Figure 7.8 shows the pressure field propagating across the square array of holes, starting nearest the source at 0.100 ms after the pulse has been sent until 0.250 ms. These times are the same as those presented in figure 7.3. This time there is a clear minimum due to an interaction with a reflection from the side of sample.

Again, Fourier analysis of the time domain data in time reveals the discrete frequency components of the 2D fields. Three sets of frequency plots above the 9.9 mm thick sample are depicted in figure 7.9. At 58.0 kHz there is directional ASW beaming at an angle of 45° from the $x$ and $y$ axes. Unlike the case of the 6.4 mm thick plate, this beaming is highly localised and is not visible more than 70 mm from the origin at 58.0 kHz.
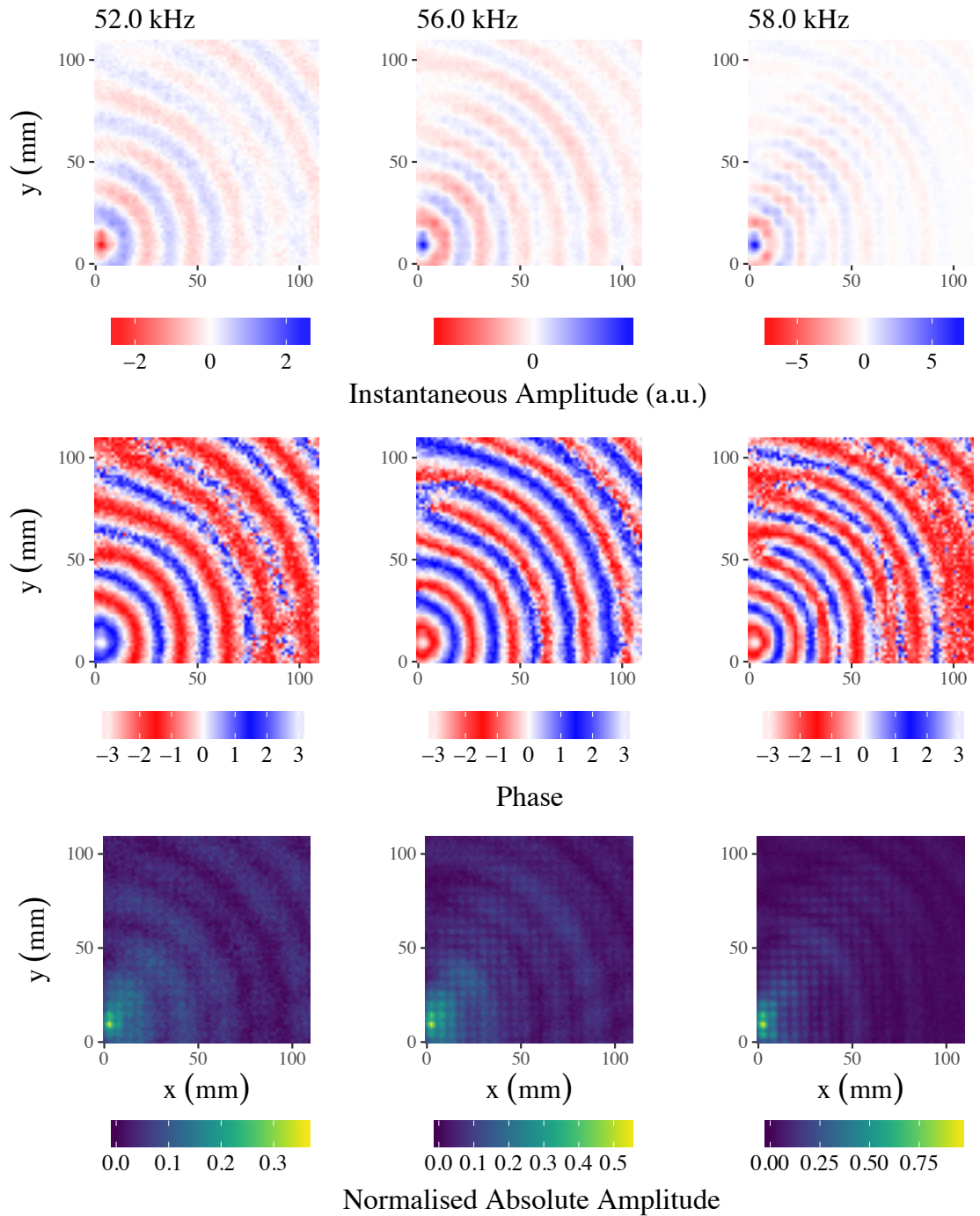
**Figure 7.9:** Three sets of frequency dependent $xy$ spatial plots showing the instantaneous amplitude (top), phase (middle) and normalised absolute amplitude (bottom) of the excited field of the square array of holes at 52.0, 56.0 and 58.0 kHz.

The 2D frequency data is spatially Fourier transformed to produces the wavevector components, $k_x$ and $k_y$. Figure 7.10 shows the experimental k-space results for four

different frequencies: 52.0, 54.0, 56.0 and 58.0 kHz. These results again show an ASW mode split away from the sound line which changes from circular as the frequency increases. However as it approaches the Brillouin zone boundary it now weakens significantly. Significantly now this thicker plate mode supports a comparatively strong mode at $k(x,y) = 0$, similar to that discussed in chapter 5, which was not seen in the 6.4 mm thick sample.
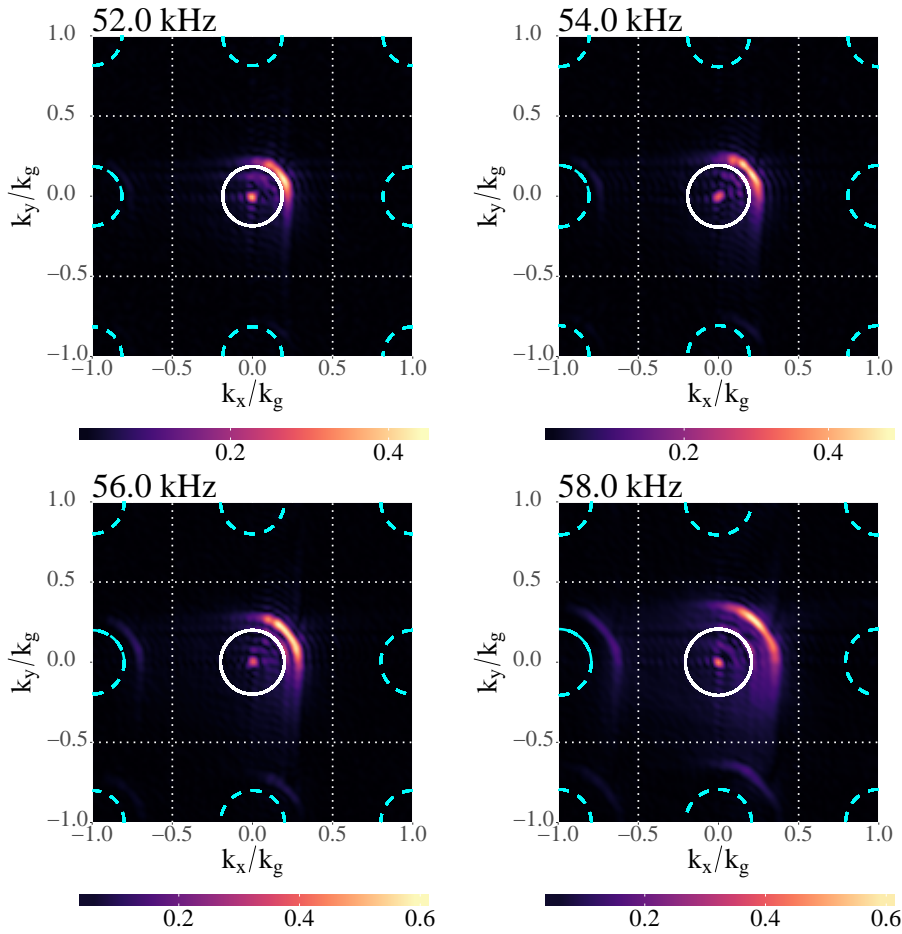


**Figure 7.10:** Wavevector plots of the field propagating over the square array of holes at four different frequencies: 52.0, 54.0, 56.0 and 58.0 kHz. The sound line is represented as a white circle, the diffracted sound lines as dashed circles and the Brillouin zone boundaries as white dotted lines.

### 7.4.2.1 Dispersion Relation

The resultant $\Gamma - X - M$ dispersion of the 9.9 mm thick plate is shown in figure 7.11. The computationally predicted ASW mode lies between 50 and 60 kHz. There is no data between $X - M$ which suggests that the majority of the coupling of this ASW

occurs between neighbouring pairs of holes in the $x$ and $y$ directions. By thickening the plate, the coupling in the diagonal direction has weakened. These results also show that the asymptotic frequency has changed, therefore demonstrating the tuneability.
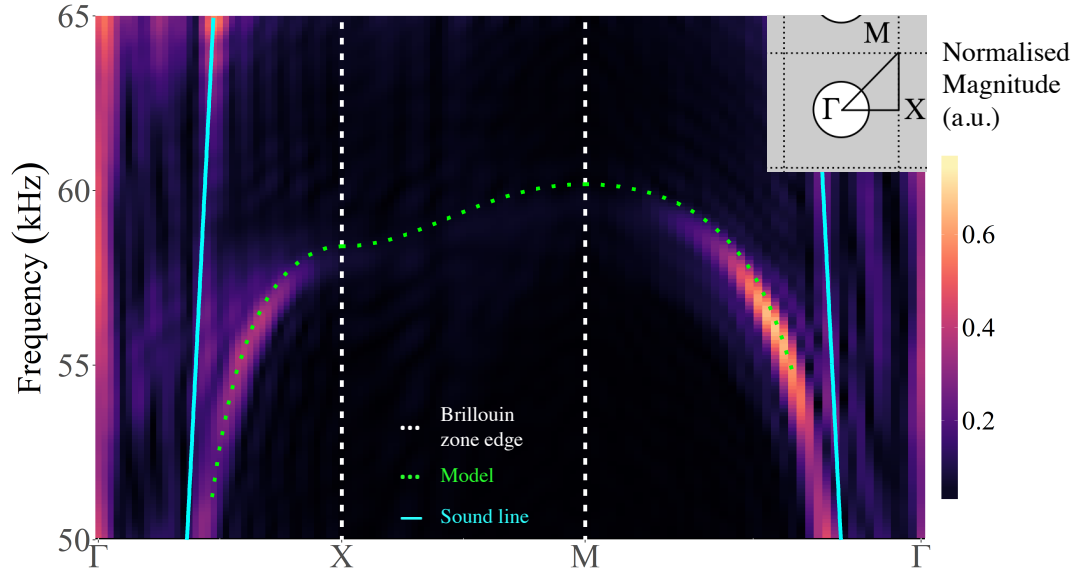


**Figure 7.11:** The directional dispersion over the 9.9 mm thick plate between the points of high symmetry $\Gamma - X - M - \Gamma$ of the square array of holes. Modelled data (green dotted line) is the result of computationally calculated FEM modelling.

## 7.5 Conclusions

This chapter presented results for the observation of underwater ultrasonic Acoustic Surface Waves (ASWs) supported by two square arrays of open-ended holes in a perforated aluminium plates of differing thickness. By Fourier analysing the fields temporally and spatially the ASWs were characterised and the dispersions plotted. Experimental data agree well with FEM modelled data of the structured elastic array, showing that the results depend significantly on the elastic properties of the material. These results also demonstrated that by varying the thickness the ASW modes are tuneable, whilst directional coupling strength varies. Moreover, ultrasonic beaming over a narrow band of frequencies has been observed. The ultrasound technique presented can be applied to any submerged flat 2D system and can be used to detect ASWs over any periodic array of diffracting structures, limited by the usable frequency range of the source-detector setup. By adding degrees of freedom or changing the geometry of the array, these surfaces can be readily adapted to support multiple ASW modes tuned to selected frequency ranges. Acoustic devices made up of similar 2D arrays could be used to harvest

directional energy surface waves using micromechanical systems (MEMS)[134], improve acoustic propagation for communications or direct unwanted sound away from an area (using acoustic waveguide-like effects[135,169] similar to that shown for SAWs to send and receive sound). The next chapter will investigate the acoustic response of structured pressure-release materials.

# Chapter 8

# Ultrasonic Observation of the Cut-off Frequency of Holes in a Pressure-release Material

## 8.1 Introduction

As mentioned in chapter 2, there are two types of idealised boundary conditions in acoustics: pressure-release and rigid boundaries. Rayleigh appears to have been the first to define the pressure-release boundary in 1885[34] as:

$$p_{\mathrm{a}} = 0. \tag{8.1}$$

Morse expanded on this, exploring the geometry of pipes[35]. But it was not until half a century later that the first extensive experimental work on fluid filled cylindrical waveguides with pressure-release boundaries was published by William J. Jacobi[170]. Jacobi explored theoretically and experimentally the dispersion of sound travelling through cylindrical waveguides and plotted the dispersion of a sound wave travelling through both a rigid and pressure-release cylindrical waveguide by probing pressure-release tubes with a needle hydrophone. Since then, there have been a variety of different studies exploring the dispersion of sound waves within acoustic waveguides with different boundaries[36,37,39,40]. A number of studies have published data on lined ducts and cylinders, effectively showing pressure-release conditions of a cylindrical waveguide[38]. More recently, Baik, Leighton and Jiang published an extensive review of the topic, discussing group velocities, attenuation and phase of sound waves travelling in liquid filled pipes[171,172,173]. Yet none of these studies have demonstrated that the acoustic cut-off exists in the radiative regime.

## 8. Ultrasonic Observation of the Cut-off Frequency of Holes in a Pressure-release Material

In this chapter the underwater ultrasonic response of a cylindrical waveguide arrays, with pressure-release boundary conditions is explored. A derivation of the approximate cut-off frequency for this system is presented. Using pulsed signals sent between a transducer and a hydrophone, the acoustic transmission through cylindrical waveguides with pressure-release walls is measured and then analysed in the frequency domain using Fast Fourier Transforms (FFTs). To verify the result further, computational modelling of the system is used and then compared with both experimental and analytic predictions.

## 8.2 Approximating the Cut-off Frequency

This work examines cylindrical holes that are made in pressure-release materials. The following section derives the approximate frequency of the acoustic cut-off, $f_c$. For this derivation of the cut-off in a cylindrical hole for simplicity, the wave equation takes the form:

$$\frac{1}{r}\frac{\partial}{\partial t^2}\left(r\frac{\partial p}{\partial r}\right) + \frac{1}{r^2}\frac{\partial^2 p}{\partial \phi^2} + \frac{\partial^2 p}{\partial z^2} = \frac{1}{c^2}\frac{\partial^2 p}{\partial t^2} \tag{8.2}$$

For the case of a pressure-release cylindrical waveguide, the boundary condition implies that the field pressure falls to zero at the walls of the waveguide. This means that the modes of this system lie at the zeros of the Bessel function, $J_n(Z_{nm}) = 0$. Here $Z_{mn}$ is the value at which the $J_n$ Bessel function is zero, fulfilling the role of a function that is zero at the walls. Thus, the solution to this equation is:

$$p = e^{in\phi}e^{ik_z z}J_n\left(Z_{mn}\right), \tag{8.3}$$

where $z$ is the distance in the direction of the propagating wave and $\phi$ is the angle.

The dispersion relation of this system is:

$$\left(\sqrt{k_0^2 - k_z^2}\right)r = Z_{mn} \rightarrow k_z = \pm\sqrt{k_0^2 - \left(\frac{Z_{nm}}{r}\right)^2}, \tag{8.4}$$

where $k_0$ is the wavevector of the sound wave and $k_z$ is its $z$ component. At the cut-off frequency the wavevector $k_z = 0$ in the waveguide. Therefore,

$$k_0 = \frac{Z_{mn}}{r}. \tag{8.5}$$

The cut-off frequency, $f_c$, is then approximated[90]:

$$f_c = \frac{Z_{mn}c}{2\pi r}. \tag{8.6}$$

## 8.3   Experimental Method

A sample was made out of flat Ethylene Vinyl-Acetate (EVA) foam sheet of thickness $L = 10 \pm 0.2$ mm by cutting into it a square array of holes with pitch $\lambda_\mathrm{g} = 12 \pm 0.2$ mm and radius $R = 5.0 \pm 0.2$ mm. The holes were cut using a sharpened tube rather than a drill, in order to preserve the cell walls of the EVA foam. This sample is depicted in figure 8.1. From equation 8.6, the cut-off of this structure is expected at $f_\mathrm{c} \approx 116$ kHz.
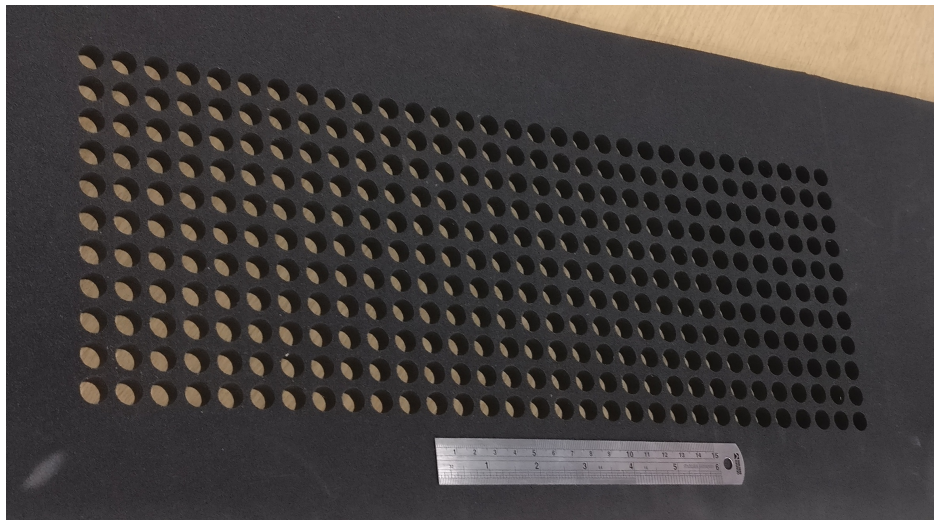


**Figure 8.1:** The EVA foam sample with the square hole array cut into it having pitch $\lambda_\mathrm{g} = 12 \pm 0.2$ mm, radius $R = 5.0 \pm 0.1$ mm and thickness $L = 10 \pm 0.1$ mm. A 15 cm ruler is present for a scale.

To explore the pressure-release array radiatively, the Neptune Sonar D70 transducer source was used to pulse 8 ms approximately double cycle Hanning-windowed pulses, positioned $400 \pm 5$ mm from the surface of the sample. This signal was then detected using the Brüel & Kjær 8103 hydrophone positioned $10.0 \pm 0.1$ mm away from the sample surface. The detector is spatially scanned in $x$ and $y$ in a 106.5 by 106.5 mm area with 0.707 by 0.707 mm resolution (see section 3.5 for further details).

The total recorded time for each scan was 0.65 ms, time-gated to remove reflections. This is with a time resolution of $\Delta t = 0.104\ \mu$s. The resultant spatially collected voltage over time is Fourier analysed with triple length zero padding with Hanning-like windows applied in time and space.

## 8.4 Results

### 8.4.1 Spatial Transmission Plots

Figure 8.2 shows the spatially plotted results at 85, 120 and 140 kHz. These results clearly show that little to no acoustic amplitude is propagating through the material at 85 kHz but above the predicted cut-off frequency ($f_c \approx 116$ kHz) the propagation is clear, highlighting the structure of the array.
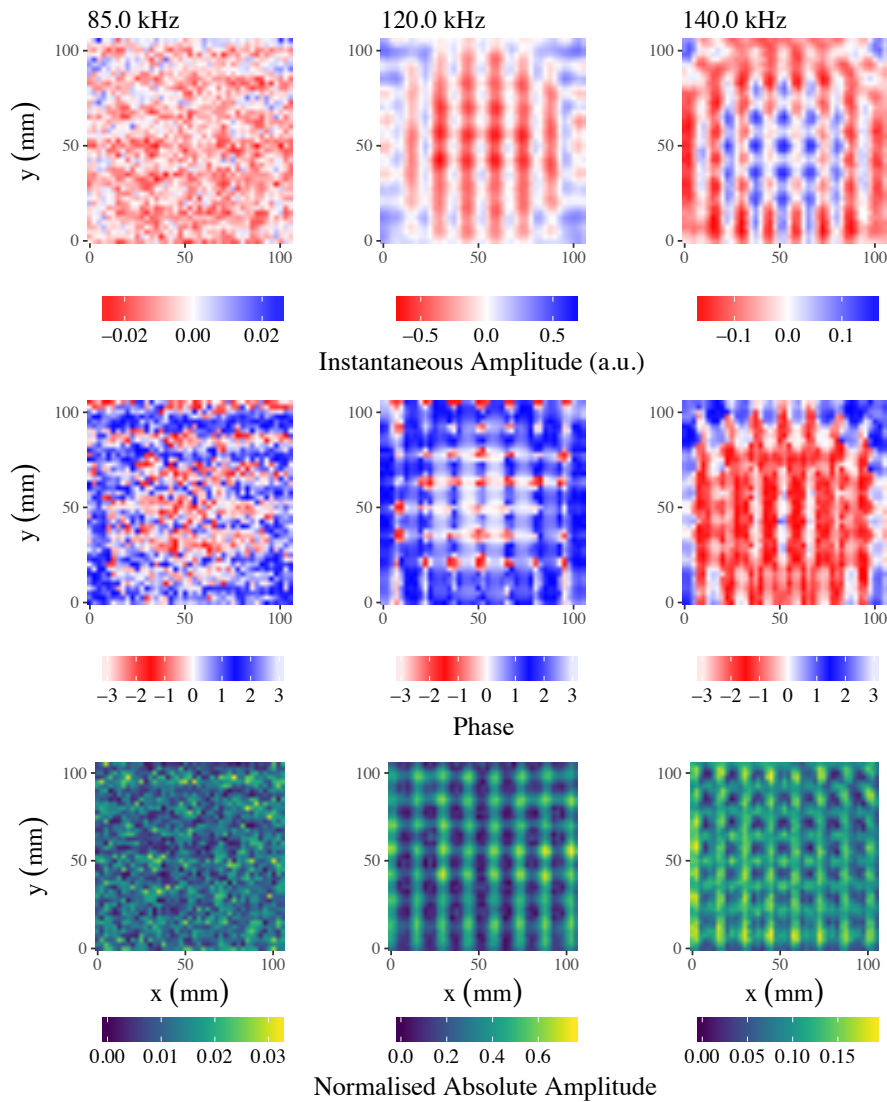


**Figure 8.2:** Spatially plotted Fourier amplitude, phase and normalised absolute amplitude of the transmitted results transmitted through the pressure-release array at 80, 120 and 140 $kHz$. 80 kHz is below the estimated cut-off frequency of $f_c \approx 116$ kHz.

### 8.4.2 Normalised Transmission

The mean signal from the transmitted Fourier absolute amplitude is extracted by Fourier transforming the time domain results and then normalising against the reference signal for an empty tank measurement to produce the results in figure 8.3. These results are compared with a Comsol Finite Element Method (FEM) model. The experimental results clearly show a cut-off with the signal at 100 kHz much smaller than the Fourier magnitude above 120 kHz. The cut-off edge of the modelled data is sharper than the experimentally measured result. The predicted position of the cut-off of $f_c \approx 116$ kHz is greater than the apparent frequency at which the signal begins to propagate through the surface, which is attributed to the edge broadening associated with variation in hole sizes.
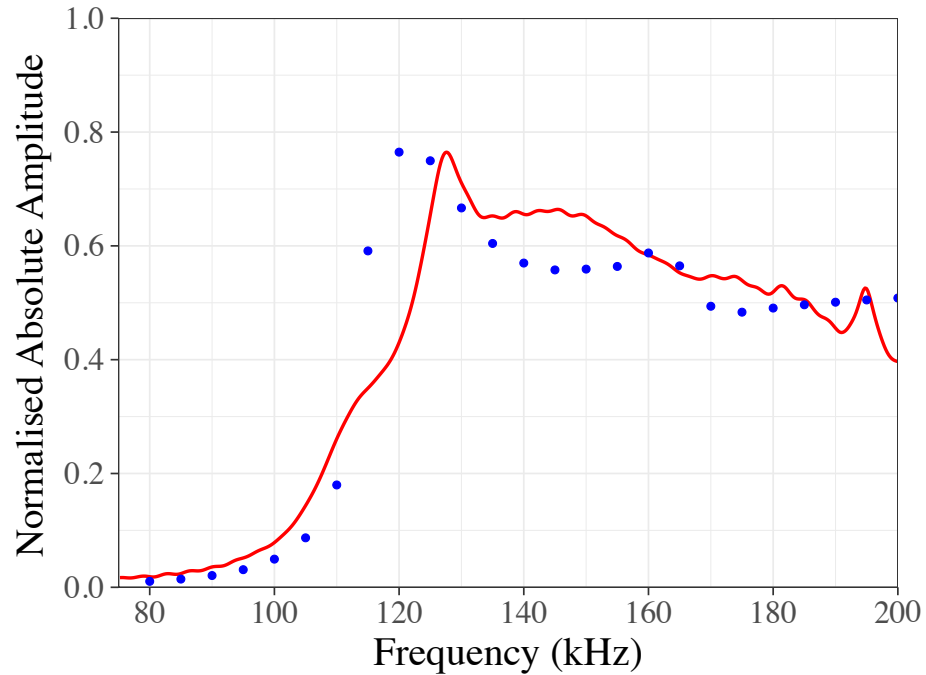


**Figure 8.3:** The normalised mean absolute amplitude of the area scan against frequency plot. This is the response of the square array of 5 mm radius holes in 10 mm thick foam. Experimental data is plotted in red and FEM modelled data is plotted in blue dots. The FEM transmission is calculated using an equivalent area integration of the absolute amplitude and is then normalised to the maximum of the experimental result to compare the acoustic response.

The FEM Comsol 5.3a modelled results are the normalised absolute amplitude of the signal propagating through the surface averaged over an area 10 mm from face of the sample, which is equivalent to the experimental method. The oscillations, above the cut-off frequency, in amplitude as a function of frequency and shown in the model

in figure 8.3 are characterised as Fabry-Perot like modes in the holes[43,44]. Yet they are not clear in the experimental data. This difference may be attributed to the material having a pore size of $\approx 100$ $\mu$m, as shown in figure 8.4, and therefore a distinct hole radius cannot be defined. The microscope image, figure 8.4 shows the how the EVA foam is made up of pores that range from $d_{\mathrm{pore}} \approx 50$ $\mu$m to $d_{\mathrm{pore}} \approx 200$ $\mu$m in size.
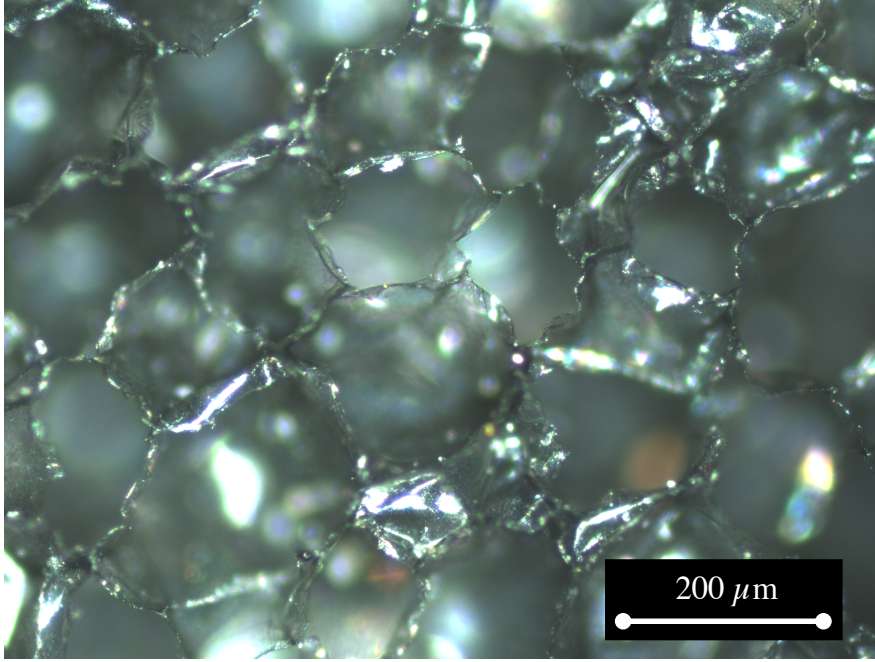


**Figure 8.4:** A 10× magnification microscope image of the closed cell EVA foam. The pore sizes of the closed cell foam ranges from $d_{\mathrm{pore}} \approx 50$ $\mu$m to $d_{\mathrm{pore}} \approx 200$ $\mu$m.

### 8.4.3   FEM Modelled Fields

Plotting the fields using Comsol multiphysics 5.3a, the Fabry-Perot like resonances can be visualised inside the holes, demonstrated in figure 8.5. The top three plots of the figure show that the self normalised absolute pressure of the fields in the holes below the cut-off frequency are negligible. In the bottom three plots, the pressure fields in the $xz$ plane show that the difference between the peak-to-peak amplitude of these modes arises from the longitudinal quantisation within the hole. These fields show that the mode within the hole is symmetric, in $x$ and $y$, and shaped like the Bessel function, used to approximate the cut-off frequency. Additionally, they show that the the peak amplitude in the transmitted signal occurs when the centre of the mode is not at $x = 0$ mm. These fields are generated for a perfect pressure-release material, without modelling pore size. It may be that for a foam-like material, the fields inside the hole are almost always asymmetric in $x$ and $y$, where the resonances become ill-defined.
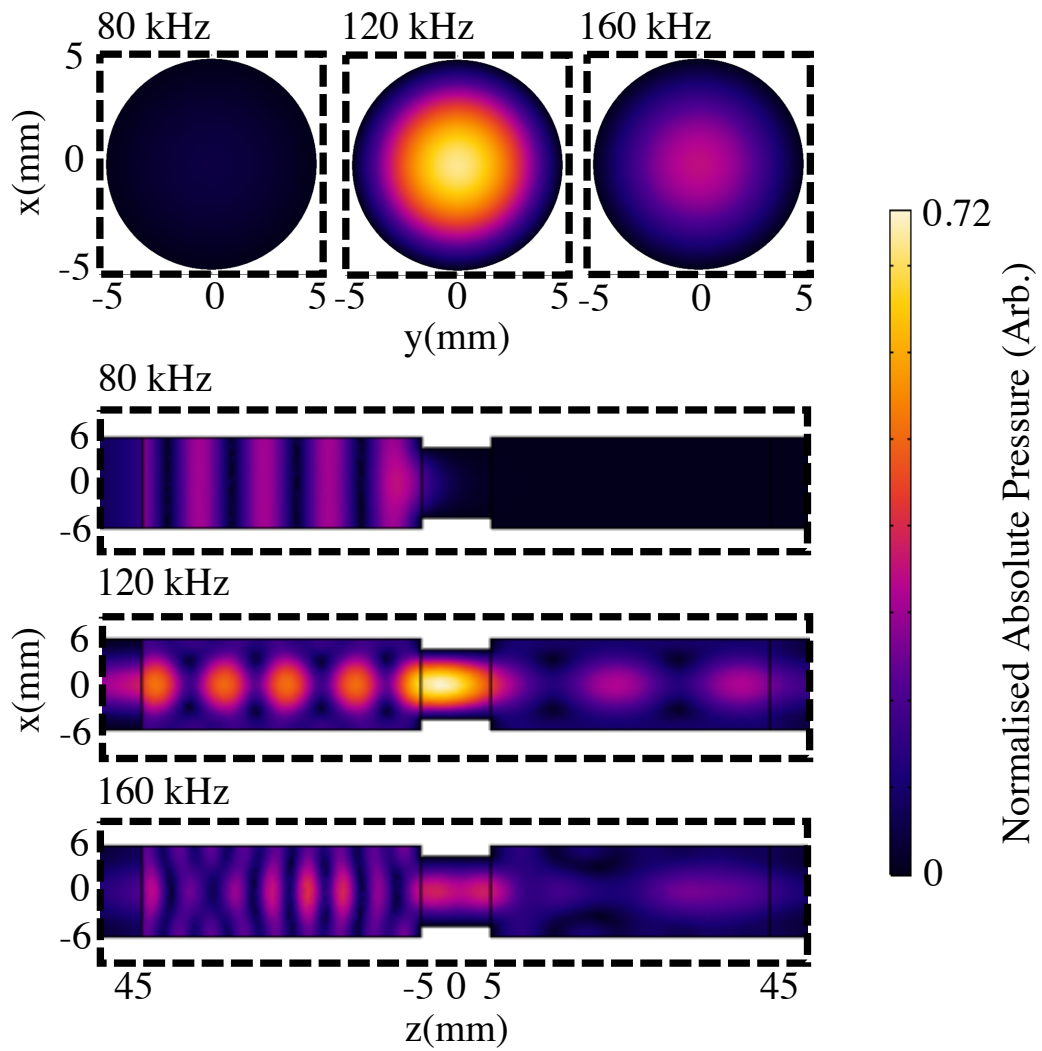
**Figure 8.5:** Comsol multiphysics 5.3a modelled spatial data of the pressure in and around a unit cell of the square array of pressure-release holes, shown at 80, 120 and 160 kHz. Top is the normalised absolute amplitude of the fields at the centre of the hole in $x$ and $y$. Bottom are the normalised absolute pressure plots in the $xz$ plane.

Note that the fields shown in figure 8.5 contain a beat pattern that differs between the transmission side, left, and the propagation side, right. Interestingly, this beat pattern differs in wavelength. This is due to the content of the fields on both sides of the array. The modulation in the transmission intensity is $k_m = k_0 - k_z = k_0 - (k_0^2 - k_g^2)^{\frac{1}{2}}$, where $k_g$ is the grating wavevector. This is fully derived along with the modulation to the reflected signal in appendix C.

## 8.5  Conclusion

In this chapter results of measurement of a square array of holes in a foam sheet have shown the ultrasonic cut-off frequency in a pressure-release material. Through careful extraction of the Fourier-analysed transmission through this structure, results clearly show the acoustic cut-off. Finite element models overlay reasonably with the transmission data, although experimental results were broader and the Fabry-Perot oscillations expected from modelling were not at all clear in the experiment. Visualising these modes with FEM modelling showed that the transmission maxima occurs where the fields inside the hole were asymmetric along the holes of the array, whilst the in-plane field inside the hole remains symmetric in the shape of the Bessel function in this frequency range. These results demonstrate for the first time the expected cut-off frequency for a pressure-release material using sound transmission. By varying the radius, the acoustic cut-off frequency can be readily changed. This type of surface can be utilised to allow the flow of a fluid through it, whilst blocking lower acoustic frequencies. Additionally, an explanation for the beat pattern seen in the transmitted and reflected signals was discussed and derived. The next and final chapter will further explore how this work and the preceding work can be adapted and applied to future projects.

# Chapter 9

# Conclusions

## 9.1  Summary of Thesis

This thesis set out original experimental investigations of the underwater radiative and evanescent fields of unstructured and structured flat plates. This thesis is divided into three main areas of research: the study of Lamb modes in unstructured plates, Acoustic Surface Wave (ASW) modes of hole arrays in aluminium alloy plates and the acoustic cut-off frequency of arrays of holes in a pressure-release material.

In the chapters 2 and 3 the background theory and methodology used throughout this work were outlined. Chapter 3 included a novel method of exciting samples using an adapted transducer, wrapped in foam to make it point-like, which was scanned spatially to collect acoustic field maps.

In the first results chapter, chapter 4, the Lamb mode dispersions supported by flat solid plates were experimentally explored, using the methods outlined in chapter 2, and analysed using Fourier analysis of spatially acquired field maps. Four samples made of aluminium alloy, mild steel and acrylic were spatially scanned and compared to analytic theory. Hence, the materials were elastically characterised using the experimental and analytic dispersions. Material parameters elastic modulus, $E$, and Poisson's ratio, $\nu$, were extracted for each sample, with most results within the expected error of industry estimates of the elastic properties. Furthermore, aluminium results were compared to a industry standard method to extract the elastic modulus and shared good agreement. This method of non-destructive testing is usable between 50 and 500 kHz. The material properties of aluminium alloy determined in chapter 4 were used in chapter 5, 6 and 7.

Plate modes were further explored in chapter 5. An investigation of the coupling between symmetric Lamb modes of an aluminium alloy plate was shown to focus transmitted acoustic energy over a very narrow frequency range. This experiment was performed using the same technique and $\approx 10$ mm thick plate used in chapter 4, but

# 9. Conclusions

with the source exciting symmetrically. The acoustic focussing was attributed to the "Negative Group Velocity" region of the $S_{1b}$ mode that was experimentally observed in the dispersion relation. The experiment agreed well with the dispersion predicted using an FEM model. Further results extracted from the model showed that the pressure phase fronts of sound within the plate are refracted inwards towards the centre of the plate between the point at which the wavevector excitation of that region switches between the symmetric $S_{1b}$ and the $S_1$ Lamb modes. In addition, a transmitted spatial beat pattern was observed. This pattern was confirmed analytically to the interference between a plane wave source and plate modes with similar wavevector components, normal to the plate (fully derived in appendix B).

Chapter 6 was the first chapter to explore structured plates, demonstrating that it is possible to fabricate simple one-dimensional periodic arrays of resonators that can support "trapped" ASWs underwater. The fields above single, double and triple rows of holes are characterised by scanning the near-fields of each sample with a method outlined in chapter 3. Then temporal and spatial Fourier analysis was utilised to plot the iso-frequency contour plots and the dispersion relations of the surface modes. The detected ASW modes are shown to propagate over narrow frequency ranges along each of the structured lines of holes. Results showed how it is possible to create degenerate ASW modes at the Brillouin Zone (BZ) boundary on glide-symmetric samples. Importantly, comparisons between FEM modelled rigid and elastic dispersions showed that there is a significant 2.53 kHz difference between the asymptotic eigenfrequencies of these one-dimensional arrays, with the experimental results agreeing with the elastic case. Finally, it was revealed there is significant coupling between the fields resulting from the ASWs and the sound line bound Scholte-Stoneley Waves (SSWs).

ASWs were further explored in chapter 7, where two different thickness square-arrays of open-ended holes in aluminium alloy plates were used. The excitation and detection methods used in chapter 6 were again employed to pulse and detect the diffracted near-fields. Temporal and spatial analysis of the evanescent fields was used to characterise the two-dimensional surface bound ASWs. The resulting $\Gamma - X - M$ directional dispersion was compared with FEM modelled data showing good agreement in both the 6.4 mm and the 9.99 mm thick cases. Moreover, in-plane ultrasonic beaming in the $\Gamma - M$ direction is observed over a very narrow band of frequencies. Finally, a 3D FEM model of the 6.4 mm thick array was used to show that these results depend significantly on the elastic properties of the material and that the holes deform differently depending on the direction of the exciting ASW wave.

In the final results chapter, chapter 8, the ultrasonic cut-off frequency of a square array of holes in a pressure-release material was explored. Through careful extraction of the Fourier-analysed transmission through this structure, results clearly showed the

acoustic cut-off frequency in the spatially plotted transmission and the normalised transmission data. FEM modelled transmission data shows good agreement with the experimental results, although Fabry-Perot-like oscillations above the cut-off frequency seen in the FEM spatially modelled data were not seen experimentally. The FEM model was employed to plot the fields of the Fabry-Perot modes inside the holes. These results showed that the transmission maxima occurs where the fields inside the holes were axially asymmetric, whilst the in-plane field inside the hole remains symmetric in the shape of the Bessel function in this frequency range. In addition, a beat pattern in the transmitted and the reflected signals was observed in the FEM models. An analytical explanation of this was then shown. These results demonstrated for the first time the expected cut-off frequency response of an underwater pressure-release hole array.

## 9.2 Future Work

In this section further extensions to the previous five chapters are discussed. Preliminary results have been gathered to establish the viability of the majority of the ideas set out here.

### 9.2.1 Hexagonal and Honeycomb Arrays

Chapter 7 demonstrated that by patterning solid plates with square arrays of open-ended holes, it is possible to support ASWs. This simple structure has an equivalently simple structure in in reciprocal space. The next step in this investigation is to use samples that have more complicated structures and that have a different lattice symmetries with different points of high symmetry.

Graphene and graphene-like structures made of honeycomb arrays of simple resonators have shown significant potential in optics[174], plasmonics[175] and electromagnetics[176]. More recently similar structures have been explored using in acoustics in air[177]. These structures can support in-plane ASWs with zero-bandgap and linear dispersion. Yet, they are still to be utilised in underwater environments.

#### 9.2.1.1 Preliminary Results

The following results were not in the scope of this thesis, but can be easily obtained and developed. An example honeycomb array sample is shown in figure 9.1. A similar method to the one used to scan the samples in chapter 6 and 7 would be used to excite and detect ASWs on this sample using near-field coupling.

## 9. Conclusions
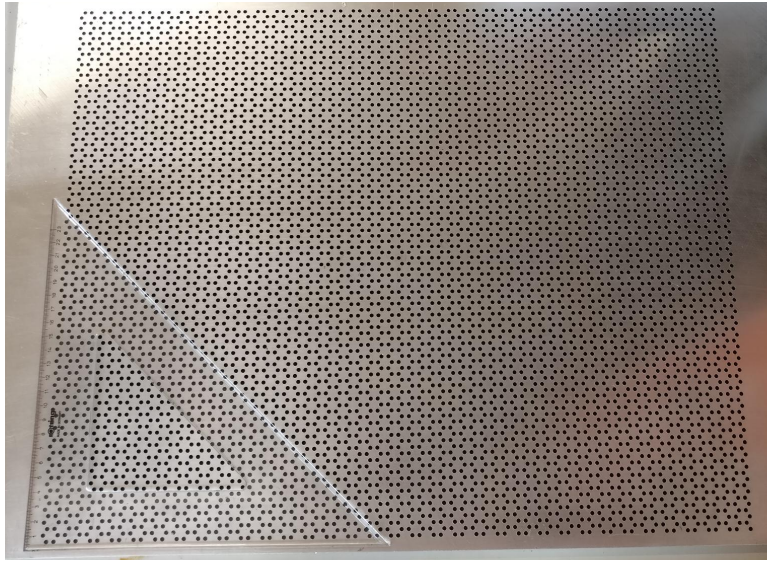


**Figure 9.1:** An aluminium alloy honeycomb array sample, fabricated using a CNC machine.

Here we demonstrate the viability of using honeycomb and hexagonal arrays of holes using FEM Comsol 5.3a models of two new arrays. For the honeycomb arrays the models were built using a unit cell that includes two holes. Preliminary results for the dispersion of the honeycomb array are shown in the left plot of figure 9.2. This figure shows the zero band gap occurring at the BZ boundary at the $K$ point of higher symmetry. Similar features are seen in the FEM modelled dispersion of the hexagonal array depicted in right plot of figure 9.2.
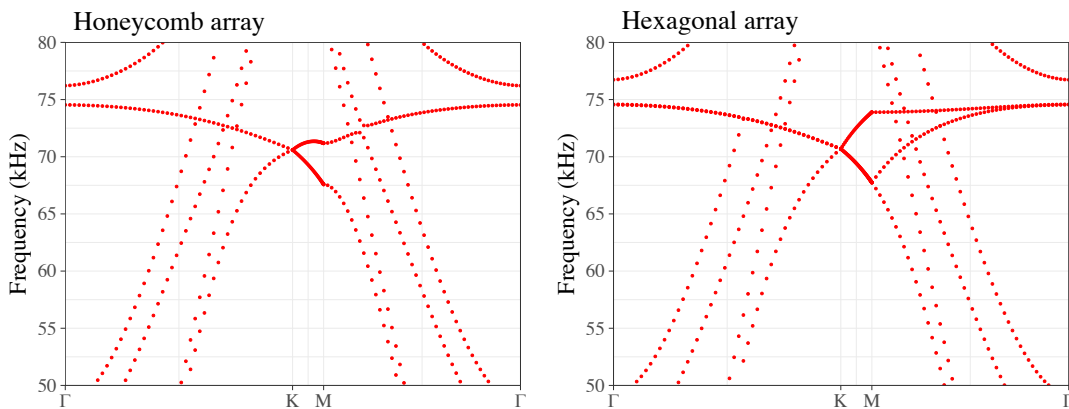


**Figure 9.2:** The Comsol multiphysics 5.3a FEM modelled directional dispersion of the perforated rigid material in a honeycomb array (left) and hexagonal array (right).

### 9.2.2 Slow Surface Waves

The work presented in chapters 4, 5, 6 and 7 used aluminium alloy for the main body of the work. Although in chapter 4 results were presented for the characterisation of the acrylic, it was intentionally decided that acrylic would not be used to observe ASW phenomena as the Rayleigh and Shear wavespeeds in acrylic fall lower than the free speed of sound in water. These "slow surface waves" or slow SAWs may have some interesting applications when coupled to the modes resulting from structuring the plates. However the preliminary results, presented in the next section, are for a flat unstructured piece of acrylic.

#### 9.2.2.1 Preliminary Results

Experimentation presented here uses the evanescent technique used in chapters 6 and 7. The sample examined as an example of a source of slow SAWs is the $7.4 \pm 0.1$ mm acrylic sample examined in chapter 4. Here the foam wrapped D70 transducer is used to excite the sample $\approx 3$ mm from the sample surface with a central Hanning-windowed pulse frequency of $f_c = 125$ kHz. The surface fields are scanned along the in the $x$ direction parallel to the surface $0.50 \pm 0.01$ mm from the sample surface using the Precision Acoustics 1 mm needle hydrophone between $x = 0$ mm, directly opposite to the source, and $x = 212.1$ mm with $\Delta x = 0.707$ mm spatial resolution. These trapped SAWs are evidenced in figure 9.3 beyond the sound line, confirming that they can be excited and detected underwater.
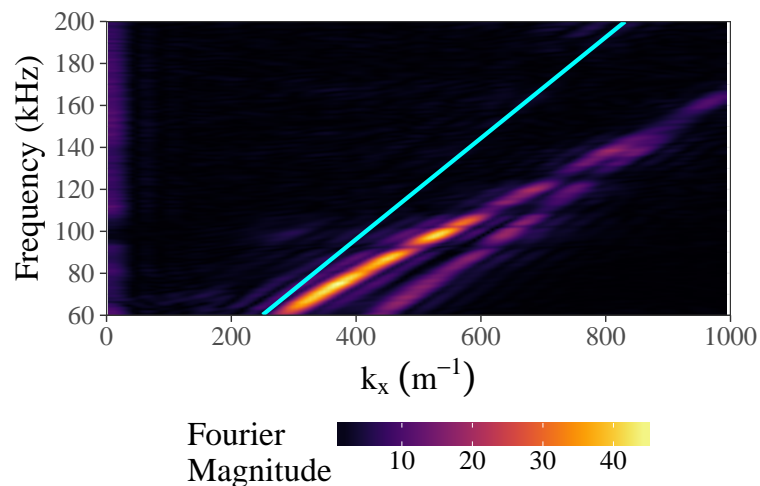


**Figure 9.3:** The dispersion of the surface excited SAW modes of a $7.4\pm0.1$ mm thick acrylic plate. Here, the wavespeed limit should be $c_R = 1198$ m/s.

### 9.2.3 Acoustic Circuitry

The work set out in chapters 6 and 7 demonstrated that it is possible to support ASWs underwater using structured elastic solid plates. This fundamentally means that it is possible to transmit and absorb slow travelling wave energy in-plane to a surface over specific frequency ranges. By patterning surfaces with arrays of simple resonators in a combinations of 1D and 2D arrays, it should be possible to transmit acoustic energy through acoustic circuits. Acoustic waveguides[178], SAW focussing[155] and topological transport of SAWs[179] have all got potential applications in this area.

#### 9.2.3.1 Preliminary Results

Samples were made using the 10 mm thick aluminium alloy plates with 100 and 50 mm radius rings drilled into them, shown in figure 9.4. These holes have a centre-to-centre pitch around the arc of $\approx$ 6 mm and radius of 1.5 mm to remain similar to the lines of holes explored in chapter 6.
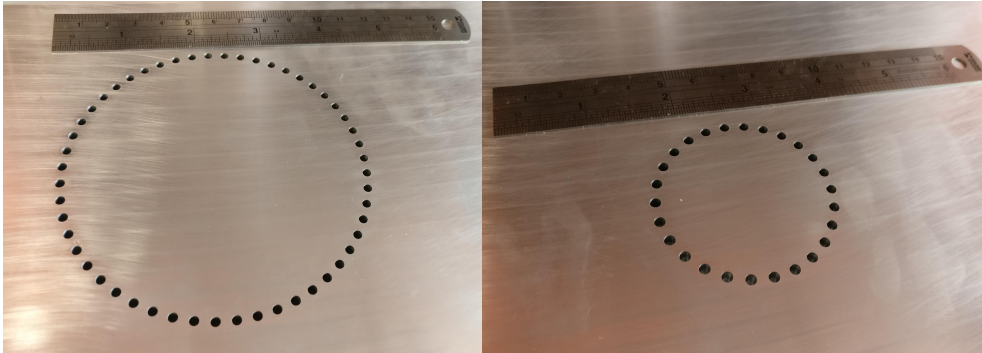


**Figure 9.4:** 50 and 100 mm radius rings of holes drilled in to a 10 mm thick aluminium alloy plate. The pitch of these holes is $\approx$ 6 mm and radius are 1.5 mm.

Initial experimentation has been performed on the coupling between the ASW modes of a line and a ring of holes. This was conducted using the wrapped Neptune Sonar D70 transducer to 1 mm needle hydrophone (as detailed in chapter 3). The source positioned $\approx$ 3 mm from one of the holes of the line and the hydrophone is scanned in a plane $0.5 \pm 0.1$ mm from the opposite side of the sample. Figure 9.5 shows the parameters of the ring and the line discussed as well as the absolute pressure plots of the fields above this surface at 52.4 kHz. This is the result of a 6.00 mm pitch line of holes coupling into the 50 mm radius ring. Where they almost meet, the distance between the centre of each hole is 3.5 mm. At the frequency depicted the ASW mode of the line appears to be coupling into the ring, with propagation along the line reduced in amplitude significantly.
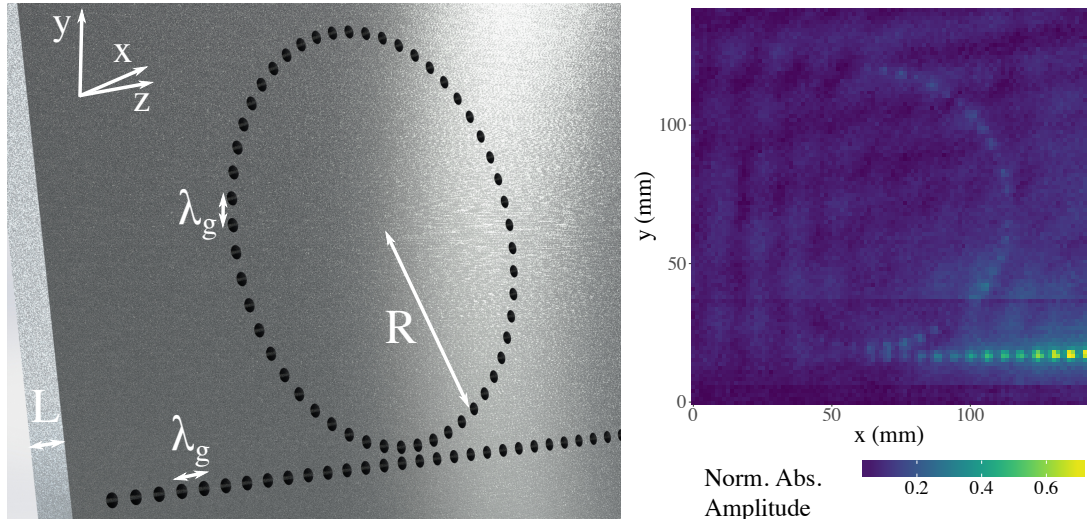
**Figure 9.5:** Left is a 3D render of the line-to-ring sample and right is is the experimentally acquired normalised absolute amplitude plotted spatially at 52.4 kHz.

### 9.2.4 The Non-existence of Pressure-release Surface Waves

The acoustically soft or pressure release boundary conditions state that $p_a = 0$ at the surface[34]. This means that any structures made out of a pressure-release material cannot support an ASW mode as the pressure is zero at the interface. Specifically, the in-plane diffracted component of the field at the entrance and exit of a resonant feature of the structure will be zero in amplitude. This is yet to be reported in the community although it has been breifly studied in similar systems of imperfect pressure-release surfaces of poro-elastic rock and soil for seismic wavelengths[180,181,182].

#### 9.2.4.1 Preliminary Results

A Comsol time-domain model was used to simulate a point source excitation over a 1D array of grooves. Figure 9.6 shows the results 0.12 ms after a single-cycle Gaussian pulse. Here a point source is placed in close proximity to a 1D array of grooves in a pressure-release material. The wave does not couple into the patterned array and the grazing acoustic pressure amplitude has dropped to zero.
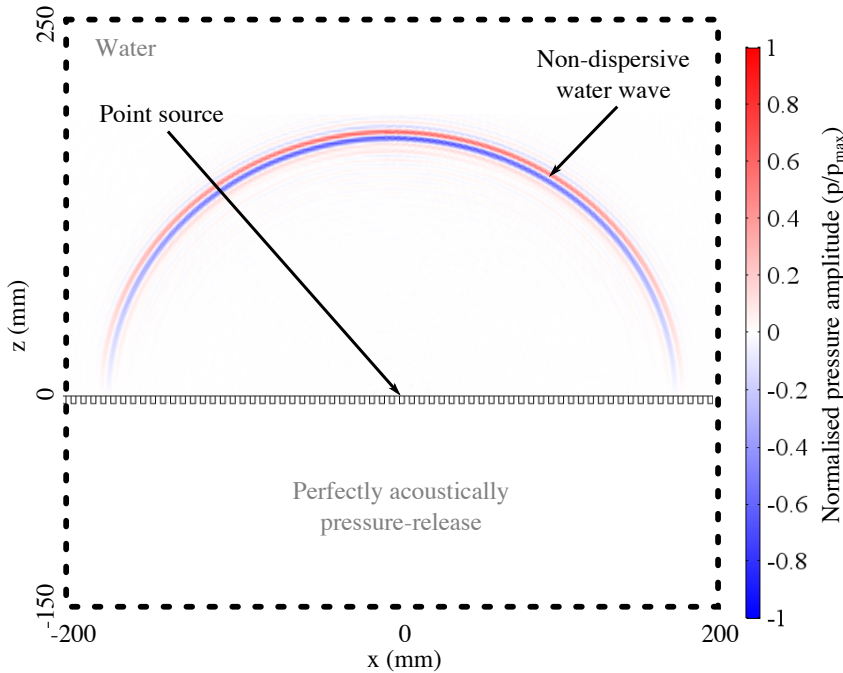
**Figure 9.6:** A Comsol modelled instantaneous snapshot plot of the normalised acoustic pressure travelling over the surface of a structured pressure release material. This idealised case shows no propagation of sound into the material of a 1D surface array. This model is infinite in the $y$ direction.

### 9.2.5 Other Ideas

In this thesis, results were acquired for static systems. By further adapting these structures, to incoperate flow, non-linearity and variation in ambient conditions, it may lead to a variety of new and exciting ways to generate and couple into surface waves. As discussed briefly in chapter 2, this involves the use of Navier-Stokes physics, and consideration of the turbulent regime and can become rather complex and, although this idea is not new, it is yet to be fully realised[183,184,185].

The work presented in thesis covered a wide variety of boundary conditions, structures and acoustic phenomena. Combinations of these may be used to create structures that support novel surface waves and to affect transmission and reflection amplitudes of sound. Furthermore, by layering these types of surfaces it would be possible to impinge multiple types of acoustic modulation on the transmitted and reflected fields. 3D acoustic metmaterials are gaining traction in the literature and are the current frontier of metamaterial research. There has been a significant amount of interest in this area of the last five years[186,187] as a results of improved additive manufacturing techniques. There are vast amounts of 3D arrays and curved geometries that could be built and utilised. This is an exciting time to be working in acoustics.

# Appendices

# Appendix A

# The EVA Foam Wrapped D70 Source

In chapters 6 and 7 it is necessary to use a point-like source to excite the surface modes. To do this a foam wrapped D70 transducer was built. This adapted source needs to work as a localised broadband source of ultrasound, whilst pulse lengths remain short.

The first step to constructing this adapter was to test the acoustic response of the exit hole. A single hole in an EVA foam sheet has an acoustic cut-off frequency, as outlined in chapter 8. Yet, by placing a thin walled hollow metal tube down the length of a hole in EVA foam, a "semi-rigid" boundary was created.

The acoustic response of the $6.00 \pm 0.01$ mm diameter $0.05 \pm 0.01$ thick tube protruding through a flat $10.0 \pm 0.2$ mm thick EVA foam plate is shown in figure A.1. The result shows a broad frequency response. This is ideal for exciting surface waves with a range of frequencies. Further spatial plots of transmitted fields of this adapted transducer are presented in section 3.5.

Using this, a cavity was constructed to contain the Neptune Sonar D70 transducer. This cavity was built to allow the "breathing" mode of the ball source to operate, whilst not supporting a high quality cavity resonance that would not function as a source of ultrasonic pulses. A schematic of the adapter is shown in figure A.2. Further details are shown in section 3.5.
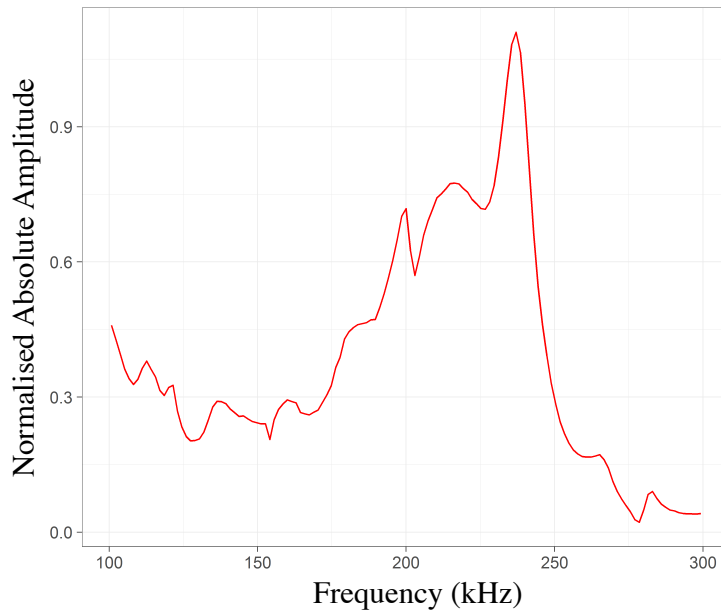
**Figure A.1:** The normalised acoustic absolute amplitude of transmission through a 6.00 mm diameter thin walled steel tube in a $10.0 \pm 0.2$ mm thick EVA foam sheet. The hole was excited with a D70 transducer $50 \pm 5$ mm from the hole and detected $5.0 \pm 0.1$ mm on the other side with a Brüel & Kjær 8103 hydrophone.
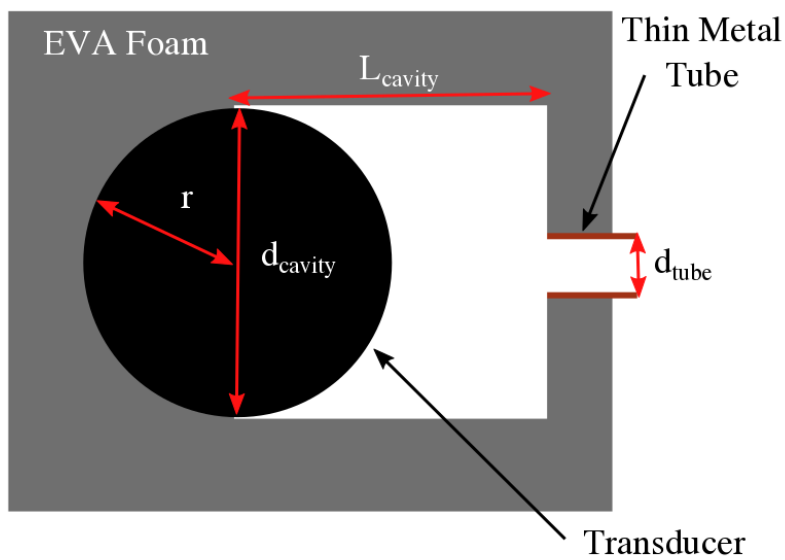


**Figure A.2:** A schematic of the foam cavity adapter. The purpose built foam adapter has $d_{\text{tube}} = 6.00$ mm, foam walls are $10.0 \pm 0.2$ mm thick and a cavity geometry of $L_{\text{cavity}} \approx 50$ mm by $d_{\text{cavity}} \approx 40$ mm.

# Appendix B

# The Spatially Modulated Transmission Through a Flat Aluminium Plate

This appendix presents the derivation of the cause of the spatially modulated transmission seen in chapter 5. This is caused by presence of two oscillating waves in $z$ with two values of $k_z$. The surface wave, $\psi_1$, and the plane wave, $\psi_2$, can be represented by the equations

$$\psi_1 = A\sin(k_\parallel x - \omega t)e^{-k_z z}, \tag{B.1}$$

$$\psi_2 = A\sin(k_\perp z - \omega t). \tag{B.2}$$

Combining these two waves results in:

$$\psi_1 + \psi_2 = \psi_t = Ae^{-k_z z}(\sin(k_\parallel x)\cos(\omega t) - \cos(k_\parallel x)\sin(\omega t))$$
$$+ B\sin(k_\perp x)\cos(\omega t) - B\cos(k_\perp x)\sin(\omega t)$$
$$= \cos(\omega t)[A\sin(k_\parallel x)e^{-k_z z} + B\sin(k_\perp z)]$$
$$- \sin(\omega t)[A\cos(k_\parallel x)e^{-k_z z} + B\cos(k_\perp z)].$$

For a surface wave with $k_z \to 0$ then,

$$\psi_t = \cos(\omega t)[A\sin(k_\parallel x) + B\sin(k_\perp z)] - \sin(\omega t)[A\cos(k_\parallel x) + B\cos(k_\perp z)].$$

## B. The Spatially Modulated Transmission Through a Flat Aluminium Plate

Squaring this wavefunction to obtain the intensity results in:

$$\psi_t^2 = \cos^2(\omega t)[A^2 \sin(k_\parallel x)^2 + 2AB \sin(k_\parallel z) \sin(k_\perp z) + B^2 \sin^2(k_\perp z)]$$
$$+ \sin^2(\omega t)[A^2 \cos(k_\parallel x)^2 + 2AB \cos(k_\parallel z) \cos(k_\perp z) + B^2 \cos^2(k_\perp z)]$$
$$- 2\cos(\omega t)\sin(\omega t)[A^2 \sin(k_\parallel x) \cos(k_\parallel x) + B^2 \sin(k_\perp z) \cos(k_\perp z)$$
$$+ AB(\sin(k_\parallel x) \cos(k_\perp z) + \sin(k_\perp z) \cos(k_\parallel x))].$$

Now integrating in time obtains:

$$\frac{\int_0^\tau \psi_t^2 dt}{\tau} = \frac{1}{2}[A^2 \sin(k_\parallel x)^2 + 2AB \sin(k_\parallel z) \sin(k_\perp z) + B^2 \sin^2(k_\perp z)]$$
$$+ \frac{1}{2}[A^2 \cos(k_\parallel x)^2 + 2AB \cos(k_\parallel z) \cos(k_\perp z) + B^2 \cos^2(k_\perp z)]$$
$$= \frac{1}{2}(A^2 + B^2) + AB[(\sin(k_\parallel x) \sin(k_\perp z) + \cos(k_\parallel x) \cos(k_\perp z)],$$

where the intensity is now:

$$\psi_t^2 = \frac{1}{2}(A^2 + B^2) + AB(\cos(k_\parallel x - k_\perp z).$$

Here the factor of $\cos(k_\parallel x - k_\perp z)$ gives the modulation that is seen in the phase of figure 5.4.

# Appendix C

# The Spatially Modulated Fields of Pressure-release Arrays of Holes

This appendix presents the derivation of the spatial modulation in the transmitted and reflected fields in chapter 8. The sample explored here is a square array of diffracting holes in a pressure-release foam. Considering only first order diffraction:

$$\boldsymbol{k}_1 = k_{1x}\hat{x} + k_{1z}\hat{y},$$

with,

$$k_{1x} = k_{\mathrm{g}}$$
$$\boldsymbol{k}_2 = -k_{1x}\hat{x} + k_{1z}\hat{y}$$
$$\boldsymbol{k}_1^2 = k_0^2 = k_{1x}^2 + k_{1z}^2 = k_g^2 + k_{1z}^2$$

Therefore:

$$k_{1z} = \left(k_0^2 - k_g^2\right)^{\frac{1}{2}}. \tag{C.1}$$

## C.1 Transmitted Spatial Modulation

On the transmission side of a square array of pressure-release holes there are five fields. The zero order $A\sin(k_0 z - \omega t)$ and two pairs of diffracted order, two in x and two in y. All four diffracted orders have the same $k_{1z} = \left(k_0^2 - k_g^2\right)^{\frac{1}{2}} = k_z$. In addition the two

## C. The Spatially Modulated Fields of Pressure-release Arrays of Holes

x diffracted orders pair up to form a standing wave in the x, with zero field between the holes. Likewise the two y diffracted orders pair up to form a standing wave in the y with zero field between the holes.

In the z direction:

$$\psi = A\sin(k_0 z - \omega t) + B\sin(k_z z - \omega t)$$
$$= A\sin(k_0 z)\cos(\omega t) - A\cos(k_0 z)\sin(\omega t)$$
$$+ B\sin(k_z z)\cos(\omega t) - B\cos(k_z z)\sin(\omega t)$$
$$= (A\sin(k_0 z) + B\sin(k_0 z))\cos(\omega t)$$
$$- (A\cos(k_0 z) + B\cos(k_0 z))\sin(\omega t)$$

,

where $B$ is the addition of the four diffracted orders with equal $k_z$. Then,

$$\psi^2 = (A\sin(k_0 z) + B\sin(k_z z))^2 \cos^2(\omega t)$$
$$+ (A\cos(k_0 z) + B\cos(k_0 z))^2 \sin^2(\omega t)$$
$$- 2(A\sin(k_0 z) + B\sin(k_z^2))(A\cos(k_0 z)$$
$$+ B\cos(k_z z))\cos(\omega t)\sin(\omega t)$$

Time averaging of $\cos^2(\omega t) = \frac{1}{2}$, $\sin^2(\omega t) = \frac{1}{2}$ and $2\cos(\omega t)\sin(\omega t) = 0$. Therefore:

$$<\psi^2> = \frac{1}{2}[A^2\sin^2(k_0^2) + B^2\sin^2(k_z^2) + 2AB\sin(k_0 z)\sin(k_z z)$$
$$+ A^2\cos^2(k_0 z) + B^2\sin^2(k_z z) + 2AB\cos(k_0 z)\cos(k_z z)]$$
$$= \frac{1}{2}(A^2 + B^2) + AB\cos(k_0 - k_z)z.$$

Here $\frac{1}{2}(A^2 + B^2)$ is a constant and $AB\cos(k_0 - k_z)z$ is the modulation in the intensity. Now, Then,

$$k_m = k_0 - k_z = k_0 - (k_0^2 - k_g^2)^{\frac{1}{2}},$$

and when:

$$k_0 = k_g \text{ then } k_m = k_g,$$
$$k_0 = \sqrt{2}k_g \text{ then } k_m = (\sqrt{2} - 1)k_g,$$
$$k_0 = 2k_g \text{ then } k_m = (2 - \sqrt{3})k_g,$$
$$k_0 = \sqrt{5}k_g \text{ then } k_m = (\sqrt{5} - 2)k_g.$$

For frequencies below $k_g$, the diffracted fields are evanescent, so only act as decaying fields in $z$ that leads to modulation at $k_0$ only.

## C.2    Reflected Spatial Modulation

On the input side there are is an extra reflected field.

$$
\begin{aligned}
\psi = {}& C\sin(k_0 z)\cos(\omega t) - C\cos(k_0 z)\sin(\omega t) \\
& -D\sin(k_0 z)\cos(\omega t) - D\cos(k_0 z)\sin(\omega t) \\
& -E\sin(k_z z)\cos(\omega t) - E\cos(k_z z)\sin(\omega t) \\
= {}& [(C-D)\sin(k_0 z) - E\cos(k_z z)]\cos(\omega t) \\
& -[(C+D)\sin(k_0 z) - E\cos(k_0 z)]\sin(\omega t)
\end{aligned}
$$

The resultant intensity is:

$$
\begin{aligned}
<\psi^2> = {}& \frac{1}{2}[(C-D)^2\sin^2(k_0 z) + E^2\sin^2(k_z z) - 2(C-D)E\sin(k_0 z)\sin(k_z z) \\
& +(C+D)^2\cos^2(k_0 z) + E^2\cos^2(k_z z) + 2(C+D)E\cos(k_0 z)\cos(k_z z)] \\
= {}& \frac{1}{2}[C^2 + D^2 + E^2 + 2CD(\cos^2(k_0 z) - \sin^2(k_0 z)) + 2CE(\cos(k_z z) \\
& - \sin(k_0 z)\sin(k_z z)) + 2DE(\cos(k_0 z)\cos(k_z z) + \sin(k_0 z)\sin(k_z z))],
\end{aligned}
$$

and finally:

$$
\begin{aligned}
<\psi^2> = {}& \frac{1}{2}(C^2 + D^2 + E^2) + CD\cos^2(2k_0 z) \\
& +CE\cos((k_0 + k_z)z) + DE\cos((k_0 - k_z)z).
\end{aligned}
$$

Here, $CD\cos^2(2k_0 z)$ is the primary source of the modulation ($\lambda = \frac{\lambda_0}{2}$) in the reflected fields and $CE\cos((k_0 + k_z)z)$ and $DE\cos((k_0 - k_z)z)$ are secondary sources of modulation.

# C. The Spatially Modulated Fields of Pressure-release Arrays of Holes

# Appendix D

# Publications and Conferences

## D.1    Publications

- Graham, T. J., Starkey, T. A., Horsley, S. A. R., Hibbins, A. P., Sambles, J. R., Underwater Acoustic Surface Waves on a 2D Square Array of Holes, *In preparation.*

- Graham, T. J., Starkey, T. A., Horsley, S. A. R., Hibbins, A. P., Sambles, J. R., Acoustic Focussing Through Coupled Excitation of Symmetric Lamb Modes, *In preparation.*

## D.2    Presentations and Conferences

### D.2.1    Poster Presentations

- Cranfield Defence Symposium, Graham, T. A., Horsley, S. A. R., Hibbins, A. P., Sambles, J. R., Ultrasonic Beaming due to Coupled Mode Excitation of Viscoelastic Plates, Swindon, UK, November 2017.

- European Workshop on Acoustic and Mechanical Metamaterials, Graham, T. J., Starkey, T. A., Horsley, S. A. R., Hibbins, A. P., Sambles, J. R., Imperial College London, London, UK, July 2018.

### D.2.2    Oral Presentations

- Smart and Multifunctional Materials, Structures and Systems (CIMTEC), Graham, T. J., Horsley, S. A. R., Hibbins, A. P., Sambles, J. R., Observation of the Ultrasonic Cut-off Frequency of Holes with Pressure-release Walls, Perugia, Italy June 2016.

## D. Publications and Conferences

- Exeter Acoustics Metamaterials Meeting (XAM3), Graham, T. J., Starkey, T. A., Horsley, S. A. R., Hibbins, A. P., Sambles, J. R., Underwater Observation of 1D Acoustic Surface Waves, Exeter, UK, April 2018.

# References

[1] McCarthy, E. *International Regulation of Underwater Sound.* Solid Mechanics and Its Applications Series. Springer Science and Business Media (2007). ISBN 9781402080784. 1

[2] Mersenne, M. *Traité de l'harmonie universelle: où est contenu la musique theorique & pratique des anciens & modernes, avec les causes de ses effets, enrichie de raisons prises de la philosophie, & des mathematiques.* Guillaume Baudry (1627). 1

[3] Walker, D.P. Some Aspects of the Musical Theory of Vincenzo Galilei and Galileo Galilei. *Proceedings of the Royal Musical Association*, **100**, 33 (1973). 1

[4] Newton, I., Motte, A., and Cajori, F. *Sir Isaac Newton's Mathematical Principles of Natural Philosophy and His System of the World*, volume 1 of *Principal.* University of California Press (1962). ISBN 9780520009288. 1, 12

[5] Laplace, P.S. and Dale, A.I. *Pierre-Simon Laplace Philosophical Essay on Probabilities: Translated from the fifth French edition of 1825 With Notes by the Translator.* Sources in the History of Mathematics and Physical Sciences. Springer New York (1998). ISBN 9780387943497. 1

[6] Bernard Finn, B.S. Laplace and the Speed of Sound. Technical Report 179 (1964). 1, 13

[7] Kirchhoff, G. Ueber den Einfluss der Wärmeleitung in einem Gase auf die Schallbewegung. *Annalen der Physik*, **210**, 177 (1868). 1

[8] Urick, R.J. *Principles of Underwater Sound.* Third edition (1983). ISBN 0070660867. 1, 2

[9] Pierce, A.D. *Acoustics. An introduction to its physical principles and applications.* Acoustical Society of America (1981). ISBN 0070499616. 1, 10, 13, 18, 41, 58

# References

[10] JACQUES, C. AND PIERRE, C. Development, via compression, of electric polarization in hemihedral crystals with inclined faces. *Bulletin de la Société Minérologique de France*, **3**, 90 (1880). 1

[11] BELL, A.G. The Production of Sound by Radiant Energy. *Science*, **2**, 242 (1881). 2

[12] FESSENDEN, R.A. Signaling by sound and other longitudinal elastic impulses. (1914). 2

[13] LASKY, M. Review of undersea acoustics to 1950. *The Journal of the Acoustical Society of America*, **61**, 283 (1977). 2

[14] KATZIR, S. Who knew piezoelectricity? Rutherford and Langevin on submarine detection and the invention of sonar. *Notes and Records of the Royal Society*, **66**, 141 LP (2012). 2

[15] RAYLEIGH, J. *The Theory of Sound*. Volumes 1 and 2. Dover Publication, second edition (1945). 2, 7, 8, 22, 25, 41

[16] LAMB, H. On Waves in an Elastic Plate. *Proceedings of the Royal Society A: Mathematical, Physical and Engineering Sciences*, **93**, 114 (1917). 2, 7, 29, 71, 72, 91, 137

[17] SCHOLTE, J. On the stoneley wave equation. *Proceedings of the Koninklijke Nederlandse Akademie van Wetenschappen*, **45**, 20 (1942). 2, 7, 28, 137

[18] BREKHOVSKIKH, L.M. *Waves in Layered Media*, volume 6. Elsevier, first edition (1960). ISBN 0066-5479. 2, 28, 31, 74, 76

[19] WOLF, J., NGOC, T., KILLE, R., AND MAYER, W. Investigation of Lamb waves having a negative group velocity. *The Journal of the Acoustical Society of America*, **83**, 122 (1988). 2, 72

[20] DILIGENT, O. Interaction between fundamental Lamb modes and defects in plates. *Mechanical Engineering*, pages 1–148 (2003). 2, 72

[21] CLORENNEC, D., PRADA, C., AND ROYER, D. Local and noncontact measurements of bulk acoustic wave velocities in thin isotropic plates and shells using zero group velocity Lamb modes. *Journal of Applied Physics*, **101**, 034908 (2007). 2, 72

[22] PRADA, C., CLORENNEC, D., AND ROYER, D. Power law decay of zero group velocity Lamb modes. *Wave Motion*, **45**, 723 (2008). 2, 31, 72, 92, 96

[23] Clorennec, D., Prada, C., and Royer, D. Laser ultrasonic inspection of plates using zero-group velocity lamb modes. *IEEE Transactions on Ultrasonics, Ferroelectrics, and Frequency Control*, **57**, 1125 (2010). 2, 72

[24] Schöpfer, F., Binder, F., Wöstehoff, A., Schuster, T., von Ende, S., Föll, S., and Lammering, R. Accurate determination of dispersion curves of guided waves in plates by applying the matrix pencil method to laser vibrometer measurement data. *CEAS Aeronautical Journal*, **4**, 61 (2013). 2, 72

[25] Kräutkramer, J. and Kräutkramer, H. *Ultrasonic testing of materials.* Springer-Verlag Berlin Heidelberg, fourth edition (1990). ISBN 9783662106808. 2, 50, 59, 72

[26] Jansen, D.P. and Hutchins, D.A. Immersion tomography using Rayleigh and Lamb waves. *Ultrasonics*, **30**, 245 (1992). 2, 72

[27] Jansen, D.P., Hutchins, D.A., and Mottrarn, J.T. Lamb Wave Tomography of Advanced Composite Laminates Containing Damage. *Ultrasonics*, **32**, 83 (1994). 2, 72

[28] Leonard, K.R., Malyarenko, E.V., and Hinders, M.K. Ultrasonic Lamb wave tomography. **18**, 1795 (2002). 2, 71, 72

[29] Yu, L., Leckey, C.A., and Tian, Z. Study on crack scattering in aluminum plates with Lamb wave frequency-wavenumber analysis. *Smart Materials and Structures*, **22**, 065019 (2013). 2, 72

[30] Wang, Q. and Xu, J. Lamb wave tomography technique for crack damage detection. In *Proceedings of the 33rd Chinese Control Conference, CCC 2014*, pages 3094–3099 (2014). ISBN 9789881563842. 2, 71, 72

[31] Rao, J., Ratassepp, M., and Fan, Z. Investigation of the reconstruction accuracy of guided wave tomography using full waveform inversion. *Journal of Sound and Vibration*, **400**, 317 (2017). 2, 72

[32] Helmholtz, H. *On the Sensations of Tone.* Dover Books on Music. Dover Publications (2013). ISBN 9780486315461. 2, 7, 24

[33] Ingard, U. On the Theory and Design of Acoustic Resonators. *The Journal of the Acoustical Society of America*, **25**, 1037 (1953). 2

[34] Rayleigh, L. On waves propagated along the plane surface of an elastic solid. *Proceedings of the London Mathematical Society*, **s1-17**, 4 (1885). 3, 7, 27, 71, 137, 151, 165

## References

[35] Morse, P.M.C. The Transmission of Sound Inside Pipes. *The Journal of the Acoustical Society of America*, **11**, 205 (1939). 3, 151

[36] Anderson, D.V. and Barnes, C. The Dispersion of a Pulse Propagated through a Cylindrical Tube. *The Journal of the Acoustical Society of America*, **25**, 525 (1953). 3, 151

[37] Lastovka, J.B. and Carome, E.F. Experimental Study of Dispersion in Ultrasonic Waveguides. *The Journal of the Acoustical Society of America*, **35**, 1279 (1963). 3, 151

[38] Snow, D. Influence of source characteristics on sound attenuation in a lined circular duct. *Journal of Sound and Vibration*, **37**, 459 (1974). 3, 151

[39] Rao, V.N.R. and Vandiver, J.K. Acoustics of fluid-filled boreholes with pipe: Guided propagation and radiation. *Journal of the Acoustical Society of America*, **105**, 3057 (1999). 3, 151

[40] Muggleton, J.M., Brennan, M.J., and Pinnington, R.J. Wavenumber prediction of waves in buried pipes for water leak detection. *Journal of Sound and Vibration*, **249**, 939 (2003). 3, 151

[41] Robinson, A. *The Last Man Who Knew Everything*. Oneworld Publications, first edition (2006). ISBN 9781851684946. 3

[42] Pesic, P. Thomas Young's Musical Optics: Translating Sound into Light. *Osiris*, **28**, 15 (2013). 3

[43] Perot, A. and Fabry, C. On the application of interference phenomena to the solution of various problems of spectroscopy and metrology. *The Astrophysical Journal*, **9**, 87 (1899). 3, 156

[44] Fabry, C. and Perot, A. On a new form of interferometer. *The Astrophysical Journal*, **13**, 265 (1901). 3, 156

[45] Wood, R.W. On a remarkable case of uneven distribution of light in a diffraction grating spectrum. *Proceedings of the Physical Society of London*, **18**, 269 (1901). 3, 102, 137

[46] Otto, A. Excitation of nonradiative surface plasma waves in silver by the method of frustrated total reflection. *Zeitschrift für Physik*, **216**, 398 (1968). 3, 102, 137

[47] SIGALAS, M. AND ECONOMOU, E. Band structure of elastic waves in two dimensional systems. *Solid State Communications*, **86**, 141 (1993). 3, 102, 137

[48] PENDRY, J.B., MARTÍN-MORENO, L., AND GARCIA-VIDAL, F.J. Mimicking surface plasmons with structured surfaces. *Science*, **305**, 847 (2004). 3, 102, 137

[49] EBBESEN, T., LEZEC, H.J., GHAEMI, H.F., T. THIO, WOLFF, P.A., THIO, T., AND A.WOLFF, P. Extraordinary optical transmission through sub-wavelength hole arrays. *Nature*, **86**, 1114 (1998). 3

[50] CHRISTENSEN, J., MARTIN-MORENO, L., AND GARCIA-VIDAL, F.J. Theory of resonant acoustic transmission through subwavelength apertures. *Physical Review Letters*, **101** (2008). 3, 32

[51] CSELYUSZKA, N., SEČUJSKI, M., ENGHETA, N., AND CRNOJEVIĆ-BENGIN, V. Temperature-controlled acoustic surface waves. *New Journal of Physics*, **18**, 103006 (2016). 3, 32, 137

[52] ALBERT, D.G. Observations of acoustic surface waves in outdoor sound propagation. *The Journal of the Acoustical Society of America*, **113**, 2495 (2003). 3, 137

[53] HESS, P. Surface acoustic waves in materials science. **55**, 42 (2002). 3, 137

[54] HE, Z., JIA, H., QIU, C., YE, Y., HAO, R., KE, M., AND LIU, Z. Nonleaky surface acoustic waves on a textured rigid surface. *Physical Review B - Condensed Matter and Materials Physics*, **83**, 132101 (2011). 3, 138

[55] KELDERS, L., ALLARD, J.F., AND LAURIKS, W. Ultrasonic surface waves above rectangular-groove gratings. *The Journal of the Acoustical Society of America*, **103**, 2730 (1998). 3, 32, 33, 138

[56] ESTRADA, H., CANDELAS, P., BELMAR, F., URIS, A., GARCÍA DE ABAJO, F.J., AND MESEGUER, F. Engineering surface waves in flat phononic plates. *Physical Review B - Condensed Matter and Materials Physics*, **85**, 174301 (2012). 3, 28, 138

[57] CRASTER, R.V. AND GUENNEAU, S. *Acoustic Metamaterials: Negative Refraction, Imaging, Lensing and Cloaking.* Springer (2013). ISBN 9789400748125. 3, 7, 59

[58] CUMMER, S.A., CHRISTENSEN, J., AND ALÙ, A. Controlling sound with acoustic metamaterials. *Nature Reviews Materials*, **1**, 16001 (2016). 3, 41

# References

[59] Ma, G. and Sheng, P. Acoustic metamaterials: From local resonances to broad horizons. *Science Advances*, **2** (2016). 7

[60] Kinsler, L.E., Frey, A.R., Coppens, A.B., and Sanders, J. *Fundamentals of acoustics*. Wiley, fourth edition (1999). ISBN 9780471847892. 8, 10, 11, 12, 21, 23, 24, 139

[61] Cheeke, J.D. and Zagzebski, J. Fundamentals and Applications of Ultrasonic Waves. *American Journal of Physics*, **72**, 719 (2004). 8, 11, 15, 21

[62] Lautrup, B. *Physics of Continuous Matter: Exotic and Everyday Phenomena in the Macroscopic World*. CRC Press, second edition (2011). ISBN 9781420077001. 8, 11, 14, 15, 16, 17, 18, 20

[63] Silvestrelli, P.L. and Parrinello, M. Water Molecule Dipole in the Gas and in the Liquid Phase. *Physical Review Letters*, **82**, 3308 (1999). 8

[64] Atanackovic, T. and Guran, A. *Theory of Elasticity for Scientists and Engineers*. Birkhäuser Basel, first edition (2001). ISBN 9780817640729. 11

[65] Groot, S.R.D. and Mazur, P. *Non-equilibrium thermodynamics*. Dover Publications (2011). ISBN 9780486647418. 11

[66] Morse, P.M.C. and Ingard, K.U. *Theoretical Acoustics*. International series in pure and applied physics. Princeton University Press (1986). ISBN 9780691024011. 11

[67] Nauenberg, M. Proposition 10, Book 2, in the "Principia", revisited. *Archive for History of Exact Sciences*, **65**, 567 (2011). 13

[68] Incropera, F.P., DeWitt, D.P., Bergman, T.L., and Lavine, A.S. *Fundamentals of Heat and Mass Transfer*. Wiley, 7th edition (2007). ISBN 9780470501979. 13

[69] Cramer, O. The variation of the specific heat ratio and the speed of sound in air with temperature, pressure, humidity, and CO2 concentration. *The Journal of the Acoustical Society of America*, **93**, 2510 (1992). 13

[70] COMSOL. Introduction to COMSOL Multiphysics 5.3. *Manual*, page 168 (2014). 14, 25, 64, 65, 66

[71] Touloukian, Y.S., Powel, R.W., Ho, C.Y., and Klemens, P.G. *Thermal conductivity of nonmetallic solids*, volume 2 (1970). ISBN 0306670224. 16

[72] REYNOLDS, O. An Experimental Investigation of the Circumstances Which Determine Whether the Motion of Water Shall Be Direct or Sinuous, and of the Law of Resistance in Parallel Channels. *Philosophical Transactions of the Royal Society of London*, **174**, 935 (1883). 16

[73] BERGGREN, M., BERNLAND, A., AND NORELAND, D. Acoustic boundary layers as boundary conditions. *Journal of Computational Physics*, **371**, 633 (2018). 17, 18

[74] BLUMM, J. AND LINDEMANN, A. Characterization of the thermophysical properties of molten polymers and liquids using the flash technique. *High Temperatures - High Pressures*, **35-36**, 627 (2003). 18

[75] MOTT, P.H. AND ROLAND, C.M. Limits to Poisson's ratio in isotropic materials. *Physical Review B - Condensed Matter and Materials Physics*, **80**, 055404 (2009). 18, 89

[76] EVANS, K.E. Auxetic polymers: a new range of materials. *Endeavour*, **15**, 170 (1991). 18

[77] ASKELAND, D.R., FULAY, P.P., AND WRIGHT, W.J. *The Science and Engineering of Materials*. Cengage Learning, 6th edition (2011). ISBN 9780495668022. 19

[78] BELYTSCHKO, T., LIU, W.K., AND MORAN, B. *Nonlinear Finite Elements For Continua And Structures*, volume 104. Wiley, first edition (2000). ISBN 9780471987741. 19

[79] SLAUGHTER, W.S. *The Linearized Theory of Elasticity*. Birkhäuser Boston, first edition (2002). ISBN 9780817641177. 19

[80] VOIGT, W. *Lehrbuch der Kristallphysik (mit Ausschluss der Kristalloptik)*. Vieweg+Teubner Verlag, first edition (1966). ISBN 9783663158844. 20

[81] ÖCHSNER, A. *Continuum Damage and Fracture Mechanics*. Springer, Singapore, first edition (2016). ISBN 9789812878656. 20

[82] FAHY, F.J. AND SCHOFIELD, C. A note on the interaction between a Helmholtz resonator and an acoustic mode of an enclosure. *Topics in Catalysis*, **72**, 365 (1980). 24

# References

[83] ESTÈVE, S.J. AND JOHNSON, M.E. Reduction of sound transmission into a circular cylindrical shell using distributed vibration absorbers and Helmholtz resonators. *The Journal of the Acoustical Society of America*, **112**, 2840 (2002). 24

[84] ESTÈVE, S.J. AND JOHNSON, M.E. Adaptive Helmholtz resonators and passive vibration absorbers for cylinder interior noise control. *Journal of Sound and Vibration*, **288**, 1105 (2005). 24

[85] ROWLEY, C.W. AND WILLIAMS, D.R. Dynamics and control of high-Reynolds-number flow over open cavities. *Annual Review of Fluid Mechanics*, **38**, 251 (2005). 24

[86] DAI, X., JING, X., AND SUN, X. Flow-excited acoustic resonance of a helmholtz resonator: Discrete vortex model compared to experiments. *Physics of Fluids*, **27**, 057102 (2015). 24

[87] RAYLEIGH, J.W.S.B. AND SPOTTISWOODE, W. On the theory of resonance. **161**, 77 (1871). 25

[88] JONES, A.T. End corrections of organ pipes. *The Journal of the Acoustical Society of America*, **12**, 387 (1941). 25

[89] ANDERSON, S.H. AND OSTENSEN, F.C. Effect of frequency on the end correction of pipes. *Physical Review*, **31**, 267 (1928). 25

[90] ROSSING, T. AND FLETCHER, N.H. *Principles of Vibration and Sound.* Springer, New York, second edition (2004). ISBN 9781475738223. 26, 152

[91] VRAHATIS, M.N., GRAPSA, T.N., RAGOS, O., AND ZAFIROPOULOS, F.A. On the localization and computation of zeros of Bessel functions. *ZAMM Zeitschrift fur Angewandte Mathematik und Mechanik*, **77**, 467 (1997). 26

[92] HESS, P. Surface acoustic waves in materials science. *Physics Today*, **55**, 42 (2002). 27, 101

[93] COLOMBI, A., COLQUITT, D., ROUX, P., GUENNEAU, S., AND CRASTER, R.V. A seismic metamaterial: The resonant metawedge. *Scientific Reports*, **6**, 27717 (2016). 28

[94] COLOMBI, A., AGEEVA, V., SMITH, R.J., CLARE, A., PATEL, R., CLARK, M., COLQUITT, D., ROUX, P., GUENNEAU, S., AND CRASTER, R.V. Enhanced sensing and conversion of ultrasonic Rayleigh waves by elastic metasurfaces. *Scientific Reports*, **7**, 6750 (2017). 28

[95] BERGMANN, L. AND HATFIELD, H. Ultrasonics and their scientific and technical applications (1942). 28

[96] BRIGGS, A. Acoustic microscopy-a summary. *Reports on Progress in Physics*, **55**, 851 (1992). 28

[97] MALISCHEWSKY, P.G. Comparison of approximated solutions for the phase velocity of Rayleigh waves (Comment on 'Characterization of surface damage via surface acoustic waves') (2005). 28

[98] ZHU, J., POPOVICS, J.S., AND SCHUBERT, F. Leaky Rayleigh and Scholte waves at the fluid–solid interface subjected to transient point loading. *The Journal of the Acoustical Society of America*, **116**, 2101 (2004). 30

[99] MERMIN AND ASHCROFT. *Solid State Physics*. Holt, Rinehart and Winston (1976). ISBN 9780030839931. 31

[100] KITTEL, C. *Introduction to Solid State Physics*, volume 8. John Wiley and Sons, 8th edition (2004). ISBN 047141526X. 31, 36, 37

[101] MOULIN, S.G., ASSAAD, J., DELEBARRE, C., BLANQUET, P., AND EMMANUEL. The propagation of Lamb waves in multilayered plates: phase-velocity measurement. *Measurement Science and Technology*, **10**, 348 (1999). 31

[102] DAYAL, V. AND KINRA, V.K. Leaky Lamb waves in an anisotropic plate. I: An exact solution and experiments. *The Journal of the Acoustical Society of America*, **85**, 2268 (1989). 32

[103] CUI, W.K.C., WU, L.T., ZHANG, C., SONG, G.Y., KE, J.C., CHENG, Q., AND JUN, T. Acoustic surface waves on three-dimensional groove gratings with sub-wavelength thickness. *Applied Physics Express*, **11**, 87301 (2018). 32

[104] WANG, X. Acoustical mechanism for the extraordinary sound transmission through subwavelength apertures. *Applied Physics Letters*, **96**, 134104 (2010). 33

[105] IVANOV-SHITS, K. AND ROZHIN, F. Investigation of surface waves in air. *Soviet Physics Acoustics*, **5**, 510 (1959). 34

[106] VAN DER MOLEN, K.L., SEGERINK, F.B., VAN HULST, N.F., AND KUIPERS, L. Influence of hole size on the extraordinary transmission through subwavelength hole arrays. *Applied Physics Letters*, **85**, 4316 (2004). 36

## References

[107] ESTRADA, H., CANDELAS, P., URIS, A., BELMAR, F., GARCÍA DE ABAJO, F.J., AND MESEGUER, F. Extraordinary Sound Screening in Perforated Plates. *Physical Review Letters*, **101**, 84302 (2008). 36

[108] HOU, B., MEI, J., KE, M., LIU, Z., SHI, J., AND WEN, W. Experimental determination for resonance-induced transmission of acoustic waves through subwavelength hole arrays. *Journal of Applied Physics*, **104** (2008). 36

[109] ESTRADA, H., GARCÍA DE ABAJO, F.J., CANDELAS, P., URIS, A., BELMAR, F., AND MESEGUER, F. Angle-Dependent Ultrasonic Transmission through Plates with Subwavelength Hole Arrays. *Physical Review Letters*, **102**, 144301 (2009). 36

[110] LURTON, X. Underwater acoustic wave propagation. *An Introduction to Underwater Acoustics: Principles and Applications*, pages 13–74 (2002). 41, 46

[111] WILLIAMS, E.G. *Fourier acoustics*. First edition (1999). ISBN 0127539603. 41, 59, 74, 93, 105

[112] RAZA, I., IANNUCCI, L., AND CURTIS, P. Additive manufacturing of locally resonant composite metamaterials. In *ECCM 2016 - Proceeding of the 17th European Conference on Composite Materials* (2016). ISBN 9783000533877. 41

[113] PARMENTER, K.E. AND MILSTEIN, F. Mechanical properties of silica aerogels. *Journal of Non-Crystalline Solids*, **223**, 179 (1998). 42

[114] BIGNELL, M.T., GIRARD, G., DAVIS, R., PEUTO, A., AND N. Recommended table for the density of water between 0 ℃ and 40 ℃ based on recent experimental reports. *Metrologia*, **38**, 301 (2001). 42

[115] PICARD, A., DAVIS, R.S., GLÄSER, M., AND FUJII, K. Revised formula for the density of moist air (CIPM-2007). *Metrologia*, **45**, 149 (2008). 42

[116] KIM, S. AND LEE, C.W. A Review on Manufacturing and Application of Open-cell Metal Foam. *Procedia Materials Science*, **4**, 305 (2014). 42

[117] BYAKOVA, A., BEZIM'YANNY, Y., GNYLOSKURENKO, S., AND NAKAMURA, T. Fabrication Method for Closed-cell Aluminium Foam with Improved Sound Absorption Ability. *Procedia Materials Science*, **4**, 9 (2014). 42

[118] VAHIDIFAR, A., NOURI KHORASANI, S., PARK, C.B., NAGUIB, H.E., AND KHONAKDAR, H.A. Fabrication and Characterization of Closed-Cell Rubber Foams Based on Natural Rubber/Carbon Black by One-Step Foam Processing. *Industrial & Engineering Chemistry Research*, **55**, 2407 (2016). 42

[119] ALTINTAS, Y. *Manufacturing automation-metal cutting mechanics-machine tool vibrations and CNC design*, volume 227. Cambridge University Press, second edition (1987). ISBN 9780511843723. 43

[120] ROBINSON, H.A. AND HUMBLE, H.A. Sacrificial anode system for protecting metals in sea water (1951). US Patent 2,571,062. 43

[121] Neptune Sonar Ltd. `http://www.neptune-sonar.co.uk/` (Accessed: 2018-06-10). 44, 46

[122] Precision Acoustics - Ultrasound Acoustics. `https://www.acoustics.co.uk/` (Accessed: 2018-06-10). 46

[123] Home - Brüel & Kjær Sound & Vibration. `https://www.bksv.com/en` (Accessed: 2018-06-10). 46, 73, 92

[124] PC Oscilloscope, Data Logger & RF Products — Pico Technology. `https://www.picotech.com/` (Accessed: 2018-06-10). 49

[125] BLITZ, J. AND SIMPSON, G. *Ultrasonic Methods of Non-destructive Testing*. Non-Destructive Evaluation Series. Springer Netherlands (1995). ISBN 9780412604706. 50

[126] BERANEK, L. AND SLEEPER, H. The Design and Construction of Anechoic Sound Chambers. *Journal Acoustical Society of America*, **18**, 140 (1946). 50

[127] SUN, D., JIN, C., VAN SCHAIK, A., AND CABRERA, D. The design and evaluation of an economically constructed anechoic chamber. *Architectural Science Review*, **52**, 312 (2009). 50

[128] MYLAVARAPU, P., LI, G., GUPTA, N., MAHARSIA, R., AND WOLDESENBET, E. Ultrasonic Signal Attenuation in Syntactic Foams Filled With Rubber Particles. In *Nondestructive Evaluation Engineering*, volume 2004, pages 25–29 (2004). ISBN 0-7918-4716-0. 50

[129] Model 7500 DC to 1MHz Wideband Power Amplifier Operating Manual. Technical report (2004). 52

[130] WA301 Waveform Amplifiers — Aim-TTi International. `https://www.aimtti.com/product-category/waveform-amplifiers/aim-wa301` (Accessed: 2018-08-20). 52

[131] RSTUDIO TEAM. RStudio: Integrated Development for R. RStudio (2015). 59

# References

[132] LANDAU, H.J. Sampling, data transmission, and the Nyquist rate. *Proceedings of the IEEE*, **55**, 1701 (1967). 61

[133] HOVDEN, R., JIANG, Y., XIN, H.L., AND KOURKOUTIS, L.F. Periodic Artifact Reduction in Fourier Transforms of Full Field Atomic Resolution Images. *Microscopy and Microanalysis*, **21**, 436 (2014). 63, 74, 93

[134] HOROWITZ, S.B., SHEPLAK, M., CATTAFESTA, L.N., AND NISHIDA, T. A MEMS acoustic energy harvester. *Journal of Micromechanics and Microengineering*, **16**, S174 (2006). 71, 150

[135] OLINER, A.A. Waveguides for acoustic surface waves: A review. *Proceedings of the IEEE*, **64**, 615 (1976). 71, 150

[136] POLET, J. AND KANAMORI, H. Upper-mantle shear velocities beneath southern California determined from long-period surface waves. *Bulletin of the Seismological Society of America*, **87**, 200 (1997). 72

[137] YANG, Y., RITZWOLLER, M.H., LEVSHIN, A.L., AND SHAPIRO, N.M. Ambient noise Rayleigh wave tomography across Europe. *Geophysical Journal International*, **168**, 259 (2007). 72

[138] ALLEYNE, D.N. AND CAWLEY, P. A 2-dimensional Fourier transform method for the quantitative measurement of Lamb modes. In *IEEE Symposium on Ultrasonics*, pages 1143–1146 vol.2 (1990). 72

[139] CAMBRIDGE UNIVERSITY ENGINEERING DEPARTMENT. Materials data book. *Materials Courses*, pages 1–41 (2003). 73

[140] VALENCIA, J. AND QUESTED P.N. Thermophysical properties. *ASM Handbook: Casting*, **15**, 468 (2008). 73

[141] HIBBELER, R. *Mechanics of Materials*, volume 8. Pearson, 9th edition (2013). ISBN 9780133254426. 73

[142] TEAM VAN MATWEB (LLC), DRIVE, .K., 3005, S., AND BLACKSBURG, V..U. MatWeb (2014). 73

[143] KOLEVA, M. Polymethyl Methacrylate (PMMA). *Kunststoffe International*, **2014**, 59 (2014). 73

[144] CASTAINGS, M. AND HOSTEN, B. The use of electrostatic, ultrasonic, air-coupled transducers to generate and receive lamb waves in anisotropic, viscoelastic plates. *Ultrasonics*, **36**, 361 (1998). Ultrasonics International 1997. 73, 80

[145] PODDER, P., KHAN, T.Z., KHAN, M.H., AND RAHMAN, M.M. Comparative Performance Analysis of Hamming, Hanning and Blackman Window. *International Journal of Computer Applications*, **96**, 975 (2014). 74, 93

[146] AG-Xplus Series: Shimadzu Corporation. `https://www.shimadzu.com/an/test/universal/ag-xplus/ag-xplus.html` (Accessed: 2018-08-07). 85, 86

[147] AMERICAN SOCIETY FOR TESTING AND MATERIALS. *ASTM E8 / E8M-16a: Standard Test Methods for Tension Testing of Metallic Materials* (2016). ISBN 5935522004. 86

[148] TOFELDT, O. AND RYDEN, N. Zero-group velocity modes in plates with continuous material variation through the thickness. *The Journal of the Acoustical Society of America*, **141**, 3302 (2017). 92

[149] PHILIPPE, F.D., MURRAY, T.W., AND PRADA, C. Focusing on Plates: Controlling Guided Waves using Negative Refraction. *Scientific Reports*, **5**, 11112 (2015). 92, 96

[150] GÉRARDIN, B., LAURENT, J., PRADA, C., AND AUBRY, A. Negative reflection of Lamb waves at a free edge: Tunable focusing and mimicking phase conjugation. *The Journal of the Acoustical Society of America*, **140**, 591 (2016). 92, 96

[151] NEDOSPASOV, I.A., MOZHAEV, V.G., AND KUZNETSOVA, I.E. Unusual energy properties of leaky backward Lamb waves in a submerged plate. *Ultrasonics*, **77**, 95 (2017). 92

[152] STOBBE, D.M. AND MURRAY, T.W. Conical dispersion of Lamb waves in elastic plates. *Physical Review B*, **96**, 144101 (2017). 92

[153] AANES, M., LOHNE, K.D., LUNDE, P., AND VESTRHEIM, M. Finite aperture influence on energy concentration, frequency shift, and signal enhancement, for acoustic transmission in the negative group velocity region of the $S_1$ leaky Lamb mode. In *2016 IEEE International Ultrasonics Symposium (IUS)*, pages 1–4 (2016). ISBN 1948-5727. 92

[154] MEI, J., HOU, B., KE, M., PENG, S., JIA, H., LIU, Z., SHI, J., WEN, W., AND SHENG, P. Acoustic wave transmission through a bull's eye structure. *Applied Physics Letters*, **92**, 124106 (2008). 92

[155] CHIOU, M.J., LIN, Y.C., ONO, T., ESASHI, M., YEH, S.L., AND WU, T.T. Focusing and waveguiding of Lamb waves in micro-fabricated piezoelectric phononic plates. *Ultrasonics*, **54**, 1984 (2014). 92, 164

# References

[156] CLAEYS, J.M., LEROY, O., JUNGMAN, A., AND ADLER, L. Diffraction of ultrasonic waves from periodically rough liquid–solid surface. *Journal of Applied Physics*, **54**, 5657 (1983). 102

[157] MOISEYENKO, R.P., BENCHABANE, S., LAUDE, V., LIU, J., AND DECLERCQ, N.F. Scholte-Stoneley waves on 2D phononic crystal gratings. In *2012 Proceedings of the International Conference Days on Diffraction*, pages 178–182 (2012). 102

[158] DECLERCQ, N.F., TEKLU, A., BREAZEALE, M.A., BRIERS, R., LEROY, O., DEGRIECK, J., AND SHKERDIN, G.N. Study of the scattering of leaky Rayleigh waves at the extremity of a fluid-loaded thick plate. *Journal of Applied Physics*, **96**, 5836 (2004). 102

[159] LEDUC, D., HLADKY, A.C., MORVAN, B., IZBICKI, J.L., AND PAREIGE, P. Propagation of Lamb waves in a plate with a periodic grating: Interpretation by phonon. *The Journal of the Acoustical Society of America*, **118**, 2234 (2005). 102

[160] LIU, C.L., KE, M., ZHANG, S., PENG, S., QIU, C., AND ZHENGYOU. Guiding spoof surface acoustic waves on a monolayer array of rigid cylinders in water. *Journal of Physics D: Applied Physics*, **49**, 125304 (2016). 102

[161] WU, L.T., SONG, G.Y., CAO, W.K., CHENG, Q., CUI, T.J., AND JING, Y. Generation of multiband spoof surface acoustic waves via high-order modes. *Physics Review B*, **97**, 214305 (2018). 102

[162] YUAN, S.M., MA, T.X., CHEN, A.L., AND WANG, Y.S. Liquid-assisted tunable metasurface for simultaneous manipulation of surface elastic and acoustic waves. *AIP Advances*, **8**, 35026 (2018). 102

[163] HESSEL, A., CHEN, M.H., LI, R.C.M., AND OLINER, A.A. Propagation in periodically loaded waveguides with higher symmetries. *Proceedings of the IEEE*, **61**, 183 (1973). 122

[164] XIE, S., OUYANG, S., HE, Z., WANG, X., DENG, K., AND ZHAO, H. Bending and splitting of spoof surface acoustic waves through structured rigid surface. *Results in Physics*, **8**, 52 (2018). 130

[165] SCHOLTE, J.G. The range of existence of Rayleigh and Stoneley waves. *Geophysical Journal International*, **5**, 120 (1947). 137

[166] HOLMES, M.J., PARKER, N.G., AND POVEY, M.J.W. Temperature dependence of bulk viscosity in water using acoustic spectroscopy. *Journal of Physics: Conference Series*, **269**, 012011 (2011). 140

[167] John M. Holt. Structural alloys handbook. *Purdue university*, **1**, 45 (1996). 140

[168] Biot, M.A. Propagation of elastic waves in a cylindrical bore containing a fluid. *Journal of Applied Physics*, **23**, 997 (1952). 145

[169] Collins, J. and Grant, P. The role of surface acoustic wave technology in communication systems. *Ultrasonics*, **10**, 59 (1972). 150

[170] Jacobi, W.J. Propagation of Sound Waves along Liquid Cylinders. *The Journal of the Acoustical Society of America*, **21**, 120 (1949). 151

[171] Baik, K., Jiang, J., and Leighton, T.G. Acoustic attenuation, phase and group velocities in liquid-filled pipes: Theory, experiment, and examples of water and mercury. *The Journal of the Acoustical Society of America*, **128**, 2610 (2010). 151

[172] Jiang, J., Baik, K., and Leighton, T.G. Acoustic attenuation, phase and group velocities in liquid-filled pipes II: Simulation for spallation neutron sources and planetary exploration. *The Journal of the Acoustical Society of America*, **130**, 695 (2011). 151

[173] Baik, K., Jiang, J., and Leighton, T.G. Acoustic attenuation, phase and group velocities in liquid-filled pipes III: Nonaxisymmetric propagation and circumferential modes in lossless conditions. *The Journal of the Acoustical Society of America*, **133**, 1225 (2013). 151

[174] Vakil, A. and Engheta, N. Transformation Optics Using Graphene. *Science*, **332**, 1291 LP (2011). 161

[175] Mann, C.R., Sturges, T.J., Weick, G., Barnes, W.L., and Mariani, E. Manipulating type-I and type-II Dirac polaritons in cavity-embedded honeycomb metasurfaces. *Nature Communications*, **9**, 2194 (2018). 161

[176] Dautova, Y.N., Shytov, A.V., Hooper, I.R., Sambles, J.R., and Hibbins, A.P. Gapless states in microwave artificial graphene. *Applied Physics Letters*, **110**, 261605 (2017). 161

[177] Khanikaev, A.B., Fleury, R., Mousavi, S.H., and Alù, A. Topologically robust sound propagation in an angular-momentum-biased graphene-like resonator lattice. *Nature Communications*, **6**, 8260 (2015). 161

# References

[178] Sun, J.H. and Wu, T.T. Propagation of surface acoustic waves through sharply bent two-dimensional phononic crystal waveguides using a finite-difference time-domain method. *Physical Review B*, **74**, 174305 (2006). 164

[179] Mousavi, S.H., Khanikaev, A.B., and Wang, Z. Topologically protected elastic waves in phononic metamaterials. *Nature Communications*, **6**, 8682 (2015). 164

[180] Edelman, I. Surface waves at vacuum/porous medium interface: low frequency range. *Wave Motion*, **39**, 111 (2004). 165

[181] Zhang, Y., Xu, Y., and Xia, J. Analysis of dispersion and attenuation of surface waves in poroelastic media in the exploration-seismic frequency band. *Geophysical Journal International*, **187**, 871 (2011). 165

[182] Adler, L. and Nagy, P.B. Measurements of acoustic surface waves on fluid-filled porous rocks. *Journal of Geophysical Research: Solid Earth*, **99**, 17863 (2018). 165

[183] Joshi, S.G. Flow sensors based on surface acoustic waves. *Sensors and Actuators A: Physical*, **44**, 191 (1994). 166

[184] Kondoh, S.I., Sugimoto, M., Matsui, Y., and Jun. Study of Surface Acoustic Wave Streaming Phenomenon Based on Temperature Measurement and Observation of Streaming in Liquids. *Japanese Journal of Applied Physics*, **46**, 4718 (2007). 166

[185] Singh, R., Sankaranarayanan, S.K.R.S., and Bhethanabotla, V.R. Enhancement of acoustic streaming induced flow on a focused surface acoustic wave device: Implications for biosensing and microfluidics. *Journal of Applied Physics*, **107**, 24503 (2010). 166

[186] Brunet, T., Merlin, A., Mascaro, B., Zimny, K., Leng, J., Poncelet, O., Aristégui, C., and Mondain-Monval, O. Soft 3D acoustic metamaterial with negative index. *Nature Materials*, **14**, 384 (2014). 166

[187] Casarini, C., Windmill, J.F.C., and Jackson, J.C. 3D printed small-scale acoustic metamaterials based on Helmholtz resonators with tuned overtones. In *2017 IEEE Sensors*, pages 1–3 (2017). 166